VORTICES IN DIPOLAR QUANTUM GASES OF DYSPROSIUM

Studies of superfluidity in exotic quantum matter

by

Lauritz Klaus

Dissertation

submitted to the University of Innsbruck
– Faculty of Mathematics, Computer Science and Physics –
in partial fulfilment of the requirements for the degree of

Doctor of Philosophy – Doktorratsstudium Physik

Advisor
Univ.-Prof. Dr. Francesca Ferlaino
Institute for Experimental Physics, University of Innsbruck
Institute for Quantum Optics and Quantum Information (IQOQI) – Austrian Academy of Science

Co-Advisor
Univ.-Prof. Dr. Rudolf Grimm
Institute for Experimental Physics, University of Innsbruck
Institute for Quantum Optics and Quantum Information (IQOQI) – Austrian Academy of Science

Innsbruck, January 2025

To my supporting parents,
my inspiring brother
and
my love, who has carried me through

Figure 1: Under the Wave off Kanagawa (Kanagawa oki nami ura), Katsushika Hokusai (ca. 1830–32). Taken from the Metropolitan Museum of Art open access library.

> *But even so, amid the tornadoed Atlantic of my being, do I myself still for ever centrally disport in mute calm; and while ponderous planets of unwaning woe revolve round me, deep down and deep inland there I still bathe me in eternal mildness of joy.*
>
> ***Ishmael***
> *Moby Dick by Herman Melville (1851)*

Synopsis

Ultracold quantum gases are driving the study of new exotic phases of matter and are promising platforms for quantum simulations. Most quantum gas experiments have focused on working with alkali and alkaline earth atoms with predominantly short-range isotropic interactions. More recently, the creation of quantum gases of strongly magnetic atoms such as dysprosium and erbium has allowed the study of systems with additional dipole-dipole interactions. These interactions are long-range and anisotropic.

A hallmark feature of superfluids undergoing rotation are quantized vortices. These vortices appear in quantum gases as holes in the density distribution and have been studied since the early days of the field. They play a crucial role not only in quantum gases but also in many other systems, such as superconductors or neutron stars.

This thesis has two main topics. The first part reports on the first nucleation of quantised vortices in a rotating dipolar Bose-Einstein condensates. To achieve this, a new technique has been developed, called magnetostirring, where angular momentum is imparted to the dipolar condensate by exploiting the anisotropy of the dipole-dipole interactions. It is also shown that the vortices arrange themselves in a striped configuration along an external magnetic field, in contrast to the triangular Abrikosov lattice for non-dipolar BECs.

The second topic concerns the superfluid nature of the quantum gas in the supersolid state. When the contact and dipolar interaction strengths are similar, trapped dysprosium spontaneously exhibits spatial modulation and is globally coherent. This state is called supersolid, because it shows both solid and superfluid properties. The reported work is concerned with confirming the superfluid nature of the supersolid. The foundation for this work is the first realisation of a cylindrical symmetric 2D supersolid. An approach to quantify the superfluid fraction of this state is described, following a proposal by Leggett, by exciting angular oscillations such as the scissors mode. However, the complex excitation spectrum of the supersolid makes it difficult to access the superfluid fraction experimentally. Finally, the direct proof of the superfluid nature is given by the observation of quantised vortices in the rotating supersolid. This work opens the door to further studies of vortices in supersolid systems and may in the future serve as a test bed for other complex vortex systems, such as superconductors or neutron stars.

Zusammenfassung

Ultrakalte Quantengase treiben die Erforschung neuer exotischer Zustände der Materie voran und sind vielversprechende Plattformen für Quantensimulationen. Die meisten Quantengasexperimente konzentrierten sich auf die Arbeit mit Alkali- und Erdalkaliatomen mit überwiegend isotropen Wechselwirkungen über kurze Distanzen. In jüngerer Zeit hat die Erzeugung von Quantengasen aus stark magnetischen Atomen wie Dysprosium und Erbium die Untersuchung von Systemen mit zusätzlichen Dipol-Dipol-Wechselwirkungen ermöglicht. Diese Wechselwirkungen sind langreichweitig und anisotrop.

Ein charakteristisches Merkmal von Supraflüssigkeiten, die rotiert werden, sind quantisierte Vortices. Diese Vortices treten in Quantengasen als Löcher in der Dichteverteilung auf und werden seit den Anfängen des Fachgebiets untersucht. Sie spielen nicht nur in Quantengasen, sondern auch in vielen anderen Systemen, wie Supraleitern oder Neutronensternen, eine entscheidende Rolle.

Diese Arbeit hat zwei Hauptthemen. Der erste Teil berichtet über die erste Nukleierung von quantisierten Vortices in einem rotierenden dipolaren Bose-Einstein-Kondensat. Um dies zu erreichen, wurde eine neue Technik entwickelt, die als Magnetostirring bezeichnet wird und bei der dem dipolaren Kondensat einen Drehimpuls verliehen wird, indem die Anisotropie der Dipol-Dipol-Wechselwirkungen ausgenutzt wird. Es wird auch gezeigt, dass sich die Vortices in einer streifenförmigen Konfiguration entlang eines externen Magnetfeldes anordnen, im Gegensatz zum dreieckigen Abrikosov-Gitter bekannt von nicht-dipolare BECs.

Das zweite Thema betrifft die supraflüssige Natur des Quantengases im suprafesten Zustand. Wenn die Stärke der Kontaktwechselwirkung und der dipolaren Wechselwirkung ähnlich sind, zeigt das gefangene Dysprosium spontan eine räumliche Modulation und ist global kohärent. Dieser Zustand wird als suprafest bezeichnet, da er sowohl feste als auch superfluide Eigenschaften aufweist. In der vorliegenden Arbeit geht es darum, die supraflüssige Natur des Suprafestkörpers zu bestätigen. Die Grundlage für diese Arbeit ist die erste Realisierung eines zylindersymmetrischen 2D-Suprafestkörpers. Ein Ansatz zur Quantifizierung des supraflüssigen Anteils dieses Zustands wird, einem Vorschlag von Leggett folgend, durch Anregung von Rotationsschwingungen wie der Scherenmode beschrieben. Das komplexe Anregungsspektrum des Suprafestkörpers erschwert jedoch den experimentellen Zugang zum suprafluiden Anteil. Der direkte Beweis für die supraflüssige Natur wird schließlich durch die Beobachtung von quantisierten Vortices in dem rotierenden Suprasfestkörper erbracht. Diese Arbeit öffnet die Tür für weitere Untersuchungen von Vortices in suprafesten Systemen und könnte in Zukunft als Testumgebung für andere komplexe

Vortexsysteme dienen, wie z. B. Supraleiter oder Neutronensterne.

Publications

Some of the concepts and results presented in this thesis have appeared previously within the following publications:

M. Sohmen, C. Politi, **L. Klaus**, L. Chomaz, M. J. Mark, M. A. Norcia, F. Ferlaino. *Birth, life, and death of a dipolar supersolid.* Physical Review Letters 126 (23), 233401 (2021) DOI: 10.1103/PhysRevLett.126.233401

M. A. Norcia[†], C. Politi[†], **L. Klaus**, E. Poli, M. Sohmen, M. J. Mark, R. N. Bisset, L. Santos, F. Ferlaino. *Two-dimensional supersolidity in a dipolar quantum gas.* Nature 596 (7872), 357-361 (2021). DOI: 10.1038/s41586-021-03725-7

E. Poli, T. Bland, C. Politi, **L. Klaus**, M. A. Norcia, F. Ferlaino, R. N. Bisset, L. Santos. *Maintaining supersolidity in one and two dimensions.* Physical Review A 104 (6), 063307 (2021) DOI: 10.1103/PhysRevA.104.063307

T. Bland, E. Poli, C. Politi, **L. Klaus**, M. A. Norcia, F. Ferlaino, L. Santos, R. N. Bisset. *Two-dimensional supersolid formation in dipolar condensates.* Physical Review Letters 128 (19), 195302 (2022) DOI: 10.1103/PhysRevLett.128.195302

M. A. Norcia, E. Poli, C. Politi, **L. Klaus**, T. Bland, M. J. Mark, L. Santos, R. N. Bisset, F. Ferlaino. *Can angular oscillations probe superfluidity in dipolar supersolids?.* Physical Review Letters 129 (4), 040403 (2022). DOI: 10.1103/PhysRevLett.129.040403

L. Klaus[†], T. Bland[†], E. Poli, C. Politi, G. Lamporesi, E. Casotti, R. N. Bisset, M. J. Mark, F. Ferlaino. *Observation of vortices and vortex stripes in a dipolar condensate.* Nat. Phys. 18, 1453–1458 (2022). DOI: 10.1038/s41567-022-01793-8

E. Casotti[†], E. Poli[†], **L. Klaus**, A. Litvinov, C. Ulm, C. Politi, M. J. Mark, T. Bland, F. Ferlaino. *Observation of vortices in a dipolar supersolid.* Nature 635, 327–331 (2024). DOI: 10.1038/s41586-024-08149-7

[†] The authors contributed equally.

Acknowledgments

When I was still in school I always dreamed of being a scientist exploring the yet unknown. But at that point I would have never thought that I actually end up working in a laboratory and writing papers that are published in scientific journals. And the truth is that I still feel anxious about new ideas to try in the experiment, which could eventually turn into projects. What if it does not work as expected? Do I do something wrong experimentally or do I not understand the physics enough and the idea is doomed to never work? These moments of doubts may probably stay with me, but what I get to understand during my time in Innsbruck is that science is not done by isolated scientists, working alone on their field of expertise. Science involves multiple people to design, build and run complex experimental machines. Science involves many discussions on what the most pressing research topics are, how to implement them experimentally, and how to interpret the resulting data. And science involves reaching outside of your own research group, talking with people working in other experiments, and getting inspired with new solutions and new ideas. In this way, the results presented in this thesis are not only the product of my own work, but that of many people whom I want to thank as best I can.

First of all I want to thank *Francesca Ferlaino* who gave me the opportunity to do my Ph.D. in her group and trusted me with working in her laboratory. I am very grateful for her scientific guidance towards new and interesting research direction and although some of the projects were very complex and needed some time and optimisation to get to work, we got the time and the trust to finish them. I am also glad that I was able to work in such a well planned experiment and that all necessary maintenance and extensions were met with immediate support. I am also grateful for the opportunities to go to many international conferences to share our results and speak to colleagues, which was stimulating and highly motivating.

Also thanks to my Cosupervisor *Rudolf Grimm* and for jumping in in the last moment due to some complications.

I also want to thank our senior scientist *Manfred Mark* for all the support, especially when it came to technical questions in the laboratory. Your experience helped us in countless discussions about the implementation of new optical setups prevent otherwise certain errors and design flaws. Although some discussions spiraled into new designs of which the implementation seemed to need more than a single Ph.D. lifetime.

I am so grateful for all the Ph.D.s and Postdocs who worked together with me on the experiments. I want to start with my former peers who have welcomed me to the group and have been such great and kind mentors. Thanks to *Maximilian Sohmen*, for your inspiring love of science and all the support. So much of the success of the experiment goes back to your designs. Thanks to *Claudia Politi* for working with me in the lab in the first half of my Ph.D. and guiding me towards mastering the experiment. Whatever question I had about whatever obscure detail of the experiments or numbers that were needed, you somehow remembered it from your head, which was always mind boggling to me. And I have to thank *Matthew Norcia*, who just started his postdoc in the Ferlaino group before me and was a great scientist and coordinator of the lab. He was always there for us finding quick solutions if the experiment was not working, always able to explain the newest data on the Bloch sphere and overall he is just an incredible experimental physicist. It was very inspiring to work with him on this experiment and I strive towards becoming such a great postdoc in the future myself. I just started a few weeks before the Covid pandemic struck Austria and they were my biggest point of contact during this time and I could not imaging it with anyone else. Thanks for the productive but especially enjoyable time, even though lunch breaks had to be outside in freezing cold and the bit of mockery about my small addiction to the Bresso spread and yoghurts. Thanks for being not only colleagues but friends as well after work and the great times we had going mountain biking or playing volleyball. Thanks for inviting to the infamous pizza at Claudia and Gabriele's place and sometimes just having some drinks.

I am so thankful for my current colleagues who have accompanied me to this point and who will continue the experiment and surely discover many great and new phenomena. Thanks to *Eva Casotti* to be such a great lab partner who brings the necessary patients and perseverance that I was lacking in frustrating days. Thanks to *Clemens Ulm* who joined the lab when I was already the 'old guy' in the group. You brought fresh air to the experiment and hinted to all the small and large flaws of the experiments that I learned to ignore over the years. And thanks to *Andrea Litvinov* who has been a great postdoc in the last years, inspiring new perspectives and with such endurance find even small signatures of interesting physics in the noisy data we sometimes produce. I am especially thankful to him for helping me in the final steps of the writing of this thesis, forming an incoherent mess of a first draft into something I am now proud of. I am so glad having them as colleague not just for all the science adventures we went through but also the social value they brought to the group. Thanks for all the 9b-eers and short detours to Treibhaus, long nights watching the superbowl or meeting you at Copacabana. Thanks for spontaneous trips to Croatia and great costume parties. Thanks for introducing of gouter to the lab, songs on infinite loop and the secret walls of shame. Also thanks for organising

together the probably best but slightly miscalculated barbecue during our time.
I also want to acknowledge *Arno Trautmann, Philipp Ilzhofer and Gianmaria Durastane* who were already finishing their work in the group when I joined, but who set up the experiment in the first place and without who the scientific results we got would obviously not have been possible. Until now, the screws that were fastened to their absolute limit into the table and the water system implemented hold this experiment together.
I am also glad that I started during a time when also the theory branch of the Ferlaino group was implemented. The first members of this branch, *Elena Poli* and *Thomas Bland*, have been crucial to understanding all the results that we saw in our experiment in the last years. I am so grateful for all the projects we work on together and that I could discuss with them all the stupid and trivial questions that crossed my mind. And even when it was not directly about science, I enjoyed the time we had. Traveling overseas to the conferences would certainly have been magnitudes less enjoyable without them. I enjoyed hunting for snakes, crocodiles, and cheap hostel rooms, honouring famous film sites and running in the morning through the flooded Miami Beach. And thanks for the great memories of our great trip to Boston witnessing an amazing whale watching tour and how shockingly in touch certain people are with the greatest in our research field.
I also want to acknowledge our Master student *Nefeli Ioli Sonnberger* as well as all the Bachelor students and interns who helped us during my time in the laboratory. It was always motivating to see everyone else so motivated and excited about our research. I hope I could give them the support they needed to become great experimental scientists as I received support from Ph.D. students when I was studying. I definitely learned a lot in this years.
And I want to thank all the current and former members of Ferlaino group. Thanks to *Arfor Houwman, Louis Lafforgue, Sarah Embacher, Ferdinand Claude, Gabriele Natale, Alex Patscheider, Bing Yang, Daniel Petter, Lauriane Chomaz, Daniel Grün, Riccardo Donofrio, Andrea Di Carli, Antonio Ortu, Samuel White, Julian Maloberti, Hagai Edri, Arina Tashchilina, Leonardo Bellinato Giacomelli and Pramodh Senarath Yapa* for all the scientific and social exchange and I am so happy that I was part of this group with such amazing colleagues. I am also very grateful for the close cooperation that exists in Innsbruck between all groups working on ultracold neutral atoms. Thanks to *Rudolf Grimm*, *Emil Kirilov*, *Hans-Chistoph Nägerl* and *Russell Bissett* and all members of their groups. Especially I want to thank *Alberto Canali, Luc Absil, Erich Dobler, Cosetta Baroni, Marian Kreyer, Isabella Fritsche, Natalia Masalaeva, Ashwath Madhusudan* and *Wyatt Kirkby* who were not only great colleagues but also great friends.
I also want to thank all the people outside of the laboratories who form the backbone

of this scientific operation. I want to thank the current and former workshop staff of the IQOQI *David Arnold* , *Bernhard Öttl* and *Andreas Strasser* for their incredible work and support on all the mechanical parts they made during the years and without which much more of the optics might have been glued to badly machined contraptions.

I want to thank *Gerhard Hendl* who designed all the critical electronics and always helped to find the best solutions.

Thanks to the IT staff *David Jordan* and *Valentin Staubmann*, who are always there when we need some new hardware or software or some new windows update crashes the experimental machine.

And thanks to the administrative staff from the University and IQOQI who keep the group run smoothly. Thanks to *Silvia Bonazza, Leonarda Garcia Lopez, Elisabeth Huck, Nikolaus Falschlunger, Angelique Sanchez* and *Birgit Weihs-Dopfer*. And I want to thank the external collaborations with *Giacomo Lamporesi* and *Luis Santos*, who supported us with their expertise and made many works presented in this thesis possible.

And I also would like to give some words to the people who supported me outside of the scientific bubble, who could pull me out of many days of frustration and who have always been a source of inspiration to me. Without the support of my family and friends, I probably would never have been able to bring this thesis to a finish. First and foremost I want to thank my parents Ute and Reinhard for supporting me through my whole life and enabling me to walk the way I walk today. Thanks for the trust in what I do, even though I am still not able to explain it concisely and comprehensibly to you. I also want to thank my brother, who is always there for me and even though it seems for most people that we might be polar opposites from the paths that we chose, me towards science and him towards art, he always gives the feeling that you understand me more than most of the people I know.

I want to thank my Innsbruck friends who made this time in Innsbruck so memorable and reminded me of the most important thing in life: enjoying it. Thanks for the great hiking trips, cookie baking parties, ski weekends, volleyball games, sauna discussions, Halloween weekend trips, game nights, train station pizza nights, Oktoberfest trips, Sziget experiences, pub crawls, holiday pitches, birthday parties and all the other amazing experiences. Thanks to my Heidelberg and Hannover friends for the spontaneous visits and always having a home there. And especially thanks to my Munich friends with whom my interest in physics just started to spark. Thanks for still having an open door and a place to sleep for me and for the weekends we spend together talking and playing games.

Finally, I want to thank my partner Maike. I feel so lucky that this city was not just a chapter about cold atoms for me, but that it became a chapter about meeting her and having a wonderful time together. I am so glad she supported me through the most challenging phases of the Ph.D. and always helped me to stand up for myself and not lose myself in the process. I am thankful for always being there for me when I come home and I am so excited to open the next chapter with you.

Table of Contents

List of Figures

List of Tables

1

From superfluids to supersolids

1.1 Introduction

> *In the case of all things which have several parts and in which the totality is not, as it were, a mere heap, but the whole is something beside the parts, there is a cause; for even in bodies contact is the cause of unity in some cases, and in others viscosity or some other such quality.*
>
> ***ARISTOTLE (TRANSLATED BY W. D. ROSS)***
> *METAPHYSICS: BOOK VIII(350 B.C.)*

The beauty of nature is that systems made up of a large number of elementary building blocks are more than just the sum of their parts. This means that the collective properties of the system can be radically altered only by, for example, a structural change in the ensemble. Probably the best known example of this is a large ensemble of H_2O-molecules, which at ambient pressure form water at room temperature, but become ice below $0\,^\circ$C and water vapour above $100\,^\circ$C. These are of course the three classical states of matter liquid, solid and gas[1] and most large systems of atoms and molecules will be in one of these states under certain conditions. Historically, these states of matter have been distinguished by their behaviour in a container: Solids retain their shape and volume, liquids retain their volume but adopt the shape of the containment and gases adopt both the volume and shape of the container. But of course there are many more collective properties that differentiate these systems. We find materials that are electrical conductors or insulators, that exhibit magnetic phases such as ferromagnetism or antiferromagnetism or that have different structural phases in solids, such as the crystalline phase or the amorphous phase [2]. An illustrative example of this is graphite and diamond: Both materials are made purely from carbon atoms, but graphite is dark gray in colour and brittle due to the hexagonal layered structure while diamond is clear, transparent and very strong due to its diamond cubic structure [3].

In condensed matter physics in particular researchers are interested in understanding how these macroscopic properties emerge from the microscopic state of the system. Especially the "quantumness" of many of these materials gives rise to many new exotic phases of matter, such as charge density wave (CDW)[4] states or topological phases[5]. A better understanding of these systems helps to synthesise materials with the desired properties and to discover new phases of matter. An enigmatic example is

---

[1] omitting the plasma state of matter

the research into high-temperature (T_c) superconducting materials. These materials, without requiring extensive cooling, lead to compact and affordable high-precision sensors [6], low-loss electrical grids [7] and quantum computing devices [8]. Since the discovery of superconductivity in mercury at below 4.2 K [9] more than 100 years ago, much research has been done to find materials with higher critical temperatures and to develop theories that could explain this phenomena [10]. In 1957 John Bardeen, Leon N. Cooper and Robert Schrieffer finally proposed the first microscopic theory [11], which could accurately predict type-I and type-II superconducting materials. However, the BCS theory fails for unconventional superconducting (UcS) materials such as cuprates[12], heavy fermions [13], organic superconductors [14], layered nitrides [15] or iron-based superconductors [16]. So far it is not clear which microscopic theory can universally describe the superconducting properties of all these materials, making it difficult to predict new types of materials. In the realm of gas-phase quantum matter these microscopic theories can be studied and even simulated on a fundamental level [17, 18]. The foundation of this new branch of studying quantum phases of matter was laid with the first experimental realisation of quantum degenerate gases in 1995 [19, 20]. Here, instead of investigating dense solids with average distances between the atoms of a few Ångström, gases provide a system with much larger average distances and a highly controllable platform to study different quantum phases. These systems have led to the direct observation of Bose-Einstein condensation [19, 20], degenerate Fermi gases [21, 22, 23] and the Mott-insulating phase [24] or topologically protected phases such as the Haldane insulator [25]. These systems can help to simulate theoretical models relevant to the above solid state systems and also lead to the discovery of new exotic phases [18].

1.1.1 Ultracold neutral atoms

Gases are typically more than ten orders of magnitude less dense than solids, and because they are so dilute, the interactions between atoms can be well controlled. However, to realise quantum phases of matter with gases, we must first cool the gas down significantly. Bose and Einstein predicted that if the ensemble comprises indistinguishable bosonic particles, cooling the ensemble below a critical temperature T_c will cause many atoms to occupy the lowest energy state [26]. This state of matter is called a Bose-Einstein condensate.

An intuitive picture comes from the fact, that at low temperatures the matter-wave character of the single atoms becomes relevant. The extent of the wave is on the order of the thermal de Broglie wavelength

$$\lambda_{\mathrm{dB}} = \sqrt{\frac{2\pi\hbar}{m k_{\mathrm{B}} T}} \tag{1.1}$$

where $\hbar$ is the Planck constant, m is the mass of the single atom, k_B is the Boltzmann constant and T is the temperature of the ensemble. By reducing the temperature the size of the matter wave grows and eventually to the length scale of the inter-particle spacing $\tilde{l} = (\frac{V}{N})^{1/3}$ [27]. For typical densities, the gas has to be cooled to temperatures of a few hundred nanokelvin to condense.

Early pioneering ideas of laser cooling [28, 29] and optical [30] and magnetic trapping [31] paved the way for cold atom experiments. Using these techniques, for the first time temperatures low enough to produce a Bose-Einstein condensate (BEC) were achieved [19, 20]. Just a few years later, the first degenerate Fermi gases were created in the laboratory [21, 22, 23].

These states are so important because through this transition the gas becomes a quantum many-body state where the atoms are in a macroscopic superposition with a single phase [27].

Another milestone was that by studying the scattering properties of the gas [32] it was found that the interactions between the atoms could be precisely tuned by controlling an external magnetic field in the vicinity of Feshbach resonances [33, 34]. These results motivated the subsequent emergence of more than a hundred groups working on quantum gas experiments around the world [35] and even in space [36]. Today, BECs are regularly created and are a state of matter that is intensly studied, from the dynamics of a collapsing gas [37, 38] and the creation of quantum vortices under rotation [39, 40], to studies of critical behaviour at the phase transition [41] and the study of interference between multiple BECs [42, 43] to name but a few.

There are many other ways to achieve different quantum phases in these gases. For instance, by tuning the interaction of quantum degenerate Fermi gases the BCS-BEC crossover can be studied[44, 45, 46, 47]. Moreover, the study of gases in strongly confined 2-D and 1-D systems, effectively freezing out the dynamics of the atoms in the other directions, allows for the creation of Tonks-Giradau (TG) gases [48, 49] and the observation of the Berezinskii-Kosterlitz-Thoules (BKT) transition [50, 51, 52, 53]. Finally, by confining atoms in optical lattices – periodic potentials created by interfering lasers – Bose- and Fermi-Hubbard models can be realised [54, 55, 56, 57], which allows to study phases of matter such as the Mott insulator phase [24], antiferromagnetism [58, 59] or many-body localisation [60, 61]. In addition, by setting up experiments with two or more different species, quasiparticle excitations such as polarons can be studied [62, 63, 64, 65].

From these examples we can see how universal these phases are. Many of the phenomena mentioned are also found in solid state systems [18], nuclear physics [66] or astronomy [67]. Ultracold quantum gas experiments can be designed to study less well understood exotic quantum phases, such as the strange metal phase [68] or topological phases [69].

Which phases can be explored in a particular quantum gas depends, among other parameters on the interactions between the atoms. Early quantum gas experiments have focused on setups with alkali metal atoms, where the dominant interactions are short-range and isotropic. Recently, new experiments have been designed in which additional long-range, anisotropic dipole-dipole interactions (DDI) play a significant role. Such systems are ultracold heteronuclear molecules [70], cavity systems with light-mediated interactions [71] or Rydberg gases [72].

There has been particular progress in systems with atoms outside the alkali metal series which have large intrinsic magnetic dipole moments, such as chromium [73] or some of the lanthanide atoms such as erbium [74] or dysprosium [75]. Fascinating new phenomena have been observed in these quantum degenerate gases such as a deformed Fermi surface [76], d-wave collapse [77] or the appearance of a roton minimum [78]. What makes these systems even more interesting is that for erbium and dysprosium, for certain parameters, they form a supersolid state (SS), a phase at which the gauge symmetry as well as the translational symmetry are spontaneously broken. This leads to a paradoxical state that has the properties of both a solid and a superfluid.

The SS state, predicted more than 50 years ago [79, 80, 81], was expected to be observable in solid helium, but convincing evidence for it in such systems is still lacking [82]. In other ultracold gas experiments also some of the defining properties of supersolids could be induced such as in spin-orbit coupled systems [83, 84] or cavity systems [85, 86].

In this thesis I discuss our recent works, which are focused on studying the dipolar BEC and the supersolid state. Especially for the supersolid phase it is discussed how this state emerges from a gas of magnetic atoms, and we study the superfluid properties of this state.

The thesis is divided into six different chapters: In Ch. 1 I introduce the interactions of the system and give an introduction to dipolar BECs and supersolids. In Ch. 2 I describe the experimental apparatus and the technical details of how to cool the gas to quantum degeneracy, tune the interactions and image the final state. Chapter 3 discusses the work on the nucleation of quantised vortices in dipolar BECs. In Ch. 4 we create a 2D supersolid state and probe the superfluidity by exciting the scissor mode and nucleating quantized vortices. In Ch. 5 the future plan of a dipolar double species quantum gas microscope is explained and the implementation of a transport setup is described.

1.2 Interactions

The ability to finely tune the interactions between atoms allows us to explore very different physical phenomena even within the same experimental setup. For example, in a bosonic system we can tune the interactions to be repulsive and obtain a stable BEC ground state, but tuning the interactions to be attractive can lead to a collapse of the system [87]. In fermionic ensembles, this tunability allows the study of the BEC-BCS crossover and the unitary regime.

In the following, I give a brief introduction to the short-range contact interactions and the long-range dipole-dipole interactions (DDI) that governs the quantum gas of magnetic atoms described in this thesis.

1.2.1 Contact interaction

Because gases are very dilute the range of interatomic forces r_0 is generally smaller than the average atomic distance $\tilde{l}$. To describe the interactions we can therefore assume that the atoms move freely and that most scattering events involve only two atoms. An elastic scattering process of two atoms can be described in the centre-of-mass frame by the atoms scattering at a central potential $U(r)$. The resulting full wave function at the position $\mathbf{r}$ far from the scattering centre $|\mathbf{r}| \gg r_0$ can be described by an incident plane wave and a radial wave function originating at the scattering centre [88]

$$e^{ikz} + f(k,\vartheta)\frac{e^{ikr}}{r} \tag{1.2}$$

where the atoms approaching each other along the z-direction with momentum $\mathbf{k}$ and ϑ is the angle between $\mathbf{k}$ and $\mathbf{r}$. The far-field scattering amplitude $f(k,\vartheta)$ can be expanded in partial waves

$$f(k,\vartheta) = \sum_{\ell=0}^{\infty}(2\ell - 1)f_\ell P_\ell(\cos\vartheta) \tag{1.3}$$

where $P_\ell(\cos\vartheta)$ are the Legendre polynomials and $f_\ell = \frac{1}{2ik}\left(e^{2i\delta_\ell} - 1\right)$ depends on a phase shift δ_ℓ. The total scattering cross section can be calculated by integrating over the full solid angle

$$\sigma(k) = \int |f(k,\vartheta) \pm f(k,\pi-\vartheta)| \mathrm{d}\Omega = \begin{cases} \sum_{\ell\in\text{even}} & \sigma_\ell(k); \text{ Bosons} \\ \sum_{\ell\in\text{odd}} & \sigma_\ell(k); \text{ Fermions} \end{cases} \tag{1.4}$$

where the partial cross sections are given by $\sigma_\ell(k) = 4\pi(2\ell+1)|f_\ell|^2$ and for symmetry reasons the amplitudes for bosons (fermions) add up (substract) [88]. For potentials of the form $U(\mathbf{r}) \propto 1/r^n$ and low energies $k \longrightarrow 0$ the phase shift can be estimated as [89, 90]

$$\delta_\ell \propto \begin{cases} k^{2\ell+1} & \text{for} \quad \ell < \frac{1}{2}(n-3) \\ k^{n-2} & \text{otherwise} \end{cases} \tag{1.5}$$

Usually the most dominant interaction between two neutral atoms is of the van der Waals type, which scales at large distances as $U_c(\mathbf{r}) \propto -C_6/r^6$. From (1.5) we see, that only the s-wave part $\ell = 0$ contributes significantly for $k \longrightarrow 0$. Therefore the interaction is isotropic in the far field and this interaction is considered to be short-range [91]. This allows the complex van der Waals potential to be replaced by a delta pseudo-potential [88]

$$U_c(\mathbf{r}) \approx g\delta(\mathbf{r}) \tag{1.6}$$

which simplifies it to a contact-type interaction. The interaction parameter g depends only on the mass m of the particle and on the s-wave scattering length a_s

$$g = \frac{2\pi\hbar^2 a_s}{m} \tag{1.7}$$

The scattering length a_s is tunable by changing the magnetic field due to Feshbach resonances. This is discussed in more detail in Sec. 2.2.5. This allows the interaction to be tuned from attractive ($a_s < 0\,\mathrm{a_0}$) to repulsive ($a_s > 0\,\mathrm{a_0}$). The strength of the scattering length can in principle be tuned arbitrarily, only limited by experimental contraints, but typical values range from $a_s = 0\,\mathrm{a_0}$ to about $a_s = 2000\,\mathrm{a_0}$. In the course of this thesis we will only consider systems with repulsive contact interactions.

1.2.2 Dipole-Dipole interaction

In addition to the contact interaction, atoms also interact due to their dipole moment. The dipole-dipole interactions (DDI) between two atoms with the dipole moments oriented along $\mathbf{e_i}$ separated by $\mathbf{r}$ are described by the potential [91]

$$U_{\text{DDI}}(\mathbf{r}) = \frac{C_d}{4\pi r^3}\left[\mathbf{e}_1 \cdot \mathbf{e}_2 - 3\frac{(\mathbf{e}_1 \cdot \mathbf{r})(\mathbf{e}_2 \cdot \mathbf{r})}{r^2}\right] \tag{1.8}$$

where C_d is the coupling strength. In this thesis we only consider interactions between magnetic dipoles, where the coupling strength is given by $C_d = \mu_0\mu_1\mu_2$, with the magnetic dipole moment μ_i and the

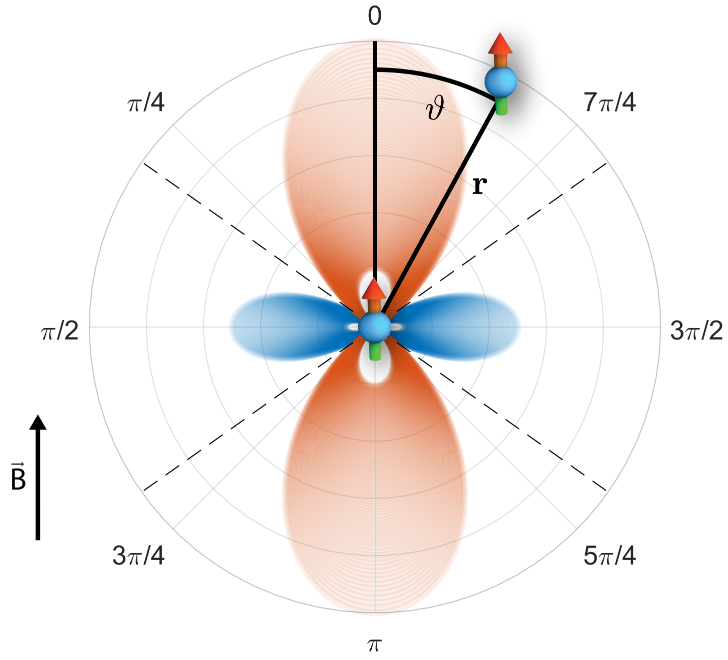

Figure 1.1: Dipole-Dipole interaction (DDI) potential between 2 atoms polarised along $\vec{B}$. Depending on the angle ϑ, the potential is attractive (red) or repulsive (blue). The magic angles $\vartheta_\mathrm{m} = [54.74°, 125.26°, 234.74°, 305.26°]$, at which $U_\mathrm{DDI} = 0$, are presented as dashed lines.

vacuum magnetic permeability μ_0. But there are also systems with strong electric dipole moments d_i such as heteronuclear molecules in electric fields, where the coupling strength is given by $C_d = d_1 d_2/\varepsilon_0$ with the electric vacuum permeability ε_0.

In typical quantum gas experiments an external magnetic field is present which aligns the magnetic dipoles along its direction such that $\mathbf{e}_1 = \mathbf{e}_2 = \mathbf{e}$. Therefore (1.8) simplified to

$$U_\mathrm{DDI}(\mathbf{r}) = \frac{C_d}{4\pi}\frac{1 - 3\cos^2\vartheta}{r^3} \tag{1.9}$$

where ϑ is the angle between $\mathbf{r}$ and $\mathbf{e}$. This potential is shown in Fig. 1.1. Two essential differences to the contact interaction potential become apparent. First, the potential has a $U_\mathrm{DDI} \propto 1/r^3$ dependence. Looking at (1.5) we see that this time the phase shift is $\delta_\ell \propto k$ for all partial waves. This means that all partial waves contribute to the scattering, leading to scattering even at distances of the atoms beyond the centrifugal barrier $\frac{2\ell(\ell+1)\hbar^2}{mr^2}$. The DDI is therefore effectively a long-range interaction [91]. Implications of this can be observed in single component Fermi gases, where systems with significant DDI thermalise even though s-wave interactions are strongly suppressed [92].

Second, unlike s-wave contact interactions, DDIs are anisotropic. When atoms scatter head-to-tail, the interactions are attractive and when the atoms scatter side-by-side, the interactions are repulsive.

To compare the relative strength between the DDI and the contact interaction we can define the dipolar length a_{dd} [93]

$$a_{\mathrm{dd}} = \frac{C_{\mathrm{d}} m}{12\pi\hbar^2} \tag{1.10}$$

The relative strength $\varepsilon_{\mathrm{dd}}$ is then defined by

$$\varepsilon_{\mathrm{dd}} = \frac{a_{\mathrm{dd}}}{a_{\mathrm{s}}} = \frac{C_{\mathrm{d}}}{3g} \tag{1.11}$$

Since the strength of the dipole-dipole coupling is fixed by the magnetic moments of the scattering atoms, we can change the relative strength by tuning a_{s}. We can then define $\varepsilon_{\mathrm{dd}} > 1$ as the dipole dominated regime and $\varepsilon_{\mathrm{dd}} < 1$ as the contact dominated regime. In the next section we will discuss the profound changes in the ground state of the system for the different regimes, but we will also see that even deep in either regime the contributions of the individual interactions are non-negligible [91].

1.3 Quantum degenerate dipolar gases

> *The above discussion would not lead one to expect B.E. (Bose-Einstein) condensation in a solid, because the assumption of no long-range configurational order is valid for a Quid phase only. In fact, it can be argued that a solid does not show B.E. condensation, at least for T=O K.*
>
> ***Oliver Penrose and Lars Onsager***
>
> *Bose-Einstein Condensation and Liquid Helium (1956) [94]*

Now that we understand the relevant interactions between the atoms in the quantum gas, we can discuss in more detail the quantum degenerate state created when the cloud is cooled beyond the critical temperature.

At temperature $T = 0$ we consider that all atoms occupy the absolute ground state. The gas can therefore be well described by mean-field theory, where we can replace the field operator $\hat{\Psi}(\mathbf{r}, t)$ by the classical field $\Psi(\mathbf{r}, t)$ [95]. The time evolution of the system is described by the extended Gross-Pitaevskii equation (eGPE), originally developed by Gross and Pitaevskii considering purely contact interactions [96, 97] and extended to include DDI [93]

$$i\hbar\frac{\partial\Psi(\mathbf{r},t)}{\partial t} = \left[\underbrace{-\frac{\hbar^2}{2m}\nabla^2}_{\text{kinetic}} + \underbrace{V(\mathbf{r})}_{\text{ext. Pot.}} + \underbrace{U_{\mathrm{c}}|\Psi(\mathbf{r},t)|^2}_{\text{CI Pot.}} + \underbrace{V_{\mathrm{dd}}^{\mathrm{mf}}(\mathbf{r})}_{\text{DDI Pot.}}\right]\Psi(\mathbf{r},t) \tag{1.12}$$

with the DDI potential given by $V_{\mathrm{dd}}^{\mathrm{mf}}(\mathbf{r}) = \int d\mathbf{r}' U_{\mathrm{DDI}}(|\mathbf{r}-\mathbf{r}'|)|\Psi(\mathbf{r}',t)|^2$. $V(\mathbf{r})$ describes the confining potential and is usually given by a harmonic trap $V(\mathbf{r}) = \frac{1}{2}m\omega_x^2x^2 + \frac{1}{2}m\omega_y^2y^2 + \frac{1}{2}m\omega_z^2z^2$.

The solution of the eGPE is given by

$$\Psi(\mathbf{r},t) = |\psi(\mathbf{r},t)|e^{iS(\mathbf{r},t)} \tag{1.13}$$

where $|\psi(\mathbf{r},t)|$ is the amplitude of the wave function and $S(\mathbf{r},t)$ is the macroscopic phase of the system. To find specific solutions for the amplitude and phase Eq. (1.12) must generally be solved numerically. However, the eGPE can be simplified if the gas is in the Thomas-Fermi regime $N\frac{a}{a_{\text{ho}}} \gg 1$, where N is the atom number of the ensemble and a_{ho} is the harmonic oscillator length $a_{\text{ho}} = \sqrt{\hbar/(m\omega_{\text{ho}})}$ and the geometric mean of the trap frequencies is $\omega_{\text{ho}} = (\omega_x\omega_y\omega_z)^{1/3}$. In this regime the kinetic term in (1.12) can be omitted and analytic solutions of the wave function can be found.

As we can see, the interactions have a profound effect on the state (1.13). Therefore, in the following I will first discuss the contact dominated regime $\varepsilon_{\text{dd}} \longrightarrow 0$ and then the intermediate and dipole dominated regime $\varepsilon_{\text{dd}} \geq 1$.

1.3.1 Dipolar Bose-Einstein condensate

In the contact dominated regime the dipolar term in Eq. (1.12) becomes almost negligible. We will see that even in this regime the DDI has noticeable effects compared to non-dipolar systems.

The ground state is given by the Bose-Einstein condensate with the typical parabolic density distribution [95]

$$n(\mathbf{r}) = n_0\left(1 - \frac{x^2}{R_x^2} - \frac{y^2}{R_y^2} - \frac{z^2}{R_z^2}\right) \tag{1.14}$$

and the phase is uniform $S(\mathbf{r}) = \phi_0$. Here the density at the centre is given by $n_0 = \frac{15N}{8\pi R_x R_y R_z}$. In an axially symmetric trap $R_x = R_y = R_\perp$ and the dipoles aligned along the z-direction. The radius is then given by [98]

$$R_\perp = \left[15\frac{gN\kappa}{4\pi m\omega_\perp^2}\left\{1 + \varepsilon_{dd}\left(\frac{3}{2}\frac{\kappa^2 f(\kappa)}{1-\kappa^2} - 1\right)\right\}\right]^{1/5} \tag{1.15}$$

with the cloud aspect ratio $\kappa = R_\perp/R_z$, $f(\kappa) = \frac{1+2\kappa^2}{1-\kappa^2} - \frac{3\kappa^2 \operatorname{arctanh}\sqrt{1-\kappa^2}}{(1-\kappa^2)^{3/2}}$ [98]. We find that for $\varepsilon \longrightarrow 0$ Eq. (1.15) is greatly simplified and the radii are given by the non-dipolar solution [95] where $R_i \propto \omega_i^{-1}$, meaning that the shape of the BEC corresponds to the shape of the trap. For finite ε the cloud stretches along the z-direction and squeezes in the radial direction compared to the non-dipolar case, which is called the magnetostriction effect [99, 100, 101]. For the more general case where the dipoles are not aligned along the z-direction and $R_x \neq R_y$ the analytical functions become much more complex [102], but the general behaviour of the atomic cloud stretching along the dipole direction persists. The effect of magnetostriction will play a crucial role in part 3 to rotate the gas.

1.3.2 Emergence of the Roton minimum

When we tune our interactions towards the dipolar dominated regime $\varepsilon > 1$ the ground state develops a density modulation. To understand this we need to look at the elementary excitation spectrum of condensed quantum gases. The spectrum can be obtained by linearising the eGPE around the ground

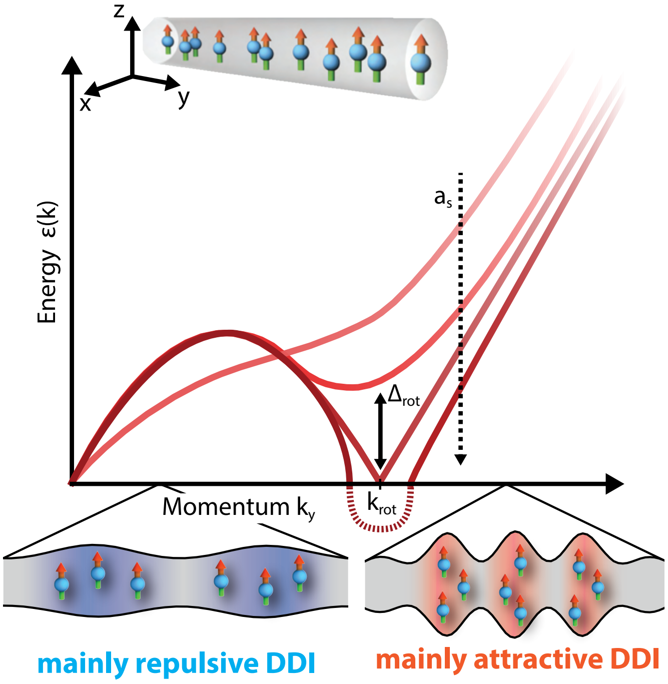

Figure 1.2: Excitation spectrum for a condensed dipolar gas in an infinite tube. Top: The atoms are confined in an infinite tube along the y-direction and the dipole moments are polarised along the z-direction. Middle: The excitation spectrum is given for decreasing a_s (bright to darker red). The spectrum develops a roton minimum at k_{rot} with an minimum energy of Δ_{rot}. Eventually the roton mode softens $\Delta_{\text{rot}} \leq 0$, leading to a macroscopic occupation of the roton excitation. Bottom: Two excitation scenarios are illustrated. For excitations $k \ll k_{\text{rot}}$ the DDI are mainly repulsive, leading to an increase in energy. For excitations $k \approx k_{\text{rot}}$ the DDI are mainly attractive, leading to a reduction on energy and the roton minimum. Figure adapted from [104]

state [91]. This gives the dispersion relation for a uniform gas [103]

$$\epsilon(\mathbf{k}) = \sqrt{\frac{\hbar^2 k^2}{2m}\left[\frac{\hbar^2 k^2}{2m} + 2gn\left(1 + \varepsilon_{\text{dd}}\left(3\cos^2\theta_k - 1\right)\right)\right]} \tag{1.16}$$

where $\epsilon(\text{k})$ is the energy of the mode with momentum $\mathbf{k}$, n is the density of the gas and θ_k is the angle between the dipole direction and $\mathbf{k}$.

For $\varepsilon \longrightarrow 0$, we recover the well-known dispersion relation for interacting non-dipolar BECs [95], with a linear phonon branch for $k < \xi^{-1}$, where $\xi = \sqrt{\frac{\hbar^2}{2mgn}}$ is the healing length, followed by the free particle branch for large k, where the dependence is quadratic.

The dispersion changes dramatically for trapped gas for finite ε_{dd} [105], as we can see in Fig 1.2. Considering that the gas is tightly confined $\omega_z > \omega_{x,y}$ in the dipole direction (oriented in the z-direction), trapping introduces a length scale l_z, at which excitations with finite $k \approx l_z^{-1}$ are energetically lowered by increasing ε_{dd}. This eventually leads to a minimum at finite k_{rot} with an energy gap Δ_{rot} called the roton minimum [78], following the studies of the dispersion relation of helium-4 by Landau [106]. An intuitive understanding comes from the fact, that the DDI is anisotropic and attractive when two atoms are head-to-tail. Therefore, by increasing the relative strength of the DDI, excitations that increase the density at finite k become energetically more favourable as more atoms are head-to-tail then side-by-side. At values of $\varepsilon \geq 1$ the energy of the modes is lowered to a level where the gap Δ_{rot} closes, or in other words, where the roton softens. At this point the finite $\mathbf{k}$ excitations are spontaneously populated, resulting in an observable density modulation with k_{rot}. The roton softening has been observed experimentally [104] which has been the entrance door to study supersolids in ultracold dipolar gases.

1.3.3 Beyond mean-field: LHY correction

These excitations were expected to be rather short-lived, as large increases in density lead to large atomic losses due to three-body collisions [88]. Similar collapses are known for BECs with strong attractive contact interactions [87] as well as for weakly dipolar systems such as chromium [77]. In addition, mean-field studies suggest a similar result for stronger dipolar systems such as dysprosium and erbium [107].

But instead it was found experimentally that the lifetimes of these modulated states were much longer than expected [108, 109]. These results were puzzling at first. The key to understanding the unexpected stability beyond mean-field effects had to be taken into account. The assumption of a pure BEC, where all particles occupy the lowest energy state is no longer valid in such dense systems. Instead, this can be corrected by assuming a spontaneous population of single-particle excited states and interactions between excited and ground state atoms. These quantum fluctuations lead to corrections of the total energy of the state.

These corrections were first calculated by Lee, Huang and Yang (LHY) in 1957 [110, 111] and were later extended to include the dipolar interactions [112, 113, 114]

$$E = \frac{g}{2}\frac{N_0^2}{V}\left[1 + \frac{128}{15\sqrt{\pi}}\sqrt{n_0 a_s^3}Q_5\left(\varepsilon_{\text{dd}}\right)\right] \tag{1.17}$$

where $n_0 = N_0/V$ is the density of atoms, and $Q_\ell\left(\varepsilon_{\text{dd}}\right) = \int \mathrm{d}\theta \sin\theta \left[1 + x\left(3\cos^2\theta - 1\right)\right]^{\ell/2}$. Considering repulsive contact interactions $a_s > 0$, the LHY correction term increases with increasing density $E \propto n_0^{3/2}$. The quantum fluctuations thus have a regulating effect on the density.

Density regulation competes with the increasing loss of atoms at large densities due to three-body interactions. If the density increases too much too many atoms are rapidly lost and the state collapses. Eq. (1.17) scales strongly with the interaction length $E \propto a_s^{5/2}$. Due to the small dipolar length of chromium $a_{\text{dd}} = 15\,\text{a}_0$ [115], the LHY corrections do not stop the collapse. But for erbium and dysprosium with dipolar lengths almost ten times larger than chromium the LHY corrections stabilise the gas at lower densities and prevent the collapse. The modulated state is stable and significantly different from the dBEC ground state discussed in sec. 1.3.1.

1.3.4 Emergence of Supersolids and droplet crystals

Before discussing supersolids and droplet crystals, let us start with a single droplet state or macrodroplet. Consider a cigar-shape confinement ($\omega_z < \omega_{x,y}$) where the dipoles are along the weakest confining axis. Increasing $\varepsilon_{\mathrm{dd}}$ will eventually lead to the roton instability, but instead of the modulated state a single droplet state is observed where the DDI leads to overall attractive interactions stabilised by quantum fluctuations [109]. Compared to the BEC, the density is increased and the droplet is more elongated [116]. Additionally, quantum droplets are self-bound, which means that even without external confinement their shape is preserved. In experiments this can be seen in time-of-flight measurements [117]. Due to continuous atom loss in experiments, the atom number eventually falls below a critical number N_c, at which point the droplet state collapses [118].

Considering now the trap discussed for the roton minimum ($\omega_z > \omega_{x,y}$), deep in the dipole-dominated regime $\varepsilon_{dd} \gg 1$ the ground state is given by multiple isolated droplets (ID), which repel each other and therefore arrange in a regular array or crystal pattern [91]. Since each of the droplets is disconnected from each other, the macroscopic phase of each droplet is independent.

Improved theoretical models, including the LHY term, allow the $T = 0$ ground states to be simulated for different parameters such as $\varepsilon_{\mathrm{dd}}$ and atom number [119]. An example of a ^{164}Dy ground state phase diagram is shown in Fig. 1.3. The simulations show that by decreasing $\varepsilon_{\mathrm{dd}}$ towards the transition to the BEC, the overlap between adjacent droplets increases monotonically. Instead of isolated droplets, we find a fully connected modulated density profile, and because the system is connected it acquires global phase coherence. This intermediate regime is the supersolid regime. And indeed, in 2019 the groups in Stuttgart [120], Pisa [121] and Innsbruck [122] were able to observe the first supersolid state in the quantum degenerate gas of ^{162}Dy , ^{166}Er and ^{164}Dy with a ground state that shows both density modulation and global phase coherence. The initial lifetime of the modulated state was only about 20 ms in the Stuttgart and Pisa experiments, but in Innsbruck ^{164}Dy the supersolid was observed for about 150 ms. Further studies in the following years now lead to states, where the supersolid survives for about a second [123].

Before discussing the supersolid state further, I need to clarify the notation used in this thesis regarding supersolids and droplet crystals. The term 'droplet' was originally termed for the self-bound state found in the single droplet regime and for the isolated droplets. In the latter case, every droplet acquires a phase independent of the other droplets, the system is separable, and the individual droplets can be discussed independently. The supersolid state is described by the single wave function (1.13) with a modulated density distribution and global phase coherence. This state is not separable and the different lobes of the modulation are not self-bound. Nevertheless, for the sake of a simplicity, the supersolid state is described in parts of this thesis as a combination of 'droplets' and a 'superfluid background'. These terms should help the reader to get a more intuitive understanding of the phenomena described.

1.3.5 How 'super' is the supersolid

A supersolid by definition paradoxically combines solid properties with superfluid flow. The solid character of the degenerate dipolar quantum gas can be seen e.g. in the appearance of crystal modes [125] and in

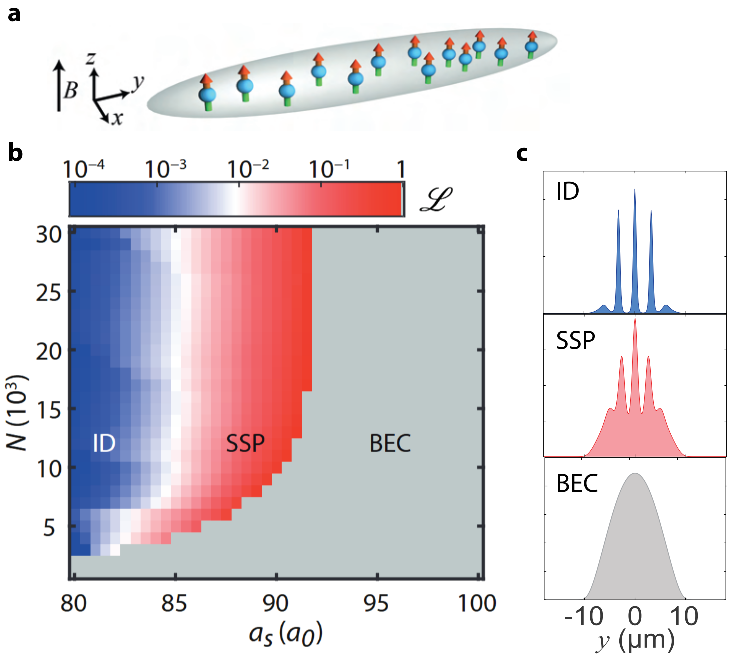

Figure 1.3: Ground state simulation of $T = 0$ phase diagram for ^{164}Dy confined in a cigar-shaped trap. a) Illustration of the trap confinement. The trap frequencies are given by $[\omega_x, \omega_y, \omega_z] = 2\pi \times [229, 37, 135]\,\mathrm{s}^{-1}$ and the magnetic moment is aligned along the z-direction. b) The ground state phase diagram for different a_s and condensed atom number N. The different regions are quantified by the link strength $\mathscr{L} = 1 - \frac{n_{\max} - n_{\min}}{n_{\max} + n_{\min}}$ where $n_{\max}(n_{\min})$ are the maximum (minimum) density in the central region. For large $a_s > 92\,\mathrm{a}_0$, the ground state is a BEC (grey). Reducing the scattering length leads to the narrow supersolid phase with significant ink strength $\mathscr{L}$ (red). Decreasing a_s leads to very weak links, leading to the isolated droplet regime (blue). c) Illustration of density profiles for the isolated droplet (ID) phase, supersolid phase (SSP) and BEC phase. Figure adapted from [124].

recent theoretical studies where solid parameters such as the shear modulus can be measured [126, 127]. The superfluid property of the gas is more subtle.

Let us first discuss, how a superfluid is defined. We are talking about fluids that can either flow through containers without losing energy, or fluids through which we can move small objects without resistance. The commonality of these to cases is that the flow is dissipationless. This flow behaviour breaks down above a critical velocity v_c defined by the Landau criteria [128]

$$v_c = \min_{\mathbf{k}} \frac{\epsilon(\mathbf{k})}{|\mathbf{k}|} \tag{1.18}$$

Eq. (1.18) let us also understand the cause of this dissipationless flow: For velocities $v < v_c$ there are no accessible modes that can be excited and therefore no energy that can be transferred. In interacting BECs the critical velocity is given by the phonon branch $v_c^{\mathrm{BEC}} = v_{\mathrm{ph}} = \sqrt{\frac{g n_0}{m}}$. It is important to note that for a non-interacting BEC $g = 0$ the critical velocity is $v_c = 0$ and therefore the state is not superfluid.

The original reasoning for a supersolid being superfluid is therefore rather indirect: since the state is globally phase coherent and the gas is interacting, all the ingredients for a BEC to be superfluid are fulfilled.

But this argument can be challenged. Landau discussed superfluidity in the context of ^{4}He, where the critical velocity is not given by the phonon branch, but by the roton minimum $v_c \approx \frac{\Delta_{\rm rot}}{|\mathbf{k}_{\rm rot}|}$. Now for our solid to exist we go to the region where the roton softens $\Delta_{\rm rot} \longrightarrow 0$. Does this mean that the state stops being superfluid due to the roton softening $v_c \longrightarrow 0$?

The question of whether a solid can be superfluid has been heavily debated for more than 50 years. While originally rejected by Penrose and Onsager [94] it was theorised later, that solids could acquire superfluid properties [79, 80, 81]. Leggett suggested that superfluidity in this context is not a binary property, but that a modulated condensed system can be fractionally superfluid. For such a system on an annular Leggett defined a bound for the superfluid fraction [81]

$$f_s \leq \left[\frac{1}{2\pi} \int_0^{2\pi} \frac{d\theta}{\rho\left(\theta\right) / \rho_0} \right]^{-1} \tag{1.19}$$

where $\rho(\theta)/\rho_0$ is the ratio of the modulated density at an angle θ on the annulus to the density without modulation. Leggett also proposed to measure the superfluidity of the system phenomenologically, in this case by measuring the non-classical moment of inertia (NCMI) of the state.

Even after the first observation much experimental and theoretical effort has gone into proving superfluidity in supersolids more directly. The measurement of the Goldstone modes shows phase rigidity, which is related to the superfluid stiffness of a system [129, 130, 125], the scissors mode oscillation of linear supersolid arrays has been measured to obtain the NCMI [131] and josephson oscillations between single droplets have been probed [132].

In Ch. 4 I will present the work of our laboratory where we have investigated the possibility of measuring the superfluid fraction by exciting scissors mode oscillations in non-linear arrays and nucleating quantized vortices in supersolids, a hallmark of superfluidity.

This concludes the introduction to dipolar quantum gases and the relevant interactions, which are the foundation of the works presented in the next chapters.

2

The Erbium-Dysprosium experiment

> *I am among those who think that science has great beauty. A scientist in his laboratory is not only a technician: he is also a child placed before natural phenomena which impress him like a fairy tale. We should not allow it to be believed that all scientific progress can be reduced to mechanisms, machines, gearings, even though such machinery also has its beauty. Neither do I believe that the spirit of adventure runs any risk of disappearing in our world. If I see anything vital around me, it is precisely that spirit of adventure, which seems indestructible and is akin to curiosity.*
>
> ***Maria Salomea Skłodowska-Curie***
> *Madame Curie: A Biography (1937)*

From the first chapter we know, that we can create "quantum matter" from a gas of neutral atoms, and by choosing magnetic atoms such as dysprosium or erbium, we get a system that interacts by the means of both short-range, isotropic contact interactions and long-range, anisotropic dipolar interactions. We are able to tune the relative strengths of these interactions, allowing us to create intriguing quantum phases such as a Bose-Einstein condensate or a supersolid and even drive phase transitions between them [91]. In this chapter, the experimental apparatus of the Erbium-Dysprosium experiment is explained. The basic properties of dysprosium (Sec. 2.1) and the relevant techniques for cooling and trapping the atoms in a magneto-optical trap (Sec. 2.2.1), evaporating them in an optical dipole trap (Sec. 2.2.2 and Sec. 2.2.3), imaging them (Sec. 2.2.4) and tuning the interactions by changing the magnetic field (Sec. 2.2.5).

2.1 Basic properties

There are 118 elements in the periodic table from which to choose from for an ultracold atom experiment. A small subset of these elements has already been brought into quantum degeneracy, such as the alkali and alkaline- earth atoms, chromium and some atoms of the lanthanide series, to name but a few. In this chapter, we will discuss the relevant properties of dysprosium such as the strong, permanent magnetic moment and the narrow optical transitions that enable us to create dipolar quantum gases.

The Erbium-Dysprosium experiment (ErDy) is, as the name implies, a quantum mixture experiment designed to cool dysprosium (Dy) and erbium (Er) [133]. The primary focus of this thesis are single species experiments conducted with dysprosium. However, many of the properties and transitions discussed have analogues counterparts for erbium. A very detailed description on the properties of erbium can be found in the thesis Albert Frisch [134].

Dysprosium is an atomic species from the lanthanide series, found in the 6th period of the periodic table. In its solid form it is comparatively soft and looks metallic, but oxidises slowly in humid air. Dy is one of the so-called rare-earth metals, which is a bit of a misnomer, because the abundance of it in the Earth's crust is much larger than, for example, the abundance of gold, but these elements are not usually found in large ore deposits [135]. Dysprosium is widely used in high-tech industries. It is most commonly known for its application in the production of high-strength neodymium-iron-boron (NdFeB) permanent magnets to enhance their performance, particularly at high temperatures [136].

In our experiment we are interested in the atomic properties of dysprosium. Dysprosium has the atomic number 66. It has four significantly abundant isotopes ($> 15\,\%$) of which two are fermionic and the other two are bosonic isotopes. The basic properties are summarised in table 2.1. Together with the isotopes of erbium, we can therefore create heteronuclear, degenerate Bose-Bose-, Fermi-Fermi-, and Bose-Fermi-mixtures [137]. But even experiments with just the bosonic isotopes of dysprosium are so rich in unexplored physics that all the publications discussed in this thesis have worked with either ^{162}Dy or ^{164}Dy .

One outstanding feature of dysprosium, which ultimately leads to the dipolar physics studied throughout this thesis, is its large permanent magnetic dipole moment of $\mu \approx 10\,\mu_B$, where $\mu_B = \frac{e\hbar}{2m_e}$ is the Bohr magneton. But why is the magnetic moment so much larger than, e.g., for the atoms of the alkali series with $\mu \approx 1\,\mu_B$? To understand this, we need to look at the electronic structure of dysprosium: The outermost shells are the 6s-shell, which is completely filled, and a submerged, sparse f-shell with 10 electrons, leading to the electronic configuration $[\mathrm{Xe}]4f^{10}6s^2$. In accordance to the Russel-Saunders coupling the electronic ground state can be characterized by the quantum number triplet $^5\mathrm{I}_8$ $(\mathrm{S} = 2, \mathrm{L} = 6, \mathrm{J} = 8)$. This state characterises the bosonic isotopes with nuclear spin quantum number $\mathrm{I} = 0$ and we find a rich spectrum of 17 internal spin states $\mathrm{m_J} \in \{-\mathrm{J}, -\mathrm{J}+1, ..., \mathrm{J}-1, \mathrm{J}\}$ for the electronic ground state. Just for completeness, the fermionic isotopes ^{161}Dy and ^{163}Dy have an additional non-zero nuclear spin of $\mathrm{I} = 5/2$ and therefore the quantum number for the hyperfine structure is $\mathrm{F} \in \{11/2, 13/2, ..., 21/2\}$. This leads to the ground states $^{161}\mathrm{Dy} : {}^5\mathrm{I}_8,\ \mathrm{F} = 21/2$ and $^{163}\mathrm{Dy} : {}^5\mathrm{I}_8,\ \mathrm{F} = 11/2$. Here the large difference in F is due to the opposite sign of their nuclear spins **I** [138]. The large spin manifold of fermionic dysprosium sparks a great interest in studying these systems, e.g. for long-lived spin-orbit coupled systems [139] or to create topological systems with synthetic dimensions to study quantum hall systems [140].

Back to the bosons: The dysprosium atoms in this experiment are always prepared in the lowest-lying stretched state $\mathrm{J} = 8$ and $\mathrm{m_J} = -8$ [1]. In our experiment the atoms are constantly exposed to an external magnetic field **B**, providing a quantisation axis for the total angular momentum vector **J** and **F** for bosons and fermions, respectively [141]. We are interested in the z-projection of the average magnetic moment

---

[1] Also the state $\mathrm{J} = 8$ and $\mathrm{m_J} = 8$ is a stretched state and can be used in experiment.

	^{161}Dy	^{162}Dy	^{163}Dy	^{164}Dy
Abundance (%)	18.89	25.48	24.90	28.26
Atomic mass (u)	160.9	161.9	162.9	163.9
Neutron number	95	96	97	98
Statistics	F	B	F	B
El. ground state ($^{2S+1}L_J$)	$^5I_8$			
Nuclear spin	$+\frac{5}{2}$	0	$-\frac{5}{2}$	0
Hyperfine quantum number (F)	$\frac{21}{2}$		$\frac{11}{2}$	

Table 2.1: Basic properties of the dysprosium isotopes with an abundance larger than 14% taken from [1]. The signs + and − describe the relative orientation of the nuclear spin I.

$\langle \mu_J \rangle_z$

$$\langle \mu_J \rangle_z = -m_J g_J \mu_B \tag{2.1}$$

$$\langle \mu_F \rangle_z = -m_F g_F \mu_B \tag{2.2}$$

with the approximate Landé factor $g_J \approx 1 + \frac{J(J+1)+S(S+1)-L(L+1)}{2J(J+1)}$ and $m_J = -8$ for bosons and $g_F \approx g_J \frac{F(F+1)-I(I+1)+J(J+1)}{2F(F+1)}$ and $m_F = -21/2$ for fermions[2] in our experiment. Using these values in eq. (2.1) leads to

$$\langle \mu_J \rangle_z \approx 10\mu_B \tag{2.3}$$

$$\langle \mu_F \rangle_z \approx 10\mu_B \tag{2.4}$$

Additional corrections have to be applied to g_J and g_F to get a more accurate expression, and experimentally it has been found that the Landé factors are $g_J = 1.24166(7)$ and $g_F = 0.94603(7)$ [142]. From this follows $\langle \mu_J \rangle_z = 9.93272\,\mu_B$ and $\langle \mu_F \rangle_z = 9.93328\,\mu_B$ for the values of the magnetic moment.

Another distinguishing feature of dysprosium is the large manifold of optical transition (see Fig. 2.1). This is due to the submerged f-shell structure of the atom. In the experiment we only drive the transitions J = 8 to J = 9. These transitions are used to optical cool, image and manipulate the atoms. The transitions important for the work of this thesis are listed in the following. The electronic structure of the excited state is given and the notation describes the closed xenon nucleus ([Xe]), followed by the LS-coupled $4f$-electrons ($4f^n(^{2S+1}L^p_{J_1})$), where n is the electron number and p is the parity. These are then coupled to the other $6s$-, $6p$- or $5d$-electrons, which are either JJ-coupled with $(J_1, J_2)^p_J$, or LS-coupled. The structures are taken from [143]:

---

[2] Note, that the term for the nucleus is neglected because the nuclear magneton μ_N is much smaller than the Bohr magneton μ_B

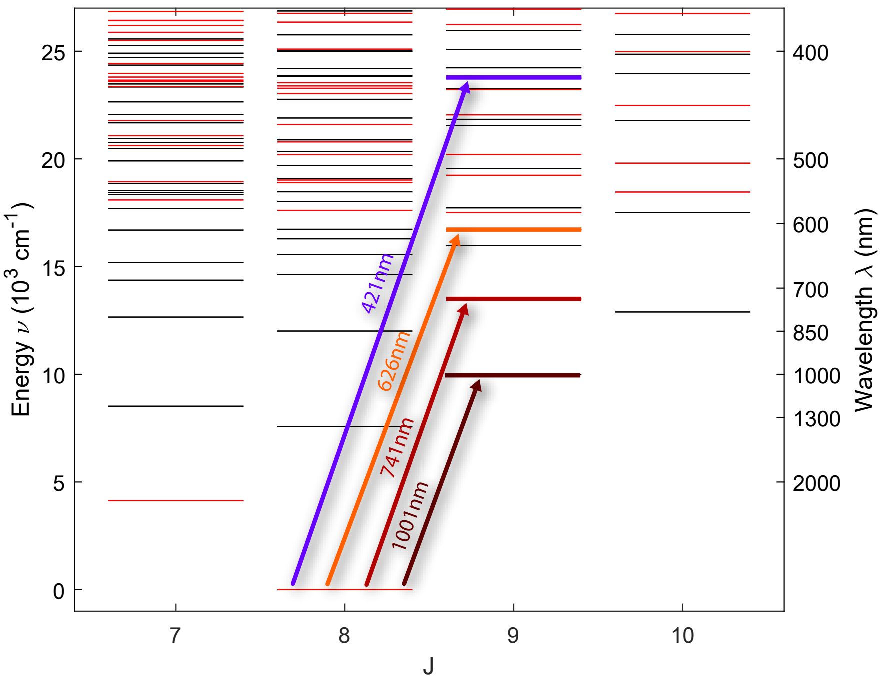

Figure 2.1: Energy level spectrum of dysprosium for the total angular momentum quantum numbers $J = 7, 8, 9, 10$ **up to the wavenumber** $\bar{\nu} < 27000\mathrm{cm}^{-1}$**.** The red and black lines represent even and odd parity states respectively. The arrows indicate the important transitions in the experiment as described in the text. This figure is a modified version of [146] with data from [147]

- 421nm – $[\mathrm{Xe}]4f^{10}(^5\mathrm{I}_8)6s6p(^1\mathrm{P}^o_1)(8,1)_9$ – promoting one s-shell electron to the 6p state which then couples with the other 6s atom to form the singlet state $^1\mathrm{P}_1$. This is reminiscent of the D2-line of the alkali atoms and results in a strong transition with a linewidth of $\Gamma_{421}/2\pi = 32.2\,\mathrm{MHz}$.
- 626nm – $[\mathrm{Xe}]4f^{10}(^5\mathrm{I}_8)6s6p(^3\mathrm{P}^o_1)(8,1)_9$ – here the 6s and 6p electron couple to the triplet state $^3\mathrm{P}_1$ and because of the $\Delta S = 1$ it is an intercombination line. This reduces the transition rate significantly leading to a narrower linewidth of $\Gamma_{626}/2\pi = 135\,\mathrm{kHz}$.
- 741nm – $[\mathrm{Xe}]4f^9(^6\mathrm{H}^o)5d6s^2\ {}^5\mathrm{K}^o_9$ – and 1001nm – $[\mathrm{Xe}]4f^9(^6\mathrm{H}^o)5d6s^2\ {}^7\mathrm{I}^o_9$ – exciting an 4f electron to the 5d state leading to a narrow linewidth of $\Gamma_{741}/2\pi = 1.78\,\mathrm{kHz}$ and a linewidth in the Hz range $\Gamma_{1001}/2\pi = 53\,\mathrm{Hz}$ [144]. In the publications of this thesis not yet applied, these transitions can function for spin manipulation and optical cooling schemes.

Having access to a strong MHz line to pre-cool the atoms and a large selection of narrow lines to either optically cool the atoms to very low temperatures or excite the atoms to states with lifetimes on the order of seconds is a great toolbox for atomic physicists. Additionally, the branching ratio for the 421 nm transition is small enough ($> 1 \times 10^{-5}$) to be used for the first cooling steps without the need of a repumping laser and the other transitions are cycling transitions [145, 138].

2.2 The experimental apparatus

> *We are stuck with technology when what we really want is just stuff that works.*
>
> ***Douglas Adams***
> *The Salmon of Doubt: Hitchhiking the Galaxy One Last Time (2002)*

As you can probably imagine, getting our ensemble of dysprosium atoms to "behave quantum mechanically" is not a trivial task, and so far not a simple do-it-yourself project in your garage[3]. Therefore before we can talk about supersolids and quantised vortices, we need to talk about the nuts and bolts and coherent light sources.

A generation of Ph.D. students, together with post-docs, masters and bachelor students and under the guidance of the professor and senior scientist have worked on creating the machine to cool down dysprosium (and erbium) atoms to the degenerate state and this is described in great details in their theses [137, 149, 150, 151]. This thesis would not have been possible without the groundwork done by these people, and I was mainly involved in maintaining, optimising and adding specific functionalities for the experiments done within this thesis, as well as the preparation for future experiments (see Ch. 5). This chapter will focus on discussing the optical cooling schemes to cool the atoms down to the microkelvin regime, the optical setup to create an optical dipole trap, the evaporation, the imaging setup and the magnetic coil setup.

2.2.1 Zeeman slower and Magneto-Optical trap

The experimental apparatus is shown in Fig. 2.2. The raw material – highly purified solid dysprosium and erbium – is inside the oven chamber on the right-hand side of the experiment. The whole apparatus is sustaining a ultra high vacuum (UHV) with ion pumps at the atomic beam shutter section ($p \approx 10^{-10}$ mbar) and getter pumps close to the chambers where the atoms are trapped and cooled to quantum degeneracy. The main chamber for the work discussed in this thesis is the FRAnZ[4] chamber. During this thesis we have extended the experimental apparatus and added a glass cell in which we will set up a quantum gas microscope for erbium and dysprosium (see Ch. 5). This chamber is referred to as SiSi[5] chamber ($p \approx 10^{-11}$ mbar) [137]. The UHV environment is necessary because any collision of dysprosium atoms with the background gas will lead to heating, loss of atoms, and eventually decoherence of the ultracold ensemble.

Dysprosium and erbium have slightly different melting temperatures of 1412 °C and 1529 °C, respectively. The atoms are evaporated from the solid at temperatures just below the melting temperature and to generate a temperature gradient towards the exit of the chamber, to avoid the atoms to condense in the chamber again, and achieve a similar vapour pressure for erbium and dysprosium, the oven chamber is separated into a hot lip section ($T = 1200\,^{\circ}$C) loaded with erbium and an effusion cell section

---

[3] Or is it? If you have enough financial assets it might be possible [148]

[4] FRAnZ: **F**erlaino's **R**are-earth **A**toms **n**ear **Z**ero

[5] SiSi: **Si**ngle **Si**te resolved

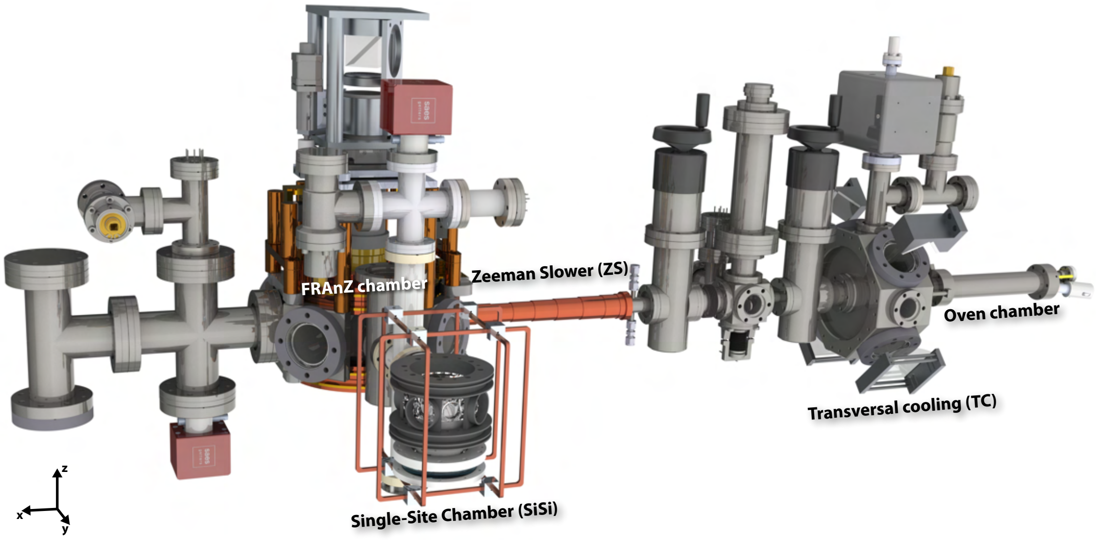

Figure 2.2: Illustration of the experimental apparatus. The atoms are coming from the oven chamber and the atomic beam is focused in the Transversal cooling chamber before they are slowed in the ZS slower part and finally trapped in the FRAnZ chamber, where the experiments are performed. The SiSi chamber is not yet used in the experiments done during this thesis, but will be discussed in Ch. 5.

($T = 1100\,^{\circ}\mathrm{C}$) loaded with erbium and dysprosium. The atoms exit the oven chamber through a 30 mm long nozzle with a 3 mm aperture, reducing the angular spread of the atomic beam towards the FRAnZ chamber [152, 153].

The mean velocity $v_{\mathrm{oven}} \approx 457\,\mathrm{m/s}$ [137] of the atom beam emitted from the oven is too large to be trapped by the magneto-optical trap in the FRAnZ chamber ($v_{\mathrm{cap}} \approx 13.4\,\mathrm{m/s}$ [137]) and we need to collimate the atomic beam more to increase the atom flux through the capture range of the MOT. For the collimation we employ a transversal cooling (TC) scheme and to slow down the atoms we use a Zeeman slower (ZS). The atoms first enter the transversal cooling (TC) stage as can be seen in Fig. 2.2. To decrease the transversal velocity of the atoms we apply two retro-reflected laser beams of the strong transition 421 nm light as illustrated in Fig. 2.3 a. The beams form a two-dimensional optical molasses, creating a linear damping force depending on the momentum of the atoms, which effectively collimates the atomic beam [154].

For the ZS setup, a 421 nm beam is sent towards the oven chamber. The atoms absorb the incoming resonant photons $-\hbar\mathbf{k}_{\mathrm{in}}$ and eventually spontaneously emit a photon in an arbitrary direction $\hbar\mathbf{k}_{\mathrm{out}}$ [154]. This leads to an effective momentum transfer of $\Delta p_{\mathrm{atom}} = -\hbar k$ per photon, where $k = \frac{2\pi}{\lambda}$ is the wavenumber of the light. However, the resonance frequency f of the light for atoms with velocity v is shifted due to the Doppler shift $\Delta f = f\frac{v}{c} \gg \Gamma_{421}/2\pi$. By applying a magnetic field $B_{\mathrm{ZS}}(x)$ we can change the energy between the ground and excited state due to the Zeeman effect to compensate for the shift. The magnetic field is also position dependent along the beam direction to account for the reduction in mean velocity towards the FRAnZ chamber (see Fig 2.3b). The exact magnetic field profile is shown in [137].

The average velocity of the atomic beam is now lower than the capture velocity of our magneto-optical trap (MOT) $v_{\text{cap}} = 13.4\,\text{m/s}$ [137], which allows efficient loading. Note that at this point we can estimate the temperature of the atomic beam to be $T \approx 1\,\text{K}$, which is still orders of magnitude too high to get close to a quantum degenerate gas. Ultimately, we want the atoms trapped in a well-defined harmonic potential and as cold as $T \approx 100\,\text{nK}$. A MOT combines a momentum selective molasses with a position dependent force due to the magnetic quadrupole field, not only slowing down the atoms but also trapping them [154]. Here it should be noted that our MOT for dysprosium has a few properties that differentiates it from the typical one of alkali atoms:

- We use the 626 nm transition, which has a very small natural linewidth compared to the D_2-lines of the alkali atoms (in the MHz range). This means, that instead of the usual linear restoring force over the whole space of the MOT, the atoms see something more similar to hard walls. Although the narrow linewidth leads to a very low capture velocity, the advantage is the very low Doppler temperature $T_D = 3.5\,\mu\text{K}$ which sets the minimum temperature the MOT can achieve. Similar approaches are used for ytterbium [155, 156] and strontium [157, 158].
- Because dysprosium is very heavy, the gravitational force is significant for the MOT.

This means that we can cool and trap the atoms in an open-top MOT which is created by two collimated, retro-reflected horizontal beams of 626 nm light, but only a non-retro-reflected vertical beam from the bottom of the chamber (see Fig. 2.3 c). The resulting cloud sits below the centre of the magnetic quadrupole field, which means that for a sufficiently large detuning mostly the σ^--polarised beam from the bottom is absorbed. Therefore, the atoms become fully spin-polarized in the lowest Zeeman sublevel $m_J = -8$ without additional optical cooling steps [146]. This setup also allows for optical access from the top, which is used for a high resolution imaging system we will discuss in Sec. 2.2.4. We typically load the MOT for $5-7\,\text{s}$ and compress the the size afterwards by decreasing the magnetic field gradient and the detuning of the MOT light. We typically obtain 7×10^7 atoms and a final temperature of $\text{T}_{\text{cMOT}} \approx 10-12\,\mu\text{K}$.

2.2.2 Optical dipole trap

From the compressed MOT we load the atoms into a far-detuned crossed optical dipole trap (cODT). The cODT plays a crucial role in the work presented in this thesis. In it we evaporate the atoms to quantum degeneracy. Whether the ground state is a BEC or a supersolid depends among other parameters on the geometry of the trap. Typically, the trap near the intensity maximum can be well approximated by a harmonic potential

$$U_{\text{dip}}(x, y, z) = \frac{1}{2}m\omega_x^2 x^2 + \frac{1}{2}m\omega_y^2 y^2 + \frac{1}{2}m\omega_z^2 z^2 \tag{2.5}$$

where the confinement is defined by the trap frequencies $\omega_{x,y,z}$. For our experiment, we want to be able to change the trap frequencies independently, so that we can create a variety of different trap geometries, such as cigar-shaped traps ($\omega_x \simeq \omega_y \gg \omega_z$) or pancake-shaped traps ($\omega_x \simeq \omega_y \ll \omega_z$).
To this end, we combine three Gaussian beams with a wavelength of $\lambda_{\text{ODT}} = 1064\,\text{nm}$. As shown in Fig.

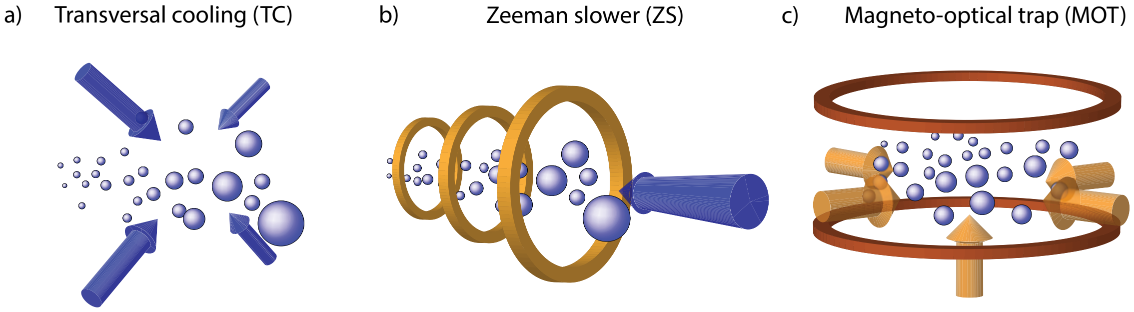

Figure 2.3: Illustration of the optical cooling techniques used in the experiment. a) Transverse cooling (TC). Two retroreflected beams are applied orthogonal to the atomic beam flux to collimate the atomic beam. b) Zeeman slower (ZS). The atoms are slowed down by a laser beam directed towards the beam flux. The detuning of the transition is varied along the length of the ZS (435 mm) by a spatially changing magnetic field along the ZS. c) Magneto-optical trap (MOT). The MOT consists of a magnetic trap created by a pair of coils in anti-Helmholtz configuration and five laser beams with $\lambda = 626\,\mathrm{nm}$ creating the velocity dependent force profile.

2.4 we cross two round beams at $\theta = 90^\circ$ with a waist of $w_{\mathrm{stat1/stat2}} = 60\,\mu\mathrm{m}$ (static ODT 1 & 2) and add another beam along the y-direction with a vertical waist of $w_{z,\mathrm{scan}} = 15\,\mu\mathrm{m}$ and an adjustable waist along the x-direction with $w_{x,\mathrm{scan}} \approx 15 - 105\,\mu\mathrm{m}$ (scanning ODT). The horizontal beam size can be adjusted by rapidly scanning the RF frequency of an AOD ($f_{\mathrm{trap}} \ll f_{\mathrm{scan}} = 20\,\mathrm{kHz}$), which leads in a rapid position change of the focus position in the x-direction. This projects an average potential onto the atoms with a maximum beam waist ratio of $w_x/w_z \approx 7$ for our setup.

For $w_{x,\mathrm{scan}}^{\max} \approx 105\,\mu\mathrm{m}$ we can approximate the trap frequencies resulting from the three overlapping beams as

$$\omega_x \approx \sqrt{\frac{4U_{0,\mathrm{stat1}}}{mw_{\mathrm{stat1}}^2} + \frac{2U_{0,\mathrm{stat2}}}{mz_{R,\mathrm{stat2}}^2}} \tag{2.6}$$

$$\omega_y \approx \sqrt{\frac{4U_{0,\mathrm{stat2}}}{mw_{\mathrm{stat2}}^2} + \frac{2U_{0,\mathrm{stat1}}}{mz_{R,\mathrm{stat1}}^2}} \tag{2.7}$$

$$\omega_z \approx \sqrt{\frac{4U_{0,\mathrm{scan}}}{mw_{z,\mathrm{scan}}^2} + \frac{4U_{0,\mathrm{stat1}}}{mw_{\mathrm{stat1}}^2} + \frac{4U_{0,\mathrm{stat2}}}{mw_{\mathrm{stat2}}^2}} \tag{2.8}$$

where $U_{0,i} = \frac{1}{\epsilon_0 c}\mathrm{Re}(\alpha)\frac{P_i}{\pi w_{x,i}(z) w_{y,i}(z)}$ where i defines the three beams and we omit the contribution of the scanning ODT beam to the horizontal trap frequencies $\omega_{x,y}$ due to the large beam size and the 45° angle between the traps. Note that the x, y, z directions of the traps are rotated by 45° to the experimental coordinate system given in Fig. 2.2.

Assuming that $U_{0,\mathrm{scan}} \approx U_{0,\mathrm{static1}} \approx U_{0,\mathrm{static2}}$, we can simplify Eq. (2.6)-(2.8). For the static traps the ratio between z_R and w is given by $\frac{z_R}{w} = \frac{\pi w}{\lambda} \approx 177$ and therefore we find that the second terms in (2.6) and (2.7) are vanishingly small. The ratio between the waists of the scanning ODT and the static ODTs is $\frac{w_{\mathrm{scan}}}{w_{\mathrm{stat1/stat2}}} = 4$ leading to a comparatively small contribution of the last two terms in (2.8), which we can therefore also omit. The resulting trap frequencies can therefore be controlled independently by

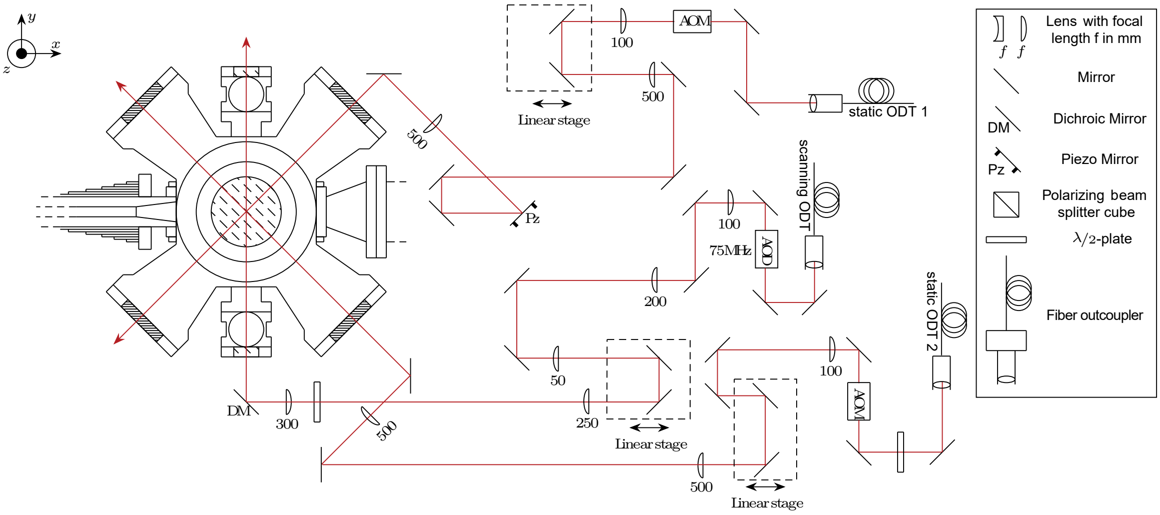

Figure 2.4: Illustration of optical dipole trap (ODT) setup. Adapted from [151]

adjusting the power in each beam, as long as the initial assumption is valid

$$\omega_x \approx \sqrt{\frac{4U_{0,\text{stat1}}}{mw^2_{\text{stat1}}}} \qquad \omega_y \approx \sqrt{\frac{4U_{0,\text{stat2}}}{mw^2_{\text{stat2}}}} \qquad \omega_z \approx \sqrt{\frac{4U_{0,\text{scan}}}{mw^2_{z,\text{scan}}}} \tag{2.9}$$

However, a challenge arises from the three-beam trap setup. The validity of the harmonic approximation depends on how well the three beams are overlapped, as can be seen in a few different cases in Fig. 2.5. Ideally the three beams overlap at their foci as shown in Fig. 2.5 a. Figure 2.5 shows the residual between the harmonic approximation and the actual potential from the overlapped beams. We see that displacements in the horizontal direction of the beams to each other of about $\Delta x_0 \approx 30\,\mu$m do not dramatically influence the potential shape (Fig. 2.5 b). But for vertical displacements $\Delta z_0 \approx 40\,\mu$m the potential is significantly anharmonic (Fig. 2.5 c). Experimentally the beams can be misaligned due to the finite precision with which we can align the beams. To mitigate this factor, we have installed piezo mirror mounts[6] for the static 1 ODT beam, which gives us a step size of $\Delta x = 185(7)$ nm for the horizontal and vertical beam position. This allows us to align the beams well within the required accuracy. Other causes of misalignment can be due to, for example, thermal lensing [159]. Figure 2.5 d also shows that we can compensate for misalignment by changing the power balance between the two static traps.

The $\lambda_{\text{ODT}} = 1064$ nm is provided by a 55 W laser system[7]. The light is distributed to three polarisation maintaining single mode fibres[8], which ensure a clean TEM$_{00}$ mode for all three beams. The optical setup of the distribution and the beam paths in front of the experimental chamber are described in great detail in Claudia Politi's thesis [151].

---

[6] Thorlabs KC1-P/M with the Thorlabs MDT693B driver

[7] Coherent Mephisto MOPA 55 W

[8] NKT Photonics LMA-PM-15

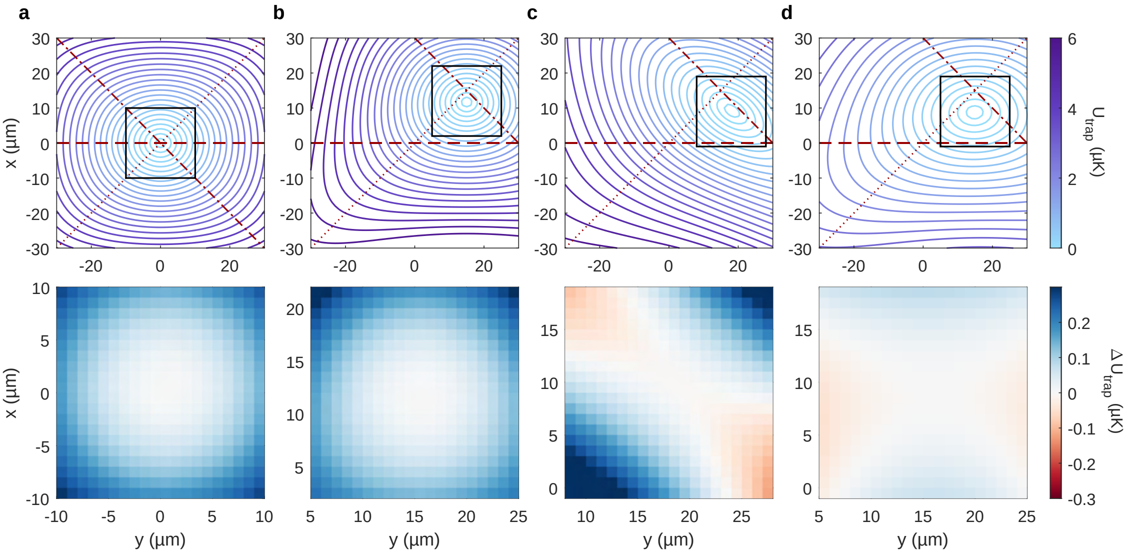

Figure 2.5: Trap potentials due to displaced beams and power imbalance. The potential depth U_{trap} (top) and the residual $\Delta U_{\text{trap}} = U_{\text{harm}} - U_{\text{trap}}$ (bottom) is shown for different beam displacements and different powers. The red lines represent the scanning ODT (dashed), the static ODT 1 (dashdotted) and the static ODT 2 (dotted). The squares around the minimum of the potential show the region of the residual. a) The beams are all overlapped in the centre of the figure. b) Displacement of the centre of the static ODT 1 beam by $\Delta x_0 = 30\,\mu$m. c) Additionally displacing the static ODT 2 beam along the z-axis by $\Delta z_0 = 40\,\mu$m. The powers of the beams for a)-c) are $P_{\text{scan}} = 0.8W$, $P_{\text{stat1}} = 0.5W$, $P_{\text{stat2}} = 0.5\,$W. d) Displacement as in c) but the power balance of the static beams ($P_{\text{stat1}} = 0.3W$, $P_{\text{stat2}} = 0.6\,$W) is changed to compensate for the misalignment.

2.2.3 Evaporation

The evaporation of atoms to achieve a PSD high enough for the atoms to condense is a crucial concept for ultracold atom experiments [27]. In the following an analytical model is discussed to illustrate how to efficiently evaporate and achieve large numbers of condensed atoms necessary to create the BEC and supersolid states the works are concerned with. The analytical model is also the basis for Monte-Carlo simulations that simulate the optimal transport of atoms to the SiSi chamber described in Ch. 5.2.

In order to reduce the temperature of the atomic gas, the high energy atoms have to be released and the cloud has to thermalise afterwards as shown in Fig 2.6. This is done by reducing the trap potential, which leads to atoms with high kinetic energy $E_{\text{kin}} > E_{\text{pot}}$ becoming untrapped. A simple semi-analytical model developed by Davis and colleagues is used to calculate the reduction in kinetic energy [160]. The temperature change can be described by

$$\frac{T'}{T} = \frac{N'}{N}^{\gamma} \tag{2.10}$$

where N and N' as well as T and T' are the atom number and temperature before and after reducing the potential. The exponent γ quantifies how much energy the evaporated atoms have removed from the gas. The larger γ, the more efficient the evaporation is. To estimate γ it is considered, that all atoms are colliding elastically and that all atoms with a kinetic energy below the truncated potential $E_{\text{atom}} < \eta k_B T$

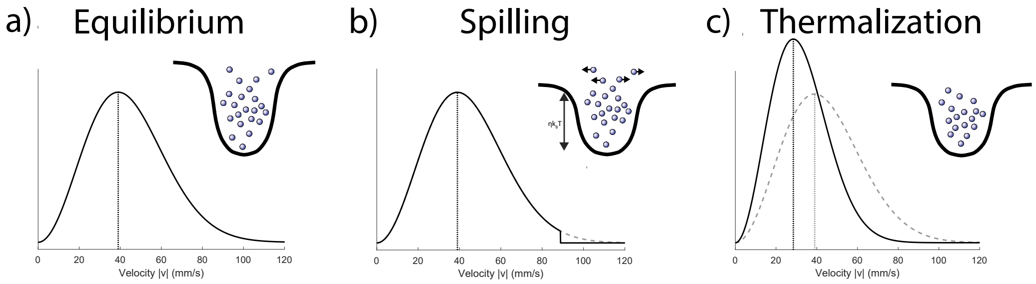

Figure 2.6: Illustration of the evaporation process of a thermal cloud. a) The cloud is thermalized in the ODT and the momentum of the atoms corresponds to a Maxwell-Boltzmann distribution. b) The ODT trap depth is truncated to $V_{\text{ODT}} = \eta k_B T$. Atoms with energies $E_{\text{atom}} > V_{\text{ODT}}$ are spilled from the trap and the velocity distribution is truncated as well. c) The atoms left in the trap are colliding elastically and the cloud thermalized. The velocity distribution is a Maxwell-Boltzmann distribution with smaller v_p and therefore the atomic cloud has a smaller temperature.

stay trapped and redistribute kinetically. γ is then given by [160]

$$\gamma = \frac{\varepsilon_{\text{eff}}(\eta)}{(3/2) + \xi} - 1 \tag{2.11}$$

where $\xi = \frac{d}{m}$ is given by the dimension of the cloud $d = 3$ and the order of the trapping potential $m = 2$ (for harmonic confinement). The term $\varepsilon_{\text{eff}}(\eta) k_B T$ gives the kinetic energy per atom removed from the cloud. For large truncation parameters $\eta \longrightarrow \infty$ the removed energy approaches $\varepsilon_{\text{eff}} \longrightarrow \eta + 1$ and therefore $\gamma \longrightarrow \infty$, so we get a very efficient but slow evaporation. For smaller η the evaporation efficiency reduces monotonically to $\gamma = 2/(3 + 2\xi)$.

The second important factor for efficient evaporation is a high thermalisation rate and a low number of inelastic collisions leading to atom loss or heating of the gas. We can estimate the thermalisation rate by estimating the average collision time of the atoms

$$\tau_{\text{therm}} = \frac{\alpha}{n v_a \sigma} \tag{2.12}$$

where $n = n_0 e^{-\eta}$ is the density of the cloud, α is the average number of collisions needed for thermalisation, $v_a = \sqrt{\frac{16 k_B T}{\pi m}}$ is the average velocity of an atom and the scattering cross section for a thermal dipolar gas is given by $\sigma = 8\pi a_s^2 + \frac{32\pi}{45} a_{\text{dd}}^2$ depending on the scattering lengths a_s and a_{dd}[161]. The shorter the thermalisation time, the faster the evaporation can take place. Therefore the density and scattering cross section should be comparably high.

The final factor is the atom loss during evaporation. These loss mechanisms can be summarised in a general equation [162]

$$\dot{N}(t) = \underbrace{-\frac{1}{\tau_v} N(t)}_{\text{one-body}} \underbrace{-\frac{1}{\beta} \int_V n^2(\mathbf{r}, t) d^3 r}_{\text{two-body}} \underbrace{-\frac{1}{\gamma} \int_V n^3(\mathbf{r}, t) d^3 r}_{\text{three-body}} - O(n^4) \tag{2.13}$$

One-body loss results mostly from atoms colliding with the background gas. The loss rate is defined by the lifetime τ_v and can be generally be reduced by improving the vacuum [163, 164]. Atoms are also lost from very shallow ODTs $U_{\mathrm{ODT}} < E_{\mathrm{rec}}$ when scattering spontaneously with the trap photons. Typical lifetimes can be on the order of minutes [90].

The second term describes atom loss due to inelastic two-body collisions of the trapped atoms. In addition to elastic collisions which lead to thermalisation, collisions can also lead to changes in the internal state of the involved atoms. In this processes the internal energy converts to kinetic energy which leads to atom loss or heating. In our experiment spin relaxation is such a process [165]. We prepare dysprosium in the lowest energetical state $m_J = -8$ as discussed in Sec. 2.1, and therefore inelastic two-body collisions are not possible.

The last term in (2.13) describes the three-body collisions of atoms. These collisions cause significant losses in dense atomic clouds, even though the atoms are prepared in their lowest energy state. In these collisions, two atoms form a bound dimer transferring the released energy to the third atom, leading to the loss of all three atoms. The loss can be minimised by reducing the interaction strength a_s between the atoms and is discussed in section 2.2.5.

Of course there are also higher order loss terms [166], but these contributions are generally omitted in our experiment, since we work at comparably small scattering lengths $a_s < 150a_0$.

The final evaporation sequence is very complex due to the three independent ODT beams. Therefore, we optimize the the sequence experimentally by tuning the powers of the different beams as well as the scanning range of the AOD of the scanning ODT beam. The final atom number and condensate fraction depend strongly on the final trap geometry and whether the achieved state is a BEC, supersolid or independent droplets. We will discuss the exact parameters for the different experiments, but commonly we achieve in a trap with $(f_x, f_y, f_z) = (50, 50, 120)$ Hz BECs with 1×10^5 atoms and a condense fraction of $\approx 60\%$.

2.2.4 Imaging system

After the degenerate gas has been prepared and manipulate, the atoms are imaged. In our experiment, we use two different imaging techniques. Absorption imaging is a robust technique to image the thermal cloud and the BEC and to measure the atom number and temperature of the cloud, and for very dense clouds such as supersolids and independent droplet states we are using the phase-contrast imaging technique.

When light, propagating along the z-direction, travels through a dielectric medium it can be described by [141]

$$E(z,t) = E_0 e^{\mathrm{i}(k'z-\omega t)} = E_0 e^{\mathrm{i}(kz-\omega t)} e^{-\beta} \tag{2.14}$$

where E_0 is the amplitude of the light field and $k = \omega/c$ and ω are the wave number and frequency in vacuum. When propagating through a medium, the speed of light and therefore the wave number $k' = \omega/c'$ is modified. This can be expressed by the exponent β which for light propagating through a

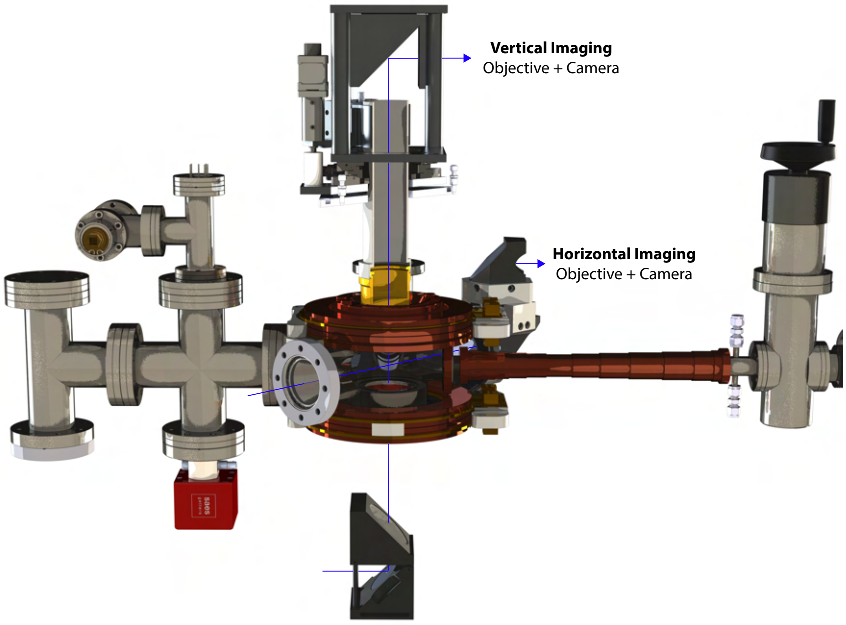

Figure 2.7: Illustration of imaging beam paths. The horizontal light is guided through the chamber onto a dichroic mirror and through a periscope to the camera. The vertical imaging beam is send from the bottom through the chamber and the objective and then send to the camera over a dichroic mirror.

dilute gas can be approximated as [141]

$$\beta = \frac{\sigma_0 n_z(x,y)}{4\Delta^2 + \Gamma^2(I/I_{\mathrm{sat}})}\left(\mathrm{i}\Gamma\Delta + \frac{\Gamma^2}{2}\right) \tag{2.15}$$

where $n_z(x,y)$ is the column density of the cloud, $\Delta = \omega - \omega_0$ is the detuning of the light to the resonance frequency ω_0 with the atoms, Γ is the spontaneous excited state decay rate, $I_{\mathrm{sat}} = \frac{\hbar\Gamma\omega_0^3}{12\pi c^2}$ is the saturation intensity of the transition and $\sigma_0 = \frac{3\lambda^2}{2\pi}$ is the atom-photon scattering cross-section. The imaginary part of Eq. (2.15) leads to a dispersive phase shift of the propagating light, and the real part leads to a damping and therefore absorption.

If the light is on resonance $\Delta \longrightarrow 0$ only the absorptive part is relevant and Eq. (2.15) turns into the Beer-Lambert law [167]. Absorption imaging is a commonly used technique in ultracold gas experiments. In our experiment we work in the low saturation regime [27] and use the $\lambda = 421$ nm light to resonantly drive the closed broad transition $|8,-8\rangle \longrightarrow |9,-9\rangle$. The column density $n_z(x,y)$ can then be inferred by the integrated Beer-Lambert law [168]

$$n_z^{\mathrm{abs}}(x,y) = -\frac{1}{\sigma_0}\ln\left(\frac{I_{\mathrm{out}}(x,y) - I_{\mathrm{dark}}(x,y)}{I_{\mathrm{in}}(x,y) - I_{\mathrm{dark}}(x,y)}\right) \tag{2.16}$$

where $\sigma_0 = \frac{3\lambda^2}{2\pi}$ is the atom-photon scattering cross-section, $I_{\mathrm{out}}(x,y)$ ($I_{\mathrm{in}}(x,y)$) is the local intensity on an image taken with (without) the atomic cloud and $I_{\mathrm{dark}}(x,y)$ is the local intensity of a picture without light, to correct for any noise from the camera such as dark currents or faulty pixels. These images are taken in rapid succession for each experimental sequence.

At large densities, our absorption imaging becomes saturated ($I_{out} \to 0$) and we use phase-contrast imaging for the modulated states instead. For this technique, the light is far detuned $\Delta \gg \Gamma$ from the resonant transition frequency, such that the dispersive term in Eq. (2.15) dominates. The phase change of the light after passing the cloud can therefore be approximated as [169]

$$\beta(x, y, \Delta) \approx \mathrm{i}\frac{1}{4}\sigma_0 n_z(x, y)\frac{\Gamma}{\Delta} \tag{2.17}$$

The information of the phase gets lost when imaging the intensity profile of the outgoing light I_{out}. Instead, we do Faraday imaging [169, 108]. By sending linear polarised light along the polarisation axis (direction of the homogeneous magnetic field), the atoms experience a 50/50 mix of right and left circularly polarised light. Atoms interact differently with σ^+ and σ^- polarised light due to the greatly different Clebsch-Gordan coefficients $\frac{C_-^2}{C_+^2} = 153$ [150], which means that the phase change of the σ^--polarised light is larger than of the σ^+-polarised light as it passes through the atom cloud. By adding a polariser in front of the camera we filter a polarisation dependent part of the light, and the resulting intensity distribution reveals the density distribution of the cloud. The relationship between phase change and intensity distribution as a function of the angle of the polariser Θ was derived in detail in Max Sohmen's thesis [150]. We introduce a polariser at an angle $\Theta = 45°$ to the original linear polarisation of the light and the intensity ratio is described by [150]

$$\frac{I_{\mathrm{p}}(x, y)}{I_0(x, y)} \approx \frac{1}{2}\left[1 - \mathrm{i}\beta(x, y, \Delta)\right] \tag{2.18}$$

where I_{p}/I_0 is the ratio of the intensity profile of the incoming and outgoing beam and ϕ is the phase acquired due to dispersion. At this angle, the intensity is linearly dependent on the phase. From (2.17) and (2.18) we find the density distribution

$$n_z^{\mathrm{PC}}(x, y) = -\frac{4\Delta}{\Gamma\sigma_0}\left[\frac{I_p^*(x, y)}{I_{\mathrm{ref}}^*(x, y)} - 1\right] \tag{2.19}$$

where $I_{p/\mathrm{ref}}^*(x, y) = I_{p/\mathrm{ref}}(x, y) - I_{\mathrm{dark}}(x, y)$ are the intensities corrected for noise from the camera, just as with the absorption imaging.

In the experiment, we have a horizontal and a vertical imaging setup. The horizontal setup consists of an objective made from a home-build 2"-lens triplet, which gives a magnification of $M = 3.2$ and a scientific CMOS-based camera[9]. Therefore, each pixel represents an area of $\approx 2\,\mu\mathrm{m} \times 2\,\mu\mathrm{m}$ but is diffraction limited to $d_{\mathrm{min}}^{\mathrm{horz}} \approx 3.5\,\mu\mathrm{m}$. This setup is used to image the atoms at any stage from the cMOT to the condensed state after a time-of-flight (TOF), and exclusively absorption imaging is performed.

To resolve small structures such as droplets ($d \approx 5\,\mu$m) or vortices ($d \lessapprox 1\,\mu$m) in-situ, a vertical objective with a higher $\mathrm{NA}_{\mathrm{max}}^{\mathrm{vert}} = 0.45$ is installed. This setup is possible due to the open-top MOT design. The

---

[9] Andor Neo 5.5 sCMOS, 16.6mm × 14.0mm chip size, 2560 × 2160 pixels, 6.5µm × 6.5µm pixel size, AR-coated window for 401nm, 421nm, 583nm and 626nm

	horizontal imaging	vertical imaging	
	absorption	absorption	phase contrast
working distance	250 mm	55 mm	
effective focal length	≈ 200 mm	65 mm	
magnification	×3.2	×15.3(1)	
pixel size	$6.5\,\mu$m × $6.5\,\mu$m	$8\,\mu$m × $8\,\mu$m	
max. NA	0.07	0.45	
FOV	≈ 2 mm	$> 130\,\mu$m	
resolution (421 nm)	$3.5\,\mu$m	$0.71(1)\,\mu$m	
detuning	0 MHz	0 MHz	1085 MHz

Table 2.2: Relevant properties of horizontal and vertical imaging systems. Data taken from [150, 137]

measured diffraction-limited resolution of the system is Res $= 0.71(1)\,\mu$m [150]. We use a magnification of $M = 15.3(1)$ leading to a pixel resolution of 0.52µm x 0.52µm[10]. This allows us to resolve droplets in-situ and vortices after a short TOF.

The vertical imaging setup is used for both in-situ and TOF measurements, where the atoms fall along the imaging axis. To keep the atoms in focus, the objective can be displaced along the vertical direction by up to 12 mm using a high-precision stepper motor. This allows to keep the gas in focus for up to $t_{\mathrm{TOF}} = 40$ ms. The vertical imaging setup is designed as such that the detuning and polarisation of the light can be switched easily to perform either absorption or phase-contrast imaging.

Due to the high resolution of the vertical imaging system, the system is also highly sensitive to blurring due to photon scattering. By absorbing and spontaneously re-emitting a photon, momentum is transferred to the atoms and its velocity changes, which can be estimated by

$$\frac{\Delta \mathbf{v}}{\Delta t} = \frac{\hbar\Gamma}{2m}\frac{I}{I_{\mathrm{sat}}}\left(\mathbf{k}_{\mathrm{ab}} - \mathbf{k}_{\mathrm{em}}\right) \tag{2.20}$$

where $\mathbf{k}_{\mathrm{ab}}$ and $\mathbf{k}_{\mathrm{em}}$ are the wave vectors of the absorbed and re-emitted photon respectively. The movement of the atoms in the imaging plane resembles a random walk and therefore leads to blurring of small structures such as vortices. To avoid this, one needs to keep the illumination duration $\Delta t = t_{\mathrm{img}}$ short. To understand what duration t_{img} is suitable for our experimental parameters, we perform Monte-Carlo simulations with Eq. (2.20) as the underlying model. The photons of the imaging light are absorbed after each time step $\tau = 1/\Gamma_{\mathrm{ph}} s$ and re-emitted in a random direction in the next step. For these simulations, interactions between atoms are not considered. The result of the simulations can be seen in Fig. 2.8.

---

[10] During the time of this thesis we have used 2 different cameras in this setup. The Andor Neo 5.5 sCMOS and the Luca EM R 604 EMCCD camera, 8mm x 8mm chip size, 1004 x 1002 pixels, $8\,\mu$m × $8\,\mu$m pixel size. The calculated pixel resolution is for the Luca camera

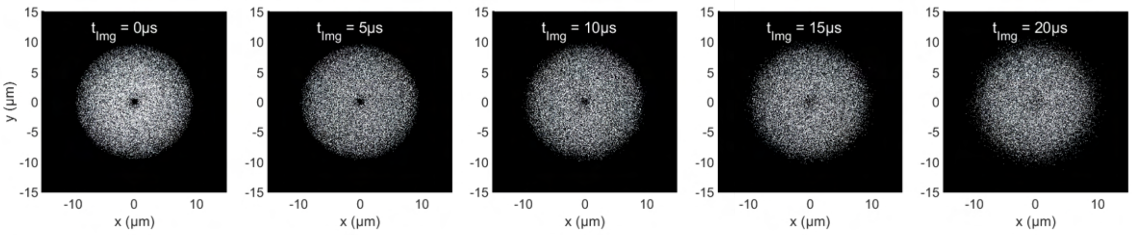

Figure 2.8: Monte-Carlo simulation of vortex blurring due to the absorption imaging for different exposure times t_{img}. The initial state at $t_{\mathrm{img}} = 0\,\mu$s is generated for $N = 50000$ generating a cloud with a Thomas-Fermi radius of $R_{\mathrm{TF}} \approx 6\,\mu$m and a density depletion is imprinted in the center of the cloud with the size $\xi \approx 1\,\mu$m. Every single atom absorbs a photon every $\tau = 1/\Gamma_{\mathrm{ph}} s$ and emitting it one simulation step later. The resulting density profile (integrated along the imaging direction) is shown for different exposure times $t_{\mathrm{img}} = [0, 5, 10, 15, 20]\,\mu$s, showing a fading of the density depletion for longer exposures. Additional blurring due to the imaging signal and defocusing are not considered.

Here we simulate, comparable to typical experimental conditions, a Thomas-Fermi distribution of 50000 randomly arranged atoms with a density depletion in the centre with a radius of $\xi \approx 1\,\mu$m. This depletion represents a small structure that is reminiscent, for example, of vortices. While the structure is clearly visible initially, the contrast decreases drastically for exposure times $t_{\mathrm{img}}^{\mathrm{max}} > 10\,\mu$s, reducing the fidelity of recognising these structures in the images. Note that this simulation does not include other sources of image blur due to the finite resolution of the imaging system or defocusing of the cloud due to momentum transfer along the imaging direction. In our experiment, the shortest possible pulse times for vertical absorption imaging before the signal-to-noise ratio becomes too small are about $t_{\mathrm{img}} = 3 - 4\,\mu$s which is well below $t_{\mathrm{img}}^{\mathrm{max}}$.

2.2.5 Magnetic fields – Controlling atomic interactions

There are many possible ways to manipulate atoms in ultracold atom experiments [170]. For the experiments discussed in this thesis we focus on controlling the scattering properties of the atoms with magnetic fields.

As already discussed in Sec. 1.2, dysprosium atoms interact through contact interactions (CI) and dipole-dipole interactions (DDI). As can be seen in Eq. (1.9) the DDI strength is set by the intrinsic dipole moment of the atoms, the distance of the atoms and the relative direction of the dipole moments of the interacting atoms. While the first two points are set by the properties of the atoms and by the trap geometry and density of the gas, we can influence the relative collision angle by setting the direction of the magnetic field relative to the trap. The DDI lead to magnetostriction, where the gas elongates along the magnetic field direction compared to non-dipolar gases [99, 100, 101], leading to a deformation of the gas that can be controlled by the magnetic field.

And in Sec. 1.3.4 it has been already discussed that the direction of the dipoles compared to the direction of the weakest and strongest confinement axis of the trap can lead to radically different condensate ground states, such as the macrodroplet state or the supersolid state.

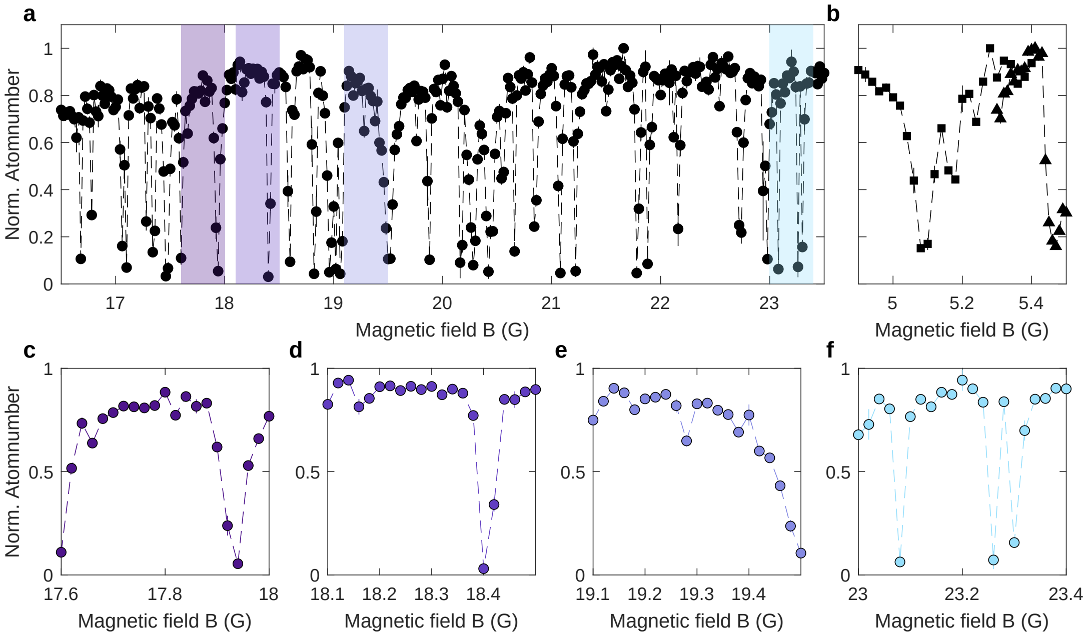

Figure 2.9: Atom-loss spectroscopy of ^{164}Dy and ^{162}Dy . a) Spectroscopy of ^{164}Dy in the magnetic field region $|\mathbf{B}| = 17 - 23$ G. b) Spectroscopy of ^{162}Dy around $|\mathbf{B}| = 5.2$ G. c)-f) Details of relevant regions marked in a). The methodology of the atom-loss spectroscopy is discussed in appendix A.

The control of the magnetic field allows us to widely tuned the contact scattering length a_s and therefore also ε_{dd} in the vicinity of Feshbach resonances [88, 33]. The contact scattering length a_s is phenomenological described by [34]

$$a_s(B) = a_{bg}\left(1 - \frac{\Delta}{B - B_0}\right) \tag{2.21}$$

where B_0 is the centre of the Feshbach resonance, Δ is the width of the resonance and a_{bg} is the background scattering length. The position and width of these Feshbach resonances depend on the internal structure of the colliding atoms and are discussed in reviews [171, 88] and textbooks [172].

As can be seen in Fig. 2.9 dysprosium exhibits a large amount of Feshbach resonances, compared to the Feshbach spectrum of, for example, alkali atoms [173]. This gives us a large variety of different magnetic field regions already at low magnetic fields, which allows us to tune the interaction strength to the desired values. However, most of the Feshbach resonances in dysprosium are much narrower than a single Gauss, which makes a high control of the magnetic field necessary.

Furthermore, the complex internal structure of the dysprosium atoms and the resulting large spectrum of resonances make it difficult to calculate the background scattering length a_{bg} and determine the scattering length depending on the magnetic field strength from coupled-channel theoretical models as done for alkali atoms [174, 175]. Therefore, other techniques are necessary to determine $a_s(B)$ for a given magnetic field, such as cross-dimensional thermalisation measurements [176, 161] or measuring on-site interactions in optical lattices [177]. For many of the magnetic field regions relevant for this thesis, the scattering length

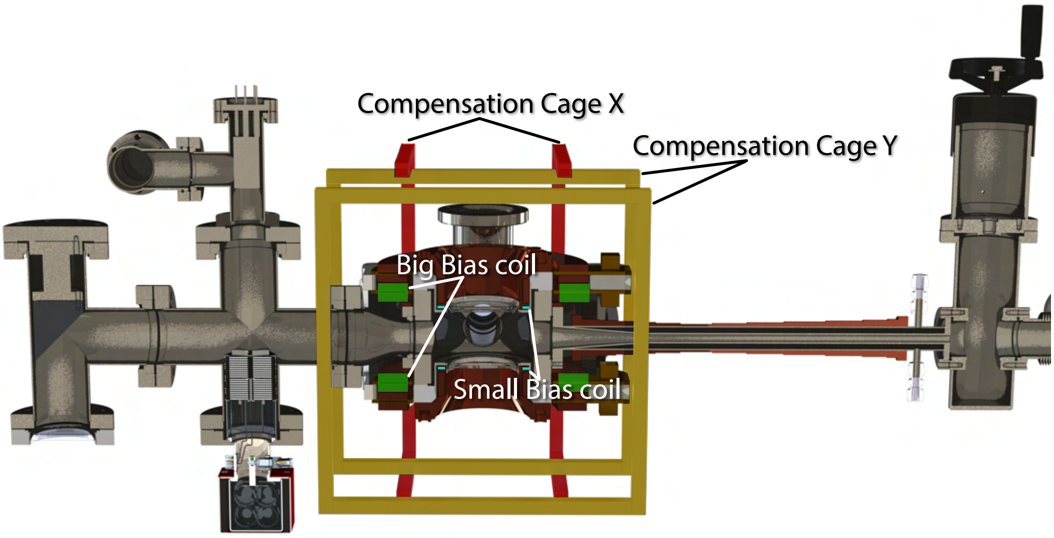

Figure 2.10: Illustration of the magnetic field coil setup. The X-&Y-Compensation Cages (red and yellow), Big Bias Coils (green) and Small Bias Coils (cyan) are indicated.

$a_s(B)$ has not been characterised before. In the experiments carried out during this thesis, the Feshbach resonances have been mapped out through atom-loss spectroscopy (described in detail in appendix A) and a_s was inferred by measuring the ground state of the degenerate state and comparing it with eGPE simulations.

The important magnetic field regions for the experiments discussed in the following chapters are shown in Fig. 2.9. The FB spectrum for ^{164}Dy from 16.5 G to 23.5 G is shown in Fig. 2.9 a where we can find BEC, SS and ID states for the trap parameters used in experiment (regions highlighted in Fig. 2.9 c-f). Figure 2.9 b shows the FB spectrum for ^{162}Dy around 5.3 G, where we find a BEC state. Additional in-situ images of the corresponding ground states are shown in the appendix A.

The magnetic field is contolled by four independent pairs of coils in Helmholtz configuration generating homogeneous fields along the three directions of space (taken from [137]):

- **Big bias coils** – The magnetic field in the main chamber is generated by a pair of large coils (27×2 windings) mounted above and below the chamber to create a homogeneous magnetic field in z-direction. Coils are rated for currents up to 200 A[11]. The magnetic field provided is $B_z = 4.372$ G/A with a flatness of 10^{-4} within ± 1.5 mm of the centre along the z-axis. Therefore, magnetic fields $B > 800$ G can be generated. To increase the stability a self-build PID is moderating the current measured with a transducer[12]. With this setup we can keep the current stable to $\Delta I < 5$ mA, which gives a magnetic field stability of $\Delta B < 20$ mG at $B = 20$ G.

---

[11] Supplied by Delta Elektronika SM 30-200

[12] LEM IT 200-S Ultrastab

- **Small bias coils** – We have an additional pair of smaller coils (6 windings). These produce a magnetic field of $B_z = 0.779\,\mathrm{G/A}$ with a (relative) flatness of 10^{-4} within ± 0.5 mm of the centre along the z-axis [137]. The connected bipolar power supply delivers a current of up to $I = \pm 10\,\mathrm{A}$ with an integrated current probe and PID circuit, and therefore the coils supply $B_z > 7\,\mathrm{G}$ with a stability of $\Delta B < 20\,\mathrm{mG}$. The smaller winding number allows the current to change faster than for the larger coils due to the smaller inductance.
- **X- and Y-Compensation coils** – Magnetic fields in the horizontal direction are generated by two pairs of rectangular coils (11x2 windings). The larger of the two pairs creates a homogeneous magnetic field in the x-direction of $B_x = 1.04\,\mathrm{G/A}$ and the smaller pair $B_y = 1.12\,\mathrm{G/A}$ in the y-direction. We can send up to $I = \pm 14\,\mathrm{A}$ to the coils with bipolar power supplies of the same type as for the small bias coils and therefore generate magnetic fields of $B_{x/y} > 14\,\mathrm{G}$ with a stability of $\Delta B < 20\,\mathrm{mG}$, which allows us not only to compensate for stray magnetic fields in the horizontal direction but also to point the magnetic field vector in any direction as long as the magnetic field strength $|\mathbf{B}| < 14\,\mathrm{G}$.

The magnetic fields at the atoms are calibrated by radio frequency spectroscopy as described in the appendix B. Our setup gives us the ability to rotate the magnetic field in all directions as long as we stay at $|B| < 14\,\mathrm{G}$. For the rotation of the supersolid we rotate at magnetic fields $|B| > 14\,\mathrm{G}$, which limits the tilt from the vertical axis to $\theta < 40°$.

This concludes the cooling, trapping, imaging, and manipulation toolbox necessary for the experiments that follow in the next chapters.

3

Vortices in dipolar Bose-Einstein condensates

> *The second part concerns the case in which vorticity of the superfluid exists. Our position here is less satisfactory and more uncertain. It is described here in considerable detail because of the interesting problem it presents.*
>
> ***Richard Feynman***
> *Progress in Low Temperature Physics I (1955)*

In this chapter we discuss the interacting Bose-Einstein condensates under rotation, which leads to quantised vortices. In particular we look at the influence of dipolar interactions, which has so far not been studied. The superfluid properties of the interacting BECs lead to the existence of vortex states with quantised 2π phase windings which can be observed as density depletions in the condensate, reminiscent of tornadoes or whirlpools.

These vortices have been of interest to physicists since the early days of quantum fluids. Experiments in rotating discs containing helium allow to measure the transition between the normal and superfluid flow at a critical temperature [178, 179]. Landau defined a critical velocity v_c up to which the fluid exhibits superfluid flow [106]. But, inconsistent with Landau's theory, in these experiments dissipation was observed at unexpectedly low rotation frequencies. The key insight came from Feynman [180] – inspired by Onsager [181] – who proposed that the nucleation of quantised vortices was the reason for the dissipative behaviour.

And indeed, vortices [182, 183, 184] as well as vortex rings [185] could be observed in superfluid helium. At the same time, quantised magnetic vortices could also be detected in superconducting materials [186, 187, 188]. And not long after the advent of ultracold atomic gas experiments and the first creation of BECs the first vortices were created and directly observed [39, 189, 190], as well as the first vortex lattice [40]. Ultracold gases proved to be ideal test beds for studying the dynamics of vortices, in particular because of the high degree of control over confinement and interactions, and the low density compared to solid-state systems, which leads to comparably large and directly observable vortices. Studies include the nucleation of vortices [191, 192, 193, 194], the precession of vortices [189], vortex bending [195], vortex lattice dynamics and Tkachenko modes [196, 197, 198] and Kelvin modes [199]. It has even been possible to bring the rotating BEC into a lowest Landau level (LLL) by geometric squeezing [200, 201]. Quantised vortices have also been studied in different geometries such as box potentials [202] and ring traps [203] and in lower-dimensional 2D systems to study, for example, the Berezinskii-Kosterlitz-Thouless (BKT) crossover [50, 53]. They play a significant role for quantum turbulence [204, 205] and have also been observed in fermionic systems [206].

So far, the work on vortices in quantum gases has been limited to systems with short-range contact interactions. With the paper "Observation of vortices and vortex stripes in a dipolar condensate" [207] we were able to create vortices for the first time within an atomic cloud of dipolar atoms in the context of ultracold gases. The following section reviews the basic properties of quantised vortices in trapped ultracold gases and discusses novel aspects brought in by the dipolar interactions between the atoms.

3.1 Quantized Vortices: Rotate the irrotatable

> *When we compare our idealised model with reality, we have to admit one profound difference: the distributions of vorticity which occur in the actual flow of normal liquids*$^{(1)}$ *are continuous [...]*
>
> $^{(1)}$*Vortices in a suprafluid are presumably quantized; the quantum of circulation is h/m, where m is the mass of a single molecule.*
>
> ***Lars Onsager***
> *Statistical Hydrodynamics (1949) [181]*

What exactly are vortices, how can we create them, and how do they show up in our system? This chapter gives an introduction to vortices in rotating dipolar condensates and additional information on the paper "Observation of vortices and vortex stripes in a dipolar condensate".

3.1.1 Basic properties of quantised vortices

A Bose-Einstein condensate is irrotational. This means that if the condensate is rotated, the curl of the velocity field of the BEC is zero

$$\nabla \times \mathbf{v}(\mathbf{r}, t) = 0 \tag{3.1}$$

This follows from the fact that the velocity field of the condensate is defined by[95]

$$\mathbf{v}(\mathbf{r}, t) = \frac{\hbar}{m} \nabla S(\mathbf{r}, t) \tag{3.2}$$

where m is the mass of an atom and $S(\mathbf{r}, t)$ is the phase of the condensate as seen in Eq. (1.13). Since $S(\mathbf{r}, t)$ is a scalar field, the identity $\nabla \times (\nabla S(\mathbf{r}, t)) = 0$ holds, leading to Eq. (3.1).

The consequence of (3.1) is that the BEC – and in general solutions of the eGPE (1.12) – can only adopt certain velocity fields $\mathbf{v}(\mathbf{r})$ when rotated. For example, a rigid body-like rotation, where the flow field around a core increases linearly with radius $|\mathbf{v}| \propto r$ would be rotational $\omega(\mathbf{r}, \mathbf{t}) \neq 0$.

Instead, a valid solution (1.13) of a rotating condensate is the flow field around a vortex, as shown in Fig. 3.1. Since the phase $S(\mathbf{r}, t)$ must be single-valued in a BEC, the total phase change along a closed loop

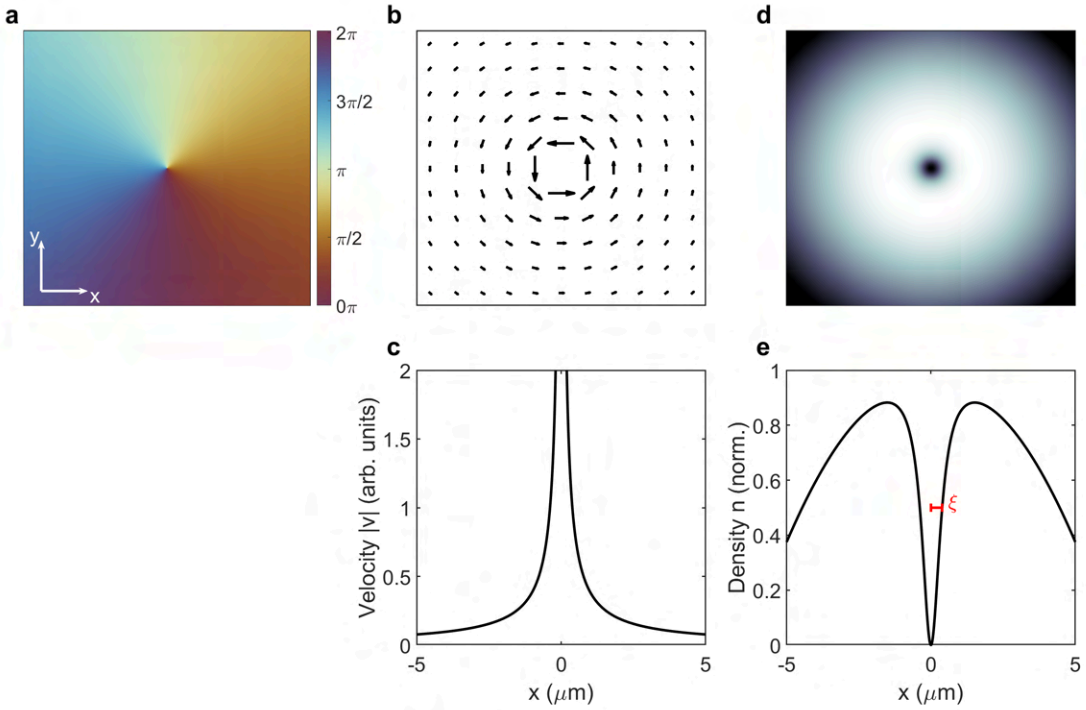

Figure 3.1: Example of phase, velocity and density around a quantized vortex. a) Looking along the rotation axis, the phase winds around the central point from $0 \longrightarrow 2\pi$. b) The resulting velocity vector field $\mathbf{v}(x,y)$, along with c) the absolute value of the velocity $|\mathbf{v}(x,y)|$ along the x-axis for $y=0$. d) An example of the density distribution $n(x,y)$ at $z=0$. e) The normalised density distribution along the x-axis for $y=0$. The corresponding healing length is indicated in red.

must be a multiple of 2π

$$\oint \nabla S d\mathbf{l} = q 2\pi \tag{3.3}$$

which leads directly to the quantity of circulation

$$\Gamma = \oint \mathbf{v} d\mathbf{l} = q 2\pi \frac{\hbar}{M} \tag{3.4}$$

In this thesis I will refer to the natural number q as the vortex charge. Eq. (3.4) shows that the circulation of the vortices is quantised as predicted by Onsager [181]. However, it has been shown theoretically and experimentally that the energy of a solution of multiple singly charged vortices is generally lower than the solution with a single multi-charged vortex [180], so $q = \pm 1$ depending on the direction of circulation will be considered in the remainder of this thesis. Higher charged vortices have so far only been stabilised in supercurrents in toroidal traps [208]. Instead, for large rotational frequencies Ω, single-charged vortices are generally found to arrange in a lattice structure, where the number of vortices is fixed by the rotational frequency [40, 206].

In the density distribution of BECs, vortices appear as local density depletions along the rotation axis, reminiscent of swirls in classical fluids or tornadoes. To understand this, we consider a constant velocity field $\mathbf{v}(\mathbf{r}_\perp, z)$ around an isotropic vortex core, as shown in Fig. 3.1

$$\mathbf{v}(\mathbf{r}_\perp, z) = \frac{\hbar}{m r_\perp}\hat{e}_\varphi \tag{3.5}$$

where the rotation axis is along the z-direction and $\mathbf{r}_\perp$ is a vector from the vortex centre perpendicular to the rotation axis. For simplicity, it is assumed that the position of the vortex centre does not change along the z-axis, leading to a straight vortex tube. This velocity field is irrotational as defined in (3.1). For $r \longrightarrow 0$, the velocity diverges. Therefore, to prevent the kinetic energy from diverging, the density at the centre of the vortex reduces to zero.

To find the density distribution including the vortex, one generally has to solve (1.12) numerically. But considering that the vortex size is much smaller than the condensate $r_\perp \ll R_\perp$, where $R_\perp$ is given by (1.15), the local density can be assumed to be homogeneous and the density distribution around a vortex can be approximated by $n_v(\mathbf{r}_\perp, z) = |\Psi_v(\mathbf{r}_\perp, z)|^2$ [95] where

$$\Psi_v(\mathbf{r}_\perp, z) = \sqrt{n_0} f\left(\frac{r_\perp}{\xi}\right) \tag{3.6}$$

where $n_0 = n(0, z)$ is the density for the solution without vortex at the centre of the BEC. The dimensionless function $f(\eta)$ satisfying the equation $\frac{1}{\eta}\frac{d}{d\eta}\left(\eta\frac{df}{d\eta}\right) + \left(1 - \frac{q^2}{\eta^2}\right) f - f^3 = 0$, which is obtained by inserting (3.6) into the stationary ($i\hbar\frac{\partial\Psi(\mathbf{r},t)}{\partial t} = 0$), homogeneous ($V(\mathbf{r}) = \text{const.}$) eGPE (1.12). For large distances from the vortex core $f(\infty) = 1$, the cloud assumes the density without the vortex, and for $\eta \longrightarrow 0$ the solution tends to zero as $f \approx \eta^q$. The size of the vortex core is given by the healing length ξ, which can be approximated in the dipolar case by [95, 91]

$$\xi(\mathbf{r}) = \frac{\hbar}{\sqrt{2m\left[g n_0 + V_{\mathrm{dd}}^{\mathrm{mf}}(\mathbf{r})\right]}} \tag{3.7}$$

A consequence of the DDI is that the healing length is anisotropic. If the axis of rotation and direction of polarisation of the dipoles are not aligned, the density around the vortex core becomes anisotropic, as has been shown in simulations [209, 98]. Vortices are expected to elongate along the projection of the polarisation direction of the dipoles in the x-y plane, orthogonal to the rotation axis.

When the vortex state is the ground state of the rotating system depends on the rotation frequency of the cloud Ω. So far, the vortex solution has been calculated in the laboratory reference frame. This is appropriate because we assume that the total angular momentum of the system is held by the vortex and that the cloud itself is not rotating. The total energy of the system is then given by the energy of the state without vortex plus the additional energy having the vortex $E = E_0 + E_v$. In general, a BEC rotating at a constant frequency Ω can be described in the rotating frame of reference, where the total energy is given by $E = E' + \boldsymbol{\Omega} \cdot \mathbf{L}$, where $E' = E_0$ is the energy of the stationary solution in the rotating frame of reference and $\mathbf{L}$ is the total angular momentum of the system. Considering the rotation axis along the z-direction, this means that there is a critical $\Omega_c = \frac{E_v}{L_z}$, above which the vortex solution is energetically favourable.

It has been shown that as long as $\varepsilon \ll 1$, the energy of a state with a single centred vortex is well approximated by the analytical solution for the non-dipolar BEC [210, 172].

$$E_v = \frac{4\pi n_0}{3}\frac{\hbar^2}{m} R_z \ln\left(0.671\frac{R_\perp}{\xi_0}\right) \tag{3.8}$$

Here the peak density n_0 is given by the non-vortex solution (1.14), the corresponding healing length ξ_0 by (3.7), and the cloud radius $R_\perp$ by (1.15) as well as R_z by κ in (1.15). All of these values are modified by the DDI compared to the non-dipolar gas.

Similarly, the angular momentum L_z in a harmonically trapped condensate is given by [172]

$$L_z = \frac{8\pi}{15} n_0 R_\perp^2 R_z \hbar \tag{3.9}$$

and therefore the critical frequency Ω_c is given by

$$\Omega_c = \frac{5}{2}\frac{\hbar}{m R_\perp^2} \ln\left(0.671\frac{R_\perp}{\xi_0}\right) \tag{3.10}$$

Eq. (3.10) gives the minimal rotation frequency, such that the vortex solution is the energetical ground state and therefore stable. In experiments dissipation due to the interactions of the vortices with the thermal part of the gas [211] leads either to expulsion of the vortex ($\Omega < \Omega_c$) or to the vortex moving towards the centre ($\Omega > \Omega_c$) [212].

We can estimate the size and energy of the vortex for the parameter used in the experiment. We trap ^{162}Dy atoms in a dipole trap with $[\omega_\perp, \omega_z] \approx 2\pi \times [50, 140]$ Hz, the condensed atom number is $N_c \approx 15,000$ and the contact interaction is $a_s \approx 111 a_0$ [207]. The Thomas-Fermi approximation $N\frac{a}{a_{\mathrm{ho}}} > 1$ is satisfied, so we can calculate the radius of the gas from Eq. (1.15). For the above parameters, we find $[R_\perp, R_z] \approx [5.2, 2.9]\,\mu$m and that the size of the vortex cores is $\xi \approx 480$ nm. We can also calculate the critical rotation frequency to be $\Omega_c \approx 0.22\omega_\perp$

3.1.2 Nucleating the vortices

> *To generate or to destroy "Wirbelbewegung" in a perfect fluid can only be an act of creative power.*
>
> ***Sir William Thomson (Lord Kelvin)***
>
> *On Vortex Atoms (1867) [213]*

In the experiment, we are starting with a non-rotating, vortex-free BEC and by rotating the system, we are nucleating vortices. As we see from Eq. (3.5), the vortex solution has a singularity in the velocity field at the centre of the vortex. This means that the state with a vortex is topologically different from the vortex-free state, where we do not have any singularity. There is no continuous deformation from one state to the other and, therefore, the vortex state is topologically protected [98]. This leads, even though the vortex state might be the energetical ground state, to a significant energy barrier that must be overcome to transition from the vortex-free state to nucleating vortices.

Therefore, to nucleate vortices in BECs, rotation frequencies much larger than $\Omega \gg \Omega_c$ have to be achieved [193]. As a nucleation mechanism, it is suggested that for a sudden application of a constant rotation frequency Ω the spontaneous formation of surface deformations drastically reduces the energy barrier and favours the nucleation of vortices. The polarity of surface deformation ℓ and the corresponding rotation frequency $\Omega = \omega_\perp/\sqrt{\ell}$ at which the instability is triggered depends on the way the condensate is rotated [214, 190]. Other possibilities are the adiabatic increase of Ω, where at $\Omega > \omega_\perp/\sqrt{\ell}$ dynamical instabilities lead to the nucleation of vortices [193, 192, 191].

In ultracold gas experiments, there are many different ways to impart angular momentum to the cloud and nucleate vortices:

- **Continuous rotation of a slightly anisotropic trap** [190, 40, 215, 196]. Reminiscent of a rotating bucket, the BEC can be rotated in a rotating anisotropic trap. In this case, a quadrupol deformation $\ell = 2$ leads to the nucleation of vortices. The advantage of this technique is that all the vortices nucleated have the same charge q. Therefore, large vortex lattices can be created at high rotation frequencies.

- **Dragging a small repulsive potential through the BEC** [216, 217, 218, 219, 204, 220]. Moving a repulsive optical potential through the condensate above the critical velocity v_c leads to the generation of turbulent flow and hence vortices with random quantised charge. However, with certain techniques, such as the chopstick method [219], it is possible to create deterministically vortex pairs of opposite charges.

- **Direct phase imprinting** [221, 222, 203, 39, 208]. By creating a gradient in the chemical potential of the cloud for a fixed period of time, the phase can be evolved into the vortex solution. There are different methods to achieve this: The phase can be imprinted by overlaying a potential gradient on the cloud for a time shorter than the density response time of the atoms [203], or by illuminating the atoms with a Laguerre-Gaussian beam for which all photons carry angular momentum, which they transfer to the atoms [208], or by an off-resonant laser beam with circular motion around the BEC providing an AC-stark gradient which changes the phase [39].

- **Rapid cooling into the BEC state** [223, 224, 41, 225, 226, 227, 228]. Rapid cooling of atoms from the thermal phase to the BEC state leads to local fragmentation of the phase, and vortices can form during homogenisation. This technique does not involve a rotating system, and therefore the created vortex state is energetically unstable.

All of these techniques have been used to create vortices in experiments. However, for most of the techniques, the ability to create arbitrary potentials and rotate them continuously is needed.

Magnetostirring

The DDI offer a different way to rotate the cloud continuously at arbitrary Ω. To rotate the atomic gas or, in other words, to impart angular momentum, we need a system with broken rotational symmetry. This can be naturally realised in dipolar condensates in radially symmetric traps. Due to magnetostriction the cloud aspect ratio is no longer identical to the trap aspect ratio. The term magnetostriction was first coined for solid magnetic materials, such as iron rods, which change their length when a magnetic field is applied along the rod [229, 230]. This effect is due to the electrons aligning themselves along the magnetic field, slightly changing the size of the atoms. Therefore, each individual atom takes more space along the magnetic field direction, and the rod effectively elongates. A very similar effect can be seen in our gas. The dipoles of the atoms align with an external magnetic field. Due to the dipolar interactions the atoms attract each other head to tail and the atomic cloud elongates along the magnetic field direction to reduce its energy compared to the non-dipolar case. In an axisymmetric trap where $\omega_x = \omega_y$ the cloud is therefore no longer symmetric ($\mathrm{R}_x \neq \mathrm{R}_y$), when the magnetic field is tilted away from the symmetry axis by a tilt angle θ. By continuously rotating the tilted magnetic field, the cloud can be rotated.
To simplify further discussion, we will call this technique magnetostirring. This technique has several advantages:

- **Simple technical setup**: The rotation of magnetic fields has been used for neutral atoms since the early days of time-averaged orbital potential (TOP) traps [231]. Most of the ultracold gas experiments have magnetic field coils for all directions to compensate for magnetic stray fields. These coils, if the magnetic field generated is large enough, can be used to generate the rotating fields, so this technique is quickly implemented.
- **Tilted magnetic field**: Since the rotation is generated by the magnetic field, the magnetic field is tilted and static in the rotating frame, which allows for studying effects such as anisotropic vortex cores and vortex stripe lattices.

The aspect ratio R_x/R_y of the stationary BEC in an isotropic trap for different magnetic field tilt angles θ can be found from numerical eGPE calculations and is shown for our experimental parameters in Fig. 3.2. Tilting the magnetic field from the z-direction into the x-y symmetry plane results in an aspect ratio $\mathrm{AR} = 1 - 2.2$. As shown in the theoretical work of Bland et al. [232] there are three stability regimes rotating at different θ. For $\theta < \theta_1^*$ the aspect ratio of the cloud during adiabatically ramping up the rotation frequency $\Omega \longrightarrow \omega_\perp$ remains almost constant and no vortices are nucleated. For $\theta_1^* < \theta < \theta_2^*$ the aspect ratio increases significantly up to a critical rotation frequency $\Omega^*(\theta)$, where the AR reduces rapidly and the vortices are nucleated due to a dynamical instability as discussed before. For large tilt angles $\theta > \theta_2^*$, the cloud continuously elongates up to the simulated $\Omega = \omega_\perp$. Here, the elongation of the cloud and the tilted magnetic field along this elongation lead to a dominantly attractive force between the atoms due to the DDI. The cloud is thereby held together, and dynamical instabilities are suppressed. For $\theta \longrightarrow 90^\circ$, the rotating BEC even transitions to a trap-bound droplet for large rotation frequencies [232]. In the study, the critical tilt angles are given by $\theta_1^* \approx 20^\circ$ and $\theta_2^* \approx 50^\circ$, but they are strongly dependent on system parameters such as the trap aspect ratio $\omega_\perp/\omega_z$ and a_s. To generalise the results, further studies

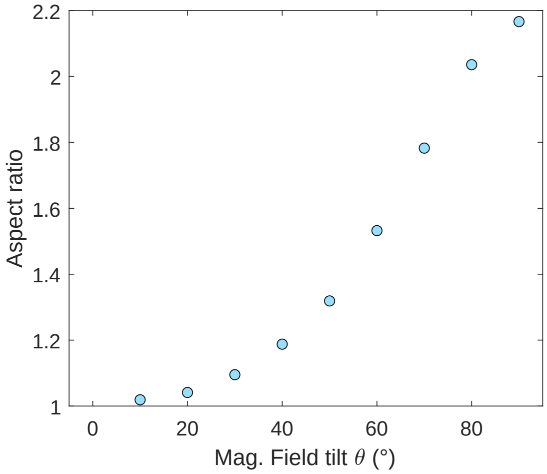

Figure 3.2: Aspect ratio R_x/R_y for different tilt angles θ. The aspect ratios are taken from eGPE simulations with the parameters $N = 15000$, $a_s = 110a0$, $[\omega_\perp, \omega_z] = 2\pi \times [50, 130]$ Hz. The data is taken from Fig. 3 from [232]

are necessary.

As described in section 2.2.5 the magnetic fields in our experiment are generated by the magnetic bias field coils B_z^{bias} and the two compensation cages for the x- (B_x^{comp}) and y-direction (B_y^{comp}). To create a rotating magnetic field of constant strength $|\mathbf{B}_{\text{tot}}|$ and constant tilt angle θ, the magnetic fields produced by the different pairs of coils are given by

$$\mathbf{B}_{\text{tot}} = B_x^{\text{comp}} + B_y^{\text{comp}} + B_z^{\text{bias}} \tag{3.11}$$

$$B_x^{\text{comp}} = |\mathbf{B}_{\text{tot}}| \sin(\theta) \cos(\Omega t + \phi_0) \tag{3.12}$$

$$B_y^{\text{comp}} = |\mathbf{B}_{\text{tot}}| \sin(\theta) \sin(\Omega t + \phi_0) \tag{3.13}$$

$$B_z^{\text{bias}} = |\mathbf{B}_{\text{tot}}| \cos(\theta) \tag{3.14}$$

with the rotation frequency Ω and the initial starting angle ϕ_0. In our experiment, we work with a tilt of $\theta = 35°$, which results in an aspect ratio of $AR \approx 1.2$ and lies inbetween θ_1^* and θ_2^* for our experimental parameters. The frequency of the current sent to the coils can be easily set between $\Omega = 0 - 50$ Hz allowing one to either adiabatically ramp the rotation frequency or quasi-instantaneously turn on the rotation frequency. The experimental results of the cloud AR during an adiabatically ramped rotation frequency are shown in the publication in Fig. 1 c.

3.1.3 Image the vortices

Vortices appear along the axis of rotation as hollow tubes in the density distribution. In our experiment both the imaging and the rotation are along the z-direction, so the vortices appear as holes. However, the in-situ size of the vortex core we calculated in Sec. 3.1.1, is on the same scale as our vertical imaging resolution.

The vortex core can be magnified in time-of-flight (TOF) [190, 194]. Due to the expansion of the BEC, the

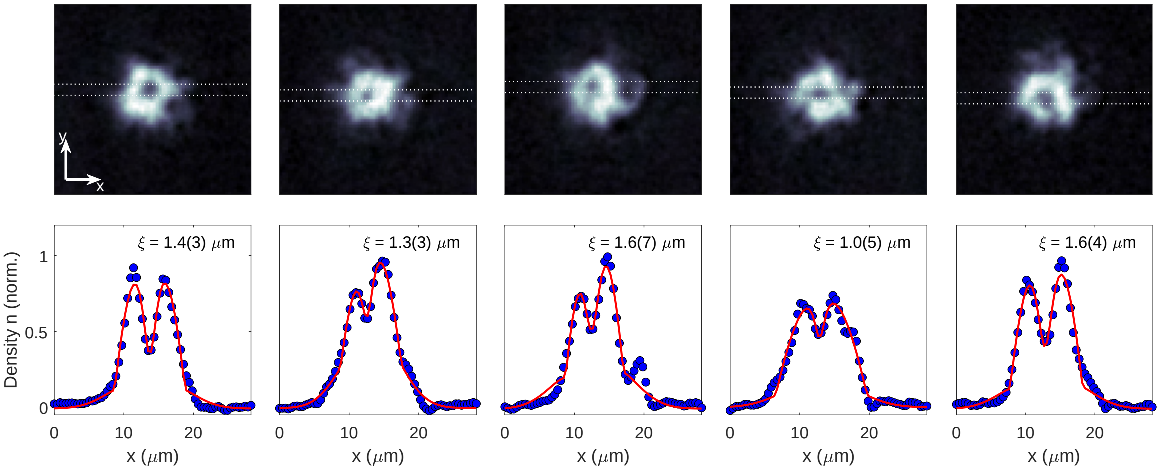

Figure 3.3: Example of vortex profiles. Density profiles after rotating the BEC for 600 ms at $\Omega = 0.75\omega_\perp$ and spiral the magnetic field to $\theta = 0$ for another 100 ms. To measure the size of the vortices the density along the y-axis is integrated between the white dotted lines and the resulting density profile is shown below the image. The density profile is fit by $n = n_{\mathrm{TF}} + n_{\mathrm{T}} + n_{\mathrm{V}}$. Hereby, pictures from the dataset were chosen, where a vortex is clearly visible near the centre of the cloud and other signatures of vortices are omitted for the fit. The experimental parameters are $a_s = 109a_0$, trap frequencies $[\omega_\perp, \omega_z] = 2\pi \times [50, 130]$ Hz, atom number $N = 10000$ and a TOF of $t_{\mathrm{TOF}} = 3$ ms.

density is reduced, leading to an increasing healing length $\xi \propto n^{-1/2}$. We can estimate the growth by assuming ballistic expansion of the cloud [27]

$$R_i(t_{\mathrm{TOF}}) = R_i(0)\left(1 + \omega_i^2 t_{\mathrm{TOF}}^2\right) \tag{3.15}$$

where ω_i are the trap frequencies in the corresponding directions and t_{TOF} is the expansion time. Since the density is given by Eq. (1.14) the healing length increases with $\xi \propto \sqrt{R_x(t)R_y(t)R_z(t)}$. In our case, we are working in an oblate trap where the rotation axis is along the flat direction. For our values, for an expansion of $t_{\mathrm{TOF}} = 3$ ms, we find that the radius of the cloud increases by $R_{\mathrm{TOF}}/R \approx (1.4, 1.4, 2.8)$ and the healing length approximately doubles from $\xi_{\mathrm{TOF}}/\xi \approx 2.3$ to about $\xi_{\mathrm{TOF}} \approx 1.1\,\mu$m, bringing the vortices into the resolution range of our imaging system.

Longer expansion times lead to a greater magnification of the vortices, but we are limited by the noise of our imaging system. With a longer TOF the density of the cloud decreases rapidly and therefore the signal-to-noise ratio for the imaging decreases as well. We find the ideal regime at $t_{\mathrm{TOF}} = 3$ ms, where the vortices are resolvable and the cloud is still dense.

From the resulting images, we count and analyse the vortices. To do this, we use an algorithm similar to that used in [233]. We take each image n_{img} and create a reference image n_{ref} by applying a 2D Gaussian filter with $\sigma = 5$ pixel to the original image. The result is a smoothed density profile, where all signatures of vortices are removed. Both images are normalised and subtracted from each other to create a residual image $n_{\mathrm{res}} = n_{\mathrm{img}}^{\mathrm{norm}} - n_{\mathrm{ref}}^{\mathrm{norm}}$. The resulting residual ideally shows a homogeneous density distribution with the vortices as density minima. To avoid overcounting vortices at the edges of the cloud, where the

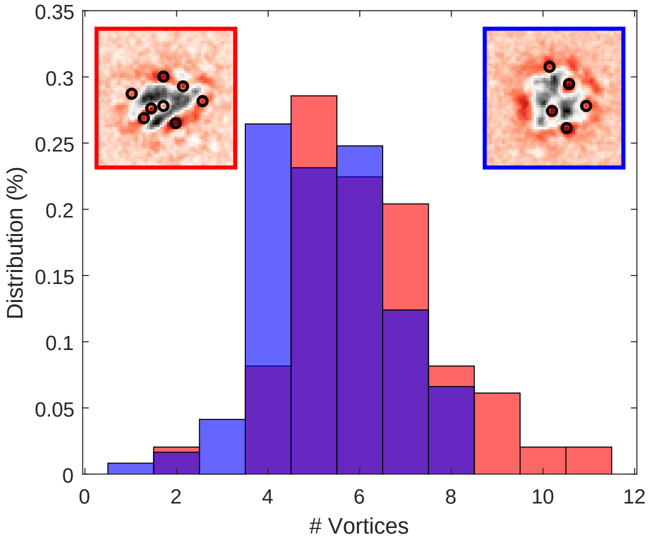

Figure 3.4: Vortex number distribution for a magnetic field angle of $\theta = 35^\circ$ and $\theta = 0^\circ$. Vortex number distribution after rotating the cloud for 500 ms at $\theta = 35^\circ$ over(red / 115 images) and after rotating the cloud for 600 ms at $\theta = 35^\circ$ and then rotating the magnetic field up to $\theta = 0^\circ$ for another 100 ms (blue / 121 images). A residual image $n_{\text{res}} = n^{\text{norm}}_{\text{img}} - n^{\text{norm}}_{\text{ref}}$ is given for the tilted and non-tilted magnetic field respectively, with the vortex positions marked as '**o**'. The experimental parameters are $a_s = 109a_0$, trap frequencies $[\omega_\perp, \omega_z] = 2\pi \times [50, 130]$ Hz, $N = 10000$ and a TOF of $t_{\text{TOF}} = 3$ ms.

signal-to-noise ratio is worse, we look for vortices only in the region where $n^{\text{norm}}_{\text{ref}} > 0.1$. We identify vortices by finding the local minima and filtering out the minima that have low contrast and are too close together in space. This results in an algorithm that robustly finds the clear signs of vortices in the centre of the cloud, but may underestimate the actual number of vortices, because vortices in the lower density regime and with low contrast are not counted. Therefore, when vortices are detected, we know with high confidence that the vortices exist and the lower limit of the vortex number.

3.1.4 Dipolar stripe vortex lattice

The maximum angular momentum carried by a vortex is $L = qN\hbar$. This means for $q = 1$ that if we impart more angular momentum to the cloud, more vortices will be created and the maximum number can be estimated by $N_v \simeq 2\pi R_\perp^2 \Omega / \Gamma$ where Γ is the quantum of circulation defined in Eq. (3.4) [194].

We can see in our experiment and in eGPE simulations that for short rotation times the vortices are nucleated on the outside of the cloud and, as the rotation continues, slowly move towards the centre of the cloud. In non-dipolar gases, once the vortices are formed, they assemble into a regular triangular [40, 197, 198]. This lattice structure was predicted by Abrikosov [234] and can be found not only in ultracold gases, but also as flux vortex lattice in superconductors [235, 236]. It is also expected in superfluid helium [237], but has not yet been directly observed.

The situation changes for gases with dipolar atoms. Theoretical studies of dipolar gases have mostly been done for quasi-2D systems and we have to distinguish between two different scenarios: First, the dipole moments of the atoms are aligned along the rotation axis, and second, the dipole moments are tilted away from the rotation axis.

For the first scenario, the interactions along the trap symmetry axes are isotropic, but due to the long-range nature of the interactions, the ground-state lattice structure acquires different geometries: for small ε the lattice is triangular and increasing ε then leads from a square to a stripe to a hexagonal lattice structure [238, 239].

In the second scenario, the tilt of the dipole moment breaks the rotational symmetry of the system. In fact, a strip pattern is predicted for interaction strengths of $\varepsilon_{\mathrm{dd}} \geq 0.8$ and tilt angles $\theta > 51°$ [240]. We can understand this by looking at the dipolar potential $V_{\mathrm{dd}}^{\mathrm{mf}}$ in (1.12). The dipolar potential can be rewritten as [99, 241, 242]

$$V_{\mathrm{dd}}^{\mathrm{mf}} = -g\varepsilon_{\mathrm{dd}} \left[3\partial_{\mathbf{nn}}\phi\left(\mathbf{r}\right) + n\left(\mathbf{r}\right)\right] \tag{3.16}$$

with $\phi(\mathbf{r}) = \frac{1}{4\pi}\int d\mathbf{r}' \frac{n(\mathbf{r}')}{|\mathbf{r}-\mathbf{r}'|}$ and $\partial_{\mathbf{nn}} = \partial_{\mathbf{n}}(\partial_{\mathbf{n}})$, where $\partial_{\mathbf{n}} = \hat{n}_x\partial_x + \hat{n}_y\partial_y + \hat{n}_z\partial_z$ and $\mathbf{n} = \hat{n}_x + \hat{n}_y + \hat{n}_z$ is the derivative along the polarisation direction of the dipoles. The "potential" $\phi(\mathbf{r})$ is reminiscent of an electrostatic potential with charge distribution $n(\mathbf{r})$. The absence of density in the vortex cores in a "charged" environment can be interpreted as anti-dipoles and the resulting potential (3.16) mimics the dipolar potential itself $V_{\mathrm{dd}}^{\mathrm{mf,vort}} \approx 1 - 3\cos^2(\theta)$, at least for the 2D limit [209]. Therefore, the total energy is reduced when the vortices are aligned "head-to-tail", forming a stripe pattern.

In our experiment, we were able to observe a vortex stripe pattern in a rotated 3D dBEC with trap frequencies $(\omega_r, \omega_z) \approx (50, 130)$ Hz and an interaction parameter of $\varepsilon_{\mathrm{dd}} \approx 1.2$, an angle of $\theta = 35°$ and a rotation frequency of $\Omega = 0.75\omega_\perp$.

As we can see in Fig. 3.4 in our experiment we are able to measure a wide spread in the vortex count for every experimental run for the magnetic field tilted at $\theta = 35°$ for the whole rotation sequence, but also when spiraling up the magnetic field in the last 100ms before imaging the cloud. The average vortex number we measure for the tilted (non-tilted) magnetic field is $N_v = 6.2(2)$ ($N_v = 5.3(1)$). For the rotation frequency used and the estimated radius from Sec. 3.1.1 we expect a maximum vortex number of $N_v^{\mathrm{estim}} \approx 13$ instead. There are several reasons for this large discrepancy:

- Due to the imaging resolution, noise and the algorithmic vortex counting, we underestimate the vortex number in our images.
- The vortex nucleation phase is not completed [243]. Many vortices are still on the edge of the cloud, where they are not identified and therefore not counted by the algorithm. An indication of this is the wide spread of the vortex number distribution, which shows images with very low number of vortices showing the very early stage of nucleation and few images with a vortex number close to N_v^{estim} at the late stage of nucleation.
- Dissipative effects can reduce the vortex number [233]. Our cloud has a finite temperature and therefore, following Landau's two-fluid model, we can separate the cloud into a superfluid and a normal part [244]. Although superfluidity is defined by the absence of dissipation, the appearance of vortices introduces the possibility of dissipation. Vortices can interact with the normal fluid and

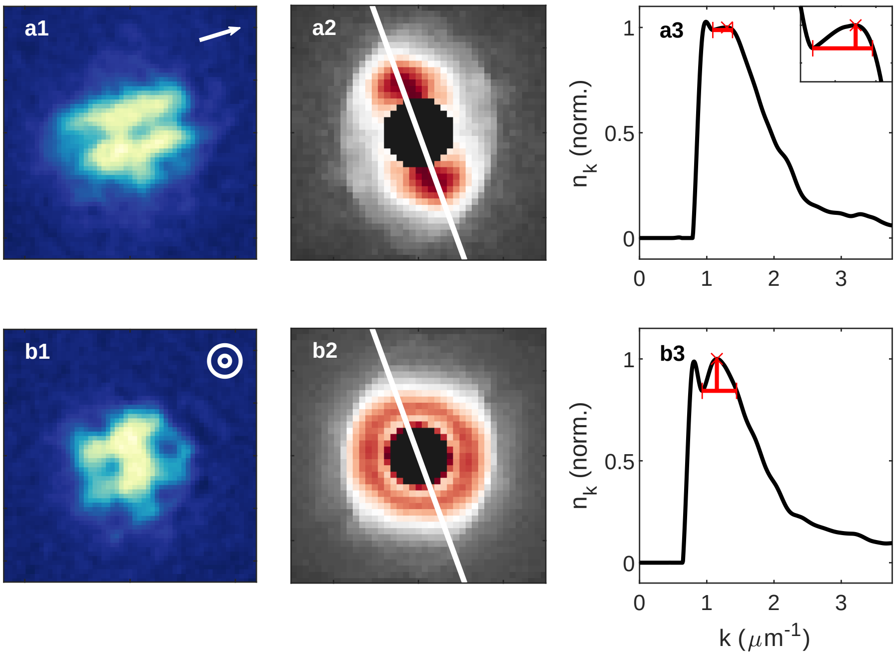

Figure 3.5: Vortex and vortex stripe spacing from averaged Fourier Transform of the residual images. a) Rotating the magnetic field for 500ms at a tilt angle of $\theta = 35°$. b) Rotating the magnetic field for 600ms at a tilt angle of $\theta = 35°$ and then spiralling the magnetic field up to $\theta = 0°$ for a further 100ms. a1/b1) A single example image taken after a TOF of $t_{\mathrm{TOF}} = 3$ms. a2/b2) Fast Fourier transform (FFT) of the residual images, averaged over 49 shots/121 shots. a3/b3) The FFT profile along the white line in a2/b2) is shown. The average wavenumber of the stripe pattern $k^{\mathrm{stripe}}_{\mathrm{FFT}}$ (a3) and the average vortex distance $k^{\mathrm{vortex}}_{\mathrm{FFT}}$ (b3) can be extracted by finding the peak position between $1\mu\mathrm{m}^{-1} > k > 2\mu\mathrm{m}^{-1}$. The upper and lower bounds of the estimate are given by the minimum at $k \approx 0.8\mu\mathrm{m}^{-1}$ and the intersection of the horizontal line with the profile for $k > k_{\mathrm{FFT}}$. The measured wavenumbers are $k^{\mathrm{stripe}}_{\mathrm{FFT}} = 1.30^{+0.08}_{-0.21}\mu\mathrm{m}^{-1}$ and $k^{\mathrm{vortex}}_{\mathrm{FFT}} = 1.15^{+0.29}_{-0.22}\mu\mathrm{m}^{-1}$. The experimental parameters are $a_s = 109a_0$, trap frequencies $(\omega_\perp, \omega_z) = 2\pi \times [50, 130]\,\mathrm{Hz}$ and $N = 10000$.

thus dissipate energy. Furthermore, vortices can dissipate energy through sound modes [233, 199].

Due to the low resolution and the turbulent positions of the vortices, the stripe pattern is not obvious from single images, as can be seen in Fig. 3.5 a1. Instead, the stripe structure is indicated by the increased density along the magnetic field. We analyse the structure by taking the absolute value of the 2D Fourier transform (FT) of the individual residual images. By taking a large number of repetitions (105 images), taking the 2D FT of the residuals and averaging them (see Fig. 3.5 a2) we find a repeatable stripe structure. The average 2D FT shows two peaks perpendicular to the x-y projection of the magnetic field direction. From the distance between the peaks we can calculate the distance between the stripes(Fig. 3.5 a3) $r_{\mathrm{str}} = 2\pi/k_{\mathrm{FFT}} = 4.83^{+0.93}_{-0.29}\,\mu$m. So we have a clear indication that the vortices are aligning in stripes along the magnetic field.

As a control, we created the vortices and then rotated the magnetic field up to $\theta = 0°$ over a time $\tau_{\mathrm{spiral}} = 100\,\mathrm{ms}$ as shown in Fig. 3.5 b1. We also perform the 2D FFT analysis and the resulting mean profile shows an isotropic ring from which we can estimate the average distance between the vortices as $r_{\text{vort}} = 2\pi/k_{\text{FFT}} = 5.46^{+1.28}_{-1.11}\,\mu$m. This indicates that the vortices are no longer aligned in stripes.

P1 Observation of vortices and vortex stripes in a dipolar condensate

The following manuscript has appeared in

Nature Physics 18, 18, 1453–1458 (2022)[1],
discussed in News & Views article: **When ultracold magnets swirl** from Zoran Hadzibabic
submitted 15 June 2022; published 31 October 2022.
DOI: 10.1038/s41567-022-01793-8

Lauritz Klaus[1,2], Thomas Bland[1,2], Elena Poli[2], Claudia Politi[1,2], Giacomo Lamporesi[3], Eva Casotti[1,2], Russell N. Bisset[2], Manfred J. Mark[1,2] and Francesca Ferlaino[1,2]

[1] *Institut für Experimentalphysik, Leopold-Franzens-Universität, 6020 Innsbruck, Austria*
[2] *Institut für Quantenoptik und Quanteninformation, Österreichische Akademie der Wissenschaften, 6020 Innsbruck, Austria*
[3] *INO-CNR BEC Center and Dipartimento di Fisica, Università di Trento, Povo, Italy*

For this publication, I (L.K.) contributed equally together with T.B. . I contributed to the work on the experiment together with C.P. and E.C., analysed the dysprosium data together with C.P., E.C. and M.J.M, and contributed to the interpretation of the results, as well as in writing the manuscript together with all other authors.

---

[1] Here the preprint version is attached

Observation of vortices and vortex stripes in a dipolar Bose-Einstein condensate

Lauritz Klaus,[1, 2, *] Thomas Bland,[1, 2, *] Elena Poli,[2] Claudia Politi,[1, 2] Giacomo Lamporesi,[3]
Eva Casotti,[1, 2] Russell N. Bisset,[2] Manfred J. Mark,[1, 2] and Francesca Ferlaino[1, 2, †]
[1] *Institut für Quantenoptik und Quanteninformation,*
Österreichische Akademie der Wissenschaften, Innsbruck, Austria
[2] *Institut für Experimentalphysik, Universität Innsbruck, Austria*
[3] *INO-CNR BEC Center and Dipartimento di Fisica, Università di Trento, 38123, Trento, Italy*

Quantized vortices are the prototypical feature of superfluidity. Pervasive in all natural systems, vortices are yet to be observed in dipolar quantum gases. Here, we exploit the anisotropic nature of the dipole-dipole interaction of a dysprosium Bose-Einstein condensate to induce angular symmetry breaking in an otherwise cylindrically symmetric pancake-shaped trap. Tilting the magnetic field towards the radial plane deforms the cloud into an ellipsoid through magnetostriction, which is then set into rotation. At stirring frequencies approaching the radial trap frequency, we observe the generation of dynamically unstable surface excitations, which cause angular momentum to be pumped into the system through vortices. Under continuous rotation, the vortices arrange into a stripe configuration along the field–in close corroboration with simulations–realizing a long sought-after prediction for dipolar vortices.

Since the first experiments on gaseous Bose-Einstein condensates (BECs), the observation of quantized vortices has been considered the most fundamental and defining signature of the superfluid nature of such systems. Their very existence sets a unifying concept encompassing a variety of quantum fluids from liquid helium[1] to the core of neutron stars[2], and from superconductors[3] to quantum fluids of light[4]. Their classical counterparts have as well fascinated scientists from different epochs and fields as vortices are found in many scales of physical systems, from tornadoes in the atmosphere to ferrohydrodynamics.

In the quantum realm, a quantized vortex may emerge as a unique response of a superfluid to rotation. It can be understood as a type of topologically protected singularity with a 2π phase winding that preserves the single-valuedness of the superfluid wavefunction and the irrotational nature of its velocity field. In contact-interacting BECs, vortical singularities have been observed experimentally in the form of single vortices[5,6], vortex-antivortex pairs[7], solitonic vortices[8,9], vortex rings[10] and vortex lattices[6,11,12] using a number of different techniques. Moreover, vortices play a fundamental role in the description of the Berezinskii-Kosterlitz-Thouless transition in two-dimensional systems[13], as well as in the evolution of quantum turbulence[14–16], and have been observed in interacting Fermi gases along the BEC-to-BCS crossover[8,17].

Recently, a new class of ultracold quantum gases are being created in various laboratories around the world, using strongly magnetic lanthanide atoms[18,19]. Such a system, providing a quantum analogue of classical ferrofluids, enables access to the physics of dipolar BECs, in which atoms feature a strong long-range anisotropic dipole-dipole interaction (DDI)[20,21] on top of the traditional contact-type isotropic one. This intriguing platform provided the key to observe, e.g., extended Bose-Hubbard dynamics[22], roton excitations[23–25], the quantum version of the Rosensweig instability[26], supersolid states of matter[27–30], and is foreseen to host novel phenomena for quantum simulation and metrology[20,21].

The dipolar interaction is predicted to also intimately change the properties of vortices in quantum gases[31]. For instance, theoretical works predict single vortices to exhibit an elliptic-shaped core for a quasi-two-dimensional setting with in-plane dipole orientation[32–35], or the presence of density oscillations around the vortex core induced by the roton minimum in the dispersion relation[32–36]. For vortex pairs, the anisotropic DDI is expected to alter the lifetime and dynamics[35,37], and can even suppress vortex-antivortex annihilation[35]. These interaction properties are predicted to give rise to a vortex lattice structure that can follow a triangular pattern[32,36], as is typical for non-dipolar BECs[11], or a square lattice for attractive or zero contact interactions[38,39] when the DDI is isotropic (dipoles aligned with the rotation axis). A very striking consequence of the dipoles tilted into the plane is the formation of vortex stripes[32,40,41]. Moreover, vortices could provide an unambiguous smoking gun of superfluidity in supersolid states[42–46]. However, despite these intriguing predictions, vortices in dipolar quantum gases have yet to be observed.

This paper presents the experimental realization of quantized vortices in a dipolar BEC of highly magnetic dysprosium atoms. Following a method proposed in Ref. [41], we show that the many-body phenomenon of magnetostriction[47], genuinely arising from the anisotropic DDI among atoms, provides a natural route to rotate the systems and nucleate vortices in a dipolar BEC. We carry out studies on the dynamics of the vortex formation, which agree very well with our theoretical predictions. Finally, we observe one of the earliest predictions for dipolar vortices: the formation of vortex stripes in the system.

In non-dipolar gases, quantized vortices have been produced using several conceptually different techniques. For instance by rotating non-symmetric optical[6,11] or magnetic[48] potentials, by rapidly shaking the gas[15], by traversing it with obstacles with large enough velocity[7,49], by rapidly cooling the gas across the BEC phase transition[50,51], or directly imprinting the vortex phase pattern[52]. Dipolar quantum gases, while able to form vortices with these same standard procedures[31], also offer unique opportunities that have no counterpart in contact-interacting gases. Crucially, the DDI gives rise to the phenomenon of magnetostriction in position space[47]. When dipolar BECs are polarized by an external magnetic field–defining the dipole orientation–the DDI causes an elongation of the cloud along the polarization direction. This is a direct consequence of the system tendency to favor head-to-tail dipole configurations, which effectively reduces the interaction energy[21].

Such a magnetostrictive effect provides a simple method to induce an elliptic effective potential and drive rotation with a single control parameter. This modification of the effective potential is shown in Fig. 1a for a BEC in an oblate trap with cylindrical symmetry about the z-axis. While a non-dipolar BEC takes the same shape as the confining trap (a1), introducing dipolar interactions with polarization axis along z stretches the cloud along this axis, yet maintains cylindrical symmetry (a2). Tilting the $\vec{\mathbf{B}}$-field leads to a breaking of the cylindrical symmetry, resulting in an ellipsoidal deformation of the cloud shape, as seen from the density projection onto the x-y plane (a3). Finally, under continuous rotation of the magnetic-field, which we coin "magnetostirring", the condensate is predicted to rotate (a4). This unique approach to stir a dipolar condensate can eventually lead to the nucleation of vortices[41,53], realizing genuinely interaction-driven vorticity through many-body phenomena.

We explore this protocol using a dipolar BEC of ^{162}Dy atoms. We create the BEC similarly to our previous work[45] with the distinction that here the magnetic field unit vector, $\hat{\mathbf{B}}$, is kept tilted at an angle of $\theta = 35°$ with respect to the z-axis both during evaporative cooling and magnetostirring (see Fig. 1a3 and Methods). After preparation, the sample contains about 2×10^4 condensed atoms confined within a cylindrically symmetric optical dipole trap (ODT) with typical radial and axial trap frequencies $(\omega_\perp, \omega_z) = 2\pi\times[50.8(2), 140(1)]$ Hz. Here, prior to stirring, the magnetostriction is expected from simulations to increase the cloud aspect ratio in the horizontal plane from 1 up to 1.03, whereas the trap anisotropy is negligible. We use a vertical (z) absorption imaging to probe the radial (x,y) atomic distribution after a short time-of-flight (TOF) expansion of 3 ms. The atom number is instead measured using horizontal absorption imaging with a TOF of 26 ms.

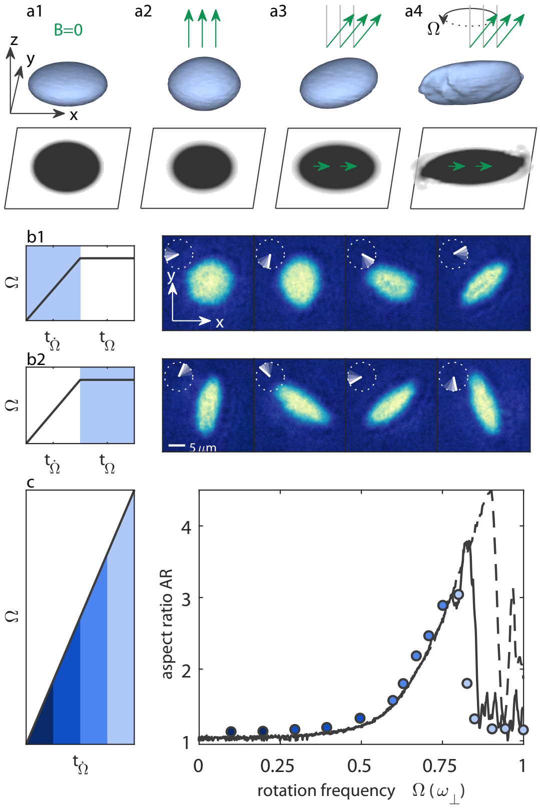

FIG. 1. **Magnetostirring of a Dy dipolar BEC and evolution of the cloud aspect ratio.** **a**, Illustration of a non-dipolar (**a1**) and dipolar BEC with B ≠ 0 (**a2-a4**) in a cylindrically symmetric, oblate trap. The magnetic-field angle with respect to the z axis varies from $\theta = 0°$ (**a2**) to $\theta = 35°$ (**a3**) and rotating at $\theta = 35°$ around z (**a4**). **b**, Representative axial absorption images showing the dipolar BEC while spinning up the magnetic field for $t_{\dot\Omega} = [140, 430, 627, 692]$ ms (**b1**) and subsequent constant rotation at $\Omega = 2\pi\times 36$ Hz for $t_\Omega = [0, 6, 11, 17]$ ms (**b2**). **c**, Cloud aspect ratio AR for different final rotation frequencies. Ω is linearly increased to its final value at a speed of $\dot\Omega = 2\pi\times 50$ Hz/s. To mitigate influences of trap anisotropies on the AR, a full period at the final rotation frequency is probed. The error bars are smaller than the symbol size. The solid (dashed) black line shows the corresponding eGPE simulations with a 2 s (1 s) ramp and $a_s = 110\,a_0$, $(\omega_\perp, \omega_z) = 2\pi\times[50, 130]$ Hz, and $N = 15000$.

Similarly to a rotation of a bucket containing superfluid helium or of a smoothly deformed ODT for non-dipolar BECs, magnetostirring is predicted to transfer angular momentum into a dipolar BEC[41,53]. In response to such an imposed rotation, the shape of an irrotational cloud is expected to elongate with an amplitude that increases with the rotation frequency Ω. This phenomenon is clearly visible in our experiments, as shown in Fig. 1b. Here, we first revolve the tilted $\hat{\mathbf{B}}$ around the z-axis with a linearly increasing rotation frequency ($\dot\Omega = 2\pi\times 50$ Hz/s) and observe that the dipolar BEC starts to rotate at the same angular speed as the field

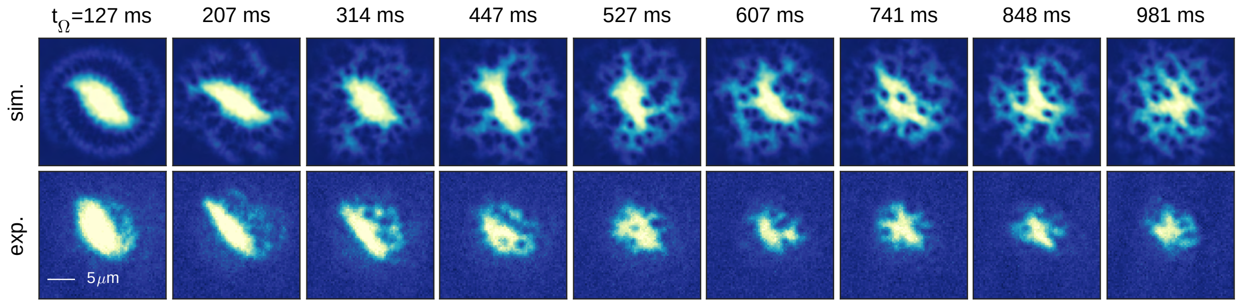

FIG. 2. **Observation of vortices in a dipolar BEC.** Each column shows the simulated (upper) and experimental (lower) images for various rotation times t_Ω. For the experiment, the atoms are imaged along the z direction. In each experimental run, we rotate the magnetic field counter-clockwise at $\Omega = 0.74\,\omega_\perp$ for different rotation times t_Ω. The magnetic field value is kept to $|\vec{\mathbf{B}}| = 5.333(5)\,\mathrm{G}$. The initial condensed atom number is $N = 15000$. The decreasing size of the cloud suggests a decrease in atom number. However, for states with vortices or spiral shapes, appearing at large t_Ω, our bimodal fit to extract the atom number breaks down. For the corresponding simulations, the parameters are $a_s = 112\,\mathrm{a}_0$, trap frequencies $(\omega_\perp, \omega_z) = 2\pi \times [50, 150]\,\mathrm{Hz}$, $N = 8000$, and $\Omega = 0.75\,\omega_\perp$.

and deforms with increasing elongation (b1). We then stop the adiabatic ramp at a given value of Ω and probe the system under continuous rotation. We now find that the cloud continues rotating in the radial plane with an almost constant shape (b2). Note that $|\vec{\mathbf{B}}|$ is held constant at $5.333(5)\,\mathrm{G}$, where we estimate a contact scattering length of about $a_s = 111\,a_0$ (Methods).

We further explore the response of our dipolar BEC to magnetostirring by repeating the measurements in Fig. 1b1, but stopping the ramp at different final values of Ω. The maximum value used for Ω approaches $\omega_\perp$, corresponding to a ramp duration of 1 s. We quantify the cloud elongation in terms of the aspect ratio AR$= \sigma_{\max}/\sigma_{\min}$, where the cloud widths $\sigma_{\max}$ and $\sigma_{\min}$ are extracted by fitting a rotated two-dimensional Gaussian function to the density profiles. Figure 1c summarizes our results. We observe that initially the AR slightly deviates from one due to magnetostriction. It then slowly grows with increasing Ω, until a rapid increase at around $0.6\,\omega_\perp$ occurs, as this allows the angular momentum to increase, which decreases the energy in the rotating frame[54]. Suddenly, at $\Omega_c \approx 0.74\,\omega_\perp$, the AR abruptly collapses back to AR ≈ 1, showing how the superfluid irrotational nature competes with the imposed rotation.

To substantiate our observation, we perform numerical simulations of the zero-temperature extended Gross-Pitaevskii equation (eGPE)[55–58] (see Methods). Quantum and thermal fluctuations are added to the initial states, which are important to seed the dynamic instabilities once they emerge at large enough Ω; see later discussion. The lines in Fig. 1c show our results. The dashed line is obtained through the same procedure as the experiment, whereas for the solid line we halve the ramp rate, spending more time at each frequency. Both ramp procedures show quantitatively the same behaviour up to $\Omega = 0.8\,\omega_\perp$, and are in excellent agreement with the experimental results. The stability of the 1s ramp exceeds the experimentally observed critical frequency. We partly attribute this discrepancy to asymmetries of the rotation in the experiment that are not present in the simulations, which may lead to an effective speedup of the dynamical instabilities. However, in all cases, the AR rapidly decreases to about one.

The growing AR and subsequent collapse to one is a signature of the dynamical instability of surface modes, known for being an important mechanism for seeding vortices and allowing them to penetrate into the high-density regions of rotated BECs[54,59,60], as also predicted for our dipolar system[41]. To search for quantum vortices in our system, we perform a new investigation where we directly set Ω close to Ω_c. We then hold the magnetic-field rotation fixed at this constant frequency for a time t_Ω. As shown in Fig. 2 (lower row), the cloud rapidly elongates, and the density starts to exhibit a spiral pattern, emanating from the tips of the ellipsoid. As early as $t_\Omega = 314\,\mathrm{ms}$ clear holes are observed in the density profile, forming in the density halo around the center, the first clear indication of vortices in a dipolar gas. These vortices, initially nucleated at the edge of the sample, persist as we continue to stir, and eventually migrate towards the central (high-density) region. Owing to their topological protection, vortices are still visible in the experiment after one second of magnetostirring, although our atom number decreases throughout this procedure. Our observations bear a remarkable resemblance to the simulations; Fig. 2 (upper row) showing the in situ column densities. Taking a fixed atom number of $N = 8000$, but otherwise repeating the experimental sequence, we observe many similar features. First, the spiral density pattern appears before the instability, forming two arms that are filled with vortices close to the central density. Next, turbulent dynamics ensue as the density surface goes unstable and vortices emerge in the central high density region. This turbulence, however, inhibits the creation of a vortex lattice on these timescales.

The observed evolution of the system under constant rotation shows some concurrence between the appearance of vortices in the absorption images and the formation of a round density pattern in the radial plane with AR ≈ 1 (Fig. 2). To study this dynamical evolution in more detail, we adopt an analysis protocol for both the experiment and theory that allows us to quantitatively track the evolution of the average number of vortices, $\mathcal{N}_v$ (Methods). The result is shown in Fig. 3a. In brief, for each single image (a1) we create a blurred reference image by applying a 2D Gaussian filter[61,62]. We then calculate the difference between each single image (a1) and the corresponding reference (a2) to obtain the residual image (a3), from which we count $\mathcal{N}_v$ by finding local minima below a certain threshold.

For the experimental density profiles, which are affected by both the limited resolution of the imaging system and the weak contrast in the low-density zones (halo) where the vortices initially nest, we expect $\mathcal{N}_v$ to be underestimated relative to the number expected by theory. However, in order to carry out a quantitative comparison with the simulations, we apply a blurring filter and add noise to the latter that mimics the actual resolution in the experiment (Methods).

Figure 3b shows both the evolution of $\mathcal{N}_v$ and cloud AR as a function of rotation time, t_Ω. Solid lines are the results from the eGPE simulations without any adjustable parameters. For $t_\Omega < 200\,\mathrm{ms}$, $\mathcal{N}_v$ is below 1, where vortices, if present, are at the edge of the cloud. For longer times, $\mathcal{N}_v$ increases and saturates to an average value of about three and a maximum of six vortices (see Fig. 3a for an example of five vortices). The observed saturation might be due to the decreased visibility and to the atom-loss-induced shrinking of the BEC size, which is not accounted for in the theory. We also compare the course of the average vortex number with the AR of the cloud. After initial large oscillations, due to the sudden jump in rotation frequency, the AR declines towards ≈ 1[60]. This happens as the vortex number simultaneously increases.

One fascinating prediction with dipolar vortices under the influence of a rotating magnetic field relates to the structure of the resulting vortex lattice. Due to magnetostriction and the anisotropic vortex cores, the resulting vortex configuration is also anisotropic, producing a stripe phase in the strongly dipolar regime[31,32], instead of the usual triangular lattice in non-dipolar BECs[6]. The ground state stripe lattice solution for our parameters is shown in Fig. 4a, with a cloud AR $= 1.08$. In the vortex stripe phase, vertical planes of high density regions, parallel to the magnetic field, alternate with low density ones, that host rows of vertical vortex filaments. Such a configuration promotes head-to-tail dipolar attraction

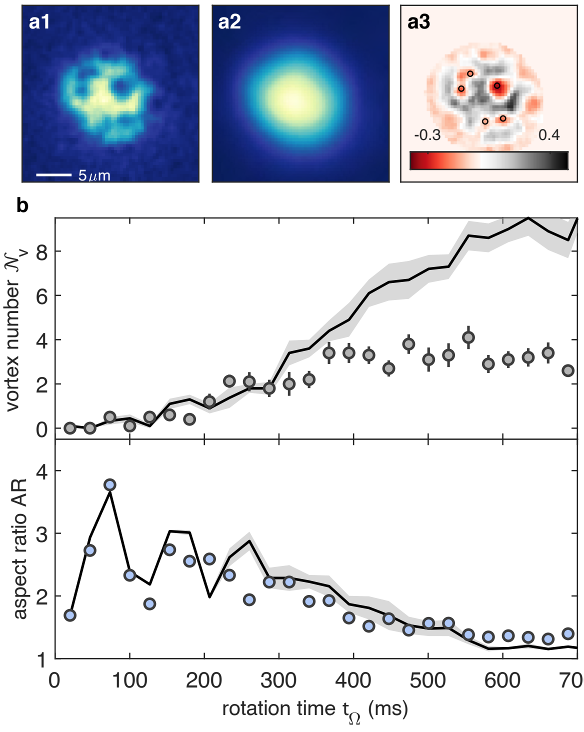

FIG. 3. **Time evolution of the average vortex number, $\mathcal{N}_v$, and cloud aspect ratio AR. a1**, Sample image after rotating for $t_\Omega = 474\,\mathrm{ms}$. **a2**, Blurred reference image ($\sigma = 2.1\,\mu\mathrm{m}$). **a3**, Residuals with markers (black circles) indicating the identified vortices. **b**, The detected vortex number $\mathcal{N}_v$ (top panel) and the AR of the cloud (bottom panel) after the rotation time t_Ω. Data points and error bars show the mean and standard error from about 10 experimental runs. Solid lines indicate the averaged results from 10 corresponding simulations with different initial noise for parameters $a_s = 110\,a_0$, $(\omega_\perp, \omega_z) = 2\pi \times [50, 130]\,\mathrm{Hz}$, $N = 10000$ and $\Omega = 0.75\,\omega_\perp$, the shaded area gives its standard error.

within the high density ridges, and this acts to lower the energy. It should be noted that these states are distinct from the oscillating vortex sheets states, which appear after squeezing a triangular vortex lattice[63].

To explore this prediction, we perform two new surveys. First, we slightly reduce the magnetic field value, reducing the scattering length to $a_s \approx 109\,a_0$ and hence making the system relatively more dipolar, while still avoiding the droplet regime. We magnetostir the BEC at a constant rotation frequency $\Omega = 0.75\,\omega_\perp$ for 500 ms, but during TOF we stop the magnetic-field rotation and keep it in place at $\theta = 35°$. The stripe structure is revealed in Fig. 4b1 for a single experimental run, and is clearly visible in the residual image, Fig. 4b2, where the vortices align along three stripes. The spatial structure of the residual image can be assessed through the absolute value of two-dimensional Fourier transform (FT). After taking the FT of each residual image, we then average the result, see Fig. 4b3, finding a clear peak at the k of the

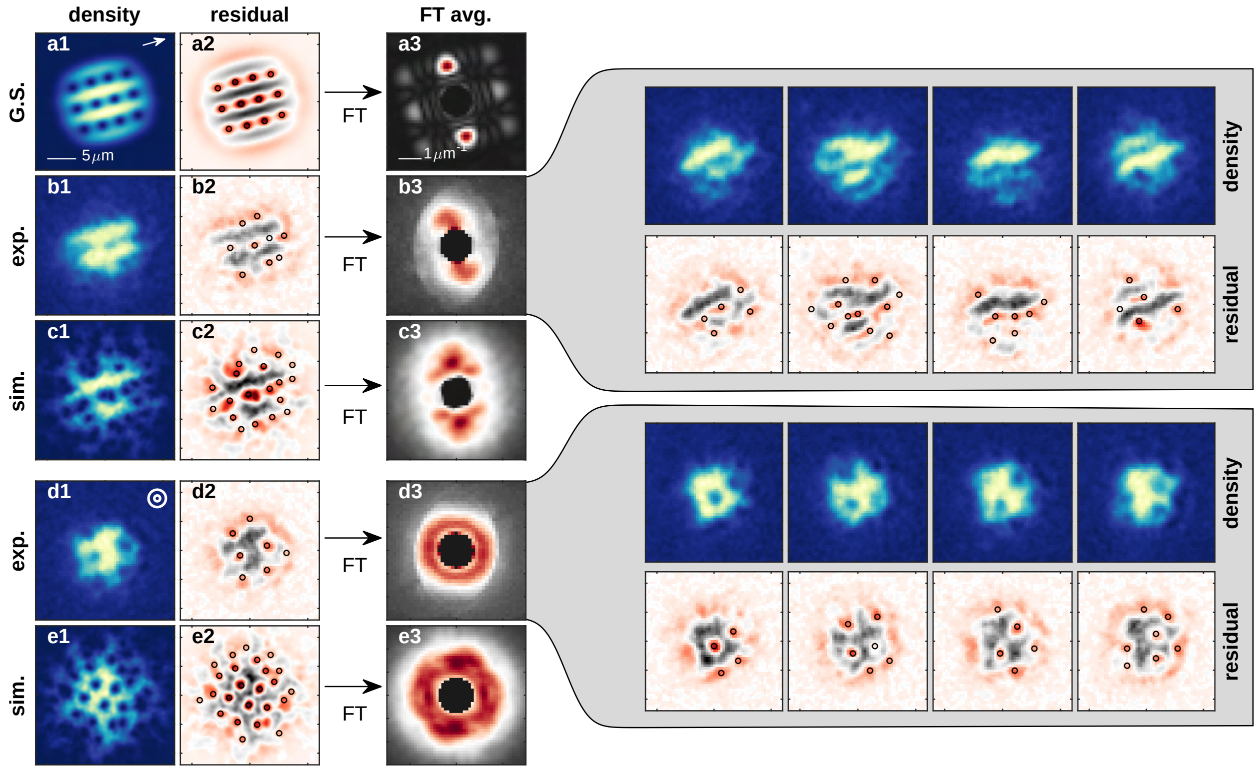

FIG. 4. **Stripe nature of dipolar vortices.** **a1**, Ground state stripe lattice solution for our experimental parameters $a_s = 109\,a_0$, trap frequencies $(\omega_\perp, \omega_z) = 2\pi \times [50, 130]$ Hz, N=10000 and $\Omega = 0.75\,\omega_\perp$. **a2**, Corresponding residual image, found by subtracting the ground state from the blurred image, with circles showing the detected vortices. **a3**, Fourier transform of the residual image. **b1**, Single experimental image after 500 ms of continuous rotation at $\Omega = 0.75\,\omega_\perp$. **b2**, The corresponding residual image. **b3**, Fourier transform of the residual images, averaged over 49 runs, with example shots shown to the right. **c1,** Simulation result for the dynamic experimental procedure in **b**. **c2-c3**, Residuals and FT analysis (115 temporal images) as in **b2-b3**. **d1-d3**, Same as **b1-b3** for 121 runs, but we rotate for an additional 100 ms and then spiral the magnetic field to $\theta = 0°$ over a further 100 ms before imaging. **e1-e3**, Simulation result for procedure in **d**. All simulation images are rotated to have the same magnetic field direction as the experiment.

inter-stripe spacing. This shows that the stripe spatial structure survives the averaging, implying that the majority of images show stripes with the same spacing, and they also have the same orientation as set by the magnetic field, as evidenced by the example images shown in the right of Fig. 4. Note that these observations do not rely on our ability to resolve individual vortices, as the stripes are an ensemble effect of many aligned vortices. In fact, by comparing with the numerical simulations of the dynamical procedure (Fig. 4c1-c3), we expect there are more vortices than detected here that fill in the stripes, forging out this structure. In general, our simulations show that the stripes appear faster when the scattering length is lower, and when the atom number is larger. In the long time limit of the scenario presented in Fig. 2, we expect the stationary solution to also be the stripe state, but this is not observable on our timescales.

Remarkably, the stripe structure washes out when we subsequently tilt the magnetic-field orientation to $\theta = 0°$ (parallel to the trap symmetry axis), as shown in Fig. 4d1. Here, after 600 ms of magnetostirring, we add another step in which we spiral up the magnetic field to $\theta = 0°$ (with Ω fixed) over 100 ms, before imaging. Under these conditions, all vortex properties are again isotropic within the plane. The final non-equilibrium positioning of the vortices is arbitrary, and if we average the FT of the residuals directly, we observe a homogeneous ring in the average FT (Fig. 4d3). Also, this behavior is confirmed by the simulations, as shown in Fig. 4e1-e3.

By exploiting magnetostirring — a novel, robust, method of generating angular momentum — we have observed quantized vortices in a dipolar quantum gas, and the appearance of the vortex stripe configuration. Future works will focus on investigations of the individual vortex shape and behaviour, such as the anisotropic nature of the vortex cores for in-plane magnetic fields[32–35], the interplay between the vortex and roton excitations[32–36], exotic vortex patterns such as square lattices[31], and investigations into anisotropic turbulence[64]. This work also opens the door to studying more complex matter under rotation, such as dipolar droplets[65–67] and supersolid states[42–45]. Such proposals will be challenging due to the intricate density patterns[68], however such observations would provide conclusive evidence of superfluidity in supersolids. Rotating the magnetic field at frequencies far larger than the radial trap frequencies, but smaller than the Larmor frequency, has been observed to tune the sign and magnitude of the dipole-dipole interaction[69,70]–a method also employed in Nuclear Magnetic Resonance spectroscopy[71]–but there remain open questions on the stability of this procedure[72,73], which if rectifiable would unlock new research directions[69]. Other vortex generation methods, such as thermally activated pairs in quasi-2D to assess the Berezinskii-Kosterlitz-Thouless transition, and stochastically generated vortex tangles through temperature quenches to assess the Kibble-Zurek mechanism, remain unexplored in dipolar gases[31]. The technique introduced here is also applicable to a wide range of systems governed by long-range interactions through the manipulation of magnetic or electric fields.

Acknowledgements:
We are grateful to S. B. Prasad, M. Norcia, R. M. W. van Bijnen, and L. Santos for helpful discussions. We acknowledge M. Norcia and A. Patscheider for experimental contributions. This study received support from the European Research Council through the Consolidator Grant RARE (No. 681432), the QuantERA grant MAQS by the Austrian Science Fund FWF No. I4391-N, the DFG/FWF via FOR 2247/PI2790 a joint-project grant from the FWF (Grant No. I4426, RSF/Russland 2019). M.J.M. acknowledges support through an ESQ Discovery Grant by the Austrian Academy of Sciences. We also acknowledge the Innsbruck Laser Core Facility, financed by the Austrian Federal Ministry of Science, Research and Economy. Part of the computational results presented have been achieved using the HPC infrastructure LEO of the University of Innsbruck. G.L. acknowledges financial support from Provincia Autonoma di Trento.

Author contributions:
L.K., C.P., G.L., E.C., M.J.M., and F.F. performed the experimental work and data analysis. E.P., T.B., and R.B. performed the theoretical work. All authors contributed to the interpretation of the results and the preparation of the manuscript.

---

[*] These two authors contributed equally to this work.

[†] Correspondence should be addressed to `Francesca.Ferlaino@uibk.ac.at`

1. R. J. Donnelly, Quantized vortices in Helium II (Cambridge University Press, Cambridge, 1991).
2. D. Pines and M. A. Alpar, Superfluidity in neutron stars, Nature **316**, 27 (1985).
3. A. A. Abrikosov, Nobel Lecture: Type-II superconductors and the vortex lattice, Rev. Mod. Phys. **76**, 975 (2004).
4. K. G. Lagoudakis, M. Wouters, M. Richard, A. Baas, I. Carusotto, R. André, L. S. Dang, and B. Deveaud-Plédran, Quantized vortices in an exciton–polariton condensate, Nat. Phys. **4**, 706 (2008).
5. M. R. Matthews, B. P. Anderson, P. C. Haljan, D. S. Hall, C. E. Wieman, and E. A. Cornell, Vortices in a Bose-Einstein condensate, Phys. Rev. Lett. **83**, 2498 (1999).
6. K. W. Madison, F. Chevy, W. Wohlleben, and J. Dalibard, Vortex formation in a stirred Bose-Einstein condensate, Phys. Rev. Lett. **84**, 806 (2000).
7. T. W. Neely, E. C. Samson, A. S. Bradley, M. J. Davis, and B. P. Anderson, Observation of vortex dipoles in an oblate Bose-Einstein condensate, Phys. Rev. Lett. **104**, 160401 (2010).
8. M. J. H. Ku, W. Ji, B. Mukherjee, E. Guardado-Sanchez, L. W. Cheuk, T. Yefsah, and M. W. Zwierlein, Motion of a solitonic vortex in the BEC-BCS crossover, Phys. Rev. Lett. **113**, 065301 (2014).
9. S. Donadello, S. Serafini, M. Tylutki, L. P. Pitaevskii, F. Dalfovo, G. Lamporesi, and G. Ferrari, Observation of solitonic vortices in bose-einstein condensates, Phys. Rev. Lett. **113**, 065302 (2014).
10. B. P. Anderson, P. C. Haljan, C. A. Regal, D. L. Feder, L. A. Collins, C. W. Clark, and E. A. Cornell, Watching dark solitons decay into vortex rings in a bose-einstein condensate, Phys. Rev. Lett. **86**, 2926 (2001).
11. J. R. Abo-Shaeer, C. Raman, J. M. Vogels, and W. Ketterle, Observation of vortex lattices in Bose-Einstein condensates, Science **292**, 476 (2001).
12. I. Coddington, P. Engels, V. Schweikhard, and E. A. Cornell, Observation of Tkachenko oscillations in rapidly rotating Bose-Einstein condensates, Phys. Rev. Lett. **91**, 100402 (2003).
13. Z. Hadzibabic, P. Krüger, M. Cheneau, B. Battelier, and J. Dalibard, Berezinskii–Kosterlitz–Thouless crossover in a trapped atomic gas, Nature (London) **441**, 1118 (2006).
14. T. W. Neely, A. S. Bradley, E. C. Samson, S. J. Rooney, E. M. Wright, K. J. H. Law, R. Carretero-González, P. G. Kevrekidis, M. J. Davis, and B. P. Anderson, Characteristics of two-dimensional quantum turbulence in a compressible superfluid, Phys. Rev. Lett. **111**, 235301 (2013).
15. N. Navon, A. L. Gaunt, R. P. Smith, and Z. Hadzibabic, Emergence of a turbulent cascade in a quantum gas, Nature (London) **539**, 72 (2016).
16. M. C. Tsatsos, P. E. Tavares, A. Cidrim, A. R. Fritsch, M. A. Caracanhas, F. E. A. dos Santos, C. F. Barenghi, and V. S. Bagnato, Quantum turbulence in trapped atomic Bose–Einstein condensates, Physics Reports **622**, 1 (2016).
17. M. W. Zwierlein, J. R. Abo-Shaeer, A. Schirotzek, C. H. Schunck, and W. Ketterle, Vortices and superfluidity in a strongly interacting Fermi gas, Nature (London) **435**, 1047 (2005).
18. M. Lu, N. Q. Burdick, S. H. Youn, and B. L. Lev, Strongly dipolar Bose-Einstein condensate of Dysprosium, Phys. Rev. Lett. **107**, 190401 (2011).
19. K. Aikawa, A. Frisch, M. Mark, S. Baier, A. Rietzler, R. Grimm, and F. Ferlaino, Bose-Einstein condensation

of Erbium, Phys. Rev. Lett. **108**, 210401 (2012).

20. M. A. Norcia and F. Ferlaino, Developments in atomic control using ultracold magnetic lanthanides, Nat. Phys. **17**, 1349 (2021).
21. L. Chomaz, I. Ferrier-Barbut, F. Ferlaino, B. Laburthe-Tolra, B. L. Lev, and T. Pfau, Dipolar physics: A review of experiments with magnetic quantum gases, arXiv:2201.02672 (2022).
22. S. Baier, M. J. Mark, D. Petter, K. Aikawa, L. Chomaz, Z. Cai, M. Baranov, P. Zoller, and F. Ferlaino, Extended Bose-Hubbard models with ultracold magnetic atoms, Science **352**, 201 (2016).
23. L. Landau, Theory of the superfluidity of Helium II, Phys. Rev. **60**, 356 (1941).
24. L. Chomaz, R. M. W. van Bijnen, D. Petter, G. Faraoni, S. Baier, J. H. Becher, M. J. Mark, F. Wächtler, L. Santos, and F. Ferlaino, Observation of roton mode population in a dipolar quantum gas, Nat. Phys. **14**, 442 (2018).
25. J.-N. Schmidt, J. Hertkorn, M. Guo, F. Böttcher, M. Schmidt, K. S. H. Ng, S. D. Graham, T. Langen, M. Zwierlein, and T. Pfau, Roton excitations in an oblate dipolar quantum gas, Phys. Rev. Lett. **126**, 193002 (2021).
26. H. Kadau, M. Schmitt, M. Wenzel, C. Wink, T. Maier, I. Ferrier-Barbut, and T. Pfau, Observing the Rosensweig instability of a quantum ferrofluid, Nature **530**, 194 (2016).
27. L. Tanzi, E. Lucioni, F. Famà, J. Catani, A. Fioretti, C. Gabbanini, R. N. Bisset, L. Santos, and G. Modugno, Observation of a dipolar quantum gas with metastable supersolid properties, Phys. Rev. Lett. **122**, 130405 (2019).
28. F. Böttcher, J.-N. Schmidt, M. Wenzel, J. Hertkorn, M. Guo, T. Langen, and T. Pfau, Transient supersolid properties in an array of dipolar quantum droplets, Phys. Rev. X **9**, 011051 (2019).
29. L. Chomaz, D. Petter, P. Ilzhöfer, G. Natale, A. Trautmann, C. Politi, G. Durastante, R. M. W. van Bijnen, A. Patscheider, M. Sohmen, M. J. Mark, and F. Ferlaino, Long-lived and transient supersolid behaviors in dipolar quantum gases, Phys. Rev. X **9**, 021012 (2019).
30. M. A. Norcia, C. Politi, L. Klaus, E. Poli, M. Sohmen, M. J. Mark, R. Bisset, L. Santos, and F. Ferlaino, Two-dimensional supersolidity in a dipolar quantum gas, Nature **596**, 357 (2021).
31. A. M. Martin, N. G. Marchant, D. H. J. O'Dell, and N. G. Parker, Vortices and vortex lattices in quantum ferrofluids, J. Phys. Condens. Matter **29**, 103004 (2017).
32. S. Yi and H. Pu, Vortex structures in dipolar condensates, Phys. Rev. A **73**, 061602 (2006).
33. C. Ticknor, R. M. Wilson, and J. L. Bohn, Anisotropic superfluidity in a dipolar Bose gas, Phys. Rev. Lett. **106**, 065301 (2011).
34. B. C. Mulkerin, R. M. W. van Bijnen, D. H. J. O'Dell, A. M. Martin, and N. G. Parker, Anisotropic and long-range vortex interactions in two-dimensional dipolar Bose gases, Phys. Rev. Lett. **111**, 170402 (2013).
35. B. C. Mulkerin, D. H. J. O'Dell, A. M. Martin, and N. G. Parker, Vortices in the two-dimensional dipolar bose gas, J. Phys. Conf. Ser. **497**, 012025 (2014).
36. M. Jona-Lasinio, K. Łakomy, and L. Santos, Roton confinement in trapped dipolar Bose-Einstein condensates, Phys. Rev. A **88**, 013619 (2013).
37. S. Gautam, Dynamics of the corotating vortices in dipolar Bose-Einstein condensates in the presence of dissipation, J. Phys. B: At. Mol. Opt. Phys. **47**, 165301 (2014).
38. N. Cooper, E. Rezayi, and S. Simon, Vortex lattices in rotating atomic bose gases with dipolar interactions, Phys. Rev. Lett. **95**, 200402 (2005).
39. R. K. Kumar, T. Sriraman, H. Fabrelli, P. Muruganandam, and A. Gammal, Three-dimensional vortex structures in a rotating dipolar bose–einstein condensate, J. Phys. B: At. Mol. Opt. Phys **49**, 155301 (2016).
40. Y. Cai, Y. Yuan, M. Rosenkranz, H. Pu, and W. Bao, Vortex patterns and the critical rotational frequency in rotating dipolar Bose-Einstein condensates, Phys. Rev. A **98**, 023610 (2018).
41. S. B. Prasad, T. Bland, B. C. Mulkerin, N. G. Parker, and A. M. Martin, Vortex lattice formation in dipolar Bose-Einstein condensates via rotation of the polarization, Phys. Rev. A **100**, 023625 (2019).
42. S. M. Roccuzzo, A. Gallemí, A. Recati, and S. Stringari, Rotating a supersolid dipolar gas, Phys. Rev. Lett. **124**, 045702 (2020).
43. A. Gallemí, S. M. Roccuzzo, S. Stringari, and A. Recati, Quantized vortices in dipolar supersolid Bose-Einstein-condensed gases, Phys. Rev. A **102**, 023322 (2020).
44. F. Ancilotto, M. Barranco, M. Pi, and L. Reatto, Vortex properties in the extended supersolid phase of dipolar Bose-Einstein condensates, Phys. Rev. A **103**, 033314 (2021).
45. M. A. Norcia, E. Poli, C. Politi, L. Klaus, T. Bland, M. J. Mark, L. Santos, R. N. Bisset, and F. Ferlaino, Can angular oscillations probe superfluidity in dipolar supersolids?, arXiv:2111.07768 (2021).
46. S. M. Roccuzzo, A. Recati, and S. Stringari, Moment of inertia and dynamical rotational response of a supersolid dipolar gas, Phys. Rev. A **105**, 023316 (2022).
47. J. Stuhler, A. Griesmaier, T. Koch, M. Fattori, T. Pfau, S. Giovanazzi, P. Pedri, and L. Santos, Observation of dipole-dipole interaction in a degenerate quantum gas, Phys. Rev. Lett. **95**, 150406 (2005).
48. P. C. Haljan, I. Coddington, P. Engels, and E. A. Cornell, Driving Bose-Einstein-Condensate Vorticity with a Rotating Normal Cloud, Phys. Rev. Lett. **87**, 210403 (2001).
49. W. J. Kwon, G. Del Pace, K. Xhani, L. Galantucci, A. Muzi Falconi, M. Inguscio, F. Scazza, and G. Roati, Sound emission and annihilations in a programmable quantum vortex collider, Nature (London) **600**, 64 (2021).
50. L. Corman, L. Chomaz, T. Bienaimé, R. Desbuquois, C. Weitenberg, S. Nascimbène, J. Dalibard, and J. Beugnon, Quench-induced supercurrents in an annular bose gas, Phys. Rev. Lett. **113**, 135302 (2014).
51. I. K. Liu, S. Donadello, G. Lamporesi, G. Ferrari, S. C. Gou, F. Dalfovo, and N. P. Proukakis, Dynamical equilibration across a quenched phase transition in a trapped quantum gas, Commun. Phys. **1**, 24 (2018).
52. G. Del Pace, K. Xhani, A. M. Falconi, M. Fedrizzi, N. Grani, D. H. Rajkov, M. Inguscio, F. Scazza, W. J. Kwon, and G. Roati, Imprinting persistent currents in tunable fermionic rings (2022), arXiv:2204.06542.
53. S. B. Prasad, B. C. Mulkerin, and A. M. Martin, Arbitrary-angle rotation of the polarization of a dipolar Bose-Einstein condensate, Phys. Rev. A **103**, 033322 (2021).
54. A. Recati, F. Zambelli, and S. Stringari, Overcritical rotation of a trapped Bose-Einstein condensate, Phys. Rev. Lett. **86**, 377 (2001).
55. F. Wächtler and L. Santos, Quantum filaments in dipo-

lar Bose-Einstein condensates, Phys. Rev. A **93**, 061603 (2016).

56. I. Ferrier-Barbut, H. Kadau, M. Schmitt, M. Wenzel, and T. Pfau, Observation of Quantum Droplets in a Strongly Dipolar Bose Gas, Phys. Rev. Lett. **116**, 215301 (2016).
57. L. Chomaz, S. Baier, D. Petter, M. J. Mark, F. Wächtler, L. Santos, and F. Ferlaino, Quantum-fluctuation-driven crossover from a dilute Bose-Einstein condensate to a macrodroplet in a dipolar quantum fluid, Phys. Rev. X **6**, 041039 (2016).
58. R. N. Bisset, R. M. Wilson, D. Baillie, and P. B. Blakie, Ground-state phase diagram of a dipolar condensate with quantum fluctuations, Phys. Rev. A **94**, 033619 (2016).
59. S. Sinha and Y. Castin, Dynamic instability of a rotating Bose-Einstein condensate, Phys. Rev. Lett. **87**, 190402 (2001).
60. K. W. Madison, F. Chevy, V. Bretin, and J. Dalibard, Stationary states of a rotating Bose-Einstein condensate: Routes to vortex nucleation, Phys. Rev. Lett. **86**, 4443 (2001).
61. J. R. Abo-Shaeer, C. Raman, and W. Ketterle, Formation and decay of vortex lattices in Bose-Einstein condensates at finite temperatures, Phys. Rev. Lett. **88**, 070409 (2002).
62. W. J. Kwon, G. Moon, J.-y. Choi, S. W. Seo, and Y.-i. Shin, Relaxation of superfluid turbulence in highly oblate Bose-Einstein condensates, Phys. Rev. A **90**, 063627 (2014).
63. P. Engels, I. Coddington, P. C. Haljan, and E. A. Cornell, Nonequilibrium effects of anisotropic compression applied to vortex lattices in Bose-Einstein condensates, Phys. Rev. Lett. **89**, 100403 (2002).
64. T. Bland, G. W. Stagg, L. Galantucci, A. W. Baggaley, and N. G. Parker, Quantum ferrofluid turbulence, Phys. Rev. Lett. **121**, 174501 (2018).
65. A. Cidrim, F. E. dos Santos, E. A. Henn, and T. Macrì, Vortices in self-bound dipolar droplets, Phys. Rev. A **98**, 023618 (2018).
66. A.-C. Lee, D. Baillie, R. N. Bisset, and P. B. Blakie, Excitations of a vortex line in an elongated dipolar condensate, Phys. Rev. A **98**, 063620 (2018).
67. I. Ferrier-Barbut, M. Wenzel, F. Böttcher, T. Langen, M. Isoard, S. Stringari, and T. Pfau, Scissors Mode of Dipolar Quantum Droplets of Dysprosium Atoms, Phys. Rev. Lett. **120**, 160402 (2018).
68. J. Hertkorn, J.-N. Schmidt, M. Guo, F. Böttcher, K. Ng, S. Graham, P. Uerlings, T. Langen, M. Zwierlein, and T. Pfau, Pattern formation in quantum ferrofluids: From supersolids to superglasses, Phys. Rev. Res. **3**, 033125 (2021).
69. Y. Tang, W. Kao, K.-Y. Li, and B. L. Lev, Tuning the Dipole-Dipole Interaction in a Quantum Gas with a Rotating Magnetic Field, Phys. Rev. Lett. **120**, 230401 (2018).
70. S. Giovanazzi, A. Görlitz, and T. Pfau, Tuning the Dipolar Interaction in Quantum Gases, Phys. Rev. Lett. **89**, 130401 (2002).
71. M. Maricq and J. S. Waugh, NMR in rotating solids, The Journal of Chemical Physics **70**, 3300 (1979).
72. S. B. Prasad, T. Bland, B. C. Mulkerin, N. G. Parker, and A. Martin, Instability of rotationally tuned dipolar bose-einstein condensates, Phys. Rev. Lett. **122**, 050401 (2019).
73. D. Baillie and P. B. Blakie, Rotational tuning of the dipole-dipole interaction in a Bose gas of magnetic atoms, Phys. Rev. A **101**, 043606 (2020).
74. Y. Tang, A. Sykes, N. Q. Burdick, J. L. Bohn, and B. L. Lev, s-wave scattering lengths of the strongly dipolar bosons 162Dy and 164Dy, Phys. Rev. A **92**, 022703 (2015).
75. Y. Tang, A. G. Sykes, N. Q. Burdick, J. M. DiSciacca, D. S. Petrov, and B. L. Lev, Anisotropic Expansion of a Thermal Dipolar Bose Gas, Phys. Rev. Lett. **117**, 155301 (2016).
76. E. Lucioni, L. Tanzi, A. Fregosi, J. Catani, S. Gozzini, M. Inguscio, A. Fioretti, C. Gabbanini, and G. Modugno, Dysprosium dipolar Bose-Einstein condensate with broad Feshbach resonances, Phys. Rev. A **97**, 060701 (2018).
77. F. Böttcher, M. Wenzel, J.-N. Schmidt, M. Guo, T. Langen, I. Ferrier-Barbut, T. Pfau, R. Bombín, J. Sánchez-Baena, J. Boronat, and F. Mazzanti, Dilute dipolar quantum droplets beyond the extended Gross-Pitaevskii equation, Phys. Rev. Res. **1**, 033088 (2019).
78. C. Chin, R. Grimm, P. Julienne, and E. Tiesinga, Feshbach resonances in ultracold gases, Rev. Mod. Phys. **82**, 1225 (2010).
79. A. Patscheider, L. Chomaz, G. Natale, D. Petter, M. J. Mark, S. Baier, B. Yang, R. R. W. Wang, J. L. Bohn, and F. Ferlaino, Determination of the scattering length of erbium atoms, Phys. Rev. A **105**, 063307 (2022).
80. A. R. P. Lima and A. Pelster, Quantum fluctuations in dipolar Bose gases, Phys. Rev. A **84**, 041604 (2011).
81. P. Blakie, A. Bradley, M. Davis, R. Ballagh, and C. Gardiner, Dynamics and statistical mechanics of ultra-cold Bose gases using c-field techniques, Adv. Phys. **57**, 363 (2008).

Methods

Experimental Procedure

We prepare an ultracold gas of ^{162}Dy atoms in an optical dipole trap (ODT). Three 1064 nm laser beams, overlapping at their foci, form the ODT. The experimental procedure to Bose-Einstein condensation is similar to the one followed in our previous work[45], but the magnetic field unit vector, $\hat{\mathbf{B}}$, is tilted by an angle of $\theta = 35°$ with respect to the z-axis during the whole sequence. After preparation, the sample contains about 2×10^4 condensed atoms. The corresponding trap frequencies are typically $(\omega_\perp, \omega_z) = 2\pi \times [50.8(2), 140(1)]\,\mathrm{Hz}$. For all our measurements, the deviation of the trap aspect ratio in the xy-plane $\mathrm{AR}_{\mathrm{trap}} = \omega_y/\omega_x$ from 1 is always smaller than 0.6%. We evaporate the atoms at $|\vec{\mathbf{B}}| = 5.423(5)\,\mathrm{G}$ and jump to the final magnetic-field value during the last evaporation ramp. After the preparation of the BEC, the magnetic field is rotated as described in the next section. We use standard absorption imaging to record the atomic distribution. We probe the vortices using the vertical imaging taken along the axis of rotation (z), for which the dark spots within the condensate correspond to the cores of individual vortices. The vertical images are taken with a short TOF of 3 ms and a pulse duration of 3-4 μs. For the data in Fig. 1-3, we let the magnetic field spinning during TOF, whereas for Fig. 4 we use a static field orientation.

Control of the magnetic field

Calibration: Three pairs of coils – each oriented along a primary axis in the laboratory frame – enable the creation of a homogeneous field with arbitrary orientations. The absolute magnetic field value $|\vec{\mathbf{B}}|$ of each pair of coils is independently calibrated using radio frequency (RF) spectroscopy. The RF drives transitions to excited Zeeman states, leading to a resonant dip in the atom number. The long-term stability – measured via the peak position of the RF resonance over the course of several days – is on the order of $\Delta B = \pm 1\,\mathrm{mG}$, while shot-to-shot fluctuations – measured via the width of the RF resonance for a single calibration set – is $\Delta B = \pm 5\,\mathrm{mG}$.

Rotation: We drive the rotation of the magnetic field by sinusoidally modulating the magnetic-field value components B_x and B_y with a phase difference of 90° between them. Since we want to keep the absolute magnetic field value $|\vec{\mathbf{B}}|$ constant during rotation, we measure it for various values of the azimuthal angle ϕ and fixed $\theta = 35°$ by performing Feshbach loss spectroscopy around 5.1 G. We find an average shift of $|\vec{\mathbf{B}}|$ of about 10 mG from the $\theta = 0°$ case, which we take into account. We also find small deviations as a function of ϕ of $\Delta|\vec{\mathbf{B}}| < 20\,\mathrm{mG}$, which might appear due to slightly non-orthogonal alignment of the magnetic fields. We did not correct these deviations for the sake of simplicity.

Scattering length

The scattering length in ^{162}Dy is currently not known with large accuracy[74–77]. To estimate the scattering length in the small magnetic-field range around $B = 5.3\,\mathrm{G}$, relevant to this work, we use the well-known relation $a_s = a_{\mathrm{bg}} \prod_i [1 - \Delta B_i/(B - B_{0,i})]$[78], where $B_{0,i}$ and ΔB_i are the center position and the width of the Feshbach loss features reported in Ref. [77], respectively.

The value of the background scattering length, a_{bg}, is empirically fixed by measuring the magnetic field value at which the supersolid transition occurs and comparing it with the corresponding critical a_s predicted from simulations. Such an approach leads to $a_s = 111(9)\,\mathrm{a}_0$ at $B = 5.333\,\mathrm{G}$. Extended Data Fig. 1 shows the resulting scattering lengths for the relevant magnetic fields. Although such an approach gives very good agreement between theory and experiments, future works on a precise determination of a_s, similar to the one achieved with erbium[79], would be desirable.

Magnetostirring

Tilting the magnetic field vector $\vec{\mathbf{B}}$ away from the symmetry axis of our cylindrical trap leads to an ellipsoidal deformation of the cloud[47] and therefore to a breaking of the cylindrical symmetry. This allows for the transfer of angular momentum to the sample by rotating the magnetic field (magnetostirring). In all our measurements we use a $\vec{\mathbf{B}}$ tilted with respect to the z-axis by 35° and a constant value $|\vec{\mathbf{B}}|$. That value is $|\vec{\mathbf{B}}| = 5.333(5)\,\mathrm{G}$ for the surveys in Figs. 1-3 and $|\vec{\mathbf{B}}| = 5.323(5)\,\mathrm{G}$ for Fig. 4. For these parameters, the magnetostricted aspect ratio of the cloud is $\mathrm{AR} = 1.03$. For all our measurements, the measured trap $\mathrm{AR}_{\mathrm{trap}} < 1.006$ is much smaller than the deformation due to magnetostriction. Additionally, we have confirmed with simulations that even with trap asymmetries of up to 10%, e.g. $(\omega_x, \omega_y) = (55, 50)\mathrm{Hz}$, this procedure can still generate vortices in a lattice configuration.

Adiabatic frequency ramp: We employ different magnetic-field rotation sequences for the different data sets. For the data set of Fig. 1c, the rotation frequency of the magnetic field is linearly increased to different final values at a speed of $\dot{\Omega} = 2\pi \times 50\,\mathrm{Hz/s}$ and for a duration of $t_{\dot{\Omega}} = 0\text{-}1\,\mathrm{s}$. The ramp time is much longer than the period of the rotation Ω^{-1} for higher rotation frequencies $\Omega \gtrsim \Omega_c$, and therefore the ramp is adiabatic for the regimes considered, until the onset of dynamical instabilities. After the ramp, the magnetic field direction is rotated at the target rotation frequency Ω for one final period (as shown in Fig. 1b2). We sample 10 different final magnetic field angles during this last rotation, measuring the corresponding aspect ratio and averaging the result in order to remove any potential biases due to latent trap anisotropies. Each data point is then obtained with 8-10 experimental runs.

Constant rotation frequency: For the dataset of Fig. 2, Fig. 3 and Fig. 4b we directly start to rotate at the final rotation frequency Ω without any acceleration phase. The magnetic field is then rotated for a variable time t_Ω, after which the atoms are released from the trap and a vertical image is taken.

Spiral up magnetic field: For the dataset of Fig. 4d we employ a similar sequence as described above. However, after constantly rotating the magnetic field at $\Omega = 0.75\,\omega_\perp$, the magnetic field is spiraled up in 100 ms to $\theta = 0°$ by linearly reducing θ while continuing rotating. Afterwards, the atoms are released from the trap and a vertical image is taken.

Theoretical model

We employ an extended Gross-Pitaevskii formalism to model our experimental setup. In this scheme, the inter-particle interactions are described by the two-body pseudo-potential,

$$U(\mathbf{r}) = \frac{4\pi\hbar^2 a_\mathrm{s}}{m}\delta(\mathbf{r}) + \frac{3\hbar^2 a_\mathrm{dd}}{m}\frac{1-3\left(\hat{\mathbf{e}}(t)\cdot\mathbf{r}\right)^2}{r^3}\,, \qquad (1)$$

with the first term describing short-range interactions governed by the s-wave scattering length a_s, with Planck's constant $\hbar$ and particle mass m. The second term represents the anisotropic and long-ranged dipole-dipole interactions, characterized by dipole length $a_\mathrm{dd} = \mu_0\mu_m^2 m/12\pi\hbar^2$, with magnetic moment μ_m and vacuum permeability μ_0. We always consider ^{162}Dy, such that $a_\mathrm{dd} = 129.2\,a_0$, where a_0 is the Bohr radius. The dipoles are polarized uniformly along a time-dependent axis, given by

$$\hat{\mathbf{e}}(t) = \left(\sin\theta(t)\cos\phi(t), \sin\theta(t)\sin\phi(t), \cos\theta(t)\right) \qquad (2)$$

with time dependent polarization angle $\theta(t)$ and $\phi(t) = \int_0^t \mathrm{d}t'\Omega(t')$, for rotation frequency protocol $\Omega(t)$.

Beyond-mean-field effects are treated through the inclusion of a Lee–Huang–Yang correction term[80]

$$\gamma_\mathrm{QF} = \frac{128\hbar^2}{3m}\sqrt{\pi a_s^5}\,\mathrm{Re}\left\{\mathcal{Q}_5(\epsilon_\mathrm{dd})\right\}\,, \qquad (3)$$

with $\mathcal{Q}_5(\epsilon_\mathrm{dd}) = \int_0^1 \mathrm{d}u\,(1-\epsilon_\mathrm{dd}+3u^2\epsilon_\mathrm{dd})^{5/2}$ being the auxiliary function, and the relative dipole strength is given by $\epsilon_\mathrm{dd} = a_\mathrm{dd}/a_\mathrm{s}$. Finally, the full extended Gross-Pitaevskii equation (eGPE) then reads[55–58]

$$i\hbar\frac{\partial\Psi(\mathbf{x},t)}{\partial t} = \Bigg[-\frac{\hbar^2\nabla^2}{2m} + \frac{1}{2}m\left(\omega_x^2x^2+\omega_y^2y^2+\omega_z^2z^2\right) + \int \mathrm{d}^3\mathbf{x}'\,U(\mathbf{x}-\mathbf{x}')|\Psi(\mathbf{x}',t)|^2 + \gamma_\mathrm{QF}|\Psi(\mathbf{x},t)|^3\Bigg]\Psi(\mathbf{x},t)\,, \qquad (4)$$

where $\omega_{x,y,z}$ are the harmonic trap frequencies. The wavefunction Ψ is normalized to the total atom number $N = \int \mathrm{d}^3\mathbf{x}|\Psi|^2$. The stationary solution for Fig. 4a from the main text is found through the imaginary time procedure in the rotating frame, introducing the usual angular momentum operator $\Omega\hat{L}_z$ into Eq. (4). The initial state $\Psi(\mathbf{x},0)$ of the real-time simulations is always obtained by adding non-interacting noise to the ground state $\Psi_0(\mathbf{x})$. Given the single-particle eigenstates ϕ_n and the complex Gaussian random variables α_n sampled with $\langle|\alpha_n|^2\rangle = (e^{\epsilon_n/k_BT}-1)^{-1}+\frac{1}{2}$ for a temperature $T = 20\,$nK, the initial state can be described as $\Psi(\mathbf{x},0) = \Psi_0(\mathbf{x}) + \sum_n' \alpha_n\phi_n(\mathbf{x})$, where the sum is restricted only to the modes with $\epsilon_n \leq 2k_BT$[81]. Throughout, the density images are presented in situ, with a scaling factor to account for the 3ms TOF for the experimental images.

In order to obtain the average residual Fourier Transform images for Figs. 4c3 and e3, we first Fourier Transform 115 frames from the simulation between 700ms and 1.1s in the rotating frame before averaging the result.

Atom number

Extended Data Fig. 2 shows the condensed atom number N_c for the measurement with an adiabatic ramp of the magnetic-field rotational velocity ($\dot{\Omega} = 2\pi\times 50\,$Hz/s), corresponding to the data of Fig.1c of the main text. To extract the atom number, we use the horizontal imaging with 26 ms of TOF. About 3 ms before flashing the imaging resonant light to the atoms, we rotate the magnetic field in the imaging plane and perform standard absorption imaging. From the absorption images, we extract N_c from a bimodal fit up to 700 ms. At later times, the system undergoes a dynamic instability (see discussion in the main text) and the density profile deviates from a simple bimodal distribution. During the observation time, we see a slight decrease of N_c and for our theory simulations we use a constant atom number of $N_c = 15000$. Note that in all following datasets, in which we abruptly accelerate the magnetic-field rotation to the desired final velocity, we observe a faster decay and our simulations are performed with either $N_c = 8000$ or $N_c = 10000$.

Vortex detection

Vortex detection algorithm: Since vortices appear as dark holes in the density profile of a BEC, which would otherwise have a smooth profile, our approach to extract the number of vortices is to look at deviations between the image and an unmodulated reference image. To extract the vortex number from the raw images, we proceed as follows:

First, we prepare the image n_{img}, the reference image n_{ref} and the residual image n_{res}. The image is normalized such that the maximum density $\max(n_{\mathrm{img}}) = 1$. We create the reference image by blurring the image via applying a 2D Gaussian filter with $\sigma = 5\,\mathrm{pixel}$, corresponding to about $2.1\,\mu\mathrm{m}$. This blurring smoothens any structure on the lengthscale of the filter width, therefore any holes in the density profile wash out. We then normalize the atom number of the reference to be the same as from the image $N_{\mathrm{ref}} = \int\int n_{\mathrm{ref}} \doteq N_{\mathrm{img}} = \int\int n_{\mathrm{img}}$. The residual image is calculated as the difference between the image and the reference $n_{\mathrm{res}} = n_{\mathrm{img}} - n_{\mathrm{ref}}$. We additionally mask the region where the density of the reference is below a certain threshold ($n_{\mathrm{res}} = 0$ where $n_{\mathrm{ref}} \leq 0.1$).

Second, we identify local minima in the residual image and determine if they are connected to vortices. For this, we create a list of local minima $(x_{\mathrm{min}}, y_{\mathrm{min}})$, defined by the condition that the pixel density $n_{\mathrm{res}}(x_{\mathrm{min}}, y_{\mathrm{min}})$ is lower than of all surrounding pixels. Then we remove minima with density values above zero $n_{\mathrm{res}}(x_{\mathrm{min}}, y_{\mathrm{min}}) \geq 0$ or which are within one pixel distance of the mask border. Now we determine a local contrast for each minimum by calculating the difference between its central density value and the mean of the density values ± 2 pixel values away from it $n_{\mathrm{con}}(x_{\mathrm{min}}, y_{\mathrm{min}}) = n_{\mathrm{res}}(x_{\mathrm{min}}, y_{\mathrm{min}}) - \mathrm{mean}(n_{\mathrm{res}}(x_{\mathrm{min}} \pm 2\,\mathrm{px}, y_{\mathrm{min}} \pm 2\,\mathrm{px}))$, and remove minima above a certain threshold $n_{\mathrm{con}} > -0.11$. As a last step we check the distance d between all remaining minima to avoid double counting of minima too close to each other. In case d is below the threshold $d < 5\,\mathrm{px}$ the minimum with the higher residual density value n_{res} is discarded.

Preparation of theory density profiles: For the direct comparison of the vortex number shown in Fig. 3b, we apply additional steps to the density profiles obtained from theory. First, we reduce the resolution by a 2×2 binning to make the pixel size of the theory density profiles $n_{\mathrm{img}}^{\mathrm{theo}}$ essentially the same as for the experimental images (sizes are within 5%). After normalizing to $\max(n_{\mathrm{img}}^{\mathrm{theo}}) = 1$ we apply Gaussian white noise with zero mean and a variance of 0.01 to each pixel, recreating the noise pattern from empty regions of experimental images. Then we blur the image using a 2D Gaussian filter with $\sigma = 1\,\mathrm{pixel}$ ($\sim 0.42\,\mu\mathrm{m}$), this recreates the same resolution condition as our experimental setup. The resulting density profile is taken as the input image for the vortex detection algorithm described above.

Benchmarking the vortex detection algorithm: As the vortex positions for the simulation images are known a priori due to the available phase map, we can derive the fidelity of the vortex detection algorithm for simulation data. For the theory data shown in Fig. 3b in the time frame between 600 and 700 ms, the average detected vortex number in the simulated density profiles (applying the preparation scheme described above) is about 9, while the real number of vortices present in the same area of the image is about 33 in average. This mismatch is explained by the conservative choice of the thresholds for vortex detection together with the added noise, which results in only counting clear density dips as vortices, throwing out many vortices in the low density region. This conservative choice of thresholds on the other hand leads to a very high fidelity of $> 97\%$, where we define the fidelity as the percentage of detected vortices which correspond to actual present vortices in the data. For raw simulation data (without resolution reduction, added noise and blurring) the vortex detection algorithm would detect up to 80% of the vortices present with a fidelity of $> 95\%$.

Note that for the visualization of the vortex positions for Fig. 4 we slightly increased the local threshold $n_{\mathrm{con}} > -0.08$ and decreased the minimum distance between vortices $d < 3\,\mathrm{px}$, which increases the overall number of vortices detected. For the density distributions obtained from theory, we additionally omit the resolution reduction, addition of noise and blurring steps.

Extended data figures

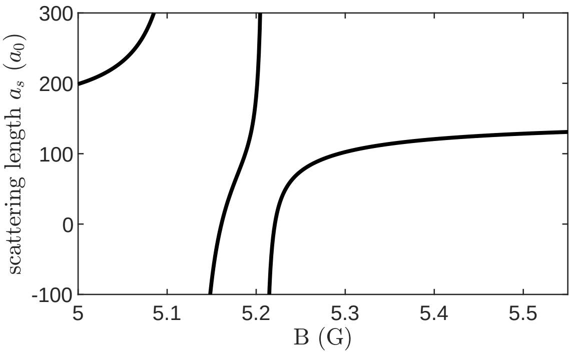

Extended Data Fig. 1. **Calculated B-to-a_s conversion for ^{162}Dy.** Scattering length as a function of the magnetic-field value with the background scattering length $a_{\mathrm{bg}} = 129(9)\,\mathrm{a}_0$. We find $a_s = 111(9)\,\mathrm{a}_0$ at $B = 5.333\,\mathrm{G}$.

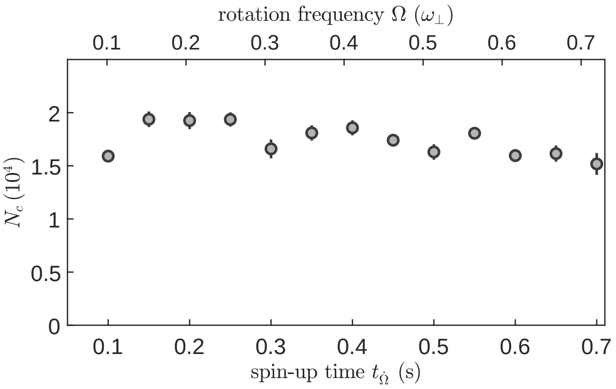

Extended Data Fig. 2. **Condensed atom number N_c during magnetostirring (Fig. 1c)**. Condensed atom number as a function of spin-up time $t_{\dot\Omega}$ for the same sequence as in Fig. 1c. The condensed atom number is extracted by fitting a two-dimensional bimodal distribution of Thomas-Fermi and Gaussian function to the horizontal density distributions.

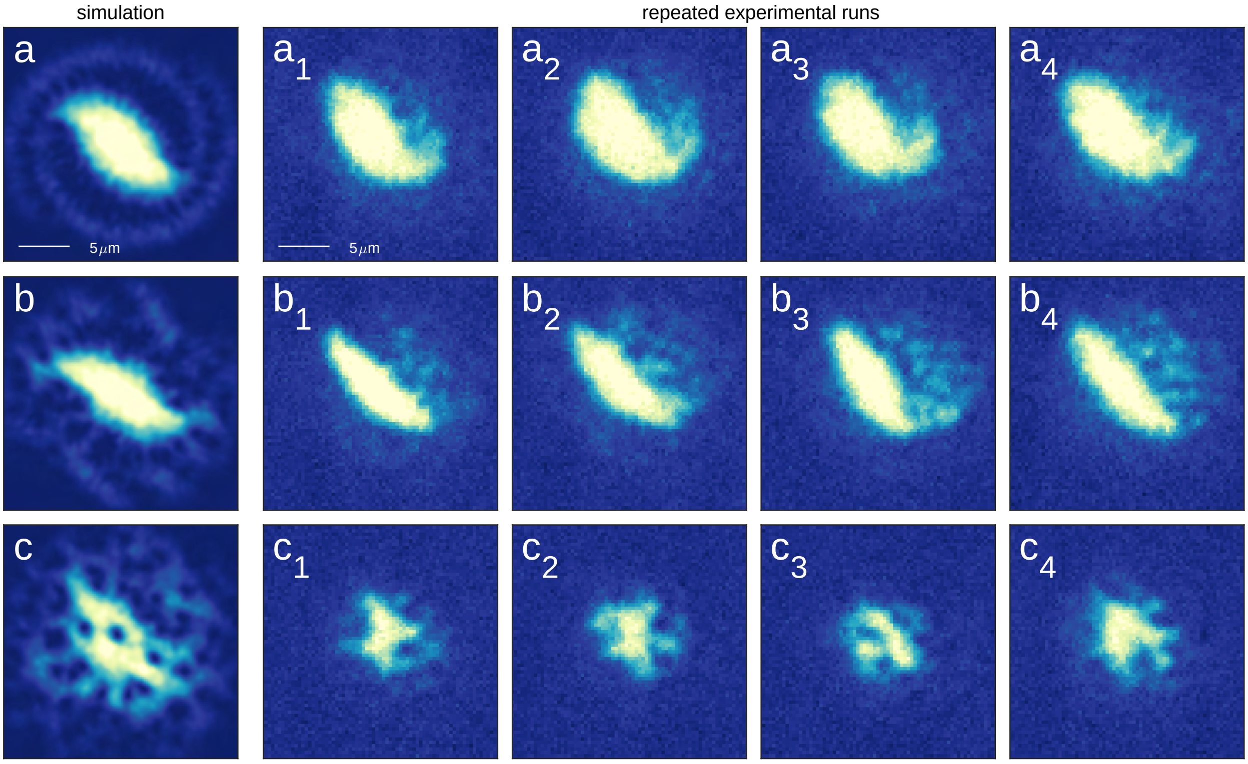

Extended Data Fig. 3. **Repeatability of the vortex generation protocol.** Each row shows the simulated image (**a, b, c**) and the corresponding vertical TOF images from independent experimental runs ($\mathbf{a}_i$, $\mathbf{b}_i$, $\mathbf{c}_i$) for a different rotation time: $t_a = 127\,\mathrm{ms}$, $t_b = 207\,\mathrm{ms}$, and $t_c = 741\,\mathrm{ms}$. The rotation frequency is $\Omega = 0.74\,\omega_\perp$ with the trap frequencies being $\omega_t = 2\pi \times [50.7(1), 50.8(1), 129(1)]\,\mathrm{Hz}$. The magnetic field value is $|\vec{\mathbf{B}}| = 5.333(5)\,\mathrm{G}$. For the simulation the scattering length used is $112\,\mathrm{a}_0$, the trap frequencies are $(50, 50, 150)\,\mathrm{Hz}$, the condensed atom number is $N = 8000$, and the rotation frequency is $0.75\,\omega_\perp$.

3.2 Outlook

> *I am an old man now, and when I die and go to Heaven there are two matters on which I hope for enlightenment. One is quantum electrodynamics, and the other is the turbulent motion of fluids. And about the former I am really rather optimisitic.*
>
> ***Sir Horace Lamb***
> *Conversation with Sydney Goldstein (1932) taken from [245]*

We were able to create vortices in a dipolar condensate for the first time. We saw the effects of the dipolar interaction on the geometry of the vortex lattice, which formed stripes in the direction of the magnetic field. And to create the vortices we developed the new technique – magnetostirring – to rotate the gas, exploiting the magnetostriction effect due to the dipolar interactions. Not only did we observe interesting new physics, but this work also laid the foundation for creating vortices in a supersolid, which will be the subject of the next part.

As the last part of my Ph.D. focused on angular oscillations and the rotation of the supersolid, I did not have time to study the dipolar BEC further. However, there are still many interesting topics and directions in rotating dipolar Bose-Einstein condensates that can hopefully be explored in this or other experiments in the future.

One topic is the change in the core structure of the vortices. Similarly to the lattice structure, the core geometry is also predicted to be influenced by the anisotropy of the DDI and to elongate along the magnetic field and to form density ripples orthogonal to the magnetic field associated with the roton minimum [246, 247, 248, 209]. The exact structure of the vortex core could not be extracted from our data because the resolution of our imaging system was insufficient, and other effects, such as vortex bending, are thought to make this effect difficult to observe. As with theoretical predictions, which are generally performed in a quasi-2D environment, it would also be helpful experimentally to work in such an environment, as effects such as vortex bending are reduced.

Another milestone will be the creation of larger vortex lattices in dipolar BECs. The early rotated non-dipolar BEC experiments showed that it is possible to create and observe vortex lattices with more than 100 vortices [40]. In our experiment, we would need to increase the number of condensed atoms by at least one order of magnitude. With the larger lattices it will be possible to study the structure of the lattice in equilibrium and to measure and create different lattice structures by changing the direction and strength of the dipolar interactions [238, 239, 98]. It would also be interesting to observe the influence of dipolar interactions on Tkachenko oscillations [237, 249, 250].

An important topic is the dissipation of superfluid systems with vortices. The friction between the superfluid and the normal part can be mediated by vortices, due to the scattering of thermal quasi-particles off the vortex core [183, 251, 252]. Additional dissipation mechanisms are the spontaneous excitation of Kelvin modes [233, 199]. All of these effects should be interaction dependent. Improving the number of vortices and the lifetime of the condensate should allow us to study the influence of dipolar interactions. Further experimental studies of the rotation for different tilts θ of the magnetic field are also interesting. In the paper by Bland et al. [232] this has been theoretically studied. Tilting the magnetic field angle further than the magic angle $\theta > \theta_c$ drastically changes the behaviour under fast rotations. The cloud elongates to a large extent, but does not collapse at $\Omega \approx 0.75\omega_\perp$. It seems that there is no dynamical instability anymore to seed the vortices. We assume that due to the reduction of the effective radial trap frequency $\omega_\perp^{\text{eff}}$, the cloud geometry moves towards the quasi-2D regime and the DDIs are mainly attractive, leading to the transition from a BEC to a macrodroplet and therefore a different behaviour. It would be interesting to study the behaviour for different trap parameters and a_s. It would also be interesting to see whether it is experimentally feasible to nucleate vortices before transition to the droplet state.

Finally, it would also be interesting to study phenomena such as quantum turbulence [253, 202] and the BKT transition in a 2D system [254, 255]. As can be seen, we have taken the first steps to open up a large field of study that will further our understanding of quantum hydrodynamics in the future.

4

Rotational dynamics in Supersolids

> *The behavior of large and complex aggregates of elementary particles, it turns out, is not to be understood in terms of a simple extrapolation of the properties of a few particles. Instead, at each level of complexity entirely new properties appear, and the understanding of the new behaviors requires research which I think is as fundamental in its nature as any other.*
>
> ***P.W. Anderson***
> *More is different (1972) [256]*

More than 50 years ago Gross [257], Andreev and Lifshitz [79], Chester [80] and Leggett [81] discussed the question "Can a solid be superfluid". This question was posed in the context of solid Helium-4 and Leggett concluded that if it could be cooled down to low enough temperatures, then it should be possible to measure very weak superfluid flow properties from this solid. However, experimental proof of supersolid Helium-4 remains elusive [258].

The experimental realisation of the supersolid state in ultracold dipolar gases [120, 121, 122] has opened another door to answer this question experimentally. Due to the anisotropic, long-range dipolar interactions the density profile of the ground state is modulated (the solid characteristic) and the whole state is still globally coherent (the BEC/superfluid characteristic). However, we discussed already in 1.3.5, that global coherence is not sufficient to claim, that the state is superfluid. This has already motivated the search for a direct probe of superfluidity in supersolids [129, 131].

To this end, we look into the rotational dynamics of the condensed cloud. First we try to measure the non-classical moment of inertia (NCMI) as suggested by Leggett [81] by exciting the scissor mode. This work is described in Sec. 4.2 and in the publication 3 "Can angular oscillations probe superfluidity in dipolar supersolids?" [259].

As we already know from Chapter 2, quantized vortices are the hallmark of superfluid flow. Using the proven method of magnetostirring to impart angular momentum to the cloud, we want to show quantized vortices in supersolids and thus prove the superfluid properties. This is described in Sec. 4.3 and in the publication 4 "Observation of vortices in a dipolar supersolid" [260].

In order to carry out these studies, we first have to create two-dimensional arrays of supersolids and prove that these systems are still globally coherent. This is described in Sec. 4.1 and in the publication 2 "Two-dimensional supersolidity in a dipolar quantum gas" [261].

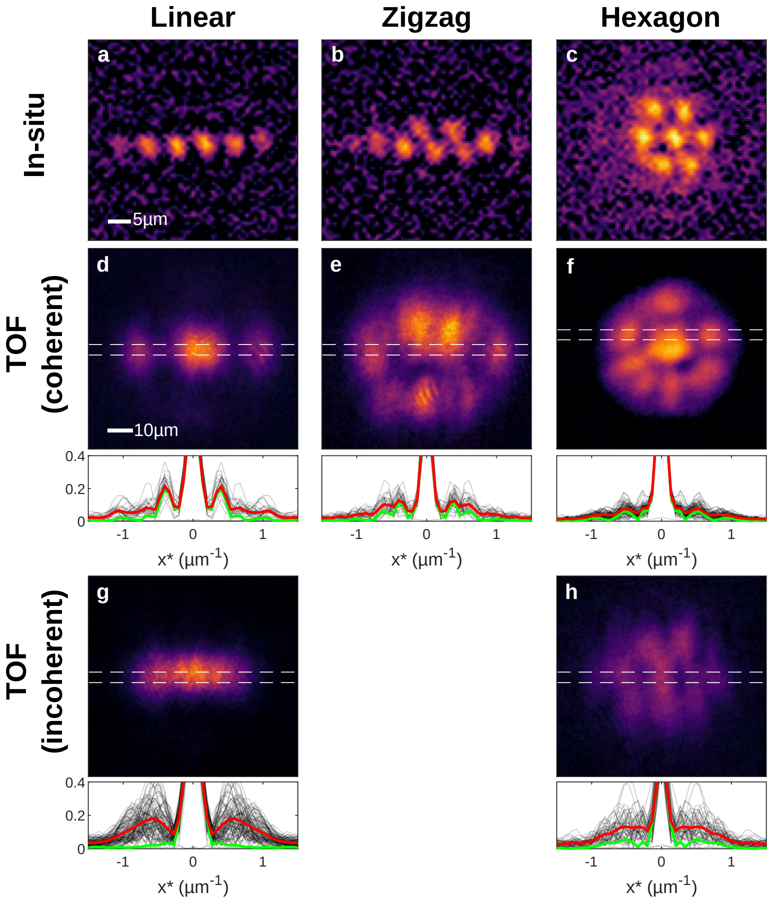

Figure 4.1: Experimental in-situ and TOF images of linear, zigzag and hexagonal supersolid states Top row: In-situ ($t_{\mathrm{TOF}} = 0.2\,\mathrm{ms}$) images of modulated states in different trap geometries resulting in a (a) linear, (b) zigzag and (c) hexagonal state. Middle row: Corresponding time-of-flight images ($t_{\mathrm{TOF}} = 36\,\mathrm{ms}$) averaged over 27-68 runs of a supersolid. Below: Normalised fourier transforms (FT) of the individual TOF images integrated along y between the dashed lines. The red and green line represent A_{M} and A_{ϕ} respectively. In the supersolid state the 'droplets' are coherent with each other and therefore A_{M} and A_{ϕ} are very similar. Bottom row: Corresponding time-of-flight images ($t_{\mathrm{TOF}} = 36\mathrm{ms}$) averaged over 46-89 runs of independent droplets. Below: The FT of the integrated density and A_{M} and A_{ϕ} are shown. In the ID state the droplets have an independent phase and therefore A_{M} and A_{ϕ} diverge strongly.

4.1 From 1D- to 2D-supersolids

We have already discussed in Sec. 3.1 that it is necessary for the nucleation of vortices to create the condensate in an almost axial-symmetric trap. We will also see in Sec. 4.2, that the roundness of the state plays a crucial role in quantifying the superfluid properties of the supersolid with the scissor mode measurements and that these axial-symmetric states exhibit a rich excitation spectrum.

From their first experimental observations [120, 122, 121] until the work described in this thesis, supersolids of dipolar gases have been produced exclusively in cigar-shaped traps, resulting in a one-dimensional density modulation[1] consisting of typically 2-6 droplets (see Fig. 4.1 a). In our recent experiments, we have been able to significantly increase the lifetime of supersolids with ^{164}Dy from a few hundred milliseconds to about a second [123] and were curious to see if we could advance supersolids beyond the one-dimensional array. We are particularly inspired by experiments with ions, which also assemble into arrays due to their strong repulsive Coulomb interactions. By loosening one of the tight trap directions, the ion systems undergo a structural transition from a single line, to a zigzag structure, to multiple lines of ions [262, 263, 264, 265]. Would we see a similar transition, if we go from a cigar shape towards a pancake-shape, where the magnetic field is along the tightest axis of the trap?

We find theoretical validation for a structural change of the supersolid that is reminiscent of ion experiments by performing eGPE simulations [266, 267]. The simulations show that the supersolid can also change from a linear chain to a zigzag to a multiple line structure. The difference between the ion systems and our supersolid is that the different droplets are composed of many atoms, which allows the droplet size to change, leading to interesting dynamics such as Goldstone modes [129]. Two-dimensional arrays promise even more complex dynamics as the degrees of freedom increase [118, 268, 126].

We can define the trap frequencies as $\omega_{\text{trap}} = (\omega_\perp, \omega_\perp/\alpha_t, \omega_z)$, where $\alpha_t \leq 1$ is the trap aspect ratio and the dipole direction is along the z-axis. To create a two-dimensional supersolid, there are a few more key factors important than just the trap aspect ratio:

- **The final state depends on the 2D density** [266]: For a fixed trap frequency ω_z along the magnetic field and a fixed dipole strength ε_{dd}, the resulting state can be assumed to remain in the supersolid state as long as the 2D density $\rho = \frac{N\omega_\perp^2}{4\pi^2\alpha_t}$ is constant. This means, that we have to compensate for an increase of α_t by increasing the total atom number of the system in order to obtain a supersolid in a pancake-shaped ODT. This can also be understood intuitively: There is a minimum atom number N_c needed for a self-bound droplet state [91]. If the density drops too low, this minimum number is not reached and no stable modulation is possible, leading to a transition back to the BEC state. Optimizing the atom number in the experiment to get to up to $N = 6.5(5) \times 10^4$ has been a major challenge.

- **Direct evaporation into a 2D supersolid reduces phase fluctuations compared to an interaction quench from a BEC into the 2D supersolid** [269]: A common technique to create supersolids is to condense the atoms into the BEC state and then perform an interaction quench into the supersolid regime. For the 1D supersolid this transition has only a weak first order character or may even be continuous, because the density pattern from the roton instability has a very similar wavenumber k_{rot} as the final density distribution of the supersolid [270, 271]. The situation changes for a two-dimensional supersolid. The modulation is seeded in the central high-density region and propagates outwards until the equilibrium state is reached. The final state has a significantly different $\mathbf{k} \neq k_{\text{rot}}$. This leads to phase fluctuations and global phase coherence is established only at about $t = 150\,\text{ms}$ after the quench [269], which is a significant part of the lifetime of the state. Additionally, crystal

---

[1] In this and the following chapters the terms "one-dimensional" and "two-dimensional" refer exclusively to the density structure (or crystal structure). The gas still has all three-dimensional degrees of freedom and is not in a quasi one- or two-dimensional confinement where the condition $\hbar\omega \gg k_{\text{B}}T$ is satisfied.

excitations are seen for up to $t = 300\,\text{ms}$. Here, further additional experimental effort could help to narrow down the dissipation parameter γ used in the theory and to better understand the mechanism in order to develop an analytical theory for the dissipation after the quench to the dipolar supersolids.

Instead, we evaporate directly into the supersolid state, where the global coherence is already established at about $t = 50\,\text{ms}$ [269]. We therefore prepare the thermal gas at $\varepsilon_{\text{dd}} > \varepsilon_{\text{dd,c}}$ and keep the magnetic field constant during evaporation. This method has already been shown to work well for the one-dimensional supersolid [123].

4.1.1 Probing the supersolid state

We measure the density modulation and the global phase coherence of the state separately:

Density modulation: To distinguish a supersolid or isolated droplet state from a Bose-Einstein condensate, we look at the in-situ density distribution of the state. While the BEC shows an unmodulated state defined by the Thomas-Fermi profile and a thermal background, the SS/ID state should show a modulated density profile on top of a superfluid background and a thermal part. Since the peak density of SS/ID systems is about one order of magnitude larger than that of the BEC state, we image it using phase contrast imaging, which allows us to see the high density region well, while the thermal and superfluid background are not visible beyond the background noise as can be seen in Fig. 4.1 a-c. The width of the density modulation is approximately $d = 5\,\mu$m which is well resolved by our objective discussed in Sec. 2.2.4.

To quantitatively characterize the modulated state we measure the number of droplets and the structure and geometry of the state. The number of droplets and the structure can be determined by using a peak finding algorithm and excluding all peaks below a certain threshold (40% of the highest peak value) to ignore peaks from the background fluctuations. We determine the aspect ratio of the state $\alpha_a = \sigma_l/\sigma_s$ by performing a 2D Gaussian fit to the state.

In the publication P2 we show that the structural transition from the linear array to a zigzag state appears as a discontinuity in α_a, where the critical trap aspect ratio is given by $\alpha_t^* \approx 0.34$ for our experimental parameters.

Global phase coherence: Once we know, that the state is modulated, we need to measure the global phase coherence to distinguish between the coherent SS state and the incoherent ID state. To obtain the relative phases between the droplets, we exploit the fact that this modulated state expands similarly to separated independent BECs: Expanding a SS/ID state during TOF leads to matter-wave interference between the different "droplets" and the resulting pattern gives us information about the relative phases (matter-wave interferometry [272]). This can be seen in Fig. 4.1 d-h. If the phase is globally coherent, the interference pattern should be repeatable for each shot (Fig. 4.1 d-f). On the other hand, if we are in the isolated droplet regime, each individual droplet acquires a unique phase independent of the rest of the state, leading to a varying interference pattern(Fig. 4.1 g-h).

The interference pattern also depends on the density distribution of the state. In anisotropic traps $\alpha_t \neq 1$, the ground state crystal structure is generally non-degenerate and hence repeatable from shot to shot. However, it should be noted that in isotropic traps or near structural transitions the density distribution may fluctuate, making the determination of the phase coherence difficult.

We can quantify the density modulation and phase coherence by performing a fourier transform (FT) on the individual TOF images. This gives us a phasor $\tilde{P}_{\mathrm{i}}(x') = \mathcal{F}\left\{n_{\mathrm{i,TOF}}\,(x)\right\}$ from which we can calculate the incoherent $\tilde{A}_{\mathrm{M}}(x')$ and the coherent means $\tilde{A}_{\Phi}(x')$

$$\tilde{A}_{\mathrm{M}}(x') = \left\langle\left|\tilde{P}_i(x')\right|\right\rangle_i \qquad \tilde{A}_{\Phi}(x') = \left|\left\langle\tilde{P}_i(x')\right\rangle_i\right| \tag{4.1}$$

For the incoherent mean $\tilde{A}_{\mathrm{M}}(x')$ we remove the phase information of the modulation before averaging, giving us a peak at x'_{mod}. The coherent mean gives a peak at x'_{mod}, where the height of the peak gives us information about the repeatability of the interference pattern. In the case of the supersolid, both values should have a peak at finite x' while for isolated droplets the peak of the coherent mean should be strongly suppressed.

As shown in Fig. 4.1 d-h, we use this method to show the global coherence for the modulated state. To do this, we take a slice of the density profile after a TOF of $t_{\mathrm{TOF}} = 36$ ms and integrate the density profile to obtain a 1D dataset. There is a clear difference between the supersolid (Fig. 4.1 d-f) and isolated droplet cases (Fig. 4.1 g-h). Hence, we have shown that it is possible to create 2D supersolids with dipolar gases and opened the doors to study the superfluidity of the supersolid.

P2 Two-dimensional supersolidity in a dipolar quantum gas

The following manuscript has appeared in

Nature 596, 357–361 (2021)[2],
discussed in News & Views article: **Supersolids go two-dimensional** from Bruno Laburthe-Tolra
submitted 10 February 2021; published 18 August 2021.
DOI: 10.1038/s41586-021-03725-7

Matthew A. Norcia[1], Claudia Politi[1,2], Lauritz Klaus[1,2], Elena Poli[2], Maximilian Sohmen[1,2], Manfred J. Mark[1,2], Russell N. Bisset[2], Luis Santos[3] and Francesca Ferlaino[1,2]

[1] *Institut für Quantenoptik und Quanteninformation, Österreichische Akademie der Wissenschaften, 6020 Innsbruck, Austria*
[2] *Institut für Experimentalphysik, Leopold-Franzens-Universität, 6020 Innsbruck, Austria*
[3] *Institut für Theoretische Physik, Leibniz, Universität Hannover, Hanover, Germany*

For this publication, I (L.K.) contributed to works on the experiment together with M.A.N., C.P. and M.S., analysed the dysprosium data together with M.A.N., C.P. and M.S., and contributed to the interpretation of the results, as well as in writing of the manuscript together with all other authors.

---

[2] Here the preprint version is attached

arXiv:2102.05555v1 [cond-mat.quant-gas] 10 Feb 2021

Two-dimensional supersolidity in a dipolar quantum gas

Matthew A. Norcia,[1, *] Claudia Politi,[1, 2, *] Lauritz Klaus,[1, 2] Elena Poli,[2] Maximilian Sohmen,[1, 2] Manfred J. Mark,[1, 2] Russell Bisset,[2] Luis Santos,[3] and Francesca Ferlaino[1, 2, †]

[1] *Institut für Quantenoptik und Quanteninformation,*
Österreichische Akademie der Wissenschaften, Innsbruck, Austria
[2] *Institut für Experimentalphysik, Universität Innsbruck, Austria*
[3] *Institut für Theoretische Physik, Leibniz Universität Hannover, Germany*

(Dated: February 11, 2021)

Supersolidity — a quantum-mechanical phenomenon characterized by the presence of both superfluidity and crystalline order — was initially envisioned in the context of bulk solid helium, as a possible answer to the question of whether a solid could have superfluid properties [1–5]. While supersolidity has not been observed in solid helium (despite much effort)[6], ultracold atomic gases have provided a fundamentally new approach, recently enabling the observation and study of supersolids with dipolar atoms [7–16]. However, unlike the proposed phenomena in helium, these gaseous systems have so far only shown supersolidity along a single direction. By crossing a structural phase transition similar to those occurring in ionic chains [17–20], quantum wires [21, 22], and theoretically in chains of individual dipolar particles [23, 24], we demonstrate the extension of supersolid properties into two dimensions, providing an important step closer to the bulk situation envisioned in helium. This opens the possibility of studying rich excitation properties [25–28], including vortex formation [29–31], as well as ground-state phases with varied geometrical structure [7, 32] in a highly flexible and controllable system.

Ultracold atoms have recently offered a fundamentally new direction for the creation of supersolids — rather than looking for superfluid properties in a solid system like ^{4}He, ultracold atoms allow one to induce a crystalline structure in a gaseous superfluid, a system which provides far greater opportunity for control and observation. This new perspective has enabled supersolid properties to be observed in systems with spin-orbit coupling [33] or long-range cavity-mediated interactions [34], though in these cases the crystalline structure is externally imposed, yielding an incompressible state. In contrast, dipolar quantum gases of highly magnetic atoms can spontaneously form crystalline structure due to intrinsic interactions [11–13], allowing for a supersolid with both crystalline and superfluid excitations [14–16]. In these demonstrations, supersolid properties have only been observed along a single dimension, as a linear chain of phase-coherent "droplets", i.e. regions of high density connected by low-density bridges of condensed atoms, confined within an elongated optical trap.

The extension of supersolidity into two dimensions is a key step towards creating an ultracold gas supersolid that is closer to the states envisioned in solid helium. Compared to previous studies of incoherent two-dimensional dipolar droplet crystals [8, 35], we work with both a substantially higher atom number N and relatively strong repulsive contact interactions between atoms. This leads to the formation of large numbers of loosely bound droplets, enabling us to establish phase coherence in two dimensions. In our system, the repulsive dipolar interactions between droplets facilitate a structural transition from a linear to a two-dimensional array, analogous to the Coulomb-interaction-mediated structural phase transitions observed with ions [17–20]. Unlike ions however, our droplets are compressible and result from the spontaneous formation of a density wave, allowing for dynamical variation in both droplet number and size. Further, the exchange of particles between droplets enables the spontaneous synchronization of the internal phase of each droplet across the system, and the associated superfluid excitations [14–16].

Dipolar quantum gases exhibit a rich set of ground- and excited-state phenomena due to the competition between many energetic contributions. These include mean-field interactions of both contact and dipolar nature, quantum fluctuations, and external confinement, parameterized by potentially anisotropic trapping frequencies $f_{x,y,z}$. Such systems can be described with great accuracy by using an extended Gross–Pitaevskii equation (eGPE) [36–39]. Even a fine variation of the

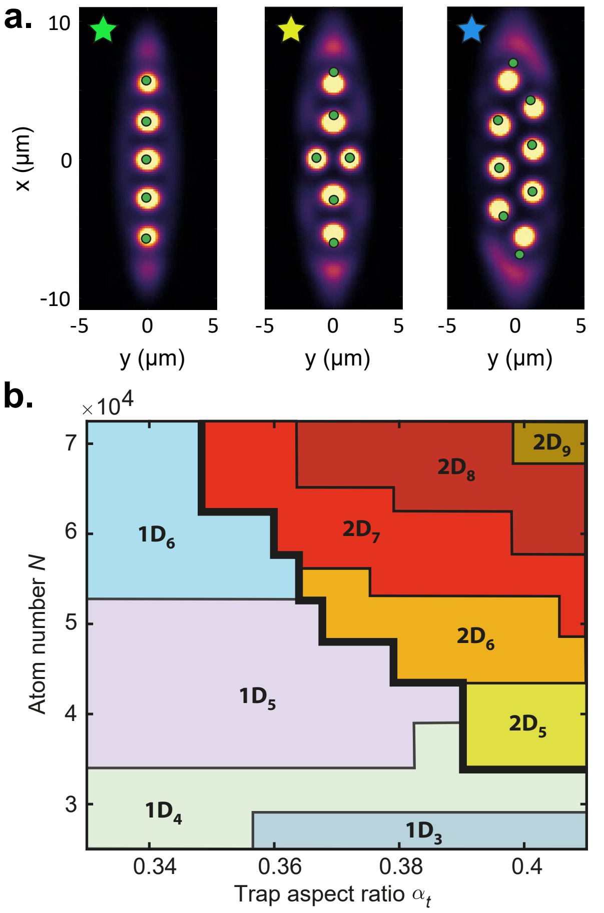

FIG. 1. **Calculated phases of dipolar droplet array. a.** In-trap ground-state density profiles calculated using eGPE for atom numbers $N \in [3.3, 4.4, 5.8] \times 10^4$ in the droplets and trap aspect ratios $\alpha_t = f_x/f_y \in [0.33, 0.35, 0.39]$ (left to right). The scattering length $a = 88\,a_0$, where a_0 is the Bohr radius. Green dots depict the droplet positions obtained from the variational model, assuming the same N and droplet number N_D as the eGPE. Stars connect to experimentally observed density profiles in Fig. 2b. **b.** Phase diagram, obtained from our variational model, as a function of N and α_t for $f_x = 33\,\text{Hz}$, $f_z = 167\,\text{Hz}$. Linear (two-dimensional) phases with N_D droplets are labelled as 1D$_{N_D}$ (2D$_{N_D}$).

strength of these energetic contributions can lead to dramatic qualitative changes in the state of the system, for example enabling a transition from a uniform condensate to a supersolid, or in our present case, from a linear supersolid to a two-dimensional one.

Fig. 1a shows ground-state density profiles calculated across this transition using the eGPE at zero temperature. These profiles feature arrays of high-density droplets, immersed in a low-density coherent “halo” that establishes phase-coherence across the system. As the trap becomes more round, the initially linear chain of droplets acquires greater transverse structure, eventually forming a zig-zag state consisting of two offset linear arrays.

Although the eGPE has remarkable predictive power, full simulations in three dimensions are numerically intensive, making a global survey of the array properties as a function of our experimental parameters difficult. To overcome this limitation, we employ a variational ansatz that captures the key behavior of the system, and allows us to disentangle the competing energetic contributions. In this approach, we describe an array of N_D droplets by the wavefunction $\psi(\mathbf{r}) = \sum_{j=1}^{N_D} \psi_j(\mathbf{r})$, where the j–th droplet is assumed to be of the form: $\psi_j(\mathbf{r}) \propto \sqrt{N_j}\exp\left(-\frac{1}{2}\left(\frac{|\boldsymbol{\rho}-\boldsymbol{\rho}_j|}{\sigma_{\rho,j}}\right)^{r_{\rho,j}}\right)\exp\left(-\frac{1}{2}\left(\frac{|z-z_j|}{\sigma_{z,j}}\right)^{r_{z,j}}\right)$, interpolating between a Gaussian and a flat-top profile characteristic of quantum droplets [40]. For a given total number of atoms N and droplet number N_D, energy minimization provides the atom number N_j in each droplet, as well as their widths $\sigma_{\rho(z),j}$, exponents $r_{\rho(z),j}$, and positions $\boldsymbol{\rho}_j = (x_j, y_j)$. Repeating this energy minimization as a function of N_D gives the optimal number of droplets. This model provides a good qualitative description of the overall phase diagram (Fig. 1b), revealing that the interplay between intra-droplet physics and inter-droplet interaction results in a rich landscape of structural transitions as a function of the atom number and the trap aspect ratio $\alpha_t = f_x/f_y$.

Several trends are immediately visible from the phase diagram. Larger N and higher α_t generally produce states with larger numbers of droplets. Further, as with ions, a large number of droplets favors a 2D configuration, while tighter transverse confinement (small α_t) favors 1D [17–20]. A transition from 1D to 2D is thus expected when moving towards larger N or to higher α_t. In stark contrast to the case of ions, the number of droplets typically increases across the 1D to 2D transition, implying a first-order nature, while only narrow regions in the phase diagram may allow for a 1D-to-2D transition at constant droplet number.

The variational results are in excellent agreement with our eGPE numerics, in terms of predicting the qualitative structure of droplet array patterns, as shown in Fig. 1a. Slight discrepancies exist between the two theories regarding the predicted droplet positions and the location of the 1D-to-2D transition. This is likely because of the presence of the halo in the eGPE simulation (and presumably in the experiment), visible in Fig. 1a, which is not accounted for in the variational model. This halo appears to accumulate at the ends of the trap, pushing the droplets toward the trap center and likely increasing the effective trap aspect ratio experienced by the droplets.

To explore the 1D to 2D transition experimentally, we

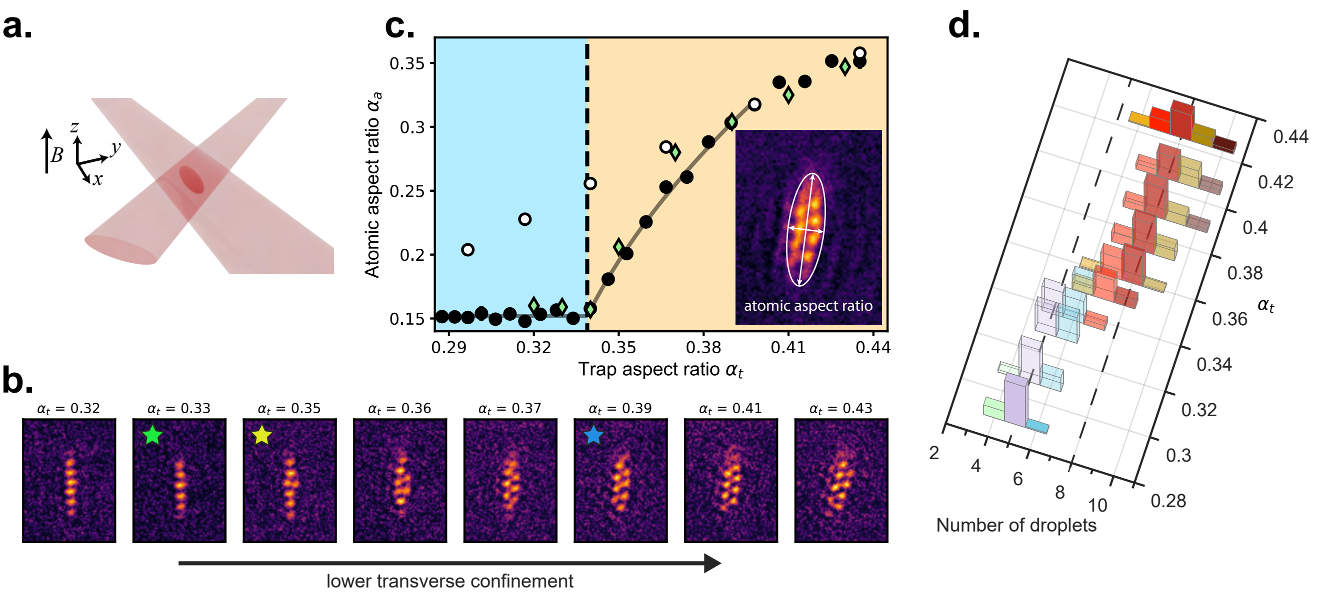

FIG. 2. **Linear to zig-zag transition in an anisotropic trap. a.** We confine and condense dipolar ^{164}Dy atoms within an anisotropic optical dipole trap (ODT) formed by the intersection of two laser beams. By tuning the aspect ratio of the trap in the x-y plane (α_t), perpendicular to an applied magnetic field B, we induce a transition between linear and zig-zag configurations of droplets. **b.** Single-trial images of the in-trap density profile of atoms at different α_t, showing structural transition from linear to zig-zag states, as well as an increase in droplet number for higher α_t. Stars indicate values α_t and N corresponding to the eGPE calculations of Fig. 1a. **c.** Atomic aspect ratio α_a versus trap aspect ratio α_t. α_a is the ratio of minor to major axes of a two-dimensional Gaussian fit to the imaged in-trap density profile (inset). For the supersolid droplet array (black markers) we see an abrupt change in α_a at the critical trap aspect ratio α_t^*, extracted from the fit (gray line, see methods). The shape of the transition agrees well with eGPE prediction (green diamonds, see methods). For an unmodulated condensate (white markers), no abrupt change is evident. **d.** Distribution of droplet number versus α_t, showing a distinct increase in droplet number at the transition of linear to zig-zag configurations.

use a condensate of highly magnetic ^{164}Dy atoms confined within an anisotropic optical dipole trap with independently tunable trap frequencies $f_{x,y,z}$. The trap, shown in Fig. 2a, is shaped like a surf-board with the tight axis along gravity and along a uniform magnetic field that orients the atomic dipoles and allows tuning of the contact interaction strength. Typically, we perform evaporation directly into our state of interest at our desired final interaction strength, as demonstrated in Refs. [13, 41]. A combination of in-trap and time-of-flight (TOF) imaging provides us with complementary probes of the density profile of our atomic states, and the phase coherence across the system.

We begin by studying the transition from one to two dimensions by changing the strength of transverse confinement provided by the trap. Our optical setup allows us to tune f_y from roughly 75 to 120 Hz, while leaving f_x, f_z nearly constant at 33(2), 167(1) Hz, and thus to vary the trap aspect ratio α_t in the plane perpendicular to the applied magnetic field and our imaging axis. For small α_t, the atoms are tightly squeezed transversely, and form a linear-chain supersolid (as seen in in-trap images of Fig. 2b). As we increase α_t above a critical value $\alpha_t^* = 0.34(2)$, we observe a structural phase transition to a two-dimensional (2D) state with two side-by-side droplets in the center of the chain. By further increasing α_t, the 2D structure extends to two offset lines of droplets in a zig-zag configuration. The observed patterns match well with the ground-state predictions from the eGPE calculations when we globally fix the scattering length to $88a_0$.

We obtain higher atom numbers in the more oblate traps (higher α_t), giving $N = 6.5(5) \times 10^4$ at $\alpha_t = 0.44$ and $N = 2.5(4) \times 10^4$ at $\alpha_t = 0.28$. This further facilitates the crossing of the 1D to 2D transition, by favoring states with larger numbers of droplets in the broader traps. In the zig-zag regime, two-dimensional modulation is clearly visible for durations beyond one second. Further, the droplet configuration patterns are fairly repeatable, with clear structure visible in averaged images

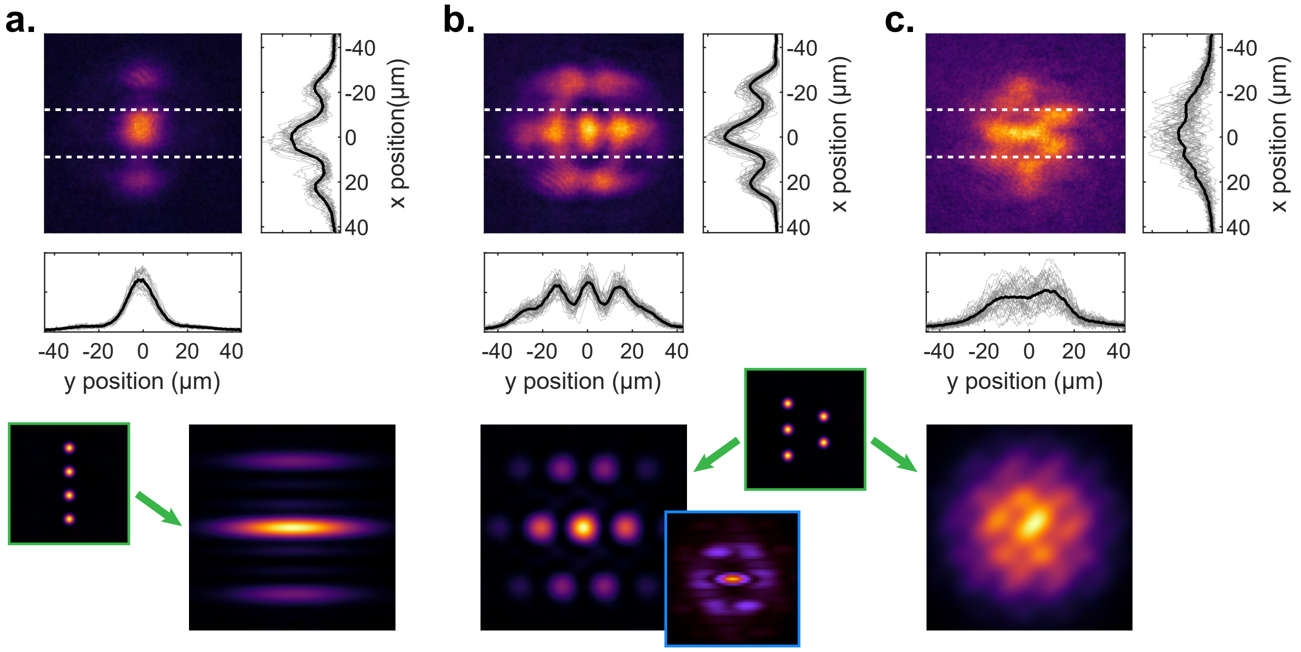

FIG. 3. **Coherence in linear and zig-zag states.** Upper panels show averaged images of experimental TOF interference patterns, along with projections along horizontal and vertical directions of average (solid black lines) and individual images (gray lines). The vertical projection is calculated between the dashed lines. Lower panels show interference patterns calculated for the pictured in-trap droplet configurations (green outlines). **a.** Linear chain of phase-coherent droplets, showing uniaxial modulation persisting in averaged image (26 trials). **b.** Zig-zag configuration of phase-coherent droplets, showing modulation along two directions that persists in averaged image (51 trials), and hexagonal structure. The spacing of rows in the simulation was adjusted to approximate the observed aspect ratio of TOF image. The image outlined in blue shows the average momentum distribution calculated from a series of 20 variational calculations converging to slightly different droplet configurations, showing the tendency of such fluctuations to broaden features in the interference pattern while maintaining the underlying structure. **c.** Zig-zag configuration of phase-incoherent droplets. Modulation remains in single images, as evidenced by the spread of gray traces in projection, but washes out in average (43 trials).

as shown in the inset of Fig. 2c, which is an average of 23 trials taken over roughly two hours.

The transition from 1D to 2D is immediately visible when plotting the atomic aspect ratio α_a versus α_t, as shown in Fig. 2c. We find that α_a undergoes a rapid change at α_t^*, as the single linear chain develops two-dimensional structure. For comparison, we plot α_a measured for an unmodulated BEC, formed at a different magnetic field, which does not feature the sharp kink present for the supersolid state.

In Fig. 2d, we show the number of droplets present for different α_t. In the 1D regime, we typically see between five and six droplets. This number abruptly jumps up by approximately one droplet for 2D states near the transition point, and then increases up to an average value of eight droplets as α_t is further increased. The change in droplet number indicates that the transition that we observe is not of simple structural nature, but is also accompanied by a reconfiguration of atoms within the droplets, as expected from theory (see Fig. 1).

The measurements of in-trap density presented above inform us about the structural nature of the transition, but not about phase coherence, which is the key distinguishing feature between an incoherent droplet crystal and a supersolid. Previous observations of 2D droplet arrays [35] were performed in traps where the ground state is a single droplet [8], and the observed droplet crystal was likely a metastable state lacking inter-droplet phase coherence. In contrast, we expect from our theoretical calculations that the 2D array is the ground state of our surfboard-shaped trap (for $\alpha_t > \alpha_t^*$), facilitating the formation of a phase-coherent, and therefore supersolid state for our experimental parameters.

We experimentally demonstrate the supersolid nature of our 2D modulated state using a matter-wave interference measurement, as previously used in linear supersolid chains [11–13], (Fig. 3a). In this measurement, an array of uniformly spaced droplets creates an interference pattern with spatial period proportional to the inverse of the in-trap droplet spacing. The relative internal phase of the droplets determines both the contrast and spatial phase of the interference pattern [42]. When averaging over many interference patterns, obtained on separate runs of the experiment, clear periodic modulation persists for phase-coherent droplets, but averages out if the relative droplet phases vary between experimental trials. Thus, the presence of periodic modulation in an average TOF image provides a clear signature of supersolidity in our system, as it indicates both periodic density modulation and phase coherence.

Figure 3a shows an example of such an averaged interference pattern for a linear chain. Uniaxial modulation is clearly present along the direction of the chain, indicating a high degree of phase coherence. For comparison, we also show the expected interference pattern calculated for a linear array of four droplets from free-expansion calculations, showing similar structure.

For conditions where in-trap imaging shows a 2D zig-zag structure, the averaged interference pattern exhibits clear hexagonal symmetry (Fig. 3b). This is consistent with our expectation, and is indicative of the triangular structure of the underlying state. To confirm that the observed modulation is not present without phase coherence, we repeat the measurement of Fig. 3b at a magnetic field corresponding to independent droplets, and also compute averaged interference pattern for a zig-zag state with the phases of the individual droplets randomized between simulated trials (Fig. 3c). In both cases, the averaged image does not show clear periodic modulation.

By exploiting the transition between linear and zig-zag states, we have accessed a regime where the supersolid properties of periodic density modulation and phase coherence exist along two separate dimensions. Future work will focus on further understanding the spectrum of collective excitations in the full two-dimensional system [26–28, 43], where both the crystalline structure and the exchange of particles between droplets will play an important role. Further investigations may elucidate in more detail the nature of the phase transitions and expected configurations in a wider range of trap aspect ratios, as well as the role that defects play in the 2D system, either as phase-slips in the zig-zag patterns [44, 45], or as vortices trapped between droplets of the array [29–31].

We thank the Innsbruck Erbium team and Blair Blakie for discussions. We acknowledge R. M. W. van Bijnen for developing the code for our eGPE ground-state simulations.

Author Contributions: M.A.N, C.P., L.K., M.S., M.J.M and F.F. contributed experimental work. E.P and R.B. performed eGPE calculations. L.S. contributed variational model. All authors contributed to interpretation of results and preparation of manuscript.

Funding: The experimental team is financially supported through an ERC Consolidator Grant (RARE, No. 681432), an NFRI grant (MIRARE, No. ÖAW0600) of the Austrian Academy of Science, the QuantERA grant MAQS by the Austrian Science Fund FWF No I4391-N. L.S and F.F. acknowledge the DFG/FWF via FOR 2247/PI2790. M.S. acknowledges support by the Austrian Science Fund FWF within the DK-ALM (No. W1259-N27). L.S. thanks the funding by the Deutsche Forschungsgemeinschaft (DFG, German Research Foundation) under Germany's Excellence Strategy – EXC-2123 QuantumFrontiers – 390837967. M.A.N. has received funding as an ESQ Postdoctoral Fellow from the European Union's Horizon 2020 research and innovation programme under the Marie Skłodowska-Curie grant agreement No. 801110 and the Austrian Federal Ministry of Education, Science and Research (BMBWF). M.J.M. acknowledges support through an ESQ Discovery Grant by the Austrian Academy of Sciences. We also acknowledge the Innsbruck Laser Core Facility, financed by the Austrian Federal Ministry of Science, Research and Economy. Part of the computational results presented have been achieved using the HPC infrastructure LEO of the University of Innsbruck.

---

[*] M. A. N. and C. P. contributed equally to this work.

[†] Correspondence should be addressed to Francesca.Ferlaino@uibk.ac.at

[1] E. P. Gross, Unified theory of interacting bosons, Phys. Rev. **106**, 161 (1957).

[2] E. P. Gross, Classical theory of boson wave fields, Annals of Physics **4**, 57 (1958).

[3] A. F. Andreev and I. M. Lifshitz, Quantum theory of defects in crystals, Sov. Phys. JETP **29**, 1107 (1969).

[4] G. V. Chester, Speculations on Bose–Einstein condensation and quantum crystals, Phys. Rev. A **2**, 256 (1970).

[5] A. J. Leggett, Can a solid be "Superfluid"?, Phys. Rev. Lett. **25**, 1543 (1970).

[6] M. H.-W. Chan, R. Hallock, and L. Reatto, Overview on solid 4 he and the issue of supersolidity, Journal of Low Temperature Physics **172**, 317 (2013).

[7] Z.-K. Lu, Y. Li, D. S. Petrov, and G. V. Shlyapnikov, Stable dilute supersolid of two-dimensional dipolar bosons, Phys. Rev. Lett. **115**, 075303 (2015).

[8] D. Baillie and P. B. Blakie, Droplet crystal ground states of a dipolar bose gas, Phys. Rev. Lett. **121**, 195301

(2018).

[9] S. M. Roccuzzo and F. Ancilotto, Supersolid behavior of a dipolar bose-einstein condensate confined in a tube, Phys. Rev. A **99**, 041601 (2019).

[10] M. Boninsegni and N. V. Prokof'ev, Colloquium: Supersolids: What and where are they?, Rev. Mod. Phys. **84**, 759 (2012).

[11] L. Tanzi, E. Lucioni, F. Famà, J. Catani, A. Fioretti, C. Gabbanini, R. N. Bisset, L. Santos, and G. Modugno, Observation of a dipolar quantum gas with metastable supersolid properties, Phys. Rev. Lett. **122**, 130405 (2019).

[12] F. Böttcher, J.-N. Schmidt, M. Wenzel, J. Hertkorn, M. Guo, T. Langen, and T. Pfau, Transient supersolid properties in an array of dipolar quantum droplets, Phys. Rev. X **9**, 011051 (2019).

[13] L. Chomaz, D. Petter, P. Ilzhöfer, G. Natale, A. Trautmann, C. Politi, G. Durastante, R. M. W. van Bijnen, A. Patscheider, M. Sohmen, M. J. Mark, and F. Ferlaino, Long-lived and transient supersolid behaviors in dipolar quantum gases, Phys. Rev. X **9**, 021012 (2019).

[14] M. Guo, F. Böttcher, J. Hertkorn, J.-N. Schmidt, M. Wenzel, H. P. Büchler, T. Langen, and T. Pfau, The low-energy goldstone mode in a trapped dipolar supersolid, Nature **574**, 386 (2019).

[15] G. Natale, R. M. W. van Bijnen, A. Patscheider, D. Petter, M. J. Mark, L. Chomaz, and F. Ferlaino, Excitation spectrum of a trapped dipolar supersolid and its experimental evidence, Phys. Rev. Lett. **123**, 050402 (2019).

[16] L. Tanzi, S. Roccuzzo, E. Lucioni, F. Famà, A. Fioretti, C. Gabbanini, G. Modugno, A. Recati, and S. Stringari, Supersolid symmetry breaking from compressional oscillations in a dipolar quantum gas, Nature **574**, 382 (2019).

[17] G. Birkl, S. Kassner, and H. Walther, Multiple-shell structures of laser-cooled 24 mg+ ions in a quadrupole storage ring, Nature **357**, 310 (1992).

[18] M. G. Raizen, J. M. Gilligan, J. C. Bergquist, W. M. Itano, and D. J. Wineland, Ionic crystals in a linear paul trap, Phys. Rev. A **45**, 6493 (1992).

[19] S. Fishman, G. De Chiara, T. Calarco, and G. Morigi, Structural phase transitions in low-dimensional ion crystals, Phys. Rev. B **77**, 064111 (2008).

[20] E. Shimshoni, G. Morigi, and S. Fishman, Quantum zigzag transition in ion chains, Phys. Rev. Lett. **106**, 010401 (2011).

[21] W. K. Hew, K. J. Thomas, M. Pepper, I. Farrer, D. Anderson, G. A. C. Jones, and D. A. Ritchie, Incipient formation of an electron lattice in a weakly confined quantum wire, Phys. Rev. Lett. **102**, 056804 (2009).

[22] A. C. Mehta, C. J. Umrigar, J. S. Meyer, and H. U. Baranger, Zigzag phase transition in quantum wires, Phys. Rev. Lett. **110**, 246802 (2013).

[23] G. E. Astrakharchik, G. Morigi, G. De Chiara, and J. Boronat, Ground state of low-dimensional dipolar gases: Linear and zigzag chains, Phys. Rev. A **78**, 063622 (2008).

[24] J. Ruhman, E. G. Dalla Torre, S. D. Huber, and E. Altman, Nonlocal order in elongated dipolar gases, Phys. Rev. B **85**, 125121 (2012).

[25] L. Santos, G. V. Shlyapnikov, and M. Lewenstein, Roton-maxon spectrum and stability of trapped dipolar bose-einstein condensates, Phys. Rev. Lett. **90**, 250403 (2003).

[26] S. Ronen, D. C. E. Bortolotti, and J. L. Bohn, Radial and angular rotons in trapped dipolar gases, Phys. Rev. Lett. **98**, 030406 (2007).

[27] R. M. Wilson, S. Ronen, J. L. Bohn, and H. Pu, Manifestations of the roton mode in dipolar bose-einstein condensates, Phys. Rev. Lett. **100**, 245302 (2008).

[28] R. N. Bisset, D. Baillie, and P. B. Blakie, Roton excitations in a trapped dipolar bose-einstein condensate, Phys. Rev. A **88**, 043606 (2013).

[29] A. Gallemí, S. M. Roccuzzo, S. Stringari, and A. Recati, Quantized vortices in dipolar supersolid bose-einstein-condensed gases, Phys. Rev. A **102**, 023322 (2020).

[30] S. M. Roccuzzo, A. Gallemí, A. Recati, and S. Stringari, Rotating a supersolid dipolar gas, Phys. Rev. Lett. **124**, 045702 (2020).

[31] F. Ancilotto, M. Barranco, M. Pi, and L. Reatto, Vortex properties in the extended supersolid phase of dipolar bose-einstein condensates, arXiv preprint arXiv:2012.15157 (2020).

[32] Y.-C. Zhang, F. Maucher, and T. Pohl, Supersolidity around a critical point in dipolar bose-einstein condensates, Phys. Rev. Lett. **123**, 015301 (2019).

[33] J.-R. Li, J. Lee, W. Huang, S. Burchesky, B. Shteynas, F. Ç. Top, A. O. Jamison, and W. Ketterle, A stripe

phase with supersolid properties in spin–orbit-coupled Bose-–Einstein condensates, Nature **543**, 91 (2017).

[34] J. Léonard, A. Morales, P. Zupancic, T. Esslinger, and T. Donner, Supersolid formation in a quantum gas breaking a continuous translational symmetry, Nature **543**, 87 (2017).

[35] H. Kadau, M. Schmitt, M. Wenzel, C. Wink, T. Maier, I. Ferrier-Barbut, and T. Pfau, Observing the rosensweig instability of a quantum ferrofluid, Nature **530**, 194 (2016).

[36] I. Ferrier-Barbut, H. Kadau, M. Schmitt, M. Wenzel, and T. Pfau, Observation of quantum droplets in a strongly dipolar bose gas, Phys. Rev. Lett. **116**, 215301 (2016).

[37] L. Chomaz, S. Baier, D. Petter, M. J. Mark, F. Wächtler, L. Santos, and F. Ferlaino, Quantum-fluctuation-driven crossover from a dilute bose-einstein condensate to a macrodroplet in a dipolar quantum fluid, Phys. Rev. X **6**, 041039 (2016).

[38] F. Wächtler and L. Santos, Quantum filaments in dipolar bose-einstein condensates, Phys. Rev. A **93**, 061603 (2016).

[39] R. N. Bisset, R. M. Wilson, D. Baillie, and P. B. Blakie, Ground-state phase diagram of a dipolar condensate with quantum fluctuations, Phys. Rev. A **94**, 033619 (2016).

[40] L. Lavoine and T. Bourdel, 1d to 3d beyond-mean-field dimensional crossover in mixture quantum droplets (2020), arXiv:2011.12394 [cond-mat.quant-gas].

[41] M. Sohmen, C. Politi, L. Klaus, L. Chomaz, M. J. Mark, M. A. Norcia, and F. Ferlaino, Birth, life, and death of a dipolar supersolid, arXiv preprint arXiv:2101.06975 (2021).

[42] Z. Hadzibabic, S. Stock, B. Battelier, V. Bretin, and J. Dalibard, Interference of an array of independent Bose–Einstein condensates, Phys. Rev. Lett. **93**, 180403 (2004).

[43] J.-N. Schmidt, J. Hertkorn, M. Guo, F. Böttcher, M. Schmidt, K. S. Ng, S. D. Graham, T. Langen, M. Zwierlein, and T. Pfau, Roton excitations in an oblate dipolar quantum gas, arXiv preprint arXiv:2102.01461 (2021).

[44] K. Pyka, J. Keller, H. Partner, R. Nigmatullin, T. Burgermeister, D. Meier, K. Kuhlmann, A. Retzker, M. B. Plenio, W. Zurek, *et al.*, Topological defect formation and spontaneous symmetry breaking in ion coulomb crystals, Nature communications **4**, 1 (2013).

[45] S. Ulm, J. Roßnagel, G. Jacob, C. Degünther, S. Dawkins, U. Poschinger, R. Nigmatullin, A. Retzker, M. Plenio, F. Schmidt-Kaler, *et al.*, Observation of the kibble–zurek scaling law for defect formation in ion crystals, Nature communications **4**, 1 (2013).

[46] A. Trautmann, P. Ilzhöfer, G. Durastante, C. Politi, M. Sohmen, M. J. Mark, and F. Ferlaino, Dipolar quantum mixtures of erbium and dysprosium atoms, Phys. Rev. Lett. **121**, 213601 (2018).

Methods

Experimental apparatus and protocols: Our experimental apparatus has been described in detail in Ref. [46]. Here, we evaporatively prepare up to $N = 6.5(5) \times 10^4$ condensed ^{164}Dy atoms in a crossed optical dipole trap formed at the intersection of two beams derived from the same 1064 nm laser, although detuned in frequency to avoid interference. One beam (the static ODT) has an approximately 60 µm waist. The second (the scanning ODT) has an 18 µm waist, whose position can be rapidly scanned horizontally at 250 kHz to create a variably anisotropic time-averaged potential. By tuning the power in each beam, and the scanning range of the scanning ODT, we gain independent control of the trap frequencies in all three directions. The two trapping beams propagate in a plane perpendicular to gravity, and cross at a 45° angle, which leads to the rotation of the zig-zag state at high α_t visible in Fig. 2b.

We apply a uniform magnetic field oriented along gravity and perpendicular to the intersecting dipole traps, with which we can tune the strength of contact interactions between atoms. This allows us to create unmodulated Bose-Einstein condensates, supersolid states, or states consisting of independent droplets at fields of $B = 23.2\,\mathrm{G}$, $17.92\,\mathrm{G}$, and $17.78\,\mathrm{G}$, respectively.

Details of our imaging setup are provided in Ref. [41]. In-trap and TOF images are performed along the vertical direction (along B and gravity), using standard phase-contrast and absorption techniques, respectively. The resolution of our in-trap images is approximately one micron. We use a 36 ms TOF duration for imaging interference patterns.

Atom number: We extract the condensed atom number N from absorption imaging performed along a horizontal direction in a separate set of experimental trials under otherwise identical experimental conditions. This allows for a larger field of view, and better fitting of thermal atoms. N is determined by subtracting the fitted thermal component from the total absorption signal.

For comparison between experiment and theory, and between the variational and eGPE theory methods, we associate N with the number of atoms in the droplets, and not in the diffuse halo that surrounds the droplets. From simulation of TOF expansion, we find that the halo is repelled at early expansion times, and is likely indistinguishable from the thermal cloud in our TOF measurements. While it is possible that some of the halo is counted in N, we neglect this possibility and assume that N includes only atoms within droplets.

Scattering length: The positions of phase boundaries between different droplet configurations are quite sensitive to the scattering length a, which is not known with high precision in our range of magnetic fields. For all theory, we use a value of $a = 88\,a_0$, where a_0 is the Bohr radius, as this value provides good agreement between experiment and theory for the 1D-to-2D transition point.

Extracting critical aspect ratio: The critical aspect ratio α_t^* is extracted from fit to the function $\alpha_a = \alpha_0$ for $\alpha_t < \alpha_t^*$, $\alpha_a = \sqrt{\alpha_0^2 + b(\alpha_t - \alpha_t^*)^2}$ for $\alpha_t > \alpha_t^*$, where α_t^*, α_0, and b are fit parameters. The error bars reported in Fig. 2c represent the standard error on the mean, and are smaller than the markers on most points.

Interference patterns: The predicted interference patterns of Fig. 3 are calculated by assuming free expansion of Gaussian droplets. In reality, the droplets are probably not Gaussian, and interactions during TOF expansion may modify the interference pattern. However, the droplet shape primarily effects the envelope of the interference pattern, which is not our primary interest here, and from eGPE simulations, we expect the effects of interactions to be minor, provided that the droplets become unbound in a time short compared to the TOF, which we verify by both looking at shorter TOFs and comparing the fringe spacing observed in TOF with that expected from the in-trap droplet spacing. The positions and size of the droplets are tuned to provide illustrative interference patterns.

Droplet number: We extract the droplet number from our in-trap images using a peak-finding algorithm applied to smoothed images. The algorithm finds the local maxima above a threshold, which is chosen to be 40% of the overall peak value. Each in-trap density distribution is classified as linear array or 2D zig-zag based on the atomic aspect ratio. Finally, the counts with a given droplet number are normalized by the total number of trials to get the probability shown in Fig. 2d. Fluctuations in the number of atoms in a given trial can push droplets above or below the threshold value, contributing to the spread in extracted droplet number for a given α_t.

4.2 Can we measure the superfluid fraction with the scissors mode?

Leggett suggested in his paper "Can a solid be 'superfluid'?" [81], that the moment of inertia of the proposed supersolid should be measured to show its superfluid character. He considered an annular container[3] of solid He-4. When a classical solid is rotated, the moment of inertia is easily calculated by $\Theta_{\text{rig}} = \text{NmR}^2$, where N is the number of atoms inside the ring, m is the mass of a single atom and R is the radius of the ring. However, if the solid also has superfluid characteristics, the moment of inertia reduces. He named the new 'reduced' value a non-classical moment of inertia (NCMI). In the case of a ring geometry, the change in moment of inertia can quantify the superfluid fraction of the system according to [81]

$$\Theta_{\text{NCMI}} = (1 - f_s)\Theta_{\text{rig}} \tag{4.2}$$

Leggett also showed, that the upper limit of the superfluid fraction is given by

$$f_s \leq \left[\frac{1}{2\pi}\int_0^{2\pi}\frac{d\theta}{\rho\left(\theta\right)/\rho_0}\right]^{-1} \tag{4.3}$$

depending on the ratio of modulated $\rho(\theta)$ and the unmodulated ρ_0 density distribution [81, 273]. This limit connects smoothly between a classical solid $f_s = 0$ and a homogeneous BEC $f_s = 1$. It is reasonable to assume that (4.3) is also applicable to supersolids in cigar- and pancake-shaped traps [131], so this means that f_s should be clearly distinguishable for the ID, SS and BEC state. And we can measure f_s by measuring the moment of inertia of our system. However, the situation turns out to be much more complex since the change of geometry between BEC and 1D-SS also introduces a structural change in the moment of inertia, giving rise to misleading observations [131, 274].

In general, one can measure the moment of inertia, by exciting the rotational modes and measuring its frequencies. We assume, that the excitation of the system is done by a small perturbations, e.g. perturbations of the external potential δV_{ext}. Different modes n are populated and the spectrum is described by the dynamical structure factor [95]

$$S(L_z,\omega) = \sum_n |\langle n|\hat{L}_z|0\rangle|^2\delta(\hbar\omega - \hbar\omega_n) \tag{4.4}$$

where $|\langle n|\hat{L}_z|0\rangle|^2$ is the coupling between the unperturbed state and a given mode n, where ω_n is its resonance frequency. Here we explicitly look for rotational modes coupled by $\hat{L}_z$ as suggested by Leggett.

4.2.1 Relation between scissors mode and moment of inertia

The relation between the structure factor and the moment of inertia is given by [274]

$$\Theta = 2\int d\omega\frac{S(L_z,\omega)}{\omega} \tag{4.5}$$

---

[3] with negligible width d

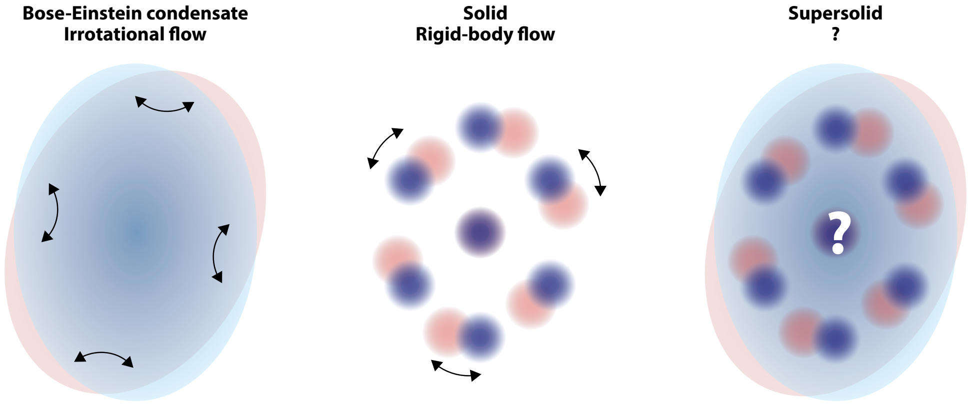

Figure 4.2: How does a supersolid respond to rotation? The flow of superfluids, such as interacting Bose-Einstein condensates, is irrotational. This leads to the scissor mode for small rotational perturbations. Solids, on the other hand, move as rigid bodies. Understanding the flow of a supersolid can give insight into its superfluid nature.

following from the static linear response of the system to a perturbation of the form $-\Omega L_z$. Since we cannot resolve the mode spectrum completely experimentally, we do not have full access to the structure factor. However, using the sum-rule approach we find a relation between the moments of the response and the minimum response frequency ω_{min} [95]

$$(\hbar\omega_{\text{min}})^2 \leq \frac{m_1(L_z)}{m_{-1}(L_z)} \tag{4.6}$$

where m_p are the energy weighted moments $m_p(L_z) = \int d\omega\omega^p S(L_z,\omega)$. The relation (4.4) gives us an upper bound on the frequency ω_{min} of the lowest state excited by the angular momentum operator $\hat{L}_z$. From Eq. (4.5) we find a direct relation between the inverse energy weighted moment $m_{-1}(L_z)$ and the moment of inertia Θ [275]

$$2m_{-1}(L_z) = N\Theta \tag{4.7}$$

with N the condensed atom number.

On the other hand, the energy weighted moment m_1 for a harmonically confined gas is described by [275]

$$2m_1(L_z) = \left\langle \left[\hat{L}_z, \left[\hat{H}, \hat{L}_z\right]\right] \right\rangle = N\hbar^2 m \left(\omega_y^2 - \omega_x^2\right) \left\langle x^2 - y^2 \right\rangle \tag{4.8}$$

where m is the mass of the atoms, $\omega_{x/y}$ are the trap frequencies in the the long and the short directions of the anisotropic trap respectively, and x and y are defined along the trap axes. In systems with dipolar interactions, Eq. (4.8) is only valid if the component $\hat{L}_z$ is along the direction of the dipole moment and therefore $\left[\sum_{ij} V_{\text{dd}}\left(\mathbf{r}_i - \mathbf{r}_j\right), \hat{L}_z\right]$ commutes.

Combining Eq. (4.6) with Eq. (4.8) and (4.7) leads finally to

$$\omega_{min}^2 \leq \frac{m\left(\omega_y^2 - \omega_x^2\right)\left\langle x^2 - y^2\right\rangle}{\Theta} \tag{4.9}$$

Therefore measuring the lowest frequency mode excited by $\hat{L}_z$ gives an upper bound on the moment of inertia and hence a lower bound on the superfluid fraction. But what is the lowest frequency mode we need to measure? Studies of non-dipolar BECs have shown that the mode corresponding to ω_{min} is the scissors mode [276]. The scissors mode is a shape-conserving, collective oscillation of the atoms, after a sudden rotation of the cloud. It is defined by a counterflow velocity field of $\mathbf{v}(x, y) \propto \nabla xy$. The systems that we are studying are different from system envisioned by Leggett in that we are not studying perfectly round annular, but depending on our trap geometries, the structure of the supersolid varies between almost round and highly elongated. The geometry of the system plays a crucial role for the moment of inertia of the system and can be described in a phenomenological way [275, 131]

$$\Theta = \left(1 - f_{\mathrm{NCRI}}\right)\Theta_{\mathrm{rig}} + f_{\mathrm{NCRI}}\beta^2\Theta_{\mathrm{rig}} \tag{4.10}$$

with the geometric factor $\beta = \frac{\langle y^2 - x^2\rangle}{\langle y^2 + x^2\rangle}$, where the first term is given by (4.2) and the second term describes the moment of inertia for superfluid systems in elliptic geometries.

Note, that even though one compares the moment of inertia of the SS and BEC state in the same trap geometry α, the geometric factor β of the supersolid can be significantly larger than of the BEC. An example is given in Fig. 4.3, where for a trap with $\alpha = 0.828(9)$ the BEC state was to be measured at $\beta = 0.806(4)$ and the SS was measured at $\beta = 0.901(4)$. If one would assume that both states have purely non-classical (irrotational) rotational inertia (NCRI) $f_{\mathrm{NCRI}} = 1$ and would insert the values of β into Eq. (4.10), one would find a significant difference in the moment of inertia for the BEC ($\Theta_{\mathrm{BEC}} = 0.650(7)\Theta_{\mathrm{rig}}$) and SS ($\Theta_{\mathrm{SS}} = 0.821(7)\Theta_{\mathrm{rig}}$) and could misinterpret the larger moment of inertia of the SS as a sign of a lower superfluid fraction.

The importance of the geometry can also be seen by inserting (4.10) into (4.9) and realising that the scissor mode frequency is bound between the case of purely classical (rigid) moment of inertia ($f_{\mathrm{NCRI}} = 0$) ω_{rig} and the case of NCRI ($f_{\mathrm{NCRI}} = 1$) ω_{irr}

$$\omega_{\mathrm{rig}} = \sqrt{(\omega_y^2 - \omega_x^2)\beta} \quad \omega_{\mathrm{irr}} = \sqrt{(\omega_y^2 - \omega_x^2)/\beta} \tag{4.11}$$

The scissors mode frequencies is then $\omega_{\mathrm{rig}} < \omega_{\mathrm{SS}} < \omega_{\mathrm{irr}}$ and Eq. (4.11) shows that ω_{rig} and ω_{irr} are indistinguishable for $\beta = 1$ and grow continously appart for $\beta \longrightarrow 0$. The scissor mode frequencies have been measured for supersolids in elongated cigar-shaped traps, where $\beta \approx 1$ [131]. In this case we see from Eq. (4.11) that the region $\omega_{\mathrm{rig}} < \omega_{\mathrm{SS}} < \omega_{\mathrm{irr}}$ becomes vanishingly small and therefore difficult to measure, as shown by the large error bars in [131]. Therefore, measuring the scissor mode frequencies in two-dimensional supersolids with $\beta \ll 1$ should provide a clearer distinction between a rigid and an irrotational response.

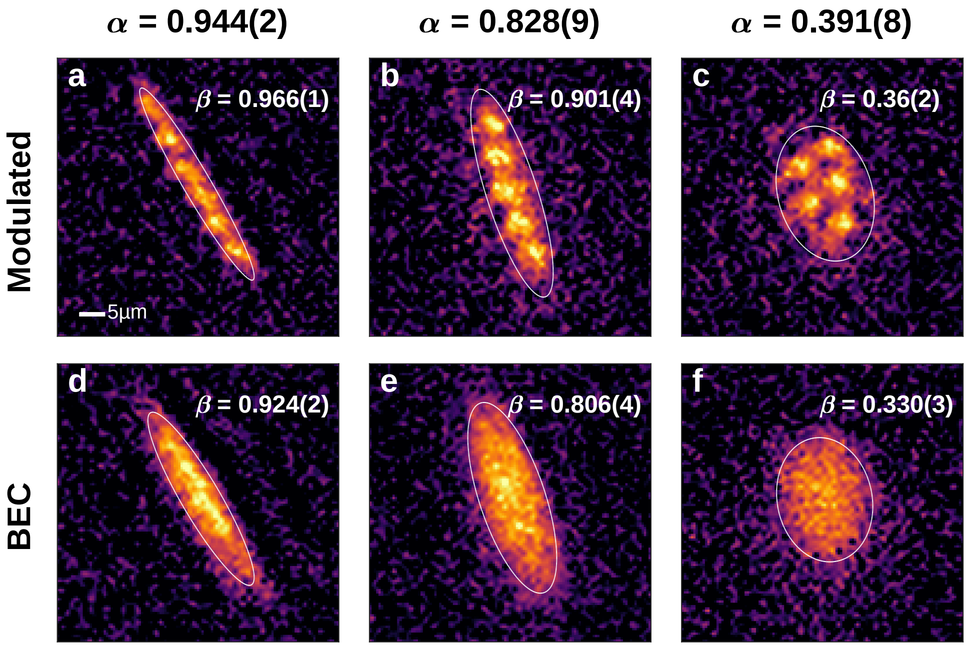

Figure 4.3: Comparison of β between modulated and BEC state for different trap aspect ratios α. In-situ images of the modulated (a,b,c) and BEC (d,e,f) states for different trap geometries $\alpha = \left|\frac{\omega_y^2-\omega_x^2}{\omega_y^2+\omega_x^2}\right| = [0.944(2), 0.828(9), 0.391(8)]$. The clouds are fitted with a 2D Gaussian fit and the contours of it are shown at 34.1%. The resulting geometric factor β shows, that the modulated state is generally much more elongated than the BEC state.

4.2.2 Complex rotational dynamics

In our experiment, we prepare BEC and modulated states in traps with variable geometry α. We apply a kick to the condensed state by varying the power of the three ODT beams for 6 ms before returning the power to the original value. Because the scanning ODT beam being crossed at an angle $\alpha = 45^\circ$ we get a perturbation of the external potential of $\delta V_{\text{ext}} \propto \sin(\alpha)\cos(\alpha)xy \neq 0$, which naturally excites the scissors mode [95]. However, it should be noted that with our excitation protocol, we cannot avoid additional excitations such as compressible modes. The scissors mode frequency is measured by taking in-situ images along the rotation axis, fitting a 2D-Gaussian to the cloud and extracting the angle θ from the fit. These data points result in a damped oscillation and the frequency can be extracted by fitting a simple damped oscillator model

$$\theta(t; \varepsilon_{\text{dd}}, \beta) = \theta_0 \sin(\omega_{\text{sci}}(\varepsilon_{\text{dd}}, \beta)t + \phi_0)\exp\{-\lambda t\} \tag{4.12}$$

where θ_0 and ϕ_0 are the initial angular deflection and phase of the shape oscillation respectively, and λ the damping factor. To change the between the modulated and the unmodulated state we tune the interactions ε_{dd} by controlling the magnetic field. And we modify β by adjusting the trap frequencies, changing the relative powers of the dipole trap beams. We measure the oscillation frequencies for the different states and varying geometries and compare them with the limiting cases (4.11) seen in Fig. 2 of the paper.

Initially we were puzzled by the experimental results. While we measured the frequency of the scissors mode in the BEC case to be in good agreement with the limiting case ω_{irr}, we would have expected to find the frequencies for the modulated state to be significantly lower, especially for nearly round geometries. Instead we find that we measure very similar frequencies and the experimental results are further strengthened by corresponding eGPE simulations. We would therefore have to conclude that the moment of inertia is very similar for the modulated and the BEC cases.

The fallacy lies in assuming, that the scissor mode is the lowest energy mode. This is no longer generally true for the modulated state. To show this, we apply the Fourier Transform Image Analysis (FTIA) protocol – a model independent method for the analysis and visualization of the cloud dynamics – to both the experiment as well as the eGPE simulations. The dynamics of the system is recorded by taking images at fixed time steps $\Delta t_{\mathrm{exp}} = 1$ ms ($\Delta t_{\mathrm{theo}} = 3$ ms) and arrange them into a 3D data set, where the third axis is time. For the experimental data we take several repetitions per time step and average the images $n_{\mathrm{exp}}(t) = \sum_{i=1} n^{i}_{\mathrm{exp}}(t)/N^{t}_{\mathrm{img}}$, where N^{t}_{img} is the number of images for the time $t = m\Delta t_{\mathrm{exp}}$. We are only interested in looking at the density change, so we subtract the average over all time $n_{\mathrm{avg}} = \sum_{t=m\Delta t} n(t)/N_t + 1$ from each individual time step image $n_{\mathrm{res}}(t) = n(t) - n_{\mathrm{avg}}$, where N_t is the total number of time steps. We then Fourier transform the 3D data along the time axis $\tilde{n}_{\mathrm{res}}(f) = \sum_{j=0}^{N_t-1} n_{\mathrm{res}}(t) \exp\{-i2\pi f j \Delta t\}$, which gives us density profiles in the frequency space with a frequency step size of $\Delta f = 1/\Delta t$. The resulting residuals $\tilde{n}_{\mathrm{res}}(f)$ give us a direct representation of the different modes and their oscillation frequencies. In addition, we can extract the spectral power of the modes by simply integrating the absolute square of each residual $\mathrm{SP}(f) = \sum_{i,j} |\tilde{n}^{(i,j)}_{\mathrm{res}}(f)|^2$ at a given f, which represents the prominence of the specific mode, similar to the dynamic structure factor.

Looking at Fig. 4 of the paper we can see the results of this analysis. For the BEC case we can see, that the scissors mode is well visualised by the FTIA and that it is the dominant and lowest energy mode excited. Already in the elongated case for the modulated state, we see from the simulations that the mode becomes very complicated, since we can observe the dynamics of the individual droplets. However, this detail is lost in the experimental analysis, since each sequence gives a slightly different ground state and slightly different dynamics. We therefore concentrate on the results of the simulations. Here we see a multimodal response due to the crystal dynamics. While the scissors mode remains the most prominent mode, we find modes that are lower in energy than the scissors mode. It is particularly noteworthy, that both the supersolid as well as the independent droplet system exhibit a rotational mode, which is significantly lower than the lower bound given by ω_{rig}. Since ω_{rig} is only an upper bound anyway, this does not contradict the generality of the sum-rule approach.

We see that the dynamics of the supersolid is much more complex due to the additional crystal dynamics. One consequence is that the scissors mode is not a robust and easily applicable tool for obtaining information about the moment of inertia of the system and thus a measure of the superfluid property of the supersolid. Our work shows, that the difference in oscillation frequency shown in [131] is rather due to the change in geometry between the BEC and the supersolid for the same trap parameters. To obtain an accurate measure of the moment of inertia and therefore a quantitative measure of the superfluid character of the supersolid we need to be able to map out the mode spectrum more accurately. To do this we would either need to improve the repeatability in creating the exact same state (or better post-processing), look at the dynamics with non-destructive imaging (using for example phase contrast imaging [277]), or develop a technique to excite different modes in an isolated way (using for example SLMs [278, 279]). There is also progress in quantifying the superfluid fraction in 1D supersolids [132] and simulations for Leggetts original idea of supersolids in an annular [280].

While this study did not provide the holy grail of experimental proof of the superfluid character of the supersolid, it gives us access to study the multimodal response of the supersolid to rotational perturbations. Further work in this direction may shed more light on the dynamic behaviour of modulated quantum states [274]. To highlight the superfluid nature of the supersolid state unambiguously, we instead study a different quanum phenomenon: quantised vortices.

P3 Can angular oscillations probe superfluidity in dipolar supersolids?

The following manuscript has appeared in

Physical Review Letters 129, 040403 (2022),
submitted 17 November 2021; published 22 July 2022.
DOI: 10.1103/PhysRevLett.129.040403

Matthew A. Norcia[1], Elena Poli[2], Claudia Politi[1,2], Lauritz Klaus[1,2], Thomas Bland[1,2], Manfred J. Mark[1,2], Luis Santos[3], Russell N. Bisset[2], and Francesca Ferlaino[1,2]

[1] *Institut für Quantenoptik und Quanteninformation, Österreichische Akademie der Wissenschaften, 6020 Innsbruck, Austria*
[2] *Institut für Experimentalphysik, Leopold-Franzens-Universität, 6020 Innsbruck, Austria*
[3] *Institut für Theoretische Physik, Leibniz Universität Hannover, 30167 Hannover, Germany*

For this publication, I (L.K.) contributed to works on the experiment together with M.A.N. and C.P., analysed the dysprosium data together with M.A.N., C.P. and M.J.M, and contributed to the interpretation of the results, as well as in writing of the manuscript together with all other authors.

Can Angular Oscillations Probe Superfluidity in Dipolar Supersolids?

Matthew A. Norcia,[1] Elena Poli,[2] Claudia Politi,[1,2] Lauritz Klaus,[1,2] Thomas Bland,[1,2] Manfred J. Mark,[1,2]
Luis Santos,[3] Russell N. Bisset,[2] and Francesca Ferlaino[1,2,*]
[1]*Institut für Quantenoptik und Quanteninformation, Österreichische Akademie der Wissenschaften, Innsbruck 6020, Austria*
[2]*Institut für Experimentalphysik, Universität Innsbruck, Innsbruck 6020, Austria*
[3]*Institut für Theoretische Physik, Leibniz Universität Hannover, 30167 Hannover, Germany*

(Received 17 November 2021; revised 3 March 2022; accepted 6 June 2022; published 22 July 2022)

Angular oscillations can provide a useful probe of the superfluid properties of a system. Such measurements have recently been applied to dipolar supersolids, which exhibit both density modulation and phase coherence, and for which robust probes of superfluidity are particularly interesting. So far, these investigations have been confined to linear droplet arrays, which feature relatively simple excitation spectra, but limited sensitivity to the effects of superfluidity. Here, we explore angular oscillations in systems with 2D structure which, in principle, have greater sensitivity to superfluidity. In both experiment and simulation, we find that the interplay of superfluid and crystalline excitations leads to a frequency of angular oscillations that remains nearly unchanged even when the superfluidity of the system is altered dramatically. This indicates that angular oscillation measurements do not always provide a robust experimental probe of superfluidity with typical experimental protocols.

DOI: 10.1103/PhysRevLett.129.040403

Some of the most distinctive manifestations of superfluidity in ultracold quantum gases relate to their behavior under rotation. These include the presence of quantized vortices [1–3] and persistent currents in ring traps [4], as well as shape-preserving angular oscillations associated with a "scissors" mode [5]. Measurements of the scissors mode frequency have long been used to illuminate the superfluid properties of a variety of systems [6–11]. With the recent advent of dipolar supersolids [12–18]—states that possess both the global phase coherence of a superfluid and the spatial density modulation of a solid—the scissors mode provides a tempting way to quantify changes in superfluidity across the superfluid-supersolid transition [19,20]. Angular oscillations have also been used to search for superfluid properties in solid helium [21]. In this case, however, a change in oscillation frequency initially attributed to superfluidity was eventually traced, instead, to other reasons [22]. In this Letter, we study more deeply the connection between angular oscillations and superfluidity in dipolar supersolids to determine the extent to which such experiments can inform our understanding of superfluidity in these systems.

The goal of these angular oscillation measurements is to infer the flow patterns allowed for a given fluid. A superfluid is constrained by the single-valued nature of its wave function to irrotational flow (IF), while a nonsuperfluid system faces no such constraint and, in certain situations, may be expected to undergo rigid-body rotation (RBR). Prototypical velocity fields for angular oscillations under IF ($\vec{v} \propto \nabla xy$) and RBR ($\vec{v} \propto r\hat{\theta}$) are depicted in Figs. 1(a) and 1(b), respectively. The velocity field associated with angular rotation is related to the moment of inertia of the system and, thus, the frequency of angular oscillations.

The ability to distinguish between RBR and IF (and, thus, in principle, between a classical and superfluid

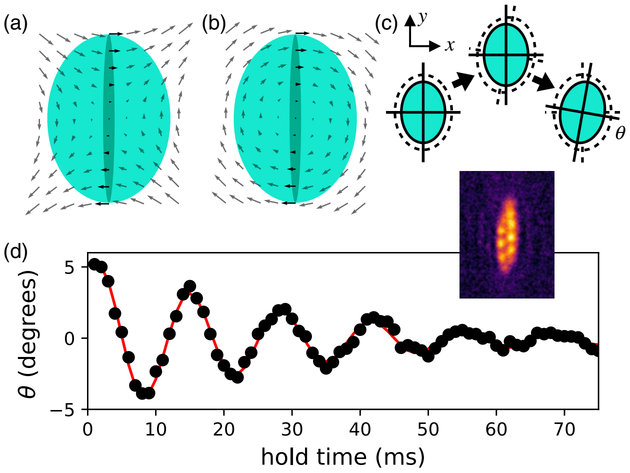

FIG. 1. Characteristic velocity profiles for irrotational flow (a) and rigid-body rotation (b). A wide atomic state (light turquoise oval) samples a region of space where the two differ significantly, while a highly elongated state (dark turquoise oval) samples a region where the two patterns are nearly indistinguishable. (c) We excite oscillations in the angle θ of our atomic gas by rapidly rotating the anisotropic trap (dashed oval), then returning it to its original orientation and observing the subsequent dynamics. (d) Typical example of experimental angular oscillation for the zigzag modulated state shown on the right (image averaged over nine iterations). In this case, the errors from the fit to the state angle are smaller than the markers. The red line is a damped sinusoidal fit used to extract the angular oscillation frequency f_{osc}.

system) depends critically on the geometry of the system, and is sensitive only to the character of the flow pattern where the atomic density is appreciable. As illustrated in Figs. 1(a) and 1(b), highly elongated states sample only the region along the weak axis of the trap (near $x = 0$) where IF and RBR are identical for small rotations (dark turquoise regions), while rounder states (light turquoise regions) sample regions of space where the flow patterns differ significantly and, thus, are far more sensitive to the irrotational constraint. Recent works have focused on systems that form a short linear chain of about two "droplets" [23] in the supersolid regime [19,20].

In this Letter, we study angular oscillations in systems with linear and two-dimensional modulation to disentangle the effect of three important contributions: (i) a narrowing of the aspect ratio of the gas (geometrical change), (ii) a reduction in the population of the low-density superfluid "halo" that occupies the outer regions of the trap, and (iii) a reduction in the density of the interdroplet connection that enables the exchange of atoms between droplets, which is key to the superfluid nature of supersolid systems. We find that, in linear systems, contributions (i) and (ii) dominate the change in oscillation frequency associated with the onset of modulation, while (iii) has a negligible effect.

In dipolar condensates with two-dimensional structure, which have been a focus of recent work [24–28], the effects of geometry and superfluidity may be disentangled, and one may expect to observe a direct link between a change of the superfluid fraction and a modification of the angular oscillation frequency. However, we find that the physics at play is much more complex. Indeed, not only does the oscillation frequency fail to approach its rigid-body value for states with a vanishing superfluid connection, but it remains very close to the value predicted for a superfluid state. We extensively investigate the system behavior as a function of geometry and interaction parameters, revealing a unique multimode response of the dipolar supersolid.

Experimentally, we use a dipolar quantum gas of ^{164}Dy atoms (up to approximately 5×10^4 condensed atoms), confined within an optical dipole trap (ODT) of tunable geometry, formed at the intersection of three laser beams [25,27,29]. The trap geometry and particle number at the end of the evaporative cooling sequence determine the character of the modulated ground state, which can form linear, zigzag, or triangular lattice configurations [28]. By varying the applied magnetic field in the vicinity of Feshbach resonances near 18–23 G, we can access scattering lengths that correspond to either unmodulated BECs or modulated states. In past works, we have demonstrated that modulated states created at the corresponding field have global phase coherence [25,27]. In this Letter, we expect the same to be true, but refer to these experimental states simply as modulated, as we do not repeat the characterization for every trap condition used. We excite angular oscillations by using the well-established protocol of applying a sudden small rotation of the trap, by varying the relative powers in the ODT beams for 6 ms before returning them to their original values [Fig. 1(c)]. Using our high-resolution imaging [30], we observe the in-trap density profile at a variable time from the excitation, and extract the angle of the major and minor axes using a two-dimensional Gaussian fit to the state [31].

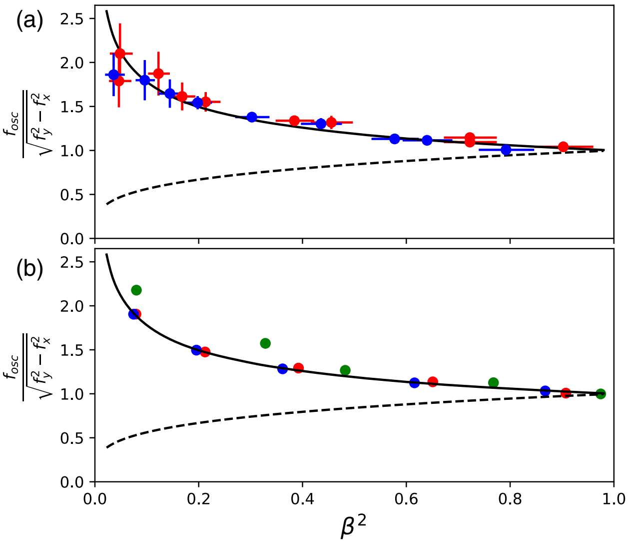

FIG. 2. Normalized oscillation frequencies f_{osc} from experiment (a) and simulation (b). Blue points represent unmodulated BECs, red points represent modulated states (expt.) and supersolid states (sim.), and green points represent independent droplet arrays. Solid lines are predictions for irrotational flow f_{irr}. Dashed lines are predictions for rigid body rotation f_{rig}. The trap frequencies used in the simulation, from left to right, are $(f_x, f_y) = [(43, 53), (40, 57), (37, 62), (32, 70), (26, 87)]$ Hz. $f_z = 122$ Hz for all cases. A similar range is used in the experiment.

A typical angular oscillation is shown in Fig. 1(d), for a "zigzag" modulated state [25]. From such oscillation traces, we extract the dominant oscillatory frequency f_{osc} using a fit to an exponentially damped sinusoid. Typically, the statistical error on our measurements of f_{osc} is on the sub-Hertz level, better than our knowledge of the trap frequencies, due to drifts between calibrations. We perform such measurements for trap geometries ranging from an elongated cigar shape to pancake shaped, and for different scattering lengths, as summarized in Fig. 2(a).

Within a single-mode approximation, the angular oscillation frequency f_{osc} can be predicted using either a sum-rule based approach [19,34], or considerations based on hydrodynamic flow [5]. For RBR, the angular oscillation frequency is given by $f_{\text{rig}} = \sqrt{(f_y^2 - f_x^2)\beta}$, whereas for IF, the predicted value is $f_{\text{irr}} = \sqrt{(f_y^2 - f_x^2)/\beta}$ [19,20]. Here, $f_{x,y}$ are the trap frequencies along directions x and y. $\beta = \langle x^2 - y^2 \rangle / \langle x^2 + y^2 \rangle$ is a geometrical factor that quantifies the degree of elongation of the atomic cloud (but carries no information about the superfluid fraction). As shown in Fig. 2, f_{rig} and f_{rig} are more distinct for smaller values of β. Remarkably, independent of trap geometry or the presence of modulation, we observe f_{osc} close to the IF prediction and far from the RBR prediction when the two predictions differ appreciably.

To gain a deeper understanding of our observations, we theoretically study the oscillation dynamics using a real-time simulation of the extended Gross-Pitaevskii equation (EGPE) [35–37]. To compare to the experimental observations of Fig. 2(a), first, we calculate the ground state for a given trap, scattering length, and atom number. Then, we apply a 0.5° rotation of the trap for 6 ms (we have confirmed that the character and frequency of the response do not change for much larger excitations), and then let the state evolve for 50 ms. Then, we perform the same fitting procedure as used in the experiment to extract f_{osc}. For the simulation, we calculate β directly for the ground state (we confirm that the exact value of β agrees with that extracted from a Gaussian fit at the 5% level). For simulations performed on states ranging from the unmodulated BEC to supersolid (SS) to independent droplet (ID) regimes, with vanishing superfluid connection between droplets, we again find that f_{osc} is always very close to f_{irr}, in very good agreement with the experimental data. For isolated droplet states in particular, f_{osc} can actually be even higher than the expected value for irrotational flow, indicating that the oscillation frequency is not necessarily in between the irrotational and rigid body values.

To further illuminate the dependence f_{osc} on superfluidity, we analyze the results of the simulation as a function of the s-wave scattering length a_s (Fig. 3). Scattering lengths of $85a_0$ yield arrays of (nearly) independent droplets, while $a_s = 97a_0$ produces an unmodulated BEC. In between, we find supersolid states, with low-density connections between droplets. Inspired by the formulation of Leggett [38], we quantify the degree of interdroplet density connection as $\mathcal{C} = [\int dx/\rho(x)]^{-1}$, where $\rho(x)$ is the projected atomic density, evaluated over the interdroplet connection [Fig. 3(a)] [39].

As shown in Fig. 3, despite the rapid reduction of $\mathcal{C}$ with a_s, the simulated f_{osc} exhibits a rather constant behavior with a value always close to the purely irrotational predictions, f_{irr}, for both a linear (1D) and hexagon state (2D). This observation indicates that (i) the degree of interdroplet connection is not actually a major determinant of the angular oscillation frequency and (ii) that the system does not undergo RBR even for vanishingly small interdroplet density connection. The latter conclusion is particularly evident for hexagon states, where the rigid-body prediction substantially departs from the irrotational one. For the linear array, the elongated geometry means that the f_{rig} and f_{irr} differ only slightly; see Supplemental Material for further discussion [31].

At this point, we can clearly see the geometrical limitations of the linear systems. In linear systems, the narrowing of the atomic density distribution that occurs with the onset of modulation causes the dominant contribution to a modification in oscillation frequency as well as a reduction in sensitivity of the oscillation frequency to superfluidity. Simultaneously, the transfer of atoms from the halo to the droplets leads to a reduction of the superfluidity of the composite halo-droplet system, which is accompanied by a small change in the oscillation frequency. However, because the motion induced by rotation in a linear system is perpendicular to the interdroplet axis, these effects should not be interpreted as a result of the weakening superfluid connection along the interdroplet axis. In contrast, systems with two-dimensional structure maintain a relatively round aspect ratio in the modulated regime, and the rotational motion does orient along certain interdroplet axes.

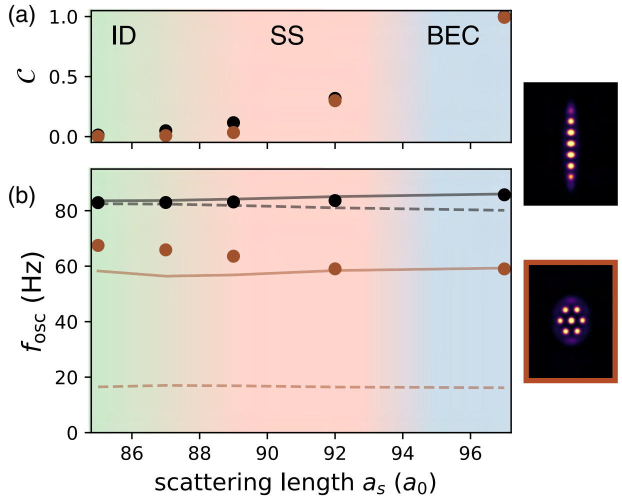

FIG. 3. Impact of scattering length on simulated scissors mode frequencies. (a) Interdroplet connection $\mathcal{C}$ (defined in text) versus scattering length for different trap geometries. The calculated ground state in each trap is shown on the right, with corresponding border colors. (b) Scissors mode frequency versus scattering length. Solid lines are predictions for irrotational flow f_{irr}. Dashed lines are predictions for rigid body rotation f_{rig}. β ranges from 0.93 to 0.99, and 0.27 to 0.31 in the linear and hexagonal cases, respectively.

To better understand the nonrigid nature of the angular oscillations, we employ a method to extract the character of the system's response by analyzing our experimental and EGPE simulation dynamics in the frequency domain with respect to time, but in the position domain with respect to the spatial coordinates. A similar technique has been applied along one dimension to understand the mode structure of an elongated condensate [40]. This technique, which for convenience we refer to as "Fourier transform image analysis" (FTIA) [31], allows us to extract a power spectrum of density fluctuations driven by the angular excitation, as well as the spatial form of the density fluctuations at each frequency. For comparison, we also

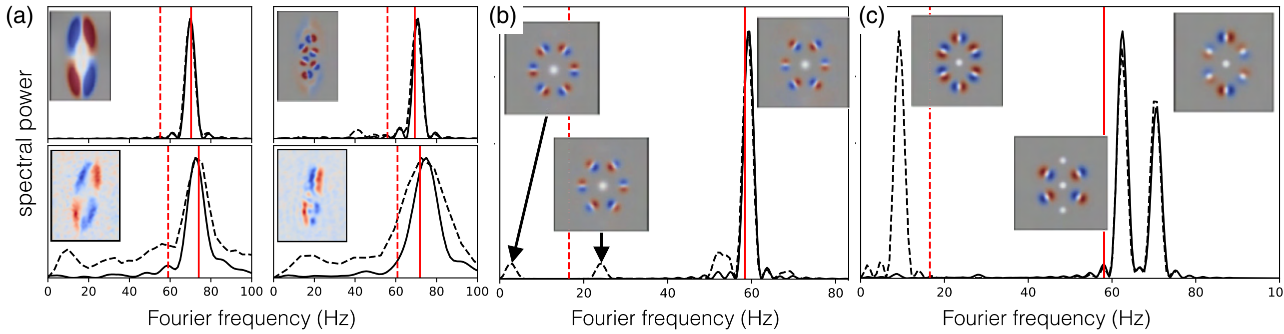

FIG. 4. Analysis of mode shapes and response due to angular excitation. Solid lines are the power spectrum obtained from the rotational signal (θ in the experiment and $\langle xy \rangle$ in the simulation), and dashed lines are obtained from FTIA (see text, Supplemental Material [31] for description). Inset panels show the mode shapes for selected modes. Red and blue indicate out-of-phase changes in density, overlaid onto the average density profile in the panels corresponding to simulation (gray to white). Solid and dashed vertical red lines represent f_{irr} and f_{rig}, respectively. (a) Responses in elongated traps from simulation (top) and experiment (bottom), for an unmodulated BEC (left) and a zigzag droplet state (right). Trap frequencies are $f_{x,y} = [31(1), 73(1), 128(1)]$ Hz, and $f_{x,y,z} = [32, 70, 122]$ Hz for the experiment and theory, respectively. (b) Simulated response of supersolid hexagon state ($a_s = 92a_0$). (c) Simulated response of droplet crystal hexagon state ($a_s = 85a_0$). Note that the ground state has a different orientation for the two scattering lengths in this trap. Trap frequencies are $f_{x,y,z} = [43, 53, 122]$ Hz for (b) and (c).

calculate the spectral power of our rotational signal through a Fourier transform. For computational robustness, we use the fitted angle θ in the experimental case, and $\langle xy \rangle$ for the simulations. To enhance our frequency resolution, we analyze simulations with longer durations than are accessible in the experiment (160 to 290 ms).

We apply the FTIA to both simulation and experimental images in Fig. 4(a). For a BEC, the FTIA gives a dominant peak in both simulation and experiment, whose frequency and shape are consistent with a scissors mode oscillation at the frequency observed from the angular response. For a zigzag modulated state, we again predominantly observe a single peak in the FTIA spectrum at the frequency of the angular oscillation. In the simulation, we can see that the mode corresponds to the motion of the different droplets in a pattern reminiscent of IF in an unmodulated superfluid, and clearly distinct from RBR. In the experiment, the response of individual droplets is not visible due to shot-to-shot fluctuations in the exact number and position of the droplets, but the overall structure is similar to the simulation.

For hexagonal supersolid [Fig. 4(b)] and isolated droplet [Fig. 4(c)] states, the FTIA reveals a clear multifrequency response. For the supersolid, we observe the excitation of modes near 3 and 25 Hz that do not contribute strongly to $\langle xy \rangle$. The droplet motion associated with the 3 Hz mode is approximately (but not exactly) shape preserving, and the frequency is much lower than would be expected for a single-mode RBR response. For the isolated droplet array, we again observe a nearly shape-preserving low-frequency response from FTIA, as well as a dominant angular response that is split into two frequencies, both above the scissors mode frequency f_{irr} expected for a superfluid with the same geometry. In the experiment, the combination of nonangular excitations associated with our method used to rotate the trap and relatively rapid damping of the oscillation prevent us from observing meaningful mode profiles for small β.

Importantly, the FTIA reveals that, even in cases where we observe an apparently single-frequency response in typical rotational observables like θ or $\langle xy \rangle$ [as in Figs. 4(a) and 4(b)], the response of the system may, in fact, be multimode in nature, breaking the single-mode approximation used to analytically extract f_{irr} and f_{rig} [19,34]. In the case of a multifrequency response, f_{irr} and f_{rig}, instead, provide an upper bound for the frequency of the lowest energy excitation—an excitation that is difficult to see with experimentally accessible observables. Features of these subdominant modes, including the lack of a strong rotational signal in the low-frequency oscillations and the apparent similarity between the droplet motion (the motion of the halo is quite different) near 25 Hz to that of the dominant rotational mode, remain interesting topics for future investigation.

As we have noted, not only does the dominant angular response frequency fail to approach the rigid-body value in the isolated droplet regime, but it also stays near to the irrotational prediction. A possible intuitive explanation for this observation is that the flow pattern of Fig. 1(a) resembles that of a quadrupolar surface mode, and it is well known that, for sufficiently strong interactions, the frequency of such modes is predominantly determined by the trap parameters, rather than the details of the interparticle interactions [34].

In conclusion, measurements of angular oscillation frequencies offer a simple way to demonstrate superfluidity in certain conditions. However, care must be taken when making and interpreting such measurements—geometrical changes can mask the effects of changing superfluidity, and usual predictions to which one might compare rely on the assumption of a single-frequency response of the lowest energy rotational mode. While the moment of inertia of the system is defined as the angular momentum of a system in response to a shape-preserving, steady-state drive, oscillation measurements involve a time-localized change in the rotation rate of the trap, which may excite modes that do not meet this criterion. In small, linear systems, the simple excitation spectra means that approximately shape-preserving oscillations can still be excited [31]. However, we find that a supersolid with 2D structure, which one might expect to be an ideal candidate for such measurements, can exhibit an apparently single-frequency response associated with a mode that is not the lowest in energy. Further, this excitation frequency is typically very close to that of a purely superfluid system, even for systems where the effects of superfluidity are minimal. Therefore, such measurements do not provide a robust indicator of superfluidity for modulated systems. In the future, it may be possible to extract information about superfluidity using a modified excitation scheme to preferentially excite the lower energy modes and a more comprehensive analysis scheme suitable for multifrequency response [41]. However, such techniques would require detailed knowledge of the exact excitation applied and measurement of response amplitudes, both of which are considerably more challenging in an experiment than measuring the frequency of an oscillation.

Finally, we note that, even in the case of single-frequency response, where the frequency of angular oscillations has a direct connection to the moment of inertia of the system, making a clear connection between the moment of inertia and quantities like a superfluid fraction can be problematic. Past works have predicted that a system which is partially superfluid should have a moment of inertia in between the RBR and IF predictions, linearly interpolated according to a superfluid fraction [20,38]. While this interpretation may be valid for systems featuring a rigid crystalline structure and a uniform distribution of crystalline and superfluid components, as in [38], it is not necessarily valid for our small dipolar supersolids, which, in addition to coupled superfluid-crystalline excitations, feature a nonuniform degree of modulation across the system.

We thank Sandro Stringari and Alessio Recati for useful discussions. We acknowledge R. M. W. van Bijnen for developing the code for our EGPE ground-state simulations. The experimental team is financially supported through an ERC Consolidator Grant (RARE, Grant No. 681432), an NFRI grant (MIRARE, Grant No. ÖAW0600) of the Austrian Academy of Science, the QuantERA grant MAQS by the Austrian Science Fund FWF Grant No. I4391-N. L. S. and F. F. acknowledge the DFG/FWF via Grant No. FOR 2247/PI2790. L. S. acknowledges funding by the Deutsche Forschungsgemeinschaft (DFG, German Research Foundation) under Germany's Excellence Strategy—Grant No. EXC-2123 QuantumFrontiers—390837967. M. A. N. has received funding as an ESQ Postdoctoral Fellow from the European Union's Horizon 2020 Research and Innovation Programme under the Marie Skłodowska Curie Grant Agreement No. 801110 and the Austrian Federal Ministry of Education, Science and Research (BMBWF). M. J. M. acknowledges support through an ESQ Discovery Grant by the Austrian Academy of Sciences. We also acknowledge the Innsbruck Laser Core Facility, financed by the Austrian Federal Ministry of Science, Research, and Economy. Part of the computational results presented have been achieved using the HPC infrastructure LEO of the University of Innsbruck.

---

[*]Corresponding author.
Francesca.Ferlaino@uibk.ac.at

[1] M. R. Matthews, B. P. Anderson, P. C. Haljan, D. S. Hall, C. E. Wieman, and E. A. Cornell, Vortices in a Bose-Einstein Condensate, Phys. Rev. Lett. **83**, 2498 (1999).

[2] K. W. Madison, F. Chevy, W. Wohlleben, and J. Dalibard, Vortex Formation in a Stirred Bose-Einstein Condensate, Phys. Rev. Lett. **84**, 806 (2000).

[3] M. W. Zwierlein, J. R. Abo-Shaeer, A. Schirotzek, C. H. Schunck, and W. Ketterle, Vortices and superfluidity in a strongly interacting Fermi gas, Nature (London) **435**, 1047 (2005).

[4] A. Ramanathan, K. C. Wright, S. R. Muniz, M. Zelan, W. T. Hill, C. J. Lobb, K. Helmerson, W. D. Phillips, and G. K. Campbell, Superflow in a Toroidal Bose-Einstein Condensate: An Atom Circuit with a Tunable Weak Link, Phys. Rev. Lett. **106**, 130401 (2011).

[5] D. Guéry-Odelin and S. Stringari, Scissors Mode and Superfluidity of a Trapped Bose-Einstein Condensed Gas, Phys. Rev. Lett. **83**, 4452 (1999).

[6] D. Bohle, A. Richter, W. Steffen, A. Dieperink, N. L. Iudice, F. Palumbo, and O. Scholten, New magnetic dipole excitation mode studied in the heavy deformed nucleus ^{156}GD by inelastic electron scattering, Phys. Lett. **137B**, 27 (1984).

[7] O. M. Maragò, S. A. Hopkins, J. Arlt, E. Hodby, G. Hechenblaikner, and C. J. Foot, Observation of the Scissors Mode and Evidence for Superfluidity of a Trapped Bose-Einstein Condensed Gas, Phys. Rev. Lett. **84**, 2056 (2000).

[8] M. J. Wright, S. Riedl, A. Altmeyer, C. Kohstall, E. R. Sanchez Guajardo, J. H. Denschlag, and R. Grimm, Finite-Temperature Collective Dynamics of a Fermi Gas in the BEC-BCS Crossover, Phys. Rev. Lett. **99**, 150403 (2007).

[9] R. M. W. van Bijnen, N. G. Parker, S. J. J. M. F. Kokkelmans, A. M. Martin, and D. H. J. O'Dell, Collective excitation frequencies and stationary states of trapped dipolar Bose-Einstein condensates in the Thomas-Fermi regime, Phys. Rev. A **82**, 033612 (2010).

[10] C. D. Rossi, R. Dubessy, K. Merloti, M. de Goër de Herve, T. Badr, A. Perrin, L. Longchambon, and H. Perrin, The scissors oscillation of a quasi two-dimensional Bose gas as a local signature of superfluidity, J. Phys. Conf. Ser. **793**, 012023 (2017).

[11] I. Ferrier-Barbut, M. Wenzel, F. Böttcher, T. Langen, M. Isoard, S. Stringari, and T. Pfau, Scissors Mode of Dipolar Quantum Droplets of Dysprosium Atoms, Phys. Rev. Lett. **120**, 160402 (2018).

[12] M. Boninsegni and N. V. Prokof'ev, Colloquium: Supersolids: What and where are they?, Rev. Mod. Phys. **84**, 759 (2012).

[13] Z.-K. Lu, Y. Li, D. S. Petrov, and G. V. Shlyapnikov, Stable Dilute Supersolid of Two-Dimensional Dipolar Bosons, Phys. Rev. Lett. **115**, 075303 (2015).

[14] D. Baillie and P. B. Blakie, Droplet Crystal Ground States of a Dipolar Bose Gas, Phys. Rev. Lett. **121**, 195301 (2018).

[15] S. M. Roccuzzo and F. Ancilotto, Supersolid behavior of a dipolar Bose-Einstein condensate confined in a tube, Phys. Rev. A **99**, 041601(R) (2019).

[16] L. Tanzi, E. Lucioni, F. Famà, J. Catani, A. Fioretti, C. Gabbanini, R. N. Bisset, L. Santos, and G. Modugno, Observation of a Dipolar Quantum Gas with Metastable Supersolid Properties, Phys. Rev. Lett. **122**, 130405 (2019).

[17] F. Böttcher, J.-N. Schmidt, M. Wenzel, J. Hertkorn, M. Guo, T. Langen, and T. Pfau, Transient Supersolid Properties in an Array of Dipolar Quantum Droplets, Phys. Rev. X **9**, 011051 (2019).

[18] L. Chomaz, D. Petter, P. Ilzhöfer, G. Natale, A. Trautmann, C. Politi, G. Durastante, R. M. W. van Bijnen, A. Patscheider, M. Sohmen, M. J. Mark, and F. Ferlaino, Long-Lived and Transient Supersolid Behaviors in Dipolar Quantum Gases, Phys. Rev. X **9**, 021012 (2019).

[19] S. M. Roccuzzo, A. Gallemí, A. Recati, and S. Stringari, Rotating a Supersolid Dipolar Gas, Phys. Rev. Lett. **124**, 045702 (2020).

[20] L. Tanzi, J. Maloberti, G. Biagioni, A. Fioretti, C. Gabbanini, and G. Modugno, Evidence of superfluidity in a dipolar supersolid from nonclassical rotational inertia, Science **371**, 1162 (2021).

[21] E. Kim and M. H.-W. Chan, Probable observation of a supersolid helium phase, Nature (London) **427**, 225 (2004).

[22] D. Y. Kim and M. H. W. Chan, Absence of Supersolidity in Solid Helium in Porous Vycor Glass, Phys. Rev. Lett. **109**, 155301 (2012).

[23] Here, the word droplet refers to a high-density region, which is not necessarily self-bound.

[24] J.-N. Schmidt, J. Hertkorn, M. Guo, F. Böttcher, M. Schmidt, K. S. H. Ng, S. D. Graham, T. Langen, M. Zwierlein, and T. Pfau, Roton Excitations in an Oblate Dipolar Quantum Gas, Phys. Rev. Lett. **126**, 193002 (2021).

[25] M. A. Norcia, C. Politi, L. Klaus, E. Poli, M. Sohmen, M. J. Mark, R. Bisset, L. Santos, and F. Ferlaino, Two-dimensional supersolidity in a dipolar quantum gas, Nature (London) **596**, 357 (2021).

[26] J. Hertkorn, J.-N. Schmidt, M. Guo, F. Böttcher, K. S. H. Ng, S. D. Graham, P. Uerlings, H. P. Büchler, T. Langen, M. Zwierlein, and T. Pfau, Supersolidity in Two-Dimensional Trapped Dipolar Droplet Arrays, Phys. Rev. Lett. **127**, 155301 (2021).

[27] T. Bland, E. Poli, C. Politi, L. Klaus, M. A. Norcia, F. Ferlaino, L. Santos, and R. N. Bisset, Two-Dimensional Supersolid Formation in Dipolar Condensates, Phys. Rev. Lett. **128**, 195302 (2022).

[28] E. Poli, T. Bland, C. Politi, L. Klaus, M. A. Norcia, F. Ferlaino, R. N. Bisset, and L. Santos, Maintaining supersolidity in one and two dimensions, Phys. Rev. A **104**, 063307 (2021).

[29] A. Trautmann, P. Ilzhöfer, G. Durastante, C. Politi, M. Sohmen, M. J. Mark, and F. Ferlaino, Dipolar Quantum Mixtures of Erbium and Dysprosium Atoms, Phys. Rev. Lett. **121**, 213601 (2018).

[30] M. Sohmen, C. Politi, L. Klaus, L. Chomaz, M. J. Mark, M. A. Norcia, and F. Ferlaino, Birth, Life, and Death of a Dipolar Supersolid, Phys. Rev. Lett. **126**, 233401 (2021).

[31] See Supplemental Material at http://link.aps.org/supplemental/10.1103/PhysRevLett.129.040403 for more information, which contains refs. [32,33].

[32] I. T. Jolliffe, *Principal Component Analysis*, Springer Series in Statistics (Springer, New York, 2002).

[33] R. Dubessy, C. D. Rossi, T. Badr, L. Longchambon, and H. Perrin, Imaging the collective excitations of an ultracold gas using statistical correlations, New J. Phys. **16**, 122001 (2014).

[34] L. Pitaevskii and S. Stringari, *Bose-Einstein Condensation and Superfluidity* (Oxford University Press, New York, 2016), Vol. 164.

[35] I. Ferrier-Barbut, H. Kadau, M. Schmitt, M. Wenzel, and T. Pfau, Observation of Quantum Droplets in a Strongly Dipolar Bose Gas, Phys. Rev. Lett. **116**, 215301 (2016).

[36] L. Chomaz, S. Baier, D. Petter, M. J. Mark, F. Wächtler, L. Santos, and F. Ferlaino, Quantum-Fluctuation-Driven Crossover from a Dilute Bose-Einstein Condensate to a Macrodroplet in a Dipolar Quantum Fluid, Phys. Rev. X **6**, 041039 (2016).

[37] F. Wächtler and L. Santos, Quantum filaments in dipolar Bose–Einstein condensates, Phys. Rev. A **93**, 061603(R) (2016).

[38] A. J. Leggett, Can a Solid be "Superfluid"?, Phys. Rev. Lett. **25**, 1543 (1970).

[39] We note that the geometry of our system is very different from that considered in Ref. [38], and so, we do not expect this quantity to have a direct connection to the nonclassical moment of inertia of the system. Rather, we simply use it as a convenient way to quantify overlap between droplets.

[40] Edmundo R. Sanchez Guajardo, M. K. Tey, L. A. Sidorenkov, and R. Grimm, Higher-nodal collective modes in a resonantly interacting Fermi gas, Phys. Rev. A **87**, 063601 (2013).

[41] S. M. Roccuzzo, A. Recati, and S. Stringari, Moment of inertia and dynamical rotational response of a supersolid dipolar gas, Phys. Rev. A **105**, 023316 (2022).

Supplemental materials for: Can angular oscillations probe superfluidity in dipolar supersolids?

Matthew A. Norcia,[1] Elena Poli,[2] Claudia Politi,[1, 2] Lauritz Klaus,[1, 2] Thomas Bland,[1, 2]
Manfred J. Mark,[1, 2] Luis Santos,[3] Russell N. Bisset,[2] and Francesca Ferlaino[1, 2, *]
[1] *Institut für Quantenoptik und Quanteninformation,*
Österreichische Akademie der Wissenschaften, Innsbruck, Austria
[2] *Institut für Experimentalphysik, Universität Innsbruck, Austria*
[3] *Institut für Theoretische Physik, Leibniz Universität Hannover, Germany*

EXCITATION PROTOCOL

In both experiment and simulation, we excite the atoms by suddenly rotating the trap, holding for 6 ms, then returning it to its initial orientation. This was important in the experiment, as the trap frequencies generally change slightly as the trap is rotated, and we want to observe the evolution of a state that is equilibrated to the trap prior to the rotation. To explore whether the exact excitation protocol influences our results, we performed additional simulations where the trap angle was rotated and held in the new orientation, but not rotated back. We find that the same modes are excited in this case, and the frequency of their responses are the same. For some parameters the relative contributions of the modes to the spectrum of $\langle xy \rangle$ can differ between the two protocols, but for the parameters we explore the frequency of the peak response remains unchanged. In particular, for the droplet crystal hexagon shown in Fig. 4c of the main text, the contribution of the low-frequency mode to the $\langle xy \rangle$ power spectrum becomes appreciable, though is still smaller than the contribution of the modes near 60 Hz. Thus, the multimode response appears to be a generic feature of possible schemes to excite angular oscillations. While the spectral content of the excitation may differ, influencing the relative amplitudes of different modes, the frequency and character of the modes is determined by the system, not the drive.

We have also performed excitation in the simulation by directly imprinting a small phase variation αxy onto the ground-state wavefunction. This protocol produces qualitatively similar results to those described above. Again, the same modes are excited and respond with the same frequencies, though sometimes with different amplitudes. The dominant mode excited is the same as the rotate-and-return protocol for all cases investigated.

EXTRACTING ANGULAR POWER SPECTRUM

Several methods can be used to extract the angular response of our system. For the experiment, we perform a two-dimensional Gaussian fit to the in-trap image, and record the angle of the major and minor axes as a function of time. For the simulation, we report the angular response obtained using one of two observables. For direct comparison to the experiment, we use the state angle extracted from a 2D Gaussian fit, as in the experiment. For more detailed spectral analysis, we use the quantity $\langle xy \rangle$, as this is expected to have a strong response to a rapid rotation of the trap and we find it to be numerically more robust. We have confirmed that these and other similar observables, such as the directions of maximal and minimal variance, provide consistent results (up to overall normalization). In some cases, the Fourier spectrum of $\langle \hat{L}_z \rangle$ (though not experimentally accessible) shows different relative response amplitudes between modes compared to $\langle xy \rangle$, particularly for those modes at low frequencies.

FOURIER TRANSFORM IMAGE ANALYSIS

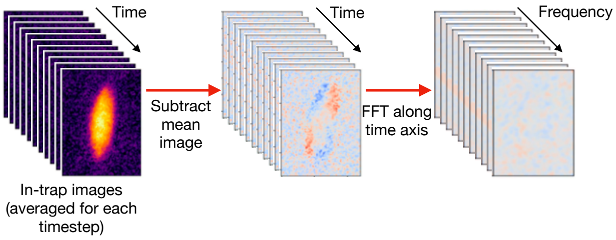

FIG. S1. Procedure for Fourier transform image analysis (FTIA). See text for description.

The goal of our Fourier transform image analysis (FTIA) protocol is to visualize the density response of our atomic system in real-space with respect to position, but in frequency space with respect to time. This provides a simple way to extract the spatial profile of excitation modes. The process is illustrated in Fig. S1. To perform the FTIA, we assemble images of projected density profiles corresponding to single time-steps (directly from the simulation, or averaged over several in-trap images from the experiment), then subtract the average (over all time-steps) image from each. We then Fourier transform the results along the time axis. The output is then a sequence of real-space images, showing the fluctuation pattern at a given frequency. Because each pixel is now represented by a complex number (encoding the amplitude and phase of the density variations at that location), we plot with respect to the global phase for each frequency that shows maximum variation, thus plotting the in-phase quadrature of the oscillation.

In order to obtain a power spectrum (useful for locating the frequencies of excited modes), we compute the sum of the absolute square of the fluctuations over a region of interest containing the atomic cloud for each frequency. This power spectrum can be used to identify the frequency and spatial character of modes, but is not expressed in physically meaningful units, and so should not necessarily be used to compare the strength of different mode responses.

We note that there are some similarities between the FTIA method and principal component analysis (PCA) [1, 2]. Both provide a model-free way of extracting the form of excitations present in a system. PCA does so by finding correlated patterns of fluctuations within a set of images, with no prior information about the time-sequence of the images. This makes it well-suited to revealing modes that are excited incoherently, for example by thermal or quantum noise. In contrast, our FTIA method explicitly incorporates the time-domain information associated with the images. This makes it well-suited to extracting modes that are coherently excited (FTIA, as we apply it, would not work for incoherently excited modes). In practice, we find that the FTIA is more robust than PCA at extracting fluctuation patterns that each exhibit a single-frequency response. While PCA often returns components whose weights vary with multiple frequencies (indicating that they actually correspond to a linear combination of eigenmodes), FTIA by construction returns a fluctuation pattern associated with a single frequency. We find that this feature makes it more robust for identifying eigenmodes of a system subject to a coherent drive.

SPECTRA/TABLE FOR ALL PARAMS

Excitation power spectra from simulation for a range of traps and scattering lengths used in the main manuscript can be found in Fig. S2.

PREDICTIONS FOR ROTATIONAL MODE FREQUENCIES

The rotational response of a gas can be calculated using hydrodynamic equations [3] or a sum-rule approach [4, 5]. From the sum-rule approach, an expression can be derived for the rotational oscillation frequency, under the assumption that the response is single-frequency:

$$\omega^2 = \frac{m\langle y^2 - x^2\rangle(\omega_x^2 - \omega_y^2)}{\Theta} \tag{1}$$

Here, Θ is the moment of inertia associated with steady-state rotation.

The numerator of Eq. 1 can be interpreted as a rotational spring constant: $k_\tau = -\tau/\theta$, where τ is the torque exerted on a state whose major and minor axes y and x are rotated relative to the their equilibrium position in the trap by an angle θ. To see this, consider a mass element m at position (x, y) in a trapping potential $V = (m\omega_x x^2 + m\omega_y y^2)/2$, which exerts a torque $\tau = xF_y - yF_x = xym(\omega_x^2 - \omega_y^2)$. We can then calculate $k_\tau = -\partial\tau/\partial\theta = -m(y\partial x/\partial\theta + x\partial y/\partial\theta)(\omega_x^2 - \omega_y^2) = m(y^2 - x^2)(\omega_x^2 - \omega_y^2)$. Summing over mass elements provides the numerator of Eq. 1. This highlights that the numerator of this expression is purely geometrical, independent of whether the state is superfluid or classical. In the case of multi-frequency response, Eq. 1 (as defined by the sum rule) becomes an inequality, defining the upper bound for the lowest frequency angular excitation in the system [4].

BETA VERSUS SCATTERING LENGTH FOR 1D AND 2D

In Fig. S3, we show the change in the anisotropy of the atomic state in response to a change in scattering length for a variety of traps, featuring both linear and 2D array modulated configurations. Here, we consider the quantity $\beta^2 = (\langle x^2 - y^2\rangle/\langle x^2 + y^2\rangle)^2$, as this quantity gives the expected change in moment of inertia between irrotational flow (IF) and rigid-body rotation (RBR). As β^2 approached unity, the difference between the two vanishes, so such states can exhibit minimal sensitivity to superfluidity.

States in more elongated traps generally have values of β^2 closer to one than their rounder counterparts. However, even in relatively round traps, such as those of Refs. [5, 6], low atom numbers can lead to the formation of linear arrays, which are highly elongated. In these cases, the sensitivity of the state to superfluidity is dramatically reduced upon entering the modulated regime. In contrast, combinations of trap parameters and atom number that lead to a 2D modulated state typically maintain values of β^2 substantially different from one even in the low scattering length, independent droplet regime.

LINEAR CASE

In Fig. S4, we explore the parameters of refs [5, 6], where a change in scattering length induces a transition from an unmodulated BEC to a linear array of two droplets. This transition is accompanied by a dramatic change in the aspect ratio of the atomic state, as evident in the near convergence of the predictions for rigid body

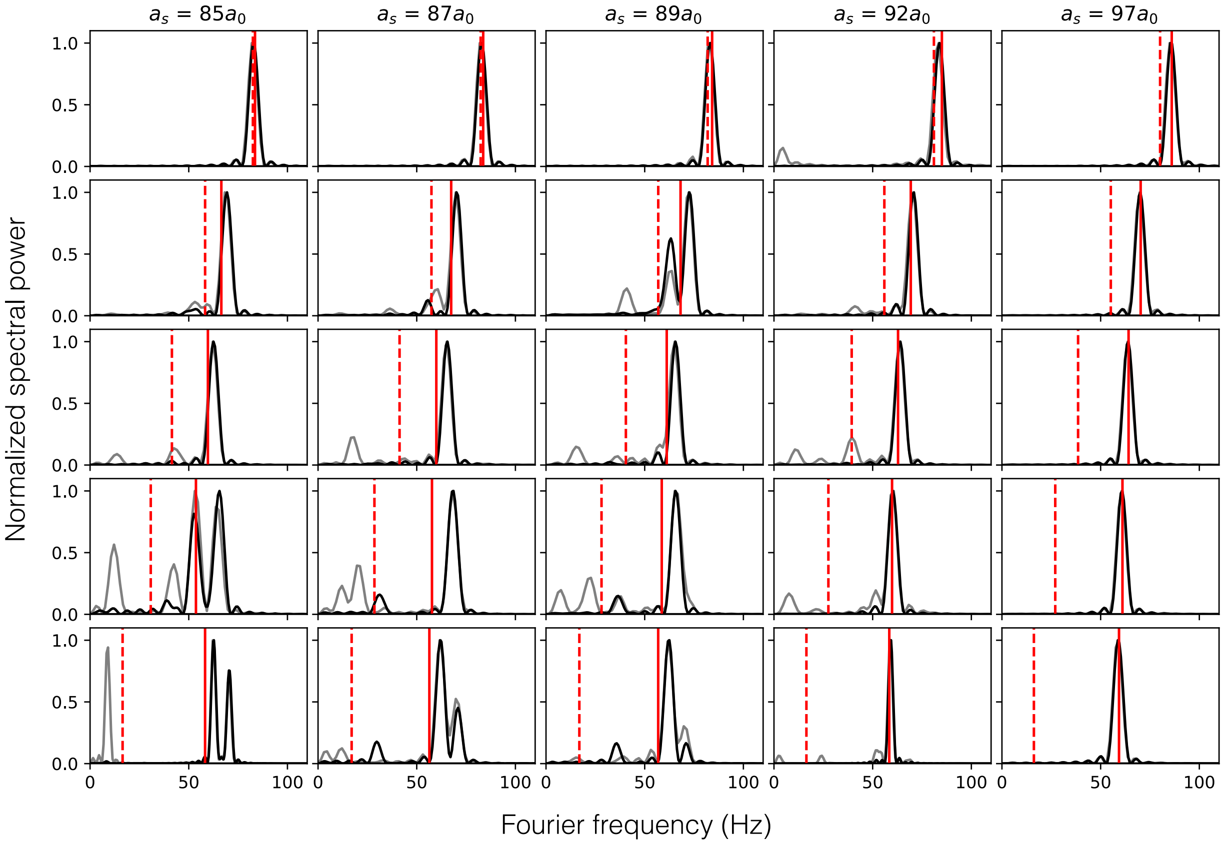

FIG. S2. Response sepctra extracted from simulations for different trap parameters (rows) and scattering lengths (columns). Upper rows correspond to more elongated traps, while lower rows correspond to more round ones. From top to bottom, $(f_x, f_y) = [(26, 87), (32, 70), (37, 62), (40, 57), (43, 53)]$ Hz. $f_z = 122$ Hz for all cases. Red vertical dashed and solid lines correspond to the rigid-body rotation and irrotational flow predictions, respectively. Gray traces are power spectra extracted from FTIA, while black traces are from $\langle xy \rangle$. In all cases, $a_s = 97a_0$ corresponds to an unmodulated BEC, while lower scattering lengths correspond to modulated states, with the overlap between droplets decreasing with scattering length. $(f_x, f_y) = (26, 87)$ is a linear droplet chain for all scattering lengths that produce a modulated state. All other modulated states have transverse structure, increasing in prevalence as the trap becomes more round.

and irrotational flow (f_{rig} and f_{irr}) at lower scattering lengths, corresponding to the droplet state.

We see that the dominant frequency of angular response is between f_{rig} and f_{irr}, indicating a change in the level of superfluidity in the system. We find that the angular response in the supersolid regime ($a_s = 90$ or 92 a_0) has two clear frequency components, though in this case the dominant frequency observed matches the prediction from the sum rule (with moment of inertia calculated under static rotation). Because of the geometry of the system, rotation does not lead to a significant transfer of mass between the two droplets. Thus, we attribute the change in superfluidity to the low-density halo that surrounds the droplets, rather than the inter-droplet connection itself.

---

[*] Correspondence should be addressed to `Francesca.Ferlaino@uibk.ac.at`

[1] I. T. Jolliffe, *Principal Component Analysis* (Springer Series in Statistics. Springer, New York, NY, 2002).
[2] R. Dubessy, C. D. Rossi, T. Badr, L. Longchambon, and H. Perrin, Imaging the collective excitations of an ultracold gas using statistical correlations, New Journal of Physics **16**, 122001 (2014).
[3] D. Guéry-Odelin and S. Stringari, Scissors mode and superfluidity of a trapped bose-einstein condensed gas, Phys. Rev. Lett. **83**, 4452 (1999).
[4] L. Pitaevskii and S. Stringari, *Bose-Einstein condensation and superfluidity*, Vol. 164 (Oxford University Press, 2016).
[5] S. M. Roccuzzo, A. Gallemí, A. Recati, and S. Stringari, Rotating a supersolid dipolar gas, Phys. Rev. Lett. **124**, 045702 (2020).
[6] L. Tanzi, J. Maloberti, G. Biagioni, A. Fioretti, C. Gab-

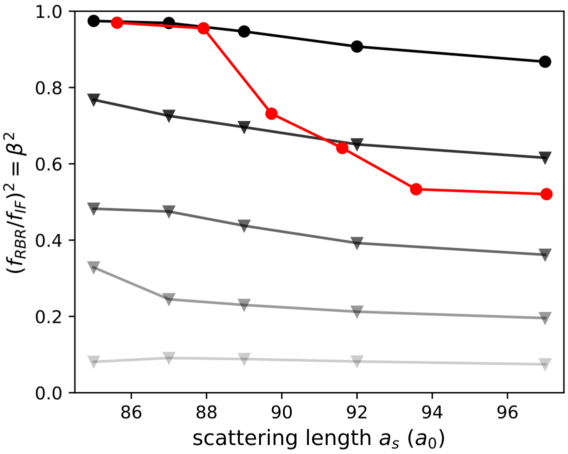

FIG. S3. Difference in moment of inertia between IF and RBR, β^2 for different traps and scattering lengths. Traps and atom numbers that correspond to linear arrays for modulated states are indicated by round markers, while those that correspond to 2D modulated arrays are indicated by triangles. All points except those at $a_s = 97a_0$ are modulated, interdroplet connection decreasing with scattering length. The states explored in Fig. S2 are shown in grey-scale, with lighter saturation corresponding to rounder traps, while the conditions similar to those of Refs. [5, 6] are shown in red.

banini, and G. Modugno, Evidence of superfluidity in a dipolar supersolid from nonclassical rotational inertia, Science **371**, 1162 (2021).

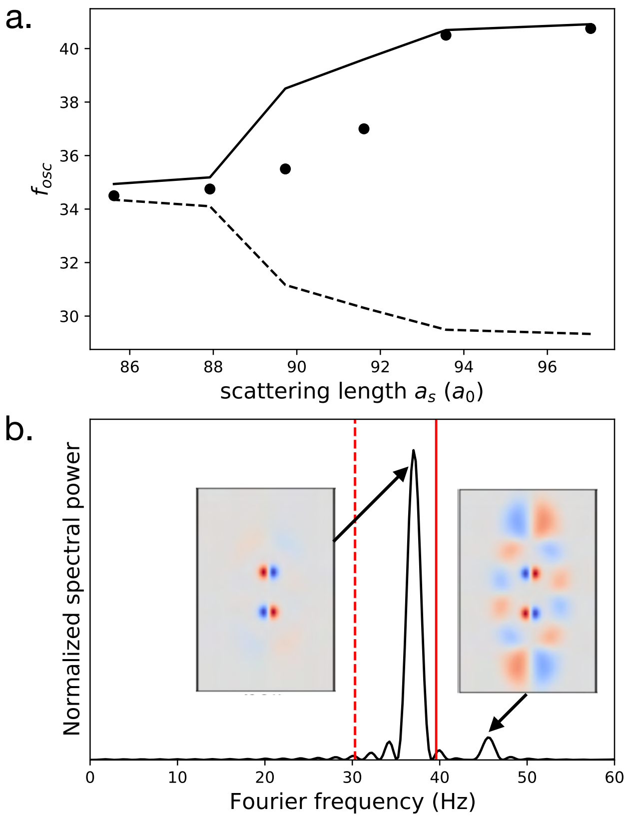

FIG. S4. Analysis of linear two-droplet arrays of [5, 6]. **a.** Dominant angular oscillation frequency (markers) extracted from simulations versus scattering length, through transition from BEC (right) to isolated droplets (left). The irrotational and rigid-body predictions f_{irr} and f_{rig} are shown as solid and dashed lines, respectively. **b.** The Fourier spectrum of $\langle xy \rangle$ for the point near $a_s = 92a_0$ exhibits a response with dominant and sub-dominant mode contributions. The fluctuation profiles associated with these two frequencies are shown in the insets. Solid and dashed vertical red lines represent f_{irr} and f_{rig}, respectively.

4.3 Vortices in supersolids

> *It is of interest to note that defects of a fundamentally new type may exist in a superfluid crystal. The question concerns vortex lines, i.e., linear defects for which the phase of the condensate's wave function changes by 2π upon going around the defect.*
>
> ***A. F. Andreev and I. M. Lifshitz***
> *Quantum Theory Of Defects In Crystals (1969) [79]*

Quantised vortices are an hallmark of supefluidity. In this chapter we report on our experimental efforts on probing the superfluid nature of the supersolid by nucleating quantised vortices. Additionally, the ability to create vortices in this modulated quantum state provides us with a toolbox to study interesting phenomena such as vortex pinning [281, 282] or the glitch mechanism in neutron stars [283, 126].

A detailed introduction to quantised vortices has already been given for dipolar BECs in Ch. 3. We know that stable vortex solutions exist for BECs rotated at the frequency $\Omega > \Omega_c = \frac{E_v - E_0}{L_z}$ and that these vortices exist due to the single-valuedness of the phase of the macroscopic wavefunction (1.13). Since the supersolid wave function is simply another solution of (1.12), which is also described by (1.13), the hydrodynamic equations are valid as described in Ch. 3.1. It can be deduced that the vortices should have very similar properties to those of BECs. Indeed, eGPE simulations suggest that stable vortex solutions should exist for supersolids [281]. However, prior to our work, vortices have not yet been observed experimentally in supersolids.

Vortices in ultracold quantum gases have only been studied in quasi-homogeneous states: The length scale in BECs at which density changes is much larger than the core size of the vortices. The vortices experience a homogeneous density distribution and therefore the vortex motion is not constrained by the superfluid but is mostly influenced by other vortices [254]. This situation changes in a supersolid. As we have seen from Eq. (3.8), the vortex reduces its kinetic energy by moving towards a lower density and therefore the vortex will sit on the interstitial site between three droplets. Not only that, but since the size of the vortex is related to the healing length ξ, which is inversely proportional to the density $\xi \propto n^{-1/2}$ as given by (3.7), the vortex core size can be on the same length scale as the density change. Therefore, the vortex dynamics is constrained by the structure of the state.

We are able to combine the knowledge of creating supersolids in axial-symmetric pancake ODTs, nucleating vortices in dipolar condensates, and understanding the multimode response of the supersolid to rotation to experimentally nucleate vortices in supersolids. We work with ^{164}Dy for which we can observe supersolid state lifetimes of $\tau \approx 1$ s [123] larger than the vortex nucleation times observed in the dBEC. However, the challenge is to create a supersolid state where the droplet number does not change during the rotation time $t_{\mathrm{rot}} = 0 - 1000$ ms and is repeatable from shot to shot. We find states with seven, four and three droplets to be well repeatable due to their symmetric hexagonal (as shown in Fig. 4.1 c), diamond (as shown in Fig. 4.4 a) and triangular structure (not shown). In experiment there can be structural transitions between these states due to atom loss, which makes the results more difficult to interpret. We find experimental parameters for which the four or three droplet state during the rotation over the duration

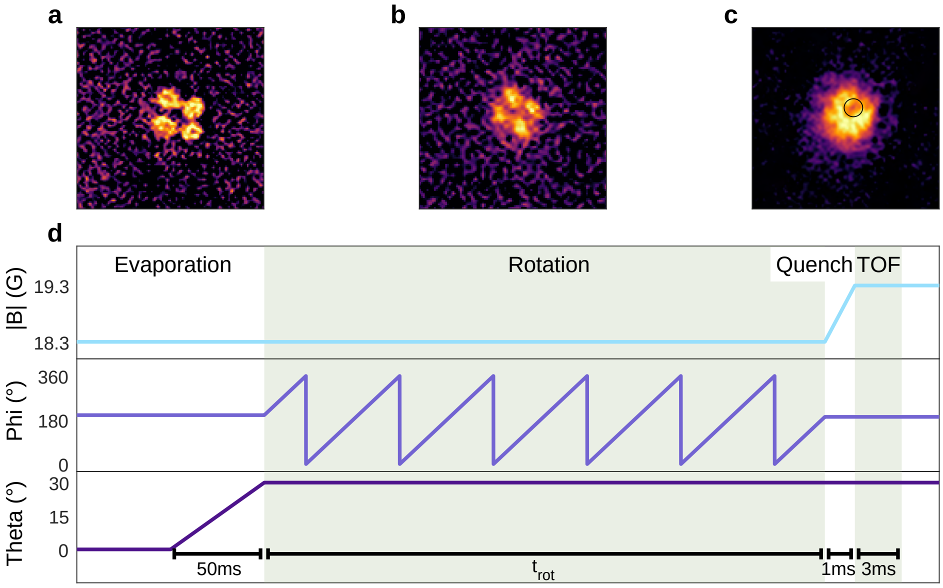

Figure 4.4: Preparation, rotation and melting sequence to observe vortices in supersolids. In-situ images of single runs are shown for a) $\theta = 0°$ before rotation ($|B| = 18.3$G), b) $\theta = 30°$ during rotation($|B| = 18.3$G) and c) $\theta = 30°$ after the rotation and after quenching the magnetic field to $|B| = 19.3$G. d) $|B|$, ϕ and θ during the last part of the experimental sequence.

of t_{rot} is stable. Another advantage of these states is that for a solution with a single vortex, this vortex tends to be in the centre of the cloud. The magnetic fields we use in the experiment to work with the four and three droplet state are $B = 18.30(2)\ G$ and $B = 18.24(2)\ G$ respectively.

The sequence to rotate the cloud is shown in Fig. 4.4 d. We use the magnetostirring technique, which is discussed in Sec. 3.1.2. In the case of the modulated state the rotation is clearly visible as the droplets align along the magnetic field (see Fig. 4.4 b), which is tilted away from the axis of rotation by $\theta = 30°$. Looking at the projection of the droplets in the x-y plane, we see that the long axis of the droplets rotates synchronously with the magnetic field. Interestingly, we observe that there is a secondary rotation of the centre of mass motion of the droplets, which initially has a different rotation frequency and eventually synchronises with the magnetic field rotation. The synchronisation is related to vortex nucleation[4] and shows the complex velocity field of the rotating modulated state. An example of such a velocity field was simulated in [275, 281] for the magnetic field along the rotation axis. And as for the BEC, tilting the magnetic field beyond $\theta > 51.3°$ will lead to a transition to a macrodroplet for large rotation frequencies [232]. Nevertheless, nucleating vortices in the supersolid presents a new challenge. Because the vortices are located at the low density region between the droplets, where our phase-contrast imaging cannot detect atoms due to the background noise (see Fig. 4.4 a), vortex and non-vortex states are indistinguishable.

---

[4] Manuscript is in preparation at the time of the submission of this thesis.

4.3.1 How to observe vortices: Melting the supersolid

How can we directly observe vortices in a supersolid? A solution was described in [284] and is also reminiscent of the method used to show vortices in degenerate Fermi gases in the BCS regime [206]. Instead of observing the vortices in the supersolid state just before the imaging sequence, when the vortices are already nucleated, we melt the supersolid into a BEC state by changing the interactions with a magnetic field quench over $t_{\text{quench}} = 1$ ms (see Fig. 4.4 d). During the transition from the supersolid to the BEC state the vortices are topologically protected and continue to exist [284]. The vortices are then well observable with absorption imaging after a short TOF $t_{\text{TOF}} = 3$ ms as described in 3.1.3 and as shown in Fig. 4.4c.

Experimentally melting the supersolid comes with a challenge. Ideally we could change the interaction strength from $\varepsilon_{\text{dd}} \approx 1.41$ (SS regime for the experimental trap parameters and atom number) to $\varepsilon_{\text{dd}} \approx 1.26$ (BEC regime) by the means of a single broad Feshbach resonance, but as we already discussed in Sec. 2.2.5, there are many narrow Feshbach resonances in between. Therefore the magnetic field for the SS regime $B = 18.30(2)$ G is separated by 1 G to the magnetic field for the BEC $B = 19.30(2)$ G with many narrow FB resonances in between. Although it was theoretically suggested to slowly ramp from the SS regime to the BEC regime in $t_{\text{ramp}} = 100$ ms, we had to go much faster with a ramp of $t_{\text{ramp}} = 1$ ms, to avoid the resonances.

4.3.2 Threshold behaviour for vortex seeding

We know from the vortices in the dipolar BEC, that it is not enough to rotate the gas at $\Omega > \Omega_c$, where the vortex state is energetically favourable compared to the vortex-free state. These two states are topological different and therefore their must be a mechanism such as the dynamical instability we discussed in Sec. 3.1.2, to nucleate the vortices, and for the BEC we find that this instability is triggered when the rotation frequency is resonant with the quadrupol oscillations $\Omega \approx \Omega_{\text{nucl}} = 1/\sqrt{2}\omega_\perp$[193].

This nucleation behaviour changes drastically for supersolids. We can see in Figure 3 of the paper, that compared to the BEC, the nucleation frequency range has become much larger, starting at $\Omega \approx 0.5\omega_\perp$ and nucleation is evident even for large $\Omega > 0.8\omega_\perp$. Therefore we see much more a threshold behaviour of the nucleation than a resonance behaviour for a very specific nucleation frequency as we know it from the BEC. This can be attributed to the multimode response to rotation that we discussed already in the last section. While for BECs only the quadrupole mode leads to a dynamic instability, due to the complex crystal structure there are additional crystal modes that can also lead to the dynamical instability. Looking at the eGPE simulations, we can identify three Goldstone modes with the appearance of vortices during rotation [285, 286, 129, 130]: one related to the broken U(1) symmetry connected to the superfluidity of the system and two related to the the broken translational symmetry in the x and y direction, which are almost degenerate due to the circular trap geometry.

The energetically lowest mode is associated with the superfluid part of the supersolid. The downshift compared to the BEC state can be understood intuitively due to the much lower density of the superfluid background compared to a BEC state in a comparable trap. This reduces the energy required to excite the quadrupole mode.

The other two modes correspond to the excitation of the droplet crystal leading to a complex mode spectrum that we have discussed in Sec. 4.2.2. This complexity leads to a threshold behaviour of the vortex nucleation.
With our work we provide for the first time evidence of the existence of vortices in the supersolid state and therefore a direct proof of the superfluid nature of the supersolid state in a dipolar quantum gas.

P4 Observation of vortices in a dipolar supersolid

The following manuscript has appeared in

Nature 635, 327-331 (2024)[5],
submitted 05 February 2024; published 06 November 2024.
DOI: 10.1038/s41586-024-08149-7

Eva Casotti[1,2], Elena Poli[2], Lauritz Klaus[1,2], Andrea Litvinov[1], Clemens Ulm[1,2], Claudia Politi[1,2,3], Manfred J. Mark[1,2], Thomas Bland[2] and Francesca Ferlaino[1,2]

[1]Institut für Quantenoptik und Quanteninformation, Österreichische Akademie der Wissenschaften, 6020 Innsbruck, Austria
[2]Institut für Experimentalphysik, Leopold-Franzens-Universität, 6020 Innsbruck, Austria
[3]Institut for Quantum Electronics, ETH Zürich, 8093 Zürich, Switzerland

For this publication, I (L.K.) contributed to works on the experiment together with E.C., A.L., C.U. and C.P., analysed the dysprosium data together with E.C, A.L. and C.U., and contributed to the interpretation of the results, as well as in writing of the manuscript together with all other authors.

---

[5] Here the preprint version is attached

Observation of vortices in a dipolar supersolid

Eva Casotti,[1,2,*] Elena Poli,[2,*] Lauritz Klaus,[1,2] Andrea Litvinov,[1] Clemens Ulm,[1,2]
Claudia Politi,[1,2,†] Manfred J. Mark,[2,1] Thomas Bland,[2] and Francesca Ferlaino[2,1,‡]

[1] *Institut für Quantenoptik und Quanteninformation, Österreichische Akademie der Wissenschaften, Technikerstr. 21A, 6020 Innsbruck, Austria*
[2] *Universität Innsbruck, Fakultät für Mathematik, Informatik und Physik, Institut für Experimentalphysik, 6020 Innsbruck, Austria*

(Dated: March 28, 2024)

Supersolids are states of matter that spontaneously break two continuous symmetries: translational invariance due to the appearance of a crystal structure and phase invariance due to phase locking of single-particle wave functions, responsible for superfluid phenomena. While originally predicted to be present in solid helium[1–5], ultracold quantum gases provided a first platform to observe supersolids[6–10], with particular success coming from dipolar atoms[8–12]. Phase locking in dipolar supersolids has been probed through e.g. measurements of the phase coherence[8–10] and gapless Goldstone modes[13], but quantized vortices, a hydrodynamic fingerprint of superfluidity, have not yet been observed. Here, with the prerequisite pieces at our disposal, namely a method to generate vortices in dipolar gases[14,15] and supersolids with two-dimensional crystalline order[11,16,17], we report on the theoretical investigation and experimental observation of vortices in the supersolid phase. Our work reveals a fundamental difference in vortex seeding dynamics between unmodulated and modulated quantum fluids. This opens the door to study the hydrodynamic properties of exotic quantum systems with multiple spontaneously broken symmetries, in disparate domains such as quantum crystals and neutron stars[18].

Rotating fluids on all scales exhibit a whirling motion known as vorticity. Unique to the interacting quantum world, however, is that this rotation is quantized due to the single-valued and continuous nature of the underlying macroscopic wavefunction[19,20]. Observing quantized vortices is regarded as unambiguous evidence of superfluidity, relevant for a wide variety of many-body quantum systems from superfluid ^{4}He [21,22] through gaseous bosonic[23] and fermionic[24] condensates, exciton-polariton condensates[25], to solid-state superconductors[26,27]. Remarkably, this phenomenon persists over a wide range of interaction scales, since it only requires the irrotational nature of the velocity field. However, all of these examples refer to the case in which the vortices are free to move in the system, and any density non-uniformity due to, e.g., the trap, occurs on scales much larger than the vortex core.

The supersolid phase does not belong to this category, spontaneously breaking this spatial uniformity. Supersolids, characterized by the coexistence of superfluid and solid properties[1–5], have been investigated through two distinct approaches. The first approach involves infusing superfluid characteristics into a solid, as demonstrated in phenomena such as pair density wave phases[28] in ^{3}He[29], superconductors[30,31], and through a ^{4}He monolayer on graphite[32]. The second approach entails imparting solid properties into superfluid systems, as observed in ultracold atomic settings in optical cavities[7], those with spin-orbit coupling[6], and with atoms exhibiting a permanent magnetic dipole moment[8–11]. Among these systems, supersolids composed of dipolar atoms have emerged as a versatile platform for exploring the superfluid characteristics and solid properties of this long sought-after state[12], including the spontaneous density modulation and the global phase coherence[8–10], the existence of two phononic branches, one for each broken symmetry[13,33,34], and Josephson-type dynamics[35,36]. Where these tests have found a roadblock is in probing the response to rotation. One consequence of irrotational flow is the scissors mode oscillation, where the signature of superfluidity is the lack of a rigid body response to a sudden rotation of an anisotropic trap[37]. However, supersolids show a mixture of rotational and irrotational behavior, leading to a multimode response to perturbation. This complexity hinders a straightforward extraction of the superfluid contribution[16,38,39]. Instead, the presence of quantized vortices is an unequivocal signal of irrotationality, and thus unambiguously proves the superfluidity of the system. These vortices are also anticipated to exhibit other distinctive characteristics, including a reduced angular momentum[40,41], and unusual dynamics due to their interplay with the crystal such as pinning and snaking[18,42,43]. Nevertheless, a critical gap exists in the current experimental exploration of supersolids — an investigation into whether the supersolid can maintain its structure and coherence under continuous stirring, as well as if, and how, vortices may manifest and behave in this unique state. The experimental challenge lies in the inherent complexity and fragility of the supersolid phase, which lives in a narrow region within the phase diagram[12]. In our work, we explore this uncharted territory by investigating the supersolid response to rotation, using a technique known as magnetostirring[14,15,44]. Combining experiment and theory, our study explores both the unmodulated and modulated states, revealing distinctive signatures associated with the presence of vortices in the supersolid.

Predicting the supersolid response to rotation

Owing to the inherent long-range interactions among atoms, a dipolar gas exhibits a density distribution that extends along the magnetic field direction, a phenomenon known as magnetostriction[45]. This imparts an elliptical shape to the cloud. The rotation of the magnetic field consequently induces stirring of the gas[44]. This method, referred to as magnetostirring, has recently been employed to generate vortices in unmodulated dipolar quantum gases[14]. These vortices eventually organize into distinctive patterns, forming either triangular or stripe vortex lattices[15,44].

Generating vortices in the supersolid phase through magnetostirring has not yet been investigated, therefore, we theoretically explore the zero temperature dynamics of our state through the so-called extended Gross-Pitaevskii equation[46–49] (eGPE). This takes into account the cylindrically symmetric harmonic trap, the short-range interactions, through the tunable s-wave interaction strength a_s, and long-range interactions, with fixed amplitude $a_{\text{dd}} = 130.8a_0$ for ^{164}Dy. Also included are beyond-mean field effects resulting from the zero-point energy of Bogoliubov quasiparticles–shown to be crucial for the energetic stability in the supersolid phase[49]. By tuning the short-range interactions, we can access both the supersolid (typically $\epsilon_{\text{dd}} = a_{\text{dd}}/a_s \gtrsim 1.3$ for experimentally relevant trap geometries) and unmodulated Bose-Einstein condensate (BEC) phases ($\epsilon_{\text{dd}} \lesssim 1.3$).

Figure 1 comparatively shows exemplar density and phase distributions of an unmodulated dipolar BEC [a] and supersolid phase (SSP) [b] rotating the magnetic field at increasing frequency Ω, from left to right. In a BEC, Fig. 1a, at small frequencies, with respect to the radial trap frequency $\omega_\perp$, the cloud density is almost unchanged from the static result [a(i)]. Rotating faster, the cloud elongates, and we observe an irrotational velocity field in the phase profile [a(ii)]. When rotating faster than a given Ω^*_{BEC}, the irrotational flow can no longer be maintained, and quantum vortices, observable as density holes and quantized 2π phase windings, penetrate the condensate surface following a quadrupole mode instability [a(iii)][14].

In contrast to unmodulated BECs, supersolids present a new scenario, see Fig. 1b. Our simulations reveal that the system is more susceptible to quantized vortex creation, happening at significantly lower frequencies than the BEC case. At small frequencies, the crystalline structure and surrounding 'halo' of atoms follow the magnetic field in lockstep without generating vortices [b(i)]. At higher frequencies, yet still $\Omega < \Omega^*_{\text{BEC}}$, we now see vortex lines smoothly entering into the interstitial regions between the crystal sites [b(ii)][40,41,43]. These vortices persist even at higher frequencies, arranging into a regular lattice structure [b(iii)].

To gain further insight, we study the total vortex number obtained after 1 s of rotation as a function of Ω. Figure 1c shows a striking difference in the response to rotation between the two quantum phases. The BEC shows the well-known resonant behavior, in which the rotation frequency must be at resonance with half the collective quadrupole mode frequency ω_Q. This drives an instability of the condensate surface, allowing vortices to enter the state. For a non-dipolar BEC $\omega_Q = \omega_\perp/\sqrt{2}$[50–52], while for dipolar quantum gases, small deviations from this value can occur depending on the dipolar interaction and the trap geometry[53]. For our system, we see the onset of the resonant behavior at $\Omega^*_{\text{BEC}} = 0.6\omega_\perp$, reaching its maximum at $\Omega \approx 0.75\omega_\perp$.

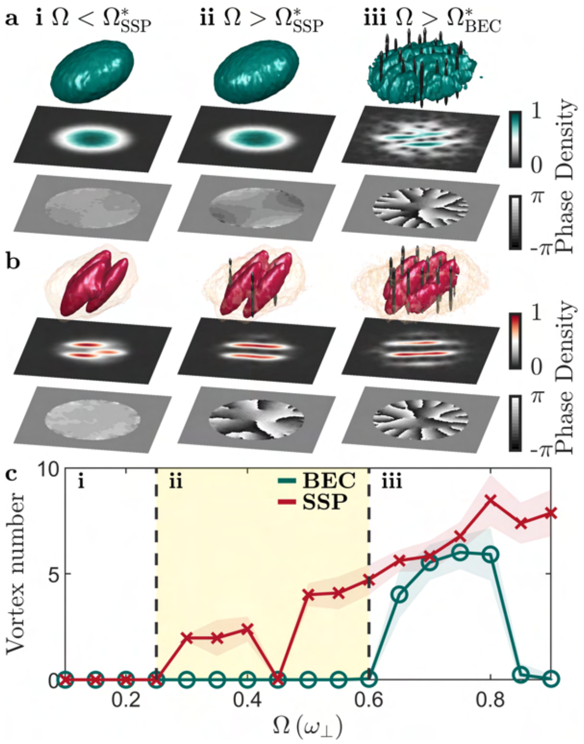

FIG. 1. **Simulation of vortex nucleation in a supersolid and unmodulated BEC.** Density isosurfaces and their corresponding normalized integrated density and phase profiles for the **a** unmodulated BEC and **b** supersolid phases after 1 s of rotation at (i) $\Omega = 0.2\omega_\perp$, (ii) $0.4\omega_\perp$, and (iii) $0.7\omega_\perp$. Isosurfaces are shown at 15% of the max density in all plots, and additionally at 0.5% in the SSP to show the halo. Vortex tubes are shown in black in the 3D images and appear as 2π windings in the phase plots. **c** Comparison of the time-averaged vortex number as a function of Ω between the SSP (red) and BEC (green), averaged between 0.75 s and 1 s of rotation, and the colored shading shows the standard deviation. The yellow shaded area highlights $\Omega^*_{\text{SSP}} < \Omega < \Omega^*_{\text{BEC}}$ (see main text). The results are obtained from eGPE calculations with $(\omega_\perp, \omega_z) = 2\pi \times [50, 103]$ Hz, magnetic-field angle from the z-axis $\theta = 30°$, atom number $N = 5 \times 10^4$, and scattering length $a_s = 95a_0$ $(104a_0)$ for the SSP (BEC) phase.

In the supersolid phase, we observe a vastly different behavior. The dual superfluid-crystalline nature of the state leads to two distinguishing features: the reduced superfluidity results in vortices nucleating at a lower rotation frequency and the solidity gives rise to a monotonic increase in vortex number at faster frequencies, reminiscent of rigid body rotation; see Fig. 1c. This can be understood by studying the excitation spectrum. A two-dimensional supersolid exhibits three quadrupole modes: one from the broken phase symmetry associated with superfluidity and one from each direction of the broken translational symmetry[40]. In our case, the latter are nearly degenerate due to the cylindrically symmetric dipole trap. Excitation of the 'superfluid' quadrupole mode is responsible for the weak resonance starting at $\Omega^*_{\text{SSP}} \approx 0.25\omega_\perp$ and centered around $\Omega \approx 0.35\omega_\perp$, where just a few vortices are created. The position of this resonance is highly depen-

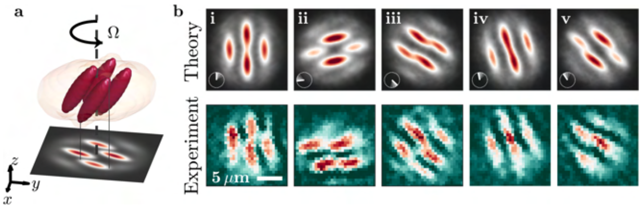

FIG. 2. **Magnetostirring of a ^{164}Dy dipolar supersolid. a** Density isosurfaces and corresponding integrated density of a four droplet supersolid. **b** Column densities of a four droplet supersolid state from theory (top row) and experiment (bottom row) with $\Omega = 0.3\omega_\perp$; the images were taken after (i-v) $1, 19, 43, 70, 274\,\mathrm{ms}$. Experimental parameters: $B = 18.24(2)\,\mathrm{G}$, $N \approx 7 \times 10^4$, and $(\omega_\perp, \omega_z) = 2\pi \times [50.5(3), 135(2)]\,\mathrm{Hz}$. Illustrative simulation parameters: $a_s = 92.5a_0$, $N = 6 \times 10^4$, and $(\omega_\perp, \omega_z) = 2\pi \times [50, 135]\,\mathrm{Hz}$.

dent on the superfluid fraction, eventually vanishing in the isolated droplet regime[40]. As we will discuss later, the detection of this subtle effect is at the edge of our current experimental capability, indicating compatibility, albeit with a low signal strength. Beginning at $\Omega \approx 0.45\omega_\perp$, the system exhibits instead a threshold response to rotation, where the angular momentum, and thus vortex number, linearly increases with Ω[40,41]. This prominent feature arises due to the near degenerate crystal quadrupole mode resonance.

Experimental magnetostirring of a dipolar supersolid

Bolstered by the acquired theoretical understanding, we experimentally explore the suitability of magnetostirring to nucleate vortices in the supersolid phase. We first produce an optically trapped supersolid quantum gas of highly magnetic bosonic ^{164}Dy atoms via direct evaporative cooling[10,11,17,54] and then apply magnetostirring[14,15,44] to rotate the gas.

In all the experiments presented, the three-dimensional optical dipole trap (ODT) is cylindrically symmetric, with radial frequency $\omega_\perp \approx 2\pi \times 50\,\mathrm{Hz}$ and a trap aspect ratio $\omega_z/\omega_\perp$ that varies between 2 and 3. Throughout the evaporation sequence, we apply a uniform magnetic field along the z-axis and tilt the magnetic field vector by $\theta = 30^\circ$ in the last cooling stage to prepare for magnetostirring[14]. With this sequence, we obtain a supersolid typically composed of four density maxima (droplets) on top of a low-density background (halo) of coherent atoms, which we probe by taking phase-contrast images after $3\,\mathrm{ms}$ of expansion. This gives us access to the 2D density profiles integrated along the axial direction, as illustrated in Fig. 2a. We magnetostir the system by rotating the magnetic-field vector around the z-axis with a constant angular velocity Ω; see Fig. 2b. As predicted by theory, the droplets align themselves along the magnetic-field direction, breaking the cylindrical symmetry, thus enabling rotation. We are able to stir the supersolid for hundreds of milliseconds without destroying the state, as shown in Fig. 2b(i-v). This result is particularly relevant since it allows several full rotations, even for small driving frequencies, giving the vortices enough time to nucleate and percolate into the system.

Observation of vortices in a dipolar supersolid

Based on our simulations, on the one hand, we anticipate vortex nucleation in the supersolid already at modest rotation frequencies, but on the other hand, the density modulated initial state poses a unique challenge in vortex detection. Traditional methods for probing quantized vortices in quasi-homogeneous ultracold quantum gases typically rely on observing density depletions of an expanded cloud[23,24,55,56]. In the context of supersolids, vortices nest within the low-density interstitial areas between the droplets, reducing the contrast[18,57]. We implement an imaging sequence inspired by recent theoretical proposals[57] that draws parallels with a protocol employed to observe vortices in strongly interacting Fermi gases[24]. In particular, we project the SSP into the BEC phase just before releasing the atoms from the trap by rapidly ($1\,\mathrm{ms}$) increasing the scattering length. This projection effectively "melts" the high density peaks, providing a more homogeneous density profile, see Methods. Since vortices are topologically protected defects, they are expected to survive during this state projection[57]. Finally, we probe the system with vertical absorption imaging after $3\,\mathrm{ms}$ of expansion, without allowing time for further dynamics in the BEC phase.

Figure 3 summarizes our main results, where we compare the behavior of a BEC and SSP under magnetostirring. Akin to theory, we see three regimes. At low frequencies ($\Omega < \Omega^*_{\mathrm{SSP}}$), we do not observe vortices in either state [b(ii)]. For $\Omega^*_{\mathrm{SSP}} < \Omega < \Omega^*_{\mathrm{BEC}}$, a striking difference between the BEC and the SSP response to rotation appears [b(iii)]. While the former does not show vortices, in the supersolid we clearly observe the appearance of a vortex in the central region of the cloud. Finally, at a larger frequency ($\Omega > \Omega^*_{\mathrm{BEC}}$), we observe multiple vortices in both cases [b(iv)]. This confirms the expected reduction in vortex nucleation frequency, the first characteristic feature of the impact of supersolidity.

In what follows, we generalize our observations to the full range of driving frequencies, in order to identify the threshold nucleation values and the vortex number behavior as a function of rotation frequency. We trace the time evolution of the rotating system both in the SSP and BEC phase and extract for each time step and Ω the number of vortices. We show the average vortex number obtained for each measurement in Fig. 3 together with the corresponding numerical simulations. In the unmodulated case (Fig. 3a), we observe the expected resonant behavior around $\Omega \approx 0.7\omega_\perp$[14]. After $0.5\,\mathrm{s}$ of rotation, both the experiment and theory show $\Omega^*_{\mathrm{BEC}} \approx 0.6\omega_\perp$.

In the supersolid case (Fig. 3c), we are able to observe clear evidence for the threshold behavior for vortex nucleation. For driving frequencies greater than $\Omega \approx 0.4\omega_\perp$, vortices persist even up to $1\,\mathrm{s}$, and there is an increase of vortex number with rotation frequency. This behavior is in contrast to the BEC case, where above $\Omega = 0.75\omega_\perp$ we do not observe vortices, unveiling the competing superfluid and solid contributions. Additionally, theory predicts a superfluid quadrupole resonance centered at $\Omega \approx 0.3\omega_\perp$, with one or at most two vortices entering the cloud. A detailed analysis of the experimental data reveals a signature compatible with the existence

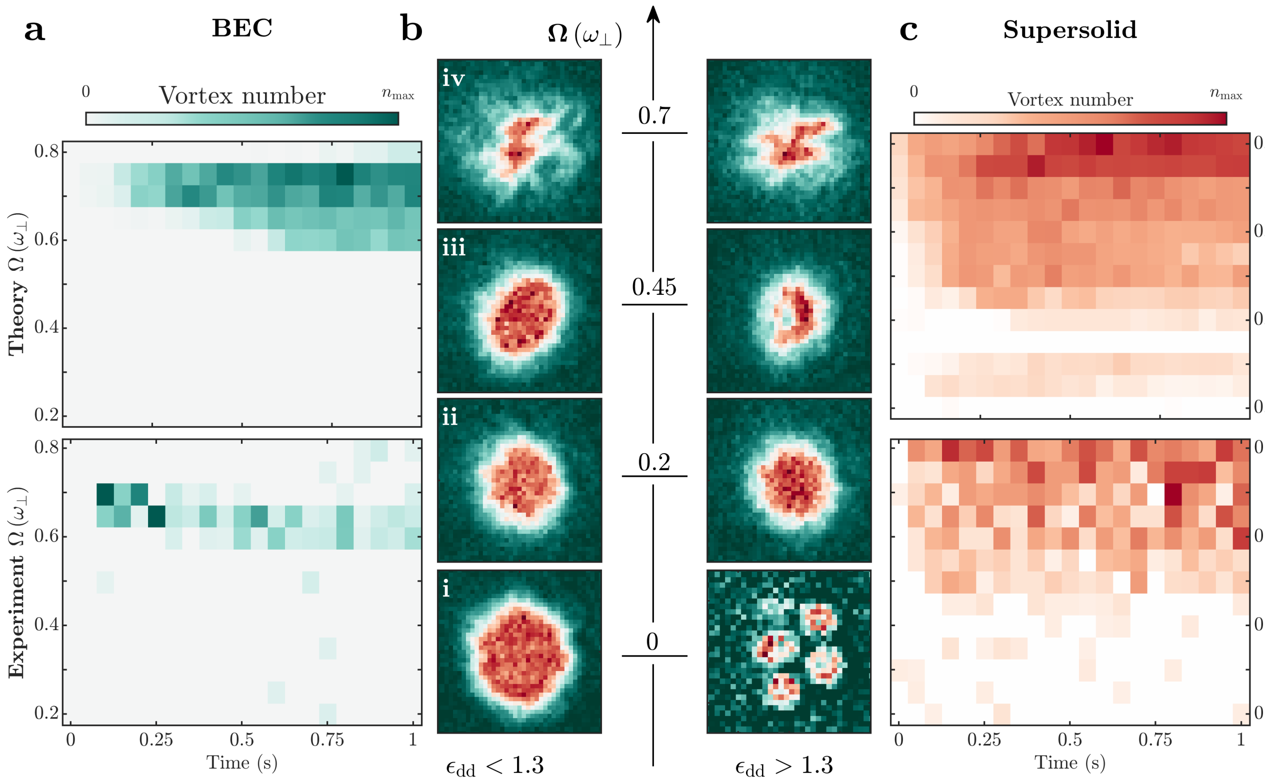

FIG. 3. **Vortex nucleation in a dipolar supersolid and BEC.** Vortex number as a function of rotation time and Ω for an **a** unmodulated BEC and **c** supersolid. Top plots show the simulations ($n_{\max}^{\mathrm{BEC}} = 8$, $n_{\max}^{\mathrm{SSP}} = 7.6429$), bottom plots the experimental observation ($n_{\max}^{\mathrm{BEC}} = 2.5$, $n_{\max}^{\mathrm{SSP}} = 2$), where in **a** the absolute value of the magnetic field is held at 19.30(2) G, but in **c** is instead ramped from 18.30(2) G to 19.30(2) G in 1 ms at the end of the rotation. Exemplar images taken after 251 ms of rotation are shown in **b**. All images are taken after 3 ms expansion, except the non-rotating supersolid state, which is a phase-contrast image with $\theta = 0^\circ$. In the experiment, the trap has frequencies $(\omega_\perp, \omega_z) = 2\pi \times [50.3(2), 107(2)]$ Hz, and the initial condensed atom number is $N \approx 3 \times 10^4$. For the simulation: $(\omega_\perp, \omega_z) = 2\pi \times [50, 103]$ Hz, with **a** $a_s = 104a_0$, initial $N = 2 \times 10^4$, and **c** $a_s = 93a_0$, $N = 3 \times 10^4$, where three-body recombination losses have been added.

of this resonance, see Methods. However, a dedicated investigation beyond the scope of this work would be required to confirm this feature.

Interference patterns

The modulation of supersolid states presents a unique possibility for extracting the phase information, as the presence or absence of a vortex strongly impacts the interference pattern after time-of-flight (TOF)[40]. This is readily observable by performing expansion calculations with the eGPE, as shown in Fig. 4a. In the presence of a vortex, the interference pattern shows a pronounced minimum in the central region of the signal [a(ii)], which is clearly not the case in a vortex free supersolid [a(i)]. This remarkable feature is a direct consequence of the phase winding and can even be reproduced by a simple toy model simulating the expansion of three non-interacting Gaussian wavepackets, as shown in the insets of Fig. 4a(i) and (ii). Note that in the eGPE, the expansion time was set to 36 ms, during which the self-bound nature of the droplets slows down the expansion corresponding to a few ms in the toy model. Furthermore, this time is strongly dependent on interaction and trap parameters, making the pattern very sensitive to parameter variations, see Methods for more details. Unlike vortex interference patterns from unmodulated states, there is no longer a simple hole left in the center of the cloud, but rather a three-pointed star structure reflecting the symmetries present in the density. The spiral arms appear due to the nonlinear azimuthal 2π phase winding[43], where between each droplet there is a line of minimum signal given by the phase difference of each droplet, in this case, $2\pi/3$. In our calculation, we opt for an initial state featuring three droplets instead of the previously used four droplet state. The symmetry of this state, characterized by equal interdroplet spacing, yields a singular and simple interference pattern when the vortex is in the center of the system, facilitating the distinction between a vortex and vortex-free state. Our simulations show that the critical nucleation frequency is $\Omega^* \approx 0.1\omega_\perp$ for this state.

When performing the experiment with similar parameters as the theory, we observe a remarkable similarity. Figure 4b shows an example interference pattern for a non-rotating sample [b(i)] and the one for a three droplet supersolid when rotating above Ω^* [b(ii)]. In the latter case, we clearly observe a signal minimum at the center, providing the observation of

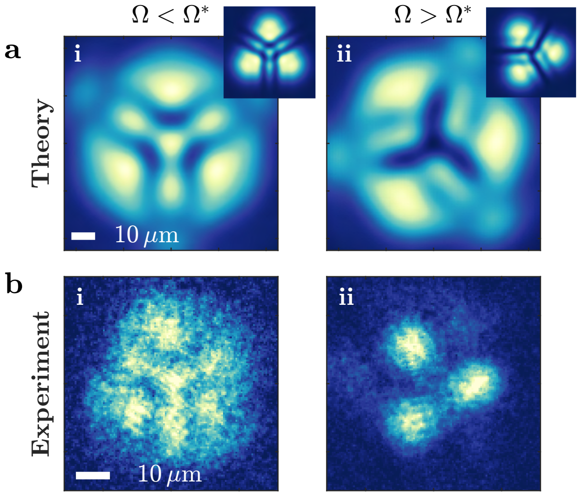

FIG. 4. **Time-of-flight interference pattern.** **a** 36 ms real-time expansion interference pattern for three droplets (i) in the absence of a vortex and (ii) with a vortex. **b** Experimental observation after TOF (i) without rotation and (ii) after 189 ms of rotation at $\Omega = 0.3\omega_\perp$ with $\theta = 30°$, before spiraling up to $\theta = 0°$ in 11 ms, while Ω is kept constant. The supersolid is produced at 18.24(2) G with $(\omega_\perp, \omega_z) = 2\pi \times [50.0(4), 113(2)]$ Hz, the condensed atom number $N \approx 5 \times 10^4$. The theoretical parameters: $N = 5 \times 10^4$, $(\omega_\perp, \omega_z) = 2\pi \times [50, 113]$ Hz and $a_s = 92.5a_0$.

vortices directly in the supersolid state. To test the robustness of this observation, we repeat the measurement many times, and study the occurrence of the non-vortex [b(i)] or vortex [b(ii)] pattern. Among the images with a clear interference pattern, about 70% contain a vortex signature when rotating above $\Omega = 0.3\omega_\perp$, see Methods. This can be understood by considering that supersolid states exist in a very small parameter regime[58], and typical shot-to-shot atom number and magnetic-field (a_s) fluctuations can significantly alter the observed interference pattern.

Conclusions

After three decades since the original predictions[59], we report on the observations of vortices in a supersolid state. This result is relevant not only because it adds the final piece to the cumulative framework of evidence for superfluidity in this state[12], but also because it reveals a distinctive vortex behavior in the supersolid. The system's characteristic response to rotation can serve as a fingerprint to identify supersolidity in diverse systems with multiple broken symmetries, over scales ranging from solid-state systems[30], high-temperature superconductors[60,61], and helium platforms[29–32], to a neutron star's inner crust[18,62].

Furthermore, in the context of supersolids, a fascinating interplay of competing length scales emerges. These include the separation between vortices, the wavelength of the self-forming crystal, and the diameter of the vortex core. This competition has the potential to lead to intriguing dynamics, ranging from constrained motion and pinning to avalanche escape. These phenomena are genuinely unique to supersolids.

Acknowledgements

We are indebted to Jean Dalibard for inspiring discussions on the interference pattern of supersolids in the presence of a vortex. We thank Wolfgang Ketterle, Sandro Stringari, Alessio Recati and Giacomo Lamporesi for discussions. This work was supported by the European Research Council through the Advanced Grant DyMETEr (No. 101054500), the QuantERA grant MAQS by the Austrian Science Fund FWF (No. I4391-N), a joint-project grant from the Austrian Science Fund FWF (No. I-4426), and a NextGeneration EU grant AQuSIM by the Austrian Research Promotion Agency FFG (No. FO999896041). E.P. acknowledges support by the Austrian Science Fund (FWF) within the DK-ALM (No. W1259-N27). T.B. acknowledges financial support through an ESQ Discovery grant by the Austrian Academy of Sciences.

Author contributions

E.C., L.K., A.L., C.U., C.P., M.J.M., and F.F. performed the experimental work and data analysis. E.P. and T.B. performed the theoretical work. All authors contributed to the interpretation of the results and the preparation of the manuscript.

Data availability

Data pertaining to this work can be found at `https://doi.org/10.5281/zenodo.10695943`.

Code availability

The codes that support the findings of this study are available from the corresponding author upon reasonable request.

---

[*] These authors contributed equally to this work.

[†] Current address: Institute for Quantum Electronics, ETH Zürich, Otto-Stern-Weg 1, 8093 Zürich, Switzerland

[‡] Correspondence should be addressed to: `francesca.ferlaino@uibk.ac.at`

1. E. P. Gross, Unified Theory of Interacting Bosons, Phys. Rev. **106**, 161 (1957).
2. E. P. Gross, Classical theory of boson wave fields, Annals of Physics **4**, 57 (1958).
3. A. Andreev and I. Lifshitz, Quantum Theory of Defects in Crystals, J. Exp. Theo. Phys. **56**, 2057 (1969).
4. G. Chester, Speculations on Bose-Einstein condensation and quantum crystals, Physical Review A **2**, 256 (1970).
5. A. J. Leggett, Can a solid be "superfluid"?, Physical Review Letters **25**, 1543 (1970).
6. J.-R. Li, J. Lee, W. Huang, S. Burchesky, B. Shteynas, F. Ç. Top, A. O. Jamison, and W. Ketterle, A stripe phase with supersolid properties in spin–orbit-coupled Bose–Einstein condensates, Nature **543**, 91 (2017).
7. J. Léonard, A. Morales, P. Zupancic, T. Esslinger, and T. Donner, Supersolid formation in a quantum gas breaking a continuous translational symmetry, Nature **543**, 87 (2017).
8. F. Böttcher, J.-N. Schmidt, M. Wenzel, J. Hertkorn, M. Guo, T. Langen, and T. Pfau, Transient Supersolid Properties in an Array of Dipolar Quantum Droplets, Phys. Rev. X **9**, 011051 (2019).
9. L. Tanzi, E. Lucioni, F. Famà, J. Catani, A. Fioretti, C. Gabbanini, R. N. Bisset, L. Santos, and G. Modugno, Observation of a Dipolar Quantum Gas with Metastable Supersolid Properties,

Phys. Rev. Lett. **122**, 130405 (2019).

10. L. Chomaz, D. Petter, P. Ilzhöfer, G. Natale, A. Trautmann, C. Politi, G. Durastante, R. M. W. van Bijnen, A. Patscheider, M. Sohmen, M. J. Mark, and F. Ferlaino, Long-Lived and Transient Supersolid Behaviors in Dipolar Quantum Gases, Phys. Rev. X **9**, 021012 (2019).
11. M. A. Norcia, C. Politi, L. Klaus, E. Poli, M. Sohmen, M. J. Mark, R. N. Bisset, L. Santos, and F. Ferlaino, Two-dimensional supersolidity in a dipolar quantum gas, Nature **596**, 357–361 (2021).
12. L. Chomaz, I. Ferrier-Barbut, F. Ferlaino, B. Laburthe-Tolra, B. L. Lev, and T. Pfau, Dipolar physics: a review of experiments with magnetic quantum gases, Reports on Progress in Physics **86**, 026401 (2022).
13. M. Guo, F. Böttcher, J. Hertkorn, J.-N. Schmidt, M. Wenzel, H. P. Büchler, T. Langen, and T. Pfau, The low-energy Goldstone mode in a trapped dipolar supersolid, Nature **564**, 386 (2019).
14. L. Klaus, T. Bland, E. Poli, C. Politi, G. Lamporesi, E. Casotti, R. N. Bisset, M. J. Mark, and F. Ferlaino, Observation of vortices and vortex stripes in a dipolar condensate, Nature Physics **18**, 1453 (2022).
15. T. Bland, G. Lamporesi, M. J. Mark, and F. Ferlaino, Vortices in dipolar Bose-Einstein condensates, Comptes Rendus. Physique (Online first) (2023).
16. M. A. Norcia, E. Poli, C. Politi, L. Klaus, T. Bland, M. J. Mark, L. Santos, R. N. Bisset, and F. Ferlaino, Can Angular Oscillations Probe Superfluidity in Dipolar Supersolids?, Phys. Rev. Lett. **129**, 040403 (2022).
17. T. Bland, E. Poli, C. Politi, L. Klaus, M. A. Norcia, F. Ferlaino, L. Santos, and R. N. Bisset, Two-Dimensional Supersolid Formation in Dipolar Condensates, Phys. Rev. Lett. **128**, 195302 (2022).
18. E. Poli, T. Bland, S. J. White, M. J. Mark, F. Ferlaino, S. Trabucco, and M. Mannarelli, Glitches in rotating supersolids, Phys. Rev. Lett. **131**, 223401 (2023).
19. L. Onsager, In discussion on paper by C. J. Gorter, Nuovo Cimento **6**, 249 (1949).
20. R. Feynman, Chapter II Application of Quantum Mechanics to Liquid Helium (Elsevier, 1955) pp. 17–53.
21. E. Yarmchuk, M. Gordon, and R. Packard, Observation of stationary vortex arrays in rotating superfluid helium, Phys. Rev. Lett. **43**, 214 (1979).
22. G. P. Bewley, D. P. Lathrop, and K. R. Sreenivasan, Visualization of quantized vortices, Nature **441**, 588 (2006).
23. J. R. Abo-Shaeer, C. Raman, J. M. Vogels, and W. Ketterle, Observation of vortex lattices in Bose-Einstein condensates, Science **292**, 476 (2001).
24. M. W. Zwierlein, J. R. Abo-Shaeer, A. Schirotzek, C. H. Schunck, and W. Ketterle, Vortices and superfluidity in a strongly interacting Fermi gas, Nature (London) **435**, 1047 (2005).
25. K. G. Lagoudakis, M. Wouters, M. Richard, A. Baas, I. Carusotto, R. André, L. S. Dang, and B. Deveaud-Plédran, Quantized vortices in an exciton–polariton condensate, Nature physics **4**, 706 (2008).
26. F. S. Wells, A. V. Pan, X. R. Wang, S. A. Fedoseev, and H. Hilgenkamp, Analysis of low-field isotropic vortex glass containing vortex groups in YBa2Cu3O7-x thin films visualized by scanning SQUID microscopy, Scientific reports **5**, 8677 (2015).
27. L. Embon, Y. Anahory, Ž. L. Jelić, E. O. Lachman, Y. Myasoedov, M. E. Huber, G. P. Mikitik, A. V. Silhanek, M. V. Milošević, A. Gurevich, *et al.*, Imaging of super-fast dynamics and flow instabilities of superconducting vortices, Nature Communications **8**, 85 (2017).
28. D. F. Agterberg, J. S. Davis, S. D. Edkins, E. Fradkin, D. J. Van Harlingen, S. A. Kivelson, P. A. Lee, L. Radzihovsky, J. M. Tranquada, and Y. Wang, The physics of pair-density waves: Cuprate superconductors and beyond, Annual Review of Condensed Matter Physics **11**, 231 (2020).
29. L. V. Levitin, B. Yager, L. Sumner, B. Cowan, A. J. Casey, J. Saunders, N. Zhelev, R. G. Bennett, and J. M. Parpia, Evidence for a Spatially Modulated Superfluid Phase of He3 under Confinement, Phys. Rev. Lett. **122**, 085301 (2019).
30. M. Hamidian, S. Edkins, S. H. Joo, A. Kostin, H. Eisaki, S. Uchida, M. Lawler, E.-A. Kim, A. Mackenzie, K. Fujita, *et al.*, Detection of a Cooper-pair density wave in Bi2Sr2CaCu2O8+ x, Nature **532**, 343 (2016).
31. Y. Liu, T. Wei, G. He, Y. Zhang, Z. Wang, and J. Wang, Pair density wave state in a monolayer high-t_c iron-based superconductor, Nature **618**, 934 (2023).
32. J. Nyéki, A. Phillis, A. Ho, D. Lee, P. Coleman, J. Parpia, B. Cowan, and J. Saunders, Intertwined superfluid and density wave order in two-dimensional ^{4}He, Nature Physics **13**, 455 (2017).
33. G. Natale, R. van Bijnen, A. Patscheider, D. Petter, M. Mark, L. Chomaz, and F. Ferlaino, Excitation spectrum of a trapped dipolar supersolid and its experimental evidence, Physical review letters **123**, 050402 (2019).
34. L. Tanzi, S. Roccuzzo, E. Lucioni, F. Famà, A. Fioretti, C. Gabbanini, G. Modugno, A. Recati, and S. Stringari, Supersolid symmetry breaking from compressional oscillations in a dipolar quantum gas, Nature **574**, 382 (2019).
35. P. Ilzhöfer, M. Sohmen, G. Durastante, C. Politi, A. Trautmann, G. Natale, G. Morpurgo, T. Giamarchi, L. Chomaz, M. J. Mark, and F. Ferlaino, Phase coherence in out-of-equilibrium supersolid states of ultracold dipolar atoms, Nature Physics **17**, 356 (2021).
36. G. Biagioni, N. Antolini, B. Donelli, L. Pezzè, A. Smerzi, M. Fattori, A. Fioretti, C. Gabbanini, M. Inguscio, L. Tanzi, and G. Modugno, Sub-unity superfluid fraction of a supersolid from self-induced josephson effect, arXiv:2311.04757 (2023).
37. O. M. Maragò, S. A. Hopkins, J. Arlt, E. Hodby, G. Hechenblaikner, and C. J. Foot, Observation of the Scissors Mode and Evidence for Superfluidity of a Trapped Bose-Einstein Condensed Gas, Phys. Rev. Lett. **84**, 2056 (2000).
38. L. Tanzi, J. Maloberti, G. Biagioni, A. Fioretti, C. Gabbanini, and G. Modugno, Evidence of superfluidity in a dipolar supersolid from nonclassical rotational inertia, Science **371**, 1162 (2021).
39. S. Roccuzzo, A. Recati, and S. Stringari, Moment of inertia and dynamical rotational response of a supersolid dipolar gas, Phys. Rev. A **105**, 023316 (2022).
40. A. Gallemí, S. Roccuzzo, S. Stringari, and A. Recati, Quantized vortices in dipolar supersolid Bose-Einstein-condensed gases, Physical Review A **102**, 023322 (2020).
41. S. Roccuzzo, A. Gallemí, A. Recati, and S. Stringari, Rotating a supersolid dipolar gas, Physical review letters **124**, 045702 (2020).
42. N. Henkel, F. Cinti, P. Jain, G. Pupillo, and T. Pohl, Supersolid vortex crystals in Rydberg-dressed Bose-Einstein condensates, Physical Review Letters **108**, 265301 (2012).
43. F. Ancilotto, M. Barranco, M. Pi, and L. Reatto, Vortex properties in the extended supersolid phase of dipolar Bose-Einstein condensates, Physical Review A **103**, 033314 (2021).
44. S. B. Prasad, T. Bland, B. C. Mulkerin, N. G. Parker, and A. M. Martin, Vortex lattice formation in dipolar Bose-Einstein condensates via rotation of the polarization, Physical Review A **100**, 023625 (2019).

45. J. Stuhler, A. Griesmaier, T. Koch, M. Fattori, T. Pfau, S. Giovanazzi, P. Pedri, and L. Santos, Observation of Dipole-Dipole Interaction in a Degenerate Quantum Gas, Phys. Rev. Lett. **95**, 150406 (2005).
46. F. Wächtler and L. Santos, Quantum filaments in dipolar Bose-Einstein condensates, Phys. Rev. A **93**, 061603 (2016).
47. I. Ferrier-Barbut, H. Kadau, M. Schmitt, M. Wenzel, and T. Pfau, Observation of Quantum Droplets in a Strongly Dipolar Bose Gas, Phys. Rev. Lett. **116**, 215301 (2016).
48. L. Chomaz, S. Baier, D. Petter, M. J. Mark, F. Wächtler, L. Santos, and F. Ferlaino, Quantum-Fluctuation-Driven Crossover from a Dilute Bose-Einstein Condensate to a Macrodroplet in a Dipolar Quantum Fluid, Phys. Rev. X **6**, 041039 (2016).
49. R. N. Bisset, R. M. Wilson, D. Baillie, and P. B. Blakie, Ground-state phase diagram of a dipolar condensate with quantum fluctuations, Phys. Rev. A **94**, 033619 (2016).
50. A. Recati, F. Zambelli, and S. Stringari, Overcritical rotation of a trapped Bose-Einstein condensate, Phys. Rev. Lett. **86**, 377 (2001).
51. S. Sinha and Y. Castin, Dynamic instability of a rotating Bose-Einstein condensate, Phys. Rev. Lett. **87**, 190402 (2001).
52. K. W. Madison, F. Chevy, V. Bretin, and J. Dalibard, Stationary states of a rotating Bose-Einstein condensate: Routes to vortex nucleation, Phys. Rev. Lett. **86**, 4443 (2001).
53. R. M. van Bijnen, D. H. O'Dell, N. G. Parker, and A. Martin, Dynamical instability of a rotating dipolar Bose-Einstein condensate, Phys. Rev. Lett. **98**, 150401 (2007).
54. M. Sohmen, C. Politi, L. Klaus, L. Chomaz, M. J. Mark, M. A. Norcia, and F. Ferlaino, Birth, Life, and Death of a Dipolar Supersolid, Phys. Rev. Lett. **126**, 233401 (2021).
55. M. R. Matthews, B. P. Anderson, P. C. Haljan, D. S. Hall, C. E. Wieman, and E. A. Cornell, Vortices in a Bose-Einstein Condensate, Phys. Rev. Lett. **83**, 2498 (1999).
56. K. W. Madison, F. Chevy, W. Wohlleben, and J. Dalibard, Vortex formation in a stirred Bose-Einstein condensate, Phys. Rev. Lett. **84**, 806 (2000).
57. M. Šindik, A. Recati, S. M. Roccuzzo, L. Santos, and S. Stringari, Creation and robustness of quantized vortices in a dipolar supersolid when crossing the superfluid-to-supersolid transition, Phys. Rev. A **106**, L061303 (2022).
58. E. Poli, T. Bland, C. Politi, L. Klaus, M. A. Norcia, F. Ferlaino, R. N. Bisset, and L. Santos, Maintaining supersolidity in one and two dimensions, Phys. Rev. A **104**, 063307 (2021).
59. Y. Pomeau and S. Rica, Dynamics of a model of supersolid, Phys. Rev. Lett. **72**, 2426 (1994).
60. G. Blatter, M. V. Feigel'man, V. B. Geshkenbein, A. I. Larkin, and V. M. Vinokur, Vortices in high-temperature superconductors, Reviews of Modern Physics **66**, 1125 (1994).
61. W.-K. Kwok, U. Welp, A. Glatz, A. E. Koshelev, K. J. Kihlstrom, and G. W. Crabtree, Vortices in high-performance high-temperature superconductors, Reports on Progress in Physics **79**, 116501 (2016).
62. N. Chamel, Neutron conduction in the inner crust of a neutron star in the framework of the band theory of solids, Phys. Rev. C **85**, 035801 (2012).
63. Y. Tang, A. Sykes, N. Q. Burdick, J. L. Bohn, and B. L. Lev, s-wave scattering lengths of the strongly dipolar bosons ^{162}Dy and ^{164}Dy, Phys. Rev. A **92**, 022703 (2015).
64. T. Maier, I. Ferrier-Barbut, H. Kadau, M. Schmitt, M. Wenzel, C. Wink, T. Pfau, K. Jachymski, and P. S. Julienne, Broad universal Feshbach resonances in the chaotic spectrum of dysprosium atoms, Phys. Rev. A **92**, 060702 (2015).
65. Y. Tang, A. G. Sykes, N. Q. Burdick, J. M. DiSciacca, D. S. Petrov, and B. L. Lev, Anisotropic Expansion of a Thermal Dipolar Bose Gas, Phys. Rev. Lett. **117**, 155301 (2016).
66. A. R. P. Lima and A. Pelster, Quantum fluctuations in dipolar Bose gases, Phys. Rev. A **84**, 041604 (2011).
67. P. Blakie, A. Bradley, M. Davis, R. Ballagh, and C. Gardiner, Dynamics and statistical mechanics of ultra-cold Bose gases using c-field techniques, Advances in Physics **57**, 363 (2008).
68. M. A. Norcia, E. Poli, C. Politi, L. Klaus, T. Bland, M. J. Mark, L. Santos, R. N. Bisset, and F. Ferlaino, Can angular oscillations probe superfluidity in dipolar supersolids?, arXiv:2111.07768 (2021).
69. M. J. D. Powell, An efficient method for finding the minimum of a function of several variables without calculating derivatives, The Computer Journal **7**, 155 (1964), https://academic.oup.com/comjnl/article-pdf/7/2/155/959784/070155.pdf.

Methods

Experimental procedure

We prepare an ultracold gas of ^{164}Dy atoms in an optical dipole trap (ODT), similar to our previous work[14]. The trap is formed through three overlapping laser beams, operating at $1064\,\mathrm{nm}$. All the studies are performed in a cylindrically symmetric trap, typically with $\omega_\perp = 2\pi \times 50.3(2)\,\mathrm{Hz}$, where $\omega_\perp$ is the geometric average $\omega_\perp = \sqrt{\omega_x \omega_y}$. The aspect ratio $\omega_z/\omega_\perp$ varies from 2 to 3; the specific values of ω_z are stated in the figures' captions. The aspect ratio ω_x/ω_y is crucial for the applicability of magnetostirring[14]: throughout the paper, the deviation of ω_x/ω_y from 1 is $< 2\%$.

For this work, we tilt the magnetic field vector $\mathbf{B}$ from the vertical position to $\theta = 30°$ from the z-axis in the last stage of evaporation, while maintaining its magnitude constant. The values of the magnetic field are: $19.30(2)$ G for the unmodulated BEC, $18.30(2)$ G for the SSP in Fig. 3, and $18.24(2)$ G for Figs. 2 and 4. The magnetic field is calibrated through radio frequency (RF) spectroscopy. Moreover, ^{164}Dy has a dense spectrum of narrow Feshbach resonances, as shown in Extended Data Fig. 1. We use the positions of such resonances as references to compensate for drifts of the magnetic field. The condensed atom number after the evaporation sequence ranges from 3×10^4 to 7×10^4, depending on the measurement.

After preparation, the magnetic field is rotated; details can be found in the following sections. Finally, we image the quantum gas using a $421\,\mathrm{nm}$ light pulse, propagating along the z-axis. For the data in Figs. 2 and 3, we let the atomic cloud expand for $3\,\mathrm{ms}$ and take a phase contrast and absorption image, respectively. When comparing theoretical and experimental images, we rescale the image size by 1.36 in the theory to account for this small expansion time. The results of Fig. 4 are instead obtained with absorption imaging after $36\,\mathrm{ms}$ TOF.

For the experimental images in Fig. 2, we enhanced the contrast of the droplets by applying a Gaussian filter of size $\sigma = 1$ px ($\simeq 0.5\,\mu$m) followed by a sharpening convolution filter with kernel F:

$$F = \begin{bmatrix} 0 & -1 & 0 \\ -1 & 5 & -1 \\ 0 & -1 & 0 \end{bmatrix}. \tag{1}$$

Magnetostirring

To magnetostir the atomic cloud, we rotate the magnetic field vector around the z-axis[14]. In brief, the breaking of cylindrical symmetry that enables the transfer of angular momentum by rotating the magnetic field vector $\mathbf{B}$ (magnetostirring) is achieved by tilting $\mathbf{B}$ into the plane. This is a direct consequence of the phenomenon of magnetostriction[45]. For all the measurements in this paper, $\mathbf{B}$ is tilted from the z-axis by an angle $\theta = 30°$. At our magnetic field values, this angle is optimal for vortex nucleation within the experimental time scales[15]. In general, smaller angles would increase the nucleation time; at the same time, a much bigger angle would make the dipolar interaction dominantly attractive, holding the cloud together and thus also increasing the nucleation time. From the experimental point of view, $\theta = 30°$ enables the observation of the droplets aligning along $\mathbf{B}$ while retaining the ability to discern individual droplets when observing the integrated density, see Fig. 2. For all datasets, we then directly rotate $\mathbf{B}$ at the chosen frequency Ω. The rotation is continued for a rotation time t_Ω after which the ODT is turned off, and an image is taken after expansion.

Scattering length

The conversion from magnetic field to scattering length for ^{164}Dy at our magnetic field values has not been mapped. However, combining knowledge on the conversion in other magnetic field ranges[63–65], together with the theoretical identification of the critical scattering lengths for the BEC to SSP transition, allows for an educated guess. It is important to highlight that the isotope ^{164}Dy has the advantage of exhibiting supersolidity at the background value of the scattering length, while the BEC phase usually requires some mild tuning of a_s. The specific values used in this paper are highlighted on the Feshbach loss spectrum in Extended Data Fig. 1. For our theoretical simulations (see below), we find that a scattering length a_s in the range $90a_0$-$95a_0$ gives a good agreement with the experimentally observed supersolid states.

Interaction quench

For the in situ detection of vortices in the supersolid phase, we map the supersolid into an unmodulated BEC, similarly to the approach used to observe them in the BCS phase of strongly interacting Fermi gases[24]. In particular, we increase the absolute value of the magnetic field from $18.30(2)$ G to $19.30(2)$ G in $1\,\mathrm{ms}$ after stopping the rotation and we then release the sample from the trap. We repeat this sequence for different values of angular velocity Ω and for different rotation times t_Ω. For each experimental point in Fig. 3a and 3c, we take 7-9 pictures. Using phase contrast imaging, we ensured that the ramp time is long enough to melt the droplets into an unmodulated state, but also short enough to avoid atom losses when crossing the Feshbach resonances present between the initial and final magnetic field values (see Extended Data Fig. 1).

Extended Gross-Pitaevskii equation

At the mean-field level, the ground state solutions, time-dependent dynamics, and nature of the BEC-to-SSP transitions are well described by the extended Gross-Pitaevskii formalism[46–49]. This combines the two-body particle interactions, described by the two-body pseudo-potential,

$$U(\mathbf{r}) = \frac{4\pi\hbar^2 a_\mathrm{s}}{m}\delta(\mathbf{r}) + \frac{3\hbar^2 a_\mathrm{dd}}{m}\frac{1 - 3\,(\hat{\mathbf{e}}(t)\cdot\mathbf{r})^2}{r^3}\,, \tag{2}$$

where the first term describes short-range interactions governed by the s-wave scattering length a_s, with Planck's constant $\hbar$ and particle mass m. This quantity is independently tunable through Feshbach resonances. The second term represents the anisotropic and long-ranged dipole-dipole interactions, characterized by dipole length $a_\mathrm{dd} = \mu_0\mu_m^2 m/12\pi\hbar^2$, with magnetic moment μ_m and vacuum permeability μ_0. We always consider ^{164}Dy, such that $a_{\text{dd}} = 130.8\,a_0$, where a_0 is the Bohr radius. For the trap parameters and atom numbers used here, the supersolid phase is found for scattering lengths in the range $a_s = [90, 95]a_0$, i.e. $\epsilon_{\text{dd}} = a_{\text{dd}}/a_{\text{s}} \geq 1.37$. The dipoles are polarized uniformly along a time-dependent axis, given by

$$\hat{\mathbf{e}}(t) = (\sin\theta(t)\cos\phi(t), \sin\theta(t)\sin\phi(t), \cos\theta(t)) \tag{3}$$

with time dependent polarization angle $\theta(t)$ and $\phi(t) = \int_0^t \mathrm{d}t'\Omega(t')$, for rotation frequency protocol $\Omega(t)$.

Three-body recombination losses are prevalent in dipolar supersolid experiments due to the increased peak density when compared to unmodulated states. In the theory, these are introduced through a time-dependent atom loss

$$\dot{N} = -L_3\langle n^2\rangle N\,, \tag{4}$$

for density n. We take the fixed coefficient $L_3 = 1.2\times10^{-41}\mathrm{m}^6\mathrm{s}^{-1}$ for our simulations[47]. This leads to an additional non-Hermitian term in the Hamiltonian $-\mathrm{i}\hbar L_3 n^2/2$.

Beyond-mean-field effects are treated through the inclusion of a Lee–Huang–Yang correction term[66]

$$\gamma_{\text{QF}} = \frac{128\hbar^2}{3m}\sqrt{\pi a_s^5}\,\mathrm{Re}\left\{\mathcal{Q}_5(\epsilon_{dd})\right\}\,, \tag{5}$$

where $\mathcal{Q}_n(x) = \int_0^1 \mathrm{d}u\,(1-x+3xu^2)^{n/2}$, which has an imaginary component for $x > 1$. Finally, the full extended Gross-Pitaevskii equation (eGPE) then reads[46–49]

$$\begin{aligned}\mathrm{i}\hbar\frac{\partial\psi(\mathbf{r},t)}{\partial t} &= \bigg[-\frac{\hbar^2\nabla^2}{2m} + V_{\text{trap}} - \mathrm{i}\hbar L_3|\psi(\mathbf{r},t)|^4/2 \\ &+ \int \mathrm{d}^3\mathbf{r}'\,U(\mathbf{r}-\mathbf{r}')|\psi(\mathbf{r}',t)|^2 + \gamma_{\text{QF}}|\psi(\mathbf{r},t)|^3\bigg]\psi(\mathbf{r},t)\,,\end{aligned} \tag{6}$$

where $\omega_{x,y,z}$ are the harmonic trap frequencies in $V_{\text{trap}} = \frac{1}{2}m\left(\omega_x^2x^2 + \omega_y^2y^2 + \omega_z^2z^2\right)$. The wavefunction ψ is normalized to the total atom number $N = \int \mathrm{d}^3\mathbf{r}|\psi|^2$. Stationary solutions to Eq. (6) are found through the standard imaginary time procedure. The initial state $\psi(\mathbf{r},0)$ of the real-time simulations is obtained by adding non-interacting noise to the stationary solution $\psi_0(\mathbf{r})$. Given the single-particle eigenstates ϕ_n and the complex Gaussian random variables α_n sampled with $\langle|\alpha_n|^2\rangle = (e^{\epsilon_n/k_BT}-1)^{-1}+\frac{1}{2}$ for a temperature $T = 20\,\mathrm{nK}$, the initial state can be described as $\psi(\mathbf{r},0) = \psi_0(\mathbf{r}) + \sum_n' \alpha_n\phi_n(\mathbf{r})$, where the sum is restricted only to the modes with $\epsilon_n \leq 2k_BT$[67].

Toy model interference pattern

Taking N_D static Gaussian wavepackets with parameters of the j^{th} wavepacket given by the widths $\boldsymbol{\sigma}_j = (\sigma_{1,j}, \sigma_{2,j}, \sigma_{3,j})$, positions $\mathbf{r}_j^0 = (r_{1,j}^0, r_{2,j}^0, r_{3,j}^0)$, atom numbers N_j, and phase ϕ_j, the initial total wavefunction is

$$\begin{aligned}\psi(\mathbf{r},0) &= \sum_j^{N_D}\sqrt{\frac{N_j}{(2\pi)^{3/2}}}\exp\left(\mathrm{i}\phi_j\right) \\ &\times \prod_{k=1,2,3}\sqrt{\frac{1}{\sigma_{k,j}}}\exp\left[-\frac{1}{4}\left(r_k - r_{k,j}^0\right)^2/\sigma_{k,j}^2\right].\end{aligned} \tag{7}$$

On the assumption that these wavepackets are non-interacting, then their expansion due to kinetic energy alone can be analytically calculated by applying the free particle propagator in three dimensions, such that the time-dependent solution is

$$\psi(\mathbf{r},t) = \int_{-\infty}^{\infty}\mathrm{d}^3\mathbf{r}'\,\psi(\mathbf{r}',0)K(\mathbf{r},t;\mathbf{r}',0)\,, \tag{8}$$

where

$$K(\mathbf{r},t;\mathbf{r}',t_0) = \left(\frac{m}{2\pi\mathrm{i}\hbar(t-t_0)}\right)^{3/2}\exp\left(\frac{\mathrm{i}m(\mathbf{r}-\mathbf{r}')^2}{2\hbar(t-t_0)}\right). \tag{9}$$

Applying Eq. (8) to Eq. (7) gives the time-dependent multi-wavepacket solution. For brevity, it is not stated here, but the exact solution transpires to be a simple time-dependent replacement of the widths $\left\{\sigma_{k,j} \to \sigma_{k,j}\sqrt{1+\mathrm{i}\hbar t/(2m\sigma_{k,j}^2)}\right\}$ appearing in Eq. (7). An example of the evolution of the TOF pattern is shown in Extended Data Fig. 2 with the parameters of Fig. 4 for longer times. Note that the 3ms TOF pattern, equivalent to the 36 ms when simulating the eGPE (i.e. including interactions), has not yet evolved into the momentum distribution.

Quadrupole modes calculation

We employ real-time simulations with the extended Gross-Pitaevskii equation to investigate the quadrupole mode frequency of the system with the tilted magnetic field, both in the BEC and in the supersolid phase. We initially perturb the system with a sudden small quadrupolar deformation of the trap and, then, we let the system evolve for 1 s. The deformation is done by increasing (decreasing) the trap frequency by 0.5 Hz in the x-direction (y-direction) for 1 ms and then restoring the trap to the original value. During the time evolution, the density distribution in the slice $z = 0$ is fitted with a Gaussian profile, from which we extract the time-dependent width of the system during the evolution. The Fourier transform of the time-dependent width gives the frequency spectrum of all the expected superfluid and crystal quadrupole modes excited by the sudden deformation[40,68]. These frequencies are in agreement with the features of the rotational response of the BEC and supersolid discussed in the main text.

Vortex detection in the theory

The number of vortices is determined by counting 2π windings in the central slice of the phase, $\arg(\psi(x,y,z=0))$. We restrict the search to a circle of radius $6\,\mu$m, such that vortices are only counted inside the condensate surface in the BEC case, or within the halo in the supersolid state. To visualize the vortex tubes plotted in Fig. 1, we plot isosurfaces of the velocity field.

In-situ vortex detection algorithm

To count the number of vortices, we identify the number of voids in the density in the in-situ images, following a similar procedure of our earlier work[14]. In short, we first apply a Gaussian filter of size $\sigma = 1$ px ($\simeq 0.5\,\mu$m), then the sharpening convolution filter of Eq. (1) to each image $n_{\rm img}$ for noise reduction. We then prepare a blurred reference image $n_{\rm ref}$ by applying a Gaussian filter of size $\sigma = 3$ px ($\simeq 1.5\,\mu$m) to each $n_{\rm img}$ and calculate the residuals between this reference and the original image $n_{\rm res} = n_{\rm ref} - n_{\rm img}$. Finally, vortices are detected as peaks in the residual image $n_{\rm res}$ using a peak detection algorithm (peak_local_max from the SKIMAGE Python library). To avoid spurious vortex detection, we discard peaks with a distance below 3 px, and peaks with an amplitude below a chosen contrast threshold of 0.34.

We verify the robustness of the vortex detection by varying this contrast threshold between 0.34 and 0.42, which changes the number of selected peaks but gives the same qualitative result on the whole data set (see Extended Data Fig. 4). In the experimental data (Extended Data Fig. 4b) there is a small peak centered at $\Omega = 0.35\omega_\perp$ for all thresholds considered, hinting towards the expected superfluid quadrupole mode resonance, see Fig. 3.

Time-of-flight vortex detection algorithm

In the interference pattern, a striking difference between a single vortex and a vortex-free state is the absence or presence of a central density feature. This feature provides us with another fingerprint of vortices, thus allowing for binary classification of the experimental TOF images and extraction of the vortex occurrence probability as a function of Ω. In the following paragraphs, our classification protocol is described.

First, we prepare all the images, $n_{\rm i}$, by denoising them with a Gaussian filter of size $\sigma = 2$ px and by normalizing to the maximum density, $\max(n_{\rm i}) = 1$. Among those, we then select two reference images, one for each case: the presence ($n_{\rm r}^{\rm v}$) or absence ($n_{\rm r}^{\emptyset}$) of a vortex; see insets in Extended Data Fig. 5a. These will be used to classify all images.

Then, using 'Powell' minimization[69], we translate and rotate each image to best overlap with the references. To quantify the similarity of the images to each reference image, we calculate the sum squared differences, $S^{\{\rm v,\emptyset\}}$, between $n_{\rm i}$ and $n^{\{\rm v,\emptyset\}}$. Here, high values of $S^{\{\rm v,\emptyset\}}$ indicate large dissimilarity between the images.

We generate a cumulative distribution function for $S^{\rm v}$ and $S^{\emptyset}$, which are normalized by the total number of images (see Extended Data Fig. 5a). Using the cumulative distribution, we generate one subset of images for each reference, which are the $X\%$ most similar images. The remaining images are not classified. Note that so far, the analysis is rotation frequency independent. Finally, we extract the number of images within each category as a function of rotation frequency (Ω), see Extended Data Fig. 5b. Renormalizing to the total number of classified images, we obtain the ratio of images that have a central vortex, see Extended Data Fig. 5c.

At low rotation frequency, the vortex-free interference pattern is dominating. Crucially, the ratio of images with a vortex increases with increasing Ω, consistent with our eGPE simulations and experimental findings shown in Fig. 3. This result is robust against choice of the classification threshold X as shown in Extended Data Fig. 5c(1-2) for $X = 15\,\%$ and $X = 30\,\%$ (see dashed-dotted line in Extended Data Fig. 5a). Note that fluctuations of the experimental parameters lead to a non-zero vortex signal even without rotation. Note that the selection threshold is kept low, ensuring unambiguous categorization of the images.

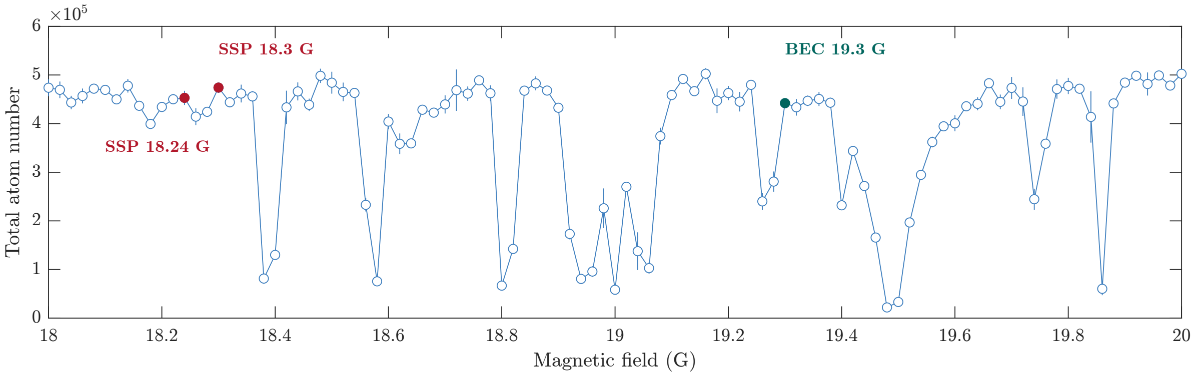

Extended Data Fig. 1. **Loss spectrum of ^{164}Dy**. The spectrum is obtained from horizontal absorption imaging, by varying the magnetic field at which the evaporative cooling ($T \approx 500\,\mathrm{nK}$) is conducted, with a step size of $20\,\mathrm{mG}$. The magnetic field values used are highlighted in red (SSP) and green (BEC). Error bars represent the standard error.

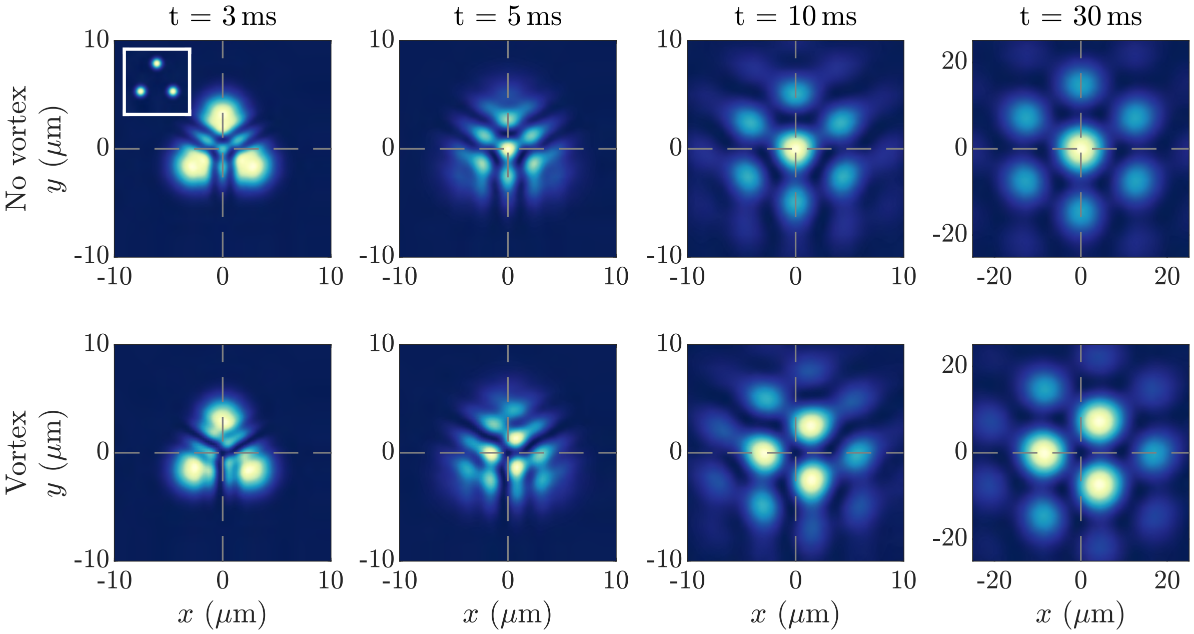

Extended Data Fig. 2. **Time of flight predictions from the Gaussian toy model**. Longer TOF density profiles for the solution shown in Fig. 4 of the main text. The inset of the first figure shows the initial condition for all states. After 10 ms the density pattern has frozen into the momentum distribution of the initial cloud. The gray lines show the axis center (0,0), highlighting the immediate difference between a no vortex and vortex expansion from the central density.

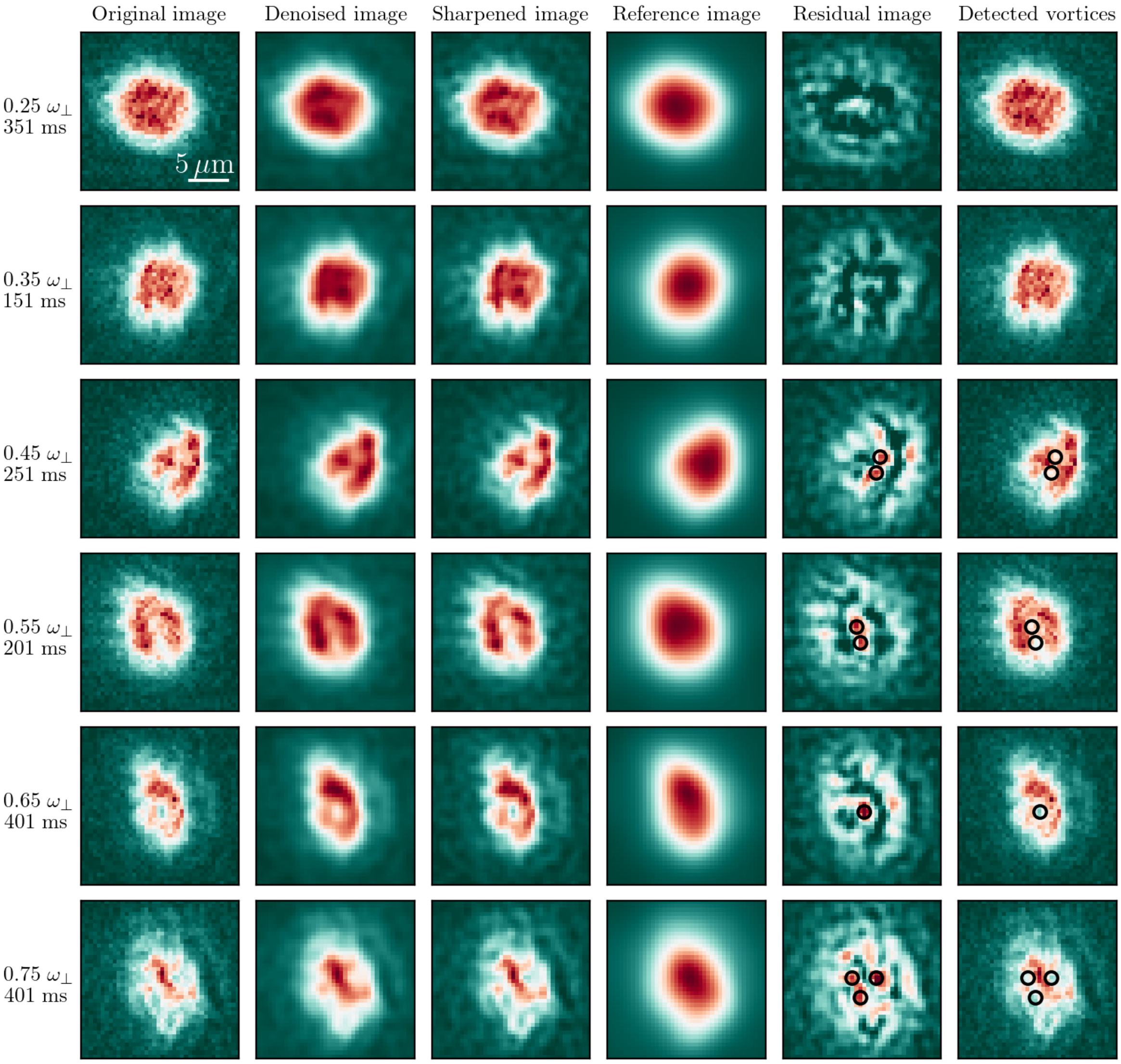

Extended Data Fig. 3. **Image processing for the detection of vortices.** Each row indicates different rotation frequency and duration parameters (indicated on the left). Each column is a step of the processing protocol which goes as follows. The data (column 1) is normalized and denoised with a Gaussian filter of size $\sigma = 1$ (column 2), and a sharpening mask is applied to magnify the presence of vortices (column 3). The reference image is built from the data image where all density variations are eliminated with a Gaussian filter of size $\sigma = 3$ (column 4). The residuals (column 5) are obtained from the subtraction of the data to the reference, converting the density depletions to a positive signal. The vortices (black circles) are detected with a peak detection algorithm with threshold 0.38. The last column shows the location of the vortices on the original image data. Varying the threshold value modifies the absolute vortex count of each individual image but not the overall qualitative result (see Extended Data Fig. 4).

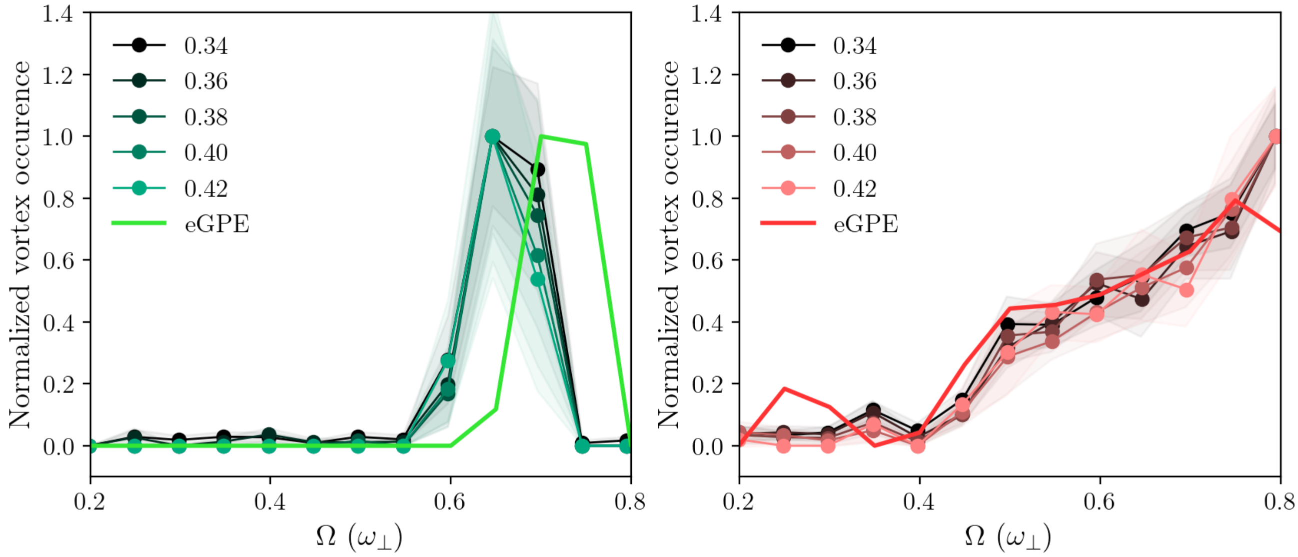

Extended Data Fig. 4. **Vortex detection as a function of the threshold parameter.** Normalized vortex occurrence integrated over 500 ms of rotation in the BEC phase (left) and in the supersolid phase (right) as a function of the rotation frequency, for varying contrast threshold between 0.34 and 0.42 (see Extended Data Fig. 3). The shaded areas indicate the error on the mean, *i.e.* the standard deviation divided by the square root of the number of points (8). The solid lines are visual help. The results of the extended-GPE simulations (see Fig. 3) are plotted in thick solid lines as a comparison.

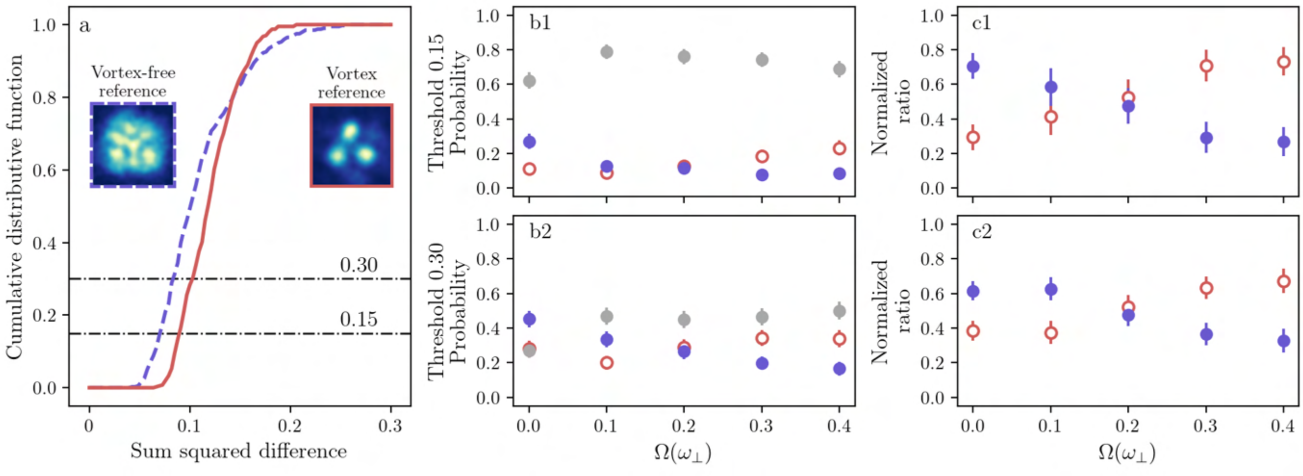

Extended Data Fig. 5. **Probability of detecting a vortex as a function of the rotation frequency**. **a** Cumulative distribution function obtained from the calculated sum squared differences over the whole data set, with each of vortex (solid line) and vortex-free (dashed line) references (see inset images). **b** With a defined threshold X (dashed-dotted lines on **a**) on the cumulative distribution function, each image is assigned to a category: vortex (red empty circles), vortex-free (blue filled circles), or no classification (grey filled circles). **c** Probability of detecting a vortex signal and vortex-free signal out of the selected images in **b**. The error bars indicate the Clopper-Pearson uncertainty associated with image classification. Top and bottom rows show the classification result for respective thresholds 0.15 and 0.30 on the cumulative distribution function, showing the independence of the signal from the threshold.

4.4 Outlook

"Can a solid be 'superfluid'?" was asked by Gross, Andreev, Lifshitz, Chester, and Leggett more than 50 years ago [257, 79, 80, 81] and we can finally answer it with a clear "Yes!". We have shown that quantized vortices are nucleated in rotating ultracold dipolar gases in the supersolid state, which is a hallmark signature of superfluid flow. Together with the observation of Goldstone modes [129] and the study of the josephson effect [124, 132], this result cements our understanding of the supersolid state exhibiting superfluid and solid properties (as studied in [126, 127]). These works open the door to further understanding of supersolids. In the following, I would like to give a brief outlook on three possible research directions:

Rotating ID regime - In our work we have compared the rotational dynamics of BECs and supersolids. The third phase of independent droplets is experimentally challenging, because the lifetime and stability of a fixed number droplet state is limited by large three-body losses due to the high densities of the droplets [287, 91]. Therefore the experiment needs further improvements to either increase the lifetime of the states, e.g. by improving the stability of the magnetic field, or to reduce the time needed to impart angular momentum while in the ID regime, e.g. by rotating the cloud before condensing [215]. This would then allow us to experimentally study, for example, the dynamics of 2D arrays of independent droplets and the fate of a vortex-bearing SS state as it crosses the transition to the ID regime, where the global coherence is lost and vortices can no longer exist.

Vortex pinning - For the first time we were able to nucleate vortices in an ultracold gas experiment with a modulated density distribution. The consequence is, that the vortex dynamics are strongly restricted by its environment. In such a system interesting phenomena such as vortex pinning can be studied. Vortex pinning (or in solid state physics often "flux pinning") means that vortices are inhibited from moving by a local potential, such as that caused by impurities in type-II-superconductors [288]. Understanding vortex pinning is valuable as effects such as vortex pinning are desirable for superconductors because they prevent "flux creep". This effect can lead to pseudo-resistance and therefore poorer performance for the superconducting material [289]. In supersolids this pinning force is defined by the density profile and therefore the interaction strength $\varepsilon_{\mathrm{dd}}$, atom number N and the external trap parameters ω_{trap}, giving us a large toolbox to study the pinning.

Rotating supersolids as simulators - A major interest lies in the possibility of constructing model systems in the laboratory with a high degree of control that can simulate physical systems that are costly to simulate on classical computers (such as frustrated magnetism [68], the Fermi-Hubbard model [290] or the quantum hall effect [291]) or inaccessible experimentally yet. Astronomical systems such as neutron stars are among the latter, since we do not have the means to look into them directly and understand their structure [292]. Earth-based simulators may allow to verify theories about these systems. In the inner crust of neutron stars heavy nuclei are forced so close together by gravity that neutrons drip into the environment and form a superfluid background around the cores [293]. Additionally, neutron stars are rapidly rotating objects, where the rotation frequency can be measured. This is reminiscent of the supersolid state that was presented in this thesis. Therefore, dipolar quantum gas experiments promise to serve as simulators of a 2D version of the inner crust of neutron stars. This already resulted in theoretical studies of the glitch mechanism [294, 295] in our group using the supersolid as a simulator platform [283, 126]. Improving the atomnumber and stability of our supersolid state as well as improving our phase-contrast imaging so that it is non-destructive [277] would allow us to follow vortex motion inside the rotating cloud and study phenomena such as the glitch mechanism experimentally in our laboratory.

5

What's next? A dipolar, double species Quantum Gas Microscope (ddQGM)

And now for something completely different.

The Announcer
Monty Python's Flying Circus (1969-1974)

So far, we have worked with large clouds of atoms, probing macroscopic observables such as density distribution, temperature or the dynamics of the system. In the previous chapters, we observed how precise control over interactions and trap geometry enables studies of the ground state phase diagram, collective modes, and quantized vortices. These studies typically involved atomic ensembles of tens- to hundredthousends of atoms in bulk ODTs. Another question that arises is how the DDI modify the ground stae and excitations in the strongly correlated regime, e.g. when the atoms are confined in crystal-like structures. To this end it is advantageous to have access to the microscopic properties such as the local density or spin down to the single atom level.

Single particle resolution and control are well established in similar systems such as arrays of ions [296]. Machines with single ion control and therefore deterministic state preparation and comprehensive state characterisation are nowadays one of the leading platforms for quantum computing [297, 298]. In these systems the ions are naturally arranged into arrays due to their long-range Coulomb interactions, resulting in typical separations of $d > 1\,\mu$m [299]. This allows for imaging systems with moderate resolution to observe the single ions with high fidelity [300].

Unlike ions, the single atoms in trapped neutral atomic clouds are not localized and have typical densities of $n \approx 10^{13} - 10^{14}\,\mathrm{cm}^{-3}$ or in other words an average distance of just a few 100 nanometres [27]. By loading these atoms into deep optical lattices – periodic potentials created by interfering laser beams – single atoms can be localized at distances of the order of the wavelength of the lattice light λ. The atoms are now separated on a length scale resolvable by state-of-the-art high-resolution objectives with signal-to-noise ratios good enough to identify the number of atoms at every lattice site. Since these systems allow for direct observation of the microscopic state of the atomic cloud, they are referred to as Quantum Gas Microscopes (QGM) [301].

Richard Feynman famously proposed to use highly controllable quantum systems to simulate other complex systems [302]. Ultracold atoms in optical lattices realize such strongly correlated, but controllable

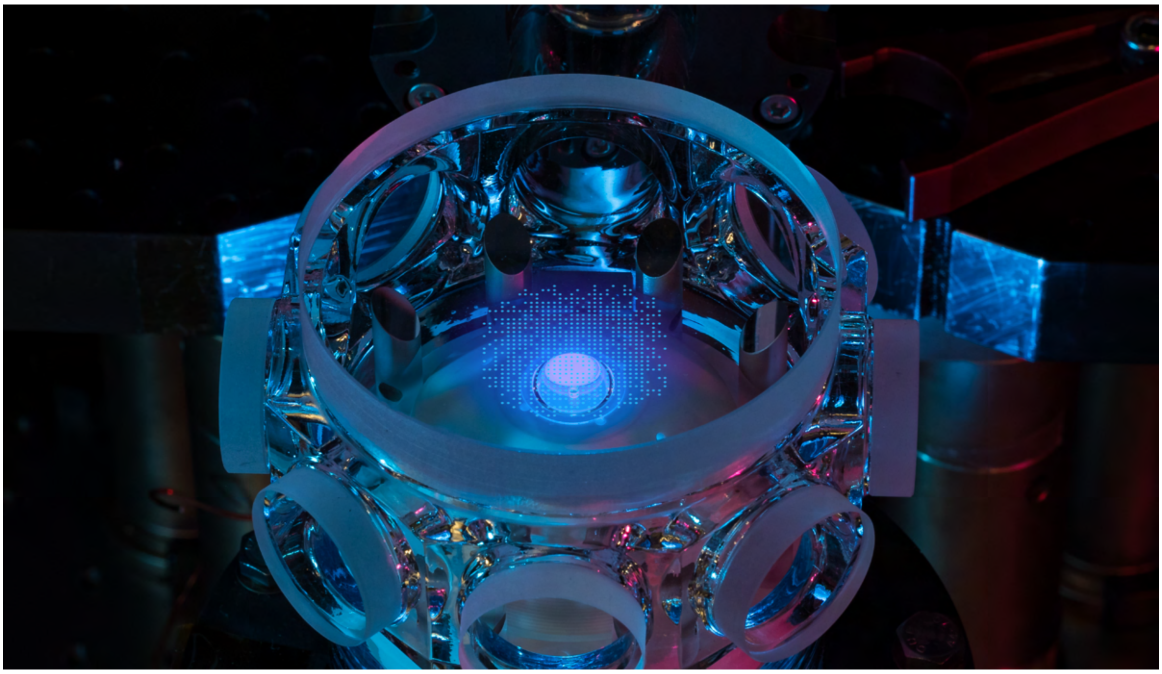

Figure 5.1: Image of the SiSi chamber. An artistic visualisation of individual atoms in an optical lattice above the high-resolution objective.

quantum systems. They enable the implementation of systems with specific Hamiltonians, such as the Bose- and Fermi-Hubbard models. For bosonic systems these systems have revealed phenomena such as the Superfluid-to-Mott insulator transition [303, 304], quantum walks of the single atoms [305], entanglement in quantum many body systems [306, 307, 308, 309] and chaotic quantum dynamics [310]. Spinor bosons have also demonstrated intriguing spin dynamics of mobile spins [311] or the superexchange dynamics [312]. With fermions, QGMs enable the observation of metallic to Band insulating states [313, 314], Magnon bound states [315], polarons [316], Doublon-hole correlations [317] and antiferromagnetic order [318, 319, 320]. Much of the pioneering QGM work has focused on systems with alkali and alkaline-earth atoms, where interactions are predominantly short-range. Therefore interactions between nearest neighbouring (NNI) atoms could be omitted. Expanding these systems to include long-range interactions promise even richer physics [321].

Recent advancements have introduced QGMs with permanent long-range interactions, achieved using ultracold molecules [322, 323] and dipolar atoms [324]. Ultracold molecules provide strong dipolar interactions [70], but their preparation and cooling to the rovibrational ground state – a prerequisite to obtain the strong dipolar interactions in the first place – remains complex and an ongoing research challenge [325, 322].

Magnetic atoms such as erbium and dysprosium have weaker dipolar interactions, but the sequences to cool the atoms to quantum degeneracy are considerable less complex. This allows for large scalable systems from sparse to unit lattice filling.

Bosonic systems of magnetic atoms allow the implementation of the extended Bose-Hubbard model (eBHM) [326, 327, 177]

$$H = \underbrace{-t \sum_{\langle i,j\rangle} \left(\hat{a}_i^\dagger \hat{a}_j + h.c.\right)}_{\text{tunneling}} + \underbrace{\mu \sum_i \hat{n}_i}_{\text{chem. Pot.}} + \underbrace{\frac{U}{2} \sum_i \hat{n}_i \left(\hat{n}_i - 1\right)}_{\text{on-site int.}} + \underbrace{\sum_{i<j} V_{i,j} \hat{n}_i \hat{n}_j}_{\text{NNI}} \tag{5.1}$$

where $\hat{a}_i^\dagger \hat{a}_j$ describes the tunneling to the nearest site with the amplitude t, the density operator is given by $\hat{n}_i$, μ is the chemical potential, U is the on-site interaction potential and $V_{i,j}$ is the NNI potential. For Dysprosium, NNI on the order of 100 Hz´can be achieved depending on the interatomic separation. These systems enable the exploration of fractional Mott insulating states with chequerboard and stripe patterns, supersolid phases and the superfluid phase in two dimensional lattices [328]. A recent realization of a QGM with erbium has shown the chequerboard pattern and the influence of the magnetic field on the stripe phase [324]. Also other exotic phases with highly non-local order parameters such as the Haldane insulator are expected to be observable in such systems [329, 330].

In spin systems, the dipolar interactions have profound effects on the observable ground state and dynamics of the system. For example, the t-J model describes the physics in a system with $t \ll U$ with a spin-exchange term J_{ex}. The spin-exchange term for lattice systems with non-dipolar gases can be realized through the superexchange $J_{\text{ex}} = -4t^2/U$, but is strongly suppressed due to its t^2-dependents [54]. In dipolar systems this term can be realized through the dipolar interactions $J_{\text{ex}} \propto V_{i,j}$ and is therefore not directly dependent on t. This allows to study a much larger parameter space of the t-J model in dipolar systems [331, 332, 91], a microscopic theory relevant to high-T_c superconductivity in cuprates [333]. Also other intriguing phenomena can be studied in these systems , for example magnetic frustration [334, 335, 336, 337], leading to spin liquid systems [338], or many-body chaos [339].

We extend the capabilities of our experiment further by developing a dual species, dipolar Quantum Gas Microscope (ddQGM) with erbium and dysprosium. An interesting application of these mixture systems would be the creation of heteronuclear molecules with large electrical dipole moments [340, 322]. However, even without creating molecules, the dipolar mixture allows us to explore effects such as the superfluid spin hall effect [341], pair-superfluid behaviour [342, 343], phase separation [344] and spin pair creation in bilayers [345]. The mixture also opens possible research directions towards quantum computation [346].

The foundation for the ddQGM was laid by attaching the SiSi chamber – a glass cell with wide optical access and an in-vacuum high-resolution objective – to the experimental apperatus. The last part of this thesis describes the first steps towards the realisation of the ddQGM, focusing on the implementation of the transport setup from the FRaNZ chamber to the SiSi chamber.

5.1 The ddQGM blueprint

For our quantum gas microscope we are planning to use a lattice with a spacing of $\lambda/2 < 300$ nm. To resolve the single atoms in the lattice and collect enough photons to detect the exact number of atoms per lattice site with high fidility, we need an objective with large numerical aperture (NA). The design of our objective with NA = 0.89 is discussed extensively in [150, 347]. It is optimized for imaging wavelengths $\lambda_{\text{img}}^{\text{Dy}} = 421$ nm and $\lambda_{\text{img}}^{\text{Er}} = 401$ nm. The large NA is possible because of the short effective focal length of

$f = 20$ mm but the FRaNZ chamber does not offer sufficient optical access to accommodate this objective. Furthermore, extensive optical access for the beams to trap, manipulate and image the atoms in the quantum gas microscope is necessary.

To address these challenges, we install an additional chamber, which is specifically designed for the quantum gas microscope (see Fig. 5.1). The glass cell provides optical access from seven horizontal viewports and a large viewport on the top. To further enhance horizontal access a mirror crown comprised of eight mirrors is installed around the in-vacuum objective, which reflects the vertical beams from the top viewport into the horizontal direction. In the center of the last lens of the objective a small mirror is installed, which allows to create a retroreflected vertical lattice. This ensures a fixed distance between the vertical lattice sites and the objective. The precise positioning is crucial, as the large NA of the objective results in a width of the focal plane of just a few microns. The design of the new chamber is described in great detail in Max Sohmen's thesis [150].

The atoms are initially cooled and trapped in the ODT within the FRaNZ chamber. To implement the ddQGM, these atoms must be transported to the SiSi chamber. An efficient transport is crucial to ensure a high initial phase-space density in the SiSi chamber, so that a cold, dense atom cloud can be loaded to the optical lattices. The design and implementation of transport setup are covered in detail in the next section.

However, achieving a single-site resolved lattice system involves many additional steps. After transportation to the SiSi chamber, the atoms are loaded into an ODT. From there they are transferred into a single lobe of a vertical lattice, which establishes the vertical confinement of the atoms. Next, the horizontal optical lattice has to be implemented and loaded. Finally, the atoms are imaged via fluorescence imaging through the objective and imaging setup, carefully aligned to avoid loss of resolution due to aberrations. This is a very schematic presentation of the intricate optical engineering tasks that have to be left to the next generation of PhD students.

5.2 Transport to the Single-Site Chamber

There are many different methods to transport an atomic cloud of neutral atoms. One common technique is magnetic transport, used on microchips [348, 349], using time-varying currents [350, 351] or employing magnetic coils on a translation stage [352, 353]. In this experiment we choose an optical transport scheme, where the focus of a single-beam trap is moved by an air-bearing translation stage, employed also in other quantum gas setups [354, 355]. Alternative methods, such as optical conveyor belts [356, 357] require large power for the optical confinement, or focus tunable lenses [358] and Moire lenses [359] are suited better for low power applications. There are also combinations of these techniques [360]. We opted for the air-bearing translation stage, due to its proven stability and useability for all ranges of laser power. However, this method is limited by the weak axial confinement – typically around $\omega_{\mathrm{ax}} \approx 10\,\mathrm{Hz}$ [354, 355] – along the transport direction. This imposes constraints on the maximum acceleration of the beam, as it acts like a force along the movement direction, reducing the effective trap depth. Consequently, typical transport durations are $T_{\mathrm{tp}} = 1 - 2\,\mathrm{s}$.

The main constraints for the optical transport setup are given by the distance of the centres of the FRaNZ

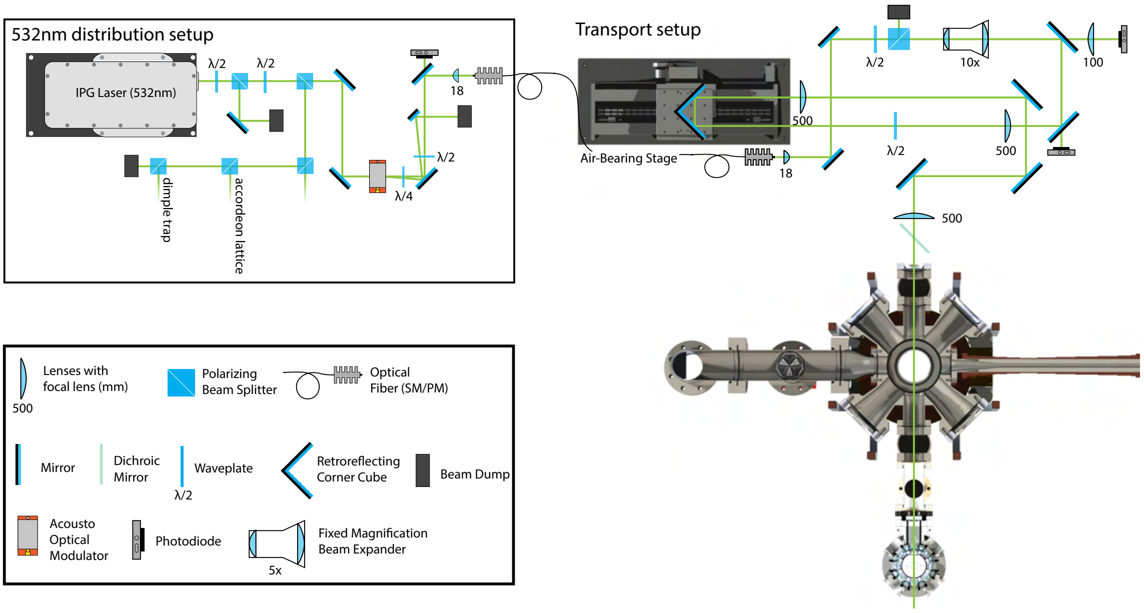

Figure 5.2: Optical setup of the 532 nm distribution and the transport. The 532 nm beam is generated by an IPG laser system and distributed to the transport setup, as well as future additional setups for a dimple trap and an accordion lattice. The light is sent to the transport setup via a polarisation-maintaining, photonic crystal fiber. There the beam is brought to a diameter of $d = 10\,\mathrm{mm}$ by a 10x beam expander before being sent through a telscope made of two lenses with $f = 500\,\mathrm{mm}$. An air-bearing translation stage changes the length of the telescope to move the focus of the beam from the FRaNZ to the SiSi chamber. The beam is focused by a $f_{\mathrm{foc}} = 500\,\mathrm{mm}$ lens and passes through a dichroic mirror, where it is superimposes on the scanODT beam.

and SiSi chamber $l_{\mathrm{F-S}} = 40.8\,\mathrm{cm}$, the viewport diameter $D = 27.5\,\mathrm{mm}$[1] of the FRaNZ chamber, as well as its distance from the center of the chamber $l_{\mathrm{v-F}} = 20.4\,\mathrm{cm}$ and the maximum powers of $P \approx 5\,\mathrm{W}$ that we can provide with either $\lambda = 1064\,\mathrm{nm}$ or $\lambda = 532\,\mathrm{nm}$. It follows, that the maximum numerical aperture for this system at the center of the SiSi chamber is $\mathrm{NA_{TP}} = 0.022$ and therefore the minimum waist is $w^{1064}_{0,min} = 23\,\mu\mathrm{m}$ and $w^{532}_{0,min} = 11.5\,\mu\mathrm{m}$. This waist sets the theoretical possible aspect ratio between the radial and the axial confinement to $\omega_{\mathrm{ax}}/\omega_{\mathrm{r}} \approx 0.01$.

The real part of the polarizability for Dysprosium in the two beams, which is responsible for the trap depth, for both wavelengths are roughly $\mathrm{Re}(\alpha^{532}) \approx 400\,\mathrm{a.u.}$[2] and $\mathrm{Re}(\alpha^{1064}) \approx 116\,\mathrm{a.u.}$ [75][3]. From these parameters we can calculate the trap frequencies for the maximum power and minimum waist and get $\omega^{1064}_{\mathrm{ax}} = 16.3\,\mathrm{Hz}$ and $\omega^{532}_{\mathrm{ax}} = 89.3\,\mathrm{Hz}$. Considering, that the experimental setup could also introduce aberrations, we choose $\lambda = 532\,\mathrm{nm}$. This provides a broader range of achievable trap frequencies and greater flexibility regarding the waist of the beam.

The laser beam is generated by an IPG Laser System[4] and distributed using polarizing beam splitter

---

[1] To get 99% of the power through this viewport the beam cannot be larger than $D_{\mathrm{beam}} \approx 18\,\mathrm{mm}$ at the viewport.

[2] Taken from simulations performed by Maxence Lepers. Note that a recent measurement of the polarisability shows a large discrepancy to the calculated value, which is still not understood [361]

[3] As for the other parts for the thesis, we are only considering dysprosium. But the transport also has to be able to transport Erbium. The polarizability for $\lambda = 1064\,\mathrm{nm}$ and $\lambda = 532\,\mathrm{nm}$ are very similar to the values given for Dysprosium, even slightly larger [362]

[4] IPG GLR-532-50-SF

cubes[5] (PBS) and $\lambda/2$-waveplates[6], shown as 532 nm distribution setup in Fig. 5.2. The other paths are eventually used for an additional ODT and an accordion lattice. The transport beam is guided through an acousto-optic modulator[7] (AOM). The AOM is used for the power regulation and the intensity of the beam is stabilized through a feedback loop, measuring the beam power at a photodiode[8] (PD) in the Transport setup. Additionally PDs monitor the coupling efficiency into the polarization maintaining photonic crystal fiber[9] and are connected to a security circuit, protecting it from damage if the efficency drops. The AOM is coupled such that $\approx 75\%$ of the light are coupled into the -1 order and the 0th order is directed into a beam dump. The light is then coupled to the fiber with an aspheric $f = 18$ mm, achieving an coupling efficiency of up to 75%.

The light is directed to the optical transport setup. There are two ways of moving the focus with an mechanical translation stage: Change the position of the last focusing lens, or keep the last lens stationary and change the divergence or convergence of the beam hitting it. We choose the latter design which allows us to use a focusing lens of $f_{\text{foc}} = 500$ mm in front of the chamber and a collimated beam of waist $w = 5$ mm to focus the beam down to $w = 17\,\mu$m in the chamber. It also allows the stage[10] to be placed at a larger distance from the FRaNZ chamber to reduce the effects of magnetic fields created by the stage on the atoms. To change the divergence of the beam, we set up a telescope of two $f = 500$ mm lenses, with a retroreflector[11] mounted between them on a low-vibration air-bearing stage. Moving the stage by a distance l_{stage} changes the distance between the lenses by $l_{\text{tele}} = 2\, l_{\text{stage}}$ which translates 1:1 to the distance the focus moves. To ensure, that the waist of the beam does not change during the transport, the last lens of the telescope and the focussing lens are spaced exactly $2f = 1000$ mm. The retroreflector ensures, that even small vibrations orthogonal to the stage movement are not transferred to the beam.

To get the beam to the right size to achieve a waist of $w = 17\,\mu$m we need a collimated beam of beam size $w = 5$ mm in front of the telescope. For this we use an aspherical outcoupling lens for the fibre of $f = 18$ mm and then a 10x beam expander[12]. The beam then passes through the focusing lens and is overlapped with the scanODT beam by passing through a two inch dichroic mirror[13]. We measure the waist of the final beam from the part of the beam reflected off the back of the mirror to be $w = 18(2)\,\mu$m. But the dichroic mirror has a thickness of 5 mm, and we have to focus the beam through it, so we cannot avoid astigmatism induced by it. Therefore we expect a slightly larger waist in the chamber, and a larger measured Rayleigh length than expected from the waist.

Once the transport beam and the scanODT beam overlap, the atoms can be loaded to the transport beam. For the initial characterisation of the transport beam we run the sequence as usual and after loading the MOT to the scanODT we ramp up the power of the transport beam before ramping down the power of the scanODT beam and handing over the atoms. The axial trap frequencies are in the kHz range, so we employ parametric heating measurements to characterise them. We modulate the trap power at different

---

[5] LensOptics PBC-532-HP

[6] LensOptics W2Z18-532

[7] G&H I-M110-2C10B6-3-GH26

[8] Built by the electronics workshop of IQOQI Innsbruck

[9] NKT LMA-PM-15

[10] Aerotech ABL 1500 with the Driver Soloist ML

[11] Newport UBBR2.5-1

[12] Thorlabs BE10-532

[13] Thorlabs DMSP650L

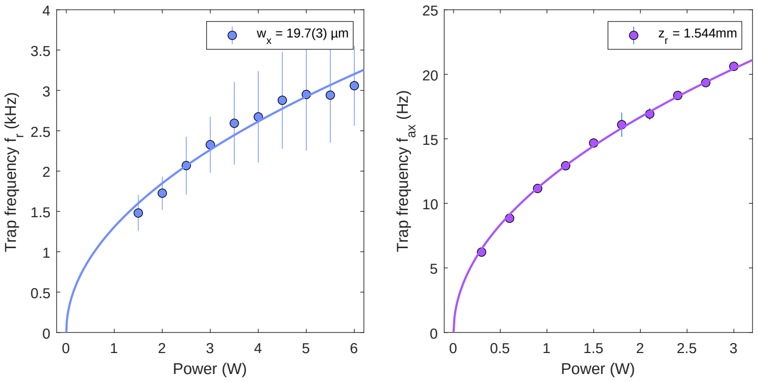

Figure 5.3: Radial and axial trap frequencies of the transport. The radial trap frequencies are measured in parametric heating measurements by modulating the power of the transport beam at different frequencies. The resulting atom loss is fitted with a Gaussian function and the centre frequency is plotted against the beam power (●). The error is estimated by the sigma width of the Gaussian. The experimental data points are fitted by (2.9), resulting in $w_0 = 19.7(3)\,\mu$m. For the axial trap frequencies, the sloshing mode is measured for different powers and fitting the data points gives $z_R = 1.544$ mm.

frequencies and measure the atom loss. The loss features appear at multiples of the trap frequency and can be fitted with a Gaussian function. We measure the frequencies for different powers of the transport beam and estimate the uncertainty of the frequencies from the width of the Gaussian σ. The axial frequencies are measured by exciting the sloshing mode in the trap and measuring the displacement of the cloud in the y-direction over time. The results can be seen in Fig. 5.3 and from fitting the measured frequencies to Eq. (2.9) we find a waist $w = 19.7(3)\,\mu$m and a Rayleigh length $z_\mathrm{R} = 1.5(3)$ mm. The discrepancy between the waists measured inside the chamber and from the backreflection of the dichroic mirror can have multiple reasons. As discussed before, we expect the beam to be astigmatic due to the dichroic mirror, which increases the effective waist. Also to extract the waist of the beam from the trap frequencies, the polarizability at the used wavelength has to be known well. However, recent measurements show a large discrepancy to the calculated value, which still has to be investigated [361].

After characterization, we improve the initial conditions before transporting the atoms to the SiSi chamber. In particular, we aim to load as many atoms as possible. We find that we can assist the loading from the MOT to the ODT by additionally applying the transport beam. Fig. 5.4 shows the increase in efficiency by about 50% of the loading when the focus is displaced 10mm along the axial direction from the centre of the MOT. The increased efficiency is due to the fact that the transport beam is larger 10 mm away from the focus and captures a spatially larger part of the MOT cloud as can be seen in Fig. 5.4 a.

For transport, we hand off the atoms by moving the focus of the transport beam to the atom cloud and ramping down the scanODT power. To characterize the transport efficiency, we install a horizontal absorption imaging setup for the Sisi chamber with $\lambda = 421$ nm light. The magnification of the system is $M = 1.976(6)$ and the light is sent to a CMOS camera[14] with a pixel size of $2.74 \times 2.74\,\mu$m. Using TOF measurements, we have verified the magnification and have calibrated the pixel size and the atom

---

[14] Balluff BVS CA-GX2-0162AG-110120-001

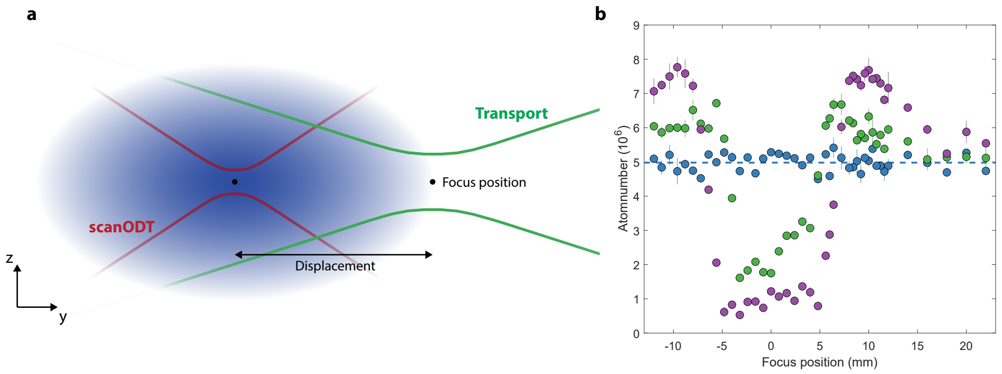

Figure 5.4: Transport beam assisted MOT to ODT loading. a) Schematic of the loading process from the MOT to the scanODT. The atomic cloud from the MOT is larger than the trap volume of the scanODT. This is assisted by the Transport beam where the focus position is shifted, trapping a larger volume of the MOT. b) The number of atoms trapped in the ODT after holding for $t_{\text{hold}} = 200$ ms for different focus positions of the transport. The atom number is plotted for transport beam powers $P = 5$ W (●), $P = 2$ W (●) and no transport beam (●) and the dashed line gives the average atom number when the transport beam is off. A strong decay in atom number can be observed at focus positions up to 5 mm from the centre. At larger distances the atom number increases rapidly exceeding that without the transport beam, with a maximum at 10 mm displacement and an increase in atom number of 54%.

number counting.

To understand possible loss mechanisms and the limits of the transport sequence we perform a numerical simulation of it. The acceleration profile of the stage is shown in Fig. 5.5 a. Atoms are lost from the trap during transport, because the acceleration reduces the effective trap frequency (shown in Fig. 5.5 b) and leads to plain evaporation. The atom loss is calculated using the model introduced in Sec. 2.2.3. During the transport the effective trap depth changes continuously and the atom number and temperature are calculated iteratively for different transport durations. The initial values such as atom number, temperature and one-body loss lifetime are measured in the experiment by holding the atoms in the transport beam for different powers for up to 5 s. The truncation parameter is set to $\eta = 8$ but changing this parameter does not significantly change the simulation result. The simulation iteratively calculates the density in the trap and from this the average collision time $\tau_{\text{coll}} = \frac{1}{n v_a \sigma} \exp(-\eta)$ with the average velocity of the atoms $v_a = \sqrt{\frac{16 k_B T}{\pi m}}$ and the scattering cross section $\sigma = 8\pi a_S^2 + \frac{32\pi}{45} a_{\text{dd}}^2$. While $a_{\text{dd}} = 130.8\,\mathrm{a}_0$ is fixed for the dysprosium atoms, the s-wave scattering length is assumed to be $a_S = 100\,\mathrm{a}_0$. The collision time gives the time interval of atom loss. The transport efficiency N_{tp}/N_0 comparing the atom number after the transport N_{tp} with the atom number N_0 held in the trap for the same time without transporting in Fig. 5.5 c. It can be seen that for long transport durations $d_{\text{tr}} > 2$, the atom number after transport in traps with $P > 1.5$ W approaches a transport efficiency of about 80% which agrees with the measured efficiencies. For low power $P < 1.5$ W the spilling effects lead to large atom losses even for transport durations > 4 s. For these powers, the simulation greatly underestimates the atom number measured in experiment. In addition, the minimal transport durations T_{tp}^*, at which not all atoms are lost during transport, are expected to be lower than the actual measured minimal transport durations. These differences could indicate that U_{eff} shown in Fig. 5.5 b does not accurately describe the potential depth in the experiment during the transport. U_{eff} might not be well approximated due to the astigmatism of the transport beam. Still, for large powers, we see efficiencies comparable to transport setups in other groups [354, 355]. However, the final atom number suffers from a low one-body lifetime of $\tau = 2 - 3\,\text{s}$, which decreases further as the power of the transport beam is increased. The short lifetime may be due to scattering of the trap light, but further investigation should help to significantly increase the lifetime and, therefore, the final atom number in the SiSi chamber. Simulating the system for atoms at lower temperatures at these trap powers also promises the possibility of moving the cloud faster. Additional optical cooling schemes could achieve this. However, a colder cloud of atoms also leads to higher densities and therefore three-body losses could lead to additional loss. In this case, a_S and L_3 have to be measured during the transport, to accurately predict atom losses due to three-body collisions. The model also assumes that the cloud is in equilibrium, instantaneously following the movement of the trap, without being excited. In reality, the cloud starts to slosh in the trap, leading to additional atom loss and heating.

At the time of writing this thesis, the atom number in the SiSi chamber was $N = 1 \times 10^6$, which can be improved, as the simulation shows. This concludes the first step towards the dipolar, double species Quantum Gas Microscope and the last step of this work.

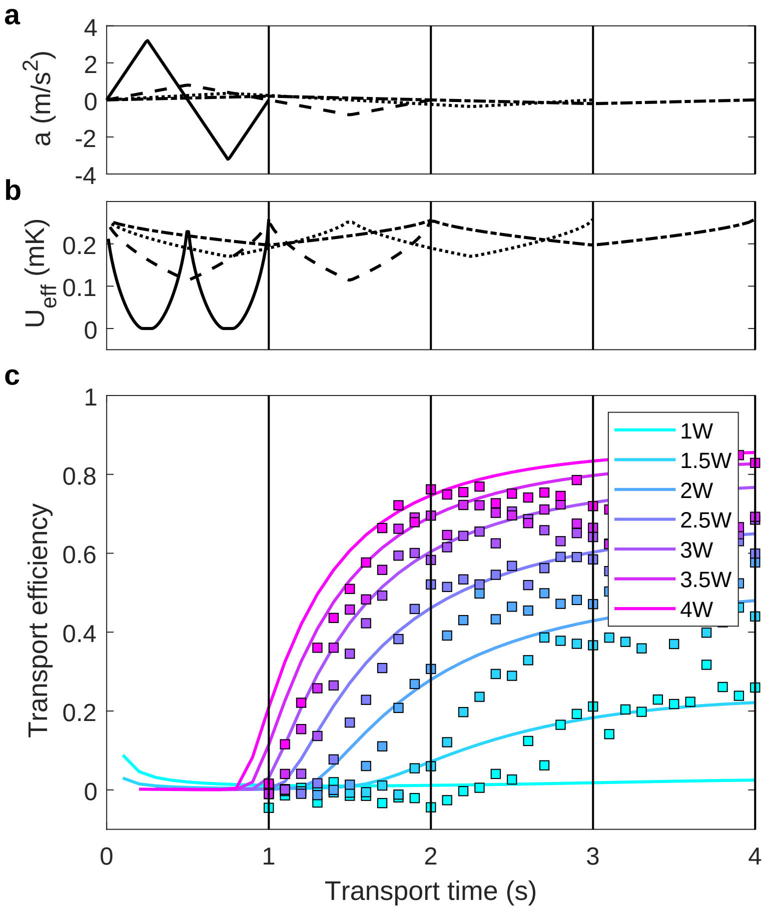

Figure 5.5: Numerical simulation of the ^{164}Dy atom number during the transport sequence. a) The acceleration profile of the translation stage is shown for different transport durations $t_{TP} = 1$ s (–), $t_{TP} = 2$ s (- -), $t_{TP} = 3$ s (···) and $t_{TP} = 4$ s (-··-). b) Shows the corresponding effective trap depths during transport. (c) Transport efficiency N_{tp}/N_0 for different transport beam powers P. The transport efficiency compares the atom number N_{tp} after transport for a time T_{tp} to the atom number N_0 after holding for T_{tp} in the static transport trap. Experimental data is plotted as squares and the corresponding simulation is shown as solid line. The initial atom number N_0, temperature T_0 and lifetime used for the simulation are extracted from the experimental data for the static transport trap. Other parameters used are the beam waist $w_r = 19.7\,\mu$m, the Rayleigh length $z_R = 3$ mm $\eta = 8$, $a_S = 100\,a_0$ and $a_{dd} = 130.8\,a_0$

6

Conclusion

Jetzt fühlt's sich wieder so an, als fängt es grade an
Ob ich noch was adden kann, ey, ich weiß es nicht
Ob es sich nochmal lohnt, alles sich wiederholt
Nochma' von hier bis zum Mond, mh, entscheidet sich

TRETTMANN
WAR DAS SCHON ALLES (YOUR LOVE IS KING 3 - 2024)

The main subject of my Ph.D. thesis is to report our work on creating and studying quantised vortices in both unmodulated dipolar condensates and supersolid phases. To the latter aim, we had first to create a 2D-SS and then rotate the state with the means of the newly developed technique of magnetostirring. All the work presented was in close collaboration with theorists and our experimental result has shown remarkable agreement with their simulations. Let me conclude this thesis by briefly summarising the results.

Only a few years after the first realisations of BECs in ultracold quantum gases, quantized vortices could already be generated in such systems. These vortices are the hallmark of the superfluid dynamics of quantum systems and have become an intensely studied research topic.

However, until the work presented in this thesis, vortices had not yet been observed in BECs with significant dipolar interactions. Theoretical studies have suggested that the DDI has profound effects on the structure of individual vortices[363] as well as on the structure of the vortex lattice[239].

In the work presented, we show the that the nucleation mechanism of vortices is universal in terms of the underlying interactions and that the DDI imposes a stripe structure to the vortex lattice. We developed the magnetostirring technique to impart angular momentum to the dBEC, exploiting the anisotropic nature of the DDI. We have seen that the nucleation of vortices is triggered by dynamic instabilities just as in non-dipolar gases. On the other hand, theoretical studies show that for large tilts of the magnetic field, the attractive part of the DDI can lead to a stabilisation of the dBEC not allowing vortices to enter to the centre[232]. The striped structure of the vortex lattice is demonstrated by a Fourier analysis of the density distribution which shows that the stripe structure is imposed by the direction of the tilted magnetic field.

The first observation of the supersolid state in quantum gases of magnetic atoms sparked a whole new subfield in the study of ultracold quantum gases[120, 121, 122]. The work presented in this thesis has been committed to the long road of experimentally probing superfluidity in the supersolid state. To this end we have looked at the rotational dynamics of the supersolid state. The door to this line of research was opened by the first realization of a two-dimensional supersolid array.

Our attempt to quantitatively measure the superfluid fraction, as proposed by Leggett has been unsuccessful due to the complex mode structure of 2D supersolids, which we cannot resolve in our current experiment. Our results extend the earlier work of the group in Pisa[131], sparking a discussion on the experimental feasibility of scissor mode measurements to extract the superfluid fraction[274, 364]. Although our measurements cannot quantify the superfluid fraction, they have given us great insight into the complex crystal dynamics of 2D supersolid arrays.

The knowledge gained from the vortex project in the dBEC allows us to successfully nucleate vortices in the supersolid state for the first time, a hallmark signature of superfluidity. We observe a distinct threshold behaviour of the vortex nucleation process compared to the resonance behaviour in dBECs. Vortices are nucleated at much lower rotation due to the complex excitation spectrum of the 2D supersolid array, where not only the quadrupole mode but also the crystal modes assist the nucleation.

The work presented in this thesis demonstrates the profound effects of long-range anisotropic DDI on phenomena such as quantised vortices. We also provide definitive evidence for the superfluid nature of supersolids in dipolar quantum gases, finally answering the over 50 year old question: Can a solid be 'superfluid'[81]?

This concludes the research topics of this thesis. But of course there are still many unanswered questions left, new questions that have arisen and further directions to explore.

6.1 Outlook

I will therefore conclude this thesis by mentioning a few selected topics that may be explored within the Erbium-Dysprosium experiment in the near future.

The "solid" character of the supersolid: The part that is defined as solid in the supersolid state is the crystal structure observable in-situ, which is reminiscent of the crystal structure of some solids. But it is also interesting to characterise the supersolid macroscopically, e.g. by probing its stiffness, which would complete the paradoxical picture of this state. There is already theoretical work studying the shear modulus of a supersolid[126, 127]. Other properties, such as energy or heat transport, or studying the study of the speed of sound, could also provide a better understanding of the solid nature of the supersolid and have implications for solid-state or other systems.

Simulation of glitches in neutron stars: The use of ultracold quantum gas experiments as simulators for other strongly correlated systems is one of the driving motivations for studying such systems. Our work on creating vortices in supersolids has inspired collaborations between the ultracold gas and neutron star communities[365]. Simulations suggest that experimentally accessible supersolids may be a suitable test bed for studying some phenomena related to neutron stars, such as the glitch mechanism[295]. So far, this work is limited to theoretical studies but by further improving the experimental system such a simulation platform could be realised experimentally.

Dipolar Quantum Gas Microscope: In part 5 I have already discussed the first technical steps towards a dipolar double species quantum gas microscope. Quantum gas microscopy is an intensive field of experimental development and existing systems have already provided insights into many important questions about strongly correlated systems, applicable to e.g. solid-state systems[301]. Populating such a QGM with atoms with significant permanent long-range interactions opens the door to even more exotic many-body states[321] and will allow models such as the t-J model to be tested and thus help in the development of new materials[366]. The first implementation of such a QGM already shows promising results and new phases of matter[324].

Mixtures of Erbium and Dysprosium: The work presented in this thesis has been exclusively about single species experiments. However, it has already been shown that this experiment is capable of producing heteronuclear Bose-Bose, Fermi-Fermi and Bose-Fermi mixtures[133]. Theoretical studies show that balanced mixtures of two dipolar gases exhibit a complex ground state phase diagram, ranging from miscible and immiscible phases to mixed supersolid-isolated domain phases[267]. These phases can be explored experimentally by tuning the inter- and intraspecies scattering lengths.

In addition, highly unbalanced mixtures promise rich polaronic physics influenced by the DDI[367].

My work on the Erbium-Dysprosium experiment started in early 2020. The first observations of the supersolid in magnetic atoms were only about a year old, and the world was soon about to hold its breath for a while. Despite the unfavourable circumstances, we had very productive years with the experiment. It was very inspiring to be part of such a young subfield of cold quantum gases and to see it evolve so rapidly in these few years. Looking back, I feel very privileged to work with such a great team, to have a profound impact on the research in this field, and to have discussed our results with many people around the world. Of course, without the many collaborations along the way the works presented in this thesis would not have been possible. Therefore I would like to thank Laurianne Chomaz (Heidelberg), Luis Santos (Hannover), Giacomo Lamporesi (Trento) and Russell Bisset (Innsbruck) for the indispensable input, as well as Elena Poli and Thomas Bland for our group internal theory collaboration.

Bibliography

[1] John R. Rumble. *CRC Handbook of Chemistry and Physics*. CRC Press, 100th edition, 2019. (cited on pages xvii, 16).

[2] Neil W Ashcroft and N David Mermin. *Solid state physics*. Saunders College Publishing, 1976. (cited on page 1).

[3] Hongxian Xie, Fuxing Yin, Tao Yu, Jian-Tao Wang, and Chunyong Liang. Mechanism for direct graphite-to-diamond phase transition. *Scientific Reports*, 4:5930, 8 2014. (cited on page 1).

[4] C. A. Balseiro and L. M. Falicov. Superconductivity and charge-density waves. *Physical Review B*, 20:4457–4464, 12 1979. (cited on page 1).

[5] Xiao-Gang Wen. Colloquium: Zoo of quantum-topological phases of matter. *Reviews of Modern Physics*, 89:041004, 12 2017. (cited on page 1).

[6] Ronny Stolz, Matthias Schmelz, Vyacheslav Zakosarenko, Cathy P Foley, Keiichi Tanabe, Xiaoming Xie, and Robert Fagaly. Superconducting sensors and methods in geophysical applications. *Superconductor Science and Technology*, 34, 1 2021. (cited on page 2).

[7] Kashem M. Muttaqi, Md. Rabiul Islam, and Danny Sutanto. Future Power Distribution Grids: Integration of Renewable Energy, Energy Storage, Electric Vehicles, Superconductor, and Magnetic Bus. *IEEE Transactions on Applied Superconductivity*, 29:1–5, 3 2019. (cited on page 2).

[8] Morten Kjaergaard, Mollie E Schwartz, Jochen Braumüller, Philip Krantz, Joel I.-J. Wang, Simon Gustavsson, and William D Oliver. Superconducting Qubits: Current State of Play. *Annual Review of Condensed Matter Physics*, 11:369–395, 2020. (cited on page 2).

[9] Per F. Dahl. Kamerlingh Onnes and the Discovery of Superconductivity: The Leyden Years, 1911-1914. *Historical Studies in the Physical Sciences*, 15:1–37, 1 1984. (cited on page 2).

[10] Dirk Van Delft. History and significance of the discovery of superconductivity by Kamerlingh Onnes in 1911. In *Physica C: Superconductivity and its Applications*, volume 479, pages 30–35, 9 2012. (cited on page 2).

[11] J. Bardeen, L. N. Cooper, and J. R. Schrieffer. Microscopic Theory of Superconductivity. *Phys. Rev.*, 106:162–164, 1957. (cited on page 2).

[12] Philip W. Anderson and Kevin S. Bedell. The Theory of Superconductivity in the High-Tc Cuprates. *Physics Today*, 51:64–65, 7 1998. (cited on page 2).

[13] G. R. Stewart. Heavy-fermion systems. *Reviews of Modern Physics*, 56:755–787, 10 1984. (cited on page 2).

[14] D. Jérome. The Physics of Organic Superconductors. *Science*, 252:1509–1514, 6 1991. (cited on page 2).

[15] Shoji Yamanaka, Ken ichi Hotehama, and Hitoshi Kawaji. Superconductivity at 25.5 K in electron-doped layered hafnium nitride. *Nature*, 392:580–582, 4 1998. (cited on page 2).

[16] Zhi-An Ren and Zhong-Xian Zhao. Research and Prospects of Iron-Based Superconductors. *Advanced Materials*, 21:4584–4592, 12 2009. (cited on page 2).

[17] Immanuel Bloch, Jean Dalibard, and Wilhelm Zwerger. Many-body physics with ultracold gases. *Rev. Mod. Phys.*, 80:885–964, Jul 2008. (cited on page 2).

[18] Immanuel Bloch, Jean Dalibard, and Sylvain Nascimbène. Quantum simulations with ultracold quantum gases. *Nat. Phys.*, 8:267, 2012. (cited on pages 2, 2, 3).

[19] M. H. Anderson, J. R. Ensher, M. R. Matthews, C. E. Wieman, and E. A. Cornell. Observation of Bose-Einstein condensation in dilute atomic vapor. *Science*, 269:198–201, 1995. (cited on pages 2, 2, 3).

[20] K. B. Davis, M. O. Mewes, M. R. Andrews, N. J. van Druten, D. S. Durfee, D. M. Kurn, and W. Ketterle. Bose-Einstein condensation in a gas of sodium atoms. *Phys. Rev. Lett.*, 75:3969–3973, 1995. (cited on pages 2, 2, 3).

[21] B. DeMarco, J. L. Bohn, J. P. Burke, M. Holland, and D. S. Jin. Measurement of p-Wave Threshold Law Using Evaporatively Cooled Fermionic Atoms. *Phys. Rev. Lett.*, 82:4208–4211, May 1999. (cited on pages 2, 3).

[22] F. Schreck, L. Khaykovich, K. L. Corwin, G. Ferrari, T. Bourdel, J. Cubizolles, and C. Salomon. Quasipure Bose-Einstein Condensate Immersed in a Fermi Sea. *Phys. Rev. Lett.*, 87:080403, 2001. (cited on pages 2, 3).

[23] Andrew G. Truscott, Kevin E. Strecker, William I. McAlexander, Guthrie B. Partridge, and Randall G. Hulet. Observation of Fermi Pressure in a Gas of Trapped Atoms. *Science*, 291:2570–2572, 2001. (cited on pages 2, 3).

[24] M. Greiner, O. Mandel, T. Esslinger, T. W. Hänsch, and I. Bloch. Quantum phase transition from a superfluid to a Mott insulator in a gas of ultracold atoms. *Nature (London)*, 415:39–44, 2002. (cited on pages 2, 3).

[25] Pimonpan Sompet, Sarah Hirthe, Dominik Bourgund, Thomas Chalopin, Julian Bibo, Joannis Koepsell, Petar Bojović, Ruben Verresen, Frank Pollmann, Guillaume Salomon, Christian Gross, Timon A. Hilker, and Immanuel Bloch. Realizing the symmetry-protected Haldane phase in Fermi–Hubbard ladders. *Nature*, 606:484–488, 6 2022. (cited on page 2).

[26] Satyendra Nath Bose. Plancksches Gesetz und Lichtquantenhypothese. *Zeitschrift für Physik*, 26:178, 1924. (cited on page 2).

[27] W. Ketterle, D. S. Durfee, and D. M. Stamper-Kurn. Making, probing and understanding Bose-Einstein condensates. *Europhys. Lett.*, 36(1):67, 1999. (cited on pages 2, 3, 23, 26, 41, 115).

[28] T.W. Hänsch and A.L. Schawlow. Cooling of gases by laser radiation. *Optics Communications*, 13:68–69, 1 1975. (cited on page 2).

[29] D. J. Wineland and H. Dehmelt. Proposed $1014\Delta\nu < \nu$ Laser Fluorescence Spectroscopy on Tl^+ Mono-Ion Oscillator. *Bulletin of the American Physical Society*, 20, 1975. (cited on page 2).

[30] A. Ashkin. Trapping of Atoms by Resonance Radiation Pressure. *Physical Review Letters*, 40:729–732, 3 1978. (cited on page 2).

[31] David E. Pritchard. Cooling Neutral Atoms in a Magnetic Trap for Precision Spectroscopy. *Physical Review Letters*, 51:1336–1339, 10 1983. (cited on page 2).

[32] E. Tiesinga, A. J. Moerdijk, B. J. Verhaar, and H. T. C. Stoof. Conditions for Bose-Einstein condensation in magnetically trapped atomic cesium. *Physical Review A*, 46:R1167–R1170, 8 1992. (cited on page 3).

[33] E. Tiesinga, B. J. Verhaar, and H. T. C. Stoof. Threshold and resonance phenomena in ultracold ground-state collisions. *Phys. Rev. A*, 47:4114–4122, 1993. (cited on pages 3, 30).

[34] A. J. Moerdijk, B. J. Verhaar, and A. Axelsson. Resonances in ultracold collisions of ^{6}Li, ^{7}Li, and ^{23}Na. *Phys. Rev. A*, 51:4852–4861, Jun 1995. (cited on pages 3, 30).

[35] University of Toronto. UltraCold Atom News, 2024. (cited on page 3).

[36] Dennis Becker, Maike D. Lachmann, Stephan T. Seidel, Holger Ahlers, Aline N. Dinkelaker, Jens Grosse, Ortwin Hellmig, Hauke Müntinga, Vladimir Schkolnik, Thijs Wendrich, André Wenzlawski, Benjamin Weps, Robin Corgier, Tobias Franz, Naceur Gaaloul, Waldemar Herr, Daniel Lüdtke, Manuel Popp, Sirine Amri, Hannes Duncker, Maik Erbe, Anja Kohfeldt, André Kubelka-Lange, Claus Braxmaier, Eric Charron, Wolfgang Ertmer, Markus Krutzik, Claus Lämmerzahl, Achim Peters, Wolfgang P. Schleich, Klaus Sengstock, Reinhold Walser, Andreas Wicht, Patrick Windpassinger, and Ernst M. Rasel. Space-borne Bose–Einstein condensation for precision interferometry. *Nature*, 562(7727):391–395, oct 2018. (cited on page 3).

[37] Elizabeth A. Donley, Neil R. Claussen, Simon L. Cornish, Jacob L. Roberts, Eric A. Cornell, and Carl E. Wieman. Dynamics of collapsing and exploding Bose-Einstein condensates. *Nature*, 412(6844):295–299, 07 2001. (cited on page 3).

[38] Logan W. Clark, Anita Gaj, Lei Feng, and Cheng Chin. Collective emission of matter-wave jets from driven Bose–Einstein condensates. *Nature*, 551(7680):356–359, nov 2017. (cited on page 3).

[39] M. R. Matthews, B. P. Anderson, P. C. Haljan, D. S. Hall, C. E. Wieman, and E. A. Cornell. Vortices in a Bose-Einstein Condensate. *Phys. Rev. Lett.*, 83:2498–2501, Sep 1999. (cited on pages 3, 33, 38, 38).

[40] J. R. Abo-Shaeer, C. Raman, J. M. Vogels, and W. Ketterle. Observation of Vortex Lattices in Bose-Einstein Condensates. *Science*, 292(5516):476–479, apr 2001. (cited on pages 3, 33, 35, 38, 42, 60).

[41] Nir Navon, Alexander L. Gaunt, Robert P. Smith, and Zoran Hadzibabic. Critical dynamics of spontaneous symmetry breaking in a homogeneous Bose gas. *Science*, 347(6218):167–170, jan 2015. (cited on pages 3, 38).

[42] M. R. Andrews, C. G. Townsend, H.-J. Miesner, D. S. Durfee, D. M. Kurn, and W. Ketterle. Observation of Interference Between Two Bose Condensates. *Science*, 275(5300):637–641, 1997. (cited on page 3).

[43] David R. Scherer, Chad N. Weiler, Tyler W. Neely, and Brian P. Anderson. Vortex Formation by Merging of Multiple Trapped Bose-Einstein Condensates. *Phys. Rev. Lett.*, 98:110402, Mar 2007. (cited on page 3).

[44] M. Bartenstein, A. Altmeyer, S. Riedl, S. Jochim, C. Chin, J. Hecker Denschlag, and R. Grimm. Collective Excitations of a Degenerate Gas at the BEC-BCS Crossover. *Phys. Rev. Lett.*, 92:20320, 2004. (cited on page 3).

[45] CA Regal, Markus Greiner, and Deborah S Jin. Observation of resonance condensation of fermionic atom pairs. *Physical review letters*, 92(4):040403, 2004. (cited on page 3).

[46] M. W. Zwierlein, C. A. Stan, C. H. Schunck, S. M. F. Raupach, A. J. Kerman, and W. Ketterle. Condensation of Pairs of Fermionic Atoms near a Feshbach Resonance. *Phys. Rev. Lett.*, 92:12040, 2004. (cited on page 3).

[47] T. Bourdel, L. Khaykovich, J. Cubizolles, J. Zhang, F. Chevy, M. Teichmann, L. Tarruell, S. J. J. M. F. Kokkelmans, and C. Salomon. Experimental Study of the BEC-BCS Crossover Region in Lithium 6. *Phys. Rev. Lett.*, 93:050401, 2004. (cited on page 3).

[48] Belén Paredes, Artur Widera, Valentin Murg, Olaf Mandel, Simon Fölling, Ignacio Cirac, Gora V Shlyapnikov, Theodor W Hänsch, and Immanuel Bloch. Tonks-Girardeau gas of ultracold atoms in an optical lattice. *Nature*, 429(6989):277–281, may 2004. (cited on page 3).

[49] Toshiya Kinoshita, Trevor Wenger, and David S Weiss. Observation of a One-Dimensional Tonks-Girardeau Gas. *Science*, 305(5687):1125–1128, aug 2004. (cited on page 3).

[50] Zoran Hadzibabic, Peter Krüger, Marc Cheneau, Baptiste Battelier, and Jean Dalibard. Berezinskii–Kosterlitz–Thouless crossover in a trapped atomic gas. *Nature (London)*, 441(7097):1118–1121, 2006. (cited on pages 3, 34).

[51] P. Cladé, C. Ryu, A. Ramanathan, K. Helmerson, and W. Phillips. Observation of a 2D Bose Gas: From Thermal to Quasicondensate to Superfluid. *Physical Review Letters*, 102(17):170401, apr 2009. (cited on page 3).

[52] S. Tung, G. Lamporesi, D. Lobser, L. Xia, and E. A. Cornell. Observation of the Presuperfluid Regime in a Two-Dimensional Bose Gas. *Phys. Rev. Lett.*, 105(23):230408, Dec 2010. (cited on page 3).

[53] Shinichi Sunami, Vijay P Singh, David Garrick, Abel Beregi, Adam J Barker, Kathrin Luksch, Elliot Bentine, Ludwig Mathey, and Christopher J Foot. Observation of the BKT Transition in a 2D Bose Gas via Matter-Wave Interferometry. *arXiv preprint arXiv:2108.08840*, 2021. (cited on pages 3, 34).

[54] Maciej Lewenstein, Anna Sanpera, Veronica Ahufinger, Bogdan Damski, Aditi Sen, and Ujjwal Sen. Ultracold atomic gases in optical lattices: mimicking condensed matter physics and beyond. *Adv. Phys.*, 56:243–379, 2007. (cited on pages 3, 117).

[55] Christophe Salomon, Georgy V. Shlyapnikov, and Leticia F. Cugliandolo. *Many-Body Physics with Ultracold Gases: Lecture Notes of the Les Houches Summer School: Volume 94, July 2010*. Oxford University Press, 2012. (cited on page 3).

[56] Daniel P. Arovas, Erez Berg, Steven A. Kivelson, and Srinivas Raghu. The Hubbard Model. *Annual Review of Condensed Matter Physics*, 13(1):239–274, mar 2022. (cited on page 3).

[57] Christian Gross and Immanuel Bloch. Quantum simulations with ultracold atoms in optical lattices. *Science*, 357(6355):995–1001, 2017. (cited on page 3).

[58] Russell A Hart, Pedro M Duarte, Tsung-Lin Yang, Xinxing Liu, Thereza Paiva, Ehsan Khatami, Richard T Scalettar, Nandini Trivedi, David A Huse, and Randall G Hulet. Observation of antiferromagnetic correlations in the Hubbard model with ultracold atoms. *Nature*, 519(7542):21, 2015. (cited on page 3).

[59] Markus Mazurenko, Antonnd Greiner. A cold-atom Fermi–Hubbard antiferromagnet. *Nature*, 545(7655):462–466, May 2017. (cited on page 3).

[60] Michael Schreiber, Sean S. Hodgman, Pranjal Bordia, Henrik P. Lüschen, Mark H. Fischer, Ronen Vosk, Ehud Altman, Ulrich Schneider, and Immanuel Bloch. Observation of many-body localization of interacting fermions in a quasirandom optical lattice. *Science*, 349:842–845, 8 2015. (cited on page 3).

[61] Jae yoon Choi, Sebastian Hild, Johannes Zeiher, Peter Schauß, Antonio Rubio-Abadal, Tarik Yefsah, Vedika Khemani, David A. Huse, Immanuel Bloch, and Christian Gross. Exploring the many-body localization transition in two dimensions. *Science*, 352:1547–1552, 6 2016. (cited on page 3).

[62] T. Rentrop, A. Trautmann, F. A. Olivares, F. Jendrzejewski, A. Komnik, and M. K. Oberthaler. Observation of the Phononic Lamb Shift with a Synthetic Vacuum. *Physical Review X*, 6(4):041041, nov 2016. (cited on page 3).

[63] Zoe Z. Yan, Yiqi Ni, Carsten Robens, and Martin W. Zwierlein. Bose polarons near quantum criticality. *Science*, 368(6487):190–194, 2020. (cited on page 3).

[64] Nils B. Jørgensen, Lars Wacker, Kristoffer T. Skalmstang, Meera M. Parish, Jesper Levinsen, Rasmus S. Christensen, Georg M. Bruun, and Jan J. Arlt. Observation of Attractive and Repulsive Polarons in a Bose-Einstein Condensate. *Phys. Rev. Lett.*, 117:055302, Jul 2016. (cited on page 3).

[65] Ming-Guang Hu, Michael J. Van de Graaff, Dhruv Kedar, John P. Corson, Eric A. Cornell, and Deborah S. Jin. Bose Polarons in the Strongly Interacting Regime. *Phys. Rev. Lett.*, 117:055301, Jul 2016. (cited on page 3).

[66] N T Zinner and A S Jensen. Comparing and contrasting nuclei and cold atomic gases. *Journal of Physics G: Nuclear and Particle Physics*, 40:053101, 5 2013. (cited on page 3).

[67] Pieter van Wyk, Hiroyuki Tajima, Daisuke Inotani, Akira Ohnishi, and Yoji Ohashi. Superfluid Fermi atomic gas as a quantum simulator for the study of the neutron-star equation of state in the low-density region. *Physical Review A*, 97:013601, 1 2018. (cited on page 3).

[68] Annabelle Bohrdt, Lukas Homeier, Christian Reinmoser, Eugene Demler, and Fabian Grusdt. Exploration of doped quantum magnets with ultracold atoms. *Annals of Physics*, 435:168651, 12 2021. (cited on pages 3, 113).

[69] Victor Galitski, Gediminas Juzeliūnas, and Ian B. Spielman. Artificial gauge fields with ultracold atoms. *Physics Today*, 72:38–44, 1 2019. (cited on page 3).

[70] Lincoln D Carr, David DeMille, Roman V Krems, and Jun Ye. Cold and ultracold molecules: Science, technology and applications. *New J. Phys.*, 11(5):055049, 2009. (cited on pages 3, 116).

[71] Sarang Gopalakrishnan, Benjamin L Lev, and Paul M Goldbart. Emergent crystallinity and frustration with Bose–Einstein condensates in multimode cavities. *Nature Physics*, 5(11):845–850, oct 2009. (cited on page 3).

[72] Thomas F. Gallagher and Pierre Pillet. *Dipole–Dipole Interactions of Rydberg Atoms*, pages 161–218. 2008. (cited on page 3).

[73] Axel Griesmaier, Jörg Werner, Sven Hensler, Jürgen Stuhler, and Tilman Pfau. Bose-Einstein Condensation of Chromium. *Phys. Rev. Lett.*, 94(16):160401, Apr 2005. (cited on page 3).

[74] K. Aikawa, A. Frisch, M. Mark, S. Baier, A. Rietzler, R. Grimm, and F. Ferlaino. Bose-Einstein Condensation of Erbium. *Phys. Rev. Lett.*, 108:210401, May 2012. (cited on page 3).

[75] Mingwu Lu, Nathaniel Q. Burdick, Seo Ho Youn, and Benjamin L. Lev. Strongly Dipolar Bose-Einstein Condensate of Dysprosium. *Phys. Rev. Lett.*, 107:190401, Oct 2011. (cited on pages 3, 119).

[76] K. Aikawa, S. Baier, A. Frisch, M. Mark, C. Ravensbergen, and F. Ferlaino. Observation of Fermi surface deformation in a dipolar quantum gas. *Science*, 345(6203):1484–1487, 2014. (cited on page 3).

[77] T. Lahaye, J. Metz, B. Fröhlich, T. Koch, M. Meister, A. Griesmaier, T. Pfau, H. Saito, Y. Kawaguchi, and M. Ueda. d-Wave Collapse and Explosion of a Dipolar Bose-Einstein Condensate. *Phys. Rev. Lett.*, 101(8):080401, 2008. (cited on pages 3, 10).

[78] D. Petter, G. Natale, R. M. W. van Bijnen, A. Patscheider, M. J. Mark, L. Chomaz, and F. Ferlaino. Probing the Roton Excitation Spectrum of a Stable Dipolar Bose Gas. *Phys. Rev. Lett.*, 122:183401, May 2019. (cited on pages 3, 9).

[79] AF Andreev and IM Lifshitz. Quantum Theory of Defects in Crystals. *J. Exp. Theo. Phys.*, 56:2057, 1969. (cited on pages 3, 13, 62, 94, 113).

[80] GV Chester. Speculations on Bose-Einstein condensation and quantum crystals. *Physical Review A*, 2(1):256, Jul 1970. (cited on pages 3, 13, 62, 113).

[81] Anthony J Leggett. Can a solid be" superfluid"? *Physical Review Letters*, 25(22):1543, Nov 1970. (cited on pages 3, 13, 13, 62, 62, 76, 76, 76, 113, 126).

[82] Adrian Cho. Reprise of First Experiment Casts Doubt on Supersolid Helium. *Science*, 336:661–661, 5 2012. (cited on page 4).

[83] Jun-Ru Li, Jeongwon Lee, Wujie Huang, Sean Burchesky, Boris Shteynas, Furkan Çağrı Top, Alan O Jamison, and Wolfgang Ketterle. A stripe phase with supersolid properties in spin–orbit-coupled Bose–Einstein condensates. *Nature*, 543(7643):91–94, 03 2017. (cited on page 4).

[84] Thomas M. Bersano, Junpeng Hou, Sean Mossman, Vandna Gokhroo, Xi-Wang Luo, Kuei Sun, Chuanwei Zhang, and Peter Engels. Experimental realization of a long-lived striped Bose-Einstein condensate induced by momentum-space hopping. *Phys. Rev. A*, 99:051602, May 2019. (cited on page 4).

[85] Julian Léonard, Andrea Morales, Philip Zupancic, Tilman Esslinger, and Tobias Donner. Supersolid formation in a quantum gas breaking a continuous translational symmetry. *Nature*, 543(7643):87–90, 03 2017. (cited on page 4).

[86] Julian Léonard, Andrea Morales, Philip Zupancic, Tobias Donner, and Tilman Esslinger. Monitoring and manipulating Higgs and Goldstone modes in a supersolid quantum gas. *Science*, 358:1415–1418, 12 2017. (cited on page 4).

[87] J L Roberts, N R Claussen, S L Cornish, E A Donley, Eric A Cornell, and C E Wieman. Controlled Collapse of a Bose-Einstein Condensate. *Phys. Rev. Lett.*, 86(19):4211–4214, may 2001. (cited on pages 4, 10).

[88] Cheng Chin, Rudolf Grimm, Paul Julienne, and Eite Tiesinga. Feshbach resonances in ultracold gases. *Rev. Mod. Phys.*, 82:1225–1286, Apr 2010. (cited on pages 4, 5, 5, 10, 30, 30, 158, 158, 158, 158).

[89] L. D. Landau and E. M. Lifshitz. *Quantum Mechanics, vol. 3 (Course of theoretical physics)*. Butterworth-Heinemann, Oxford, 1977. (cited on page 5).

[90] Jean Dalibard. Collisional dynamics of ultra-cold atomic gases. In *Proceedings of the International School of Physics-Enrico Fermi*, volume 321, page 1, 1999. (cited on pages 5, 25).

[91] Lauriane Chomaz, Igor Ferrier-Barbut, Francesca Ferlaino, Bruno Laburthe-Tolra, Benjamin L Lev, and Tilman Pfau. Dipolar physics: a review of experiments with magnetic quantum gases. *Reports on Progress in Physics*, 86(2):026401, feb 2023. (cited on pages 5, 5, 6, 7, 9, 11, 14, 36, 64, 113, 117).

[92] K Aikawa, A Frisch, M Mark, S Baier, R Grimm, J L Bohn, D S Jin, G M Bruun, and F Ferlaino. Anisotropic Relaxation Dynamics in a Dipolar Fermi Gas Driven Out of Equilibrium. *Phys. Rev. Lett.*, 113(26):26320, dec 2014. (cited on page 6).

[93] T Lahaye, C Menotti, L Santos, M Lewenstein, and T Pfau. The physics of dipolar bosonic quantum gases. *Reports on Progress in Physics*, 72(12):126401, 2009. (cited on page 7, 7).

[94] Oliver Penrose and Lars Onsager. Bose-Einstein Condensation and Liquid Helium. *Phys. Rev.*, 104:576, Nov 1956. (cited on pages 7, 13).

[95] Sandro Stringari and Lev Pitaevskii. *Bose-Einstein condensation and superfluidity*. Oxford Science Publications, Oxford, 2016. (cited on pages 7, 8, 8, 9, 34, 36, 36, 76, 77, 79).

[96] Eugene P Gross. Structure of a quantized vortex in boson systems. *Il Nuovo Cimento (1955-1965)*, 20(3):454–477, 1961. (cited on page 7).

[97] LP Pitaevskii. Vortex lines in an imperfect Bose gas. *Sov. Phys. JETP*, 13(2):451–454, 1961. (cited on page 7).

[98] A M Martin, N G Marchant, D H J O'Dell, and N G Parker. Vortices and vortex lattices in quantum ferrofluids. *Journal of Physics: Condensed Matter*, 29(10):103004, feb 2017. (cited on pages 8, 8, 36, 37, 60).

[99] Duncan H. J. O'Dell, Stefano Giovanazzi, and Claudia Eberlein. Exact Hydrodynamics of a Trapped Dipolar Bose-Einstein Condensate. *Phys. Rev. Lett.*, 92:250401, Jun 2004. (cited on pages 8, 29, 43).

[100] Claudia Eberlein, Stefano Giovanazzi, and Duncan H. J. O'Dell. Exact solution of the Thomas-Fermi equation for a trapped Bose-Einstein condensate with dipole-dipole interactions. *Phys. Rev. A*, 71(3):033618, Mar 2005. (cited on pages 8, 29).

[101] Jürgen Stuhler, Axel Griesmaier, Tobias Koch, Marco Fattori, and Tilman Pfau. Magnetostriction in a degenerate quantum gas. *Journal of Magnetism and Magnetic Materials*, 316(2):429–432, sep 2007. (cited on pages 8, 29).

[102] R. M. W. van Bijnen, N. G. Parker, S. J. J. M. F. Kokkelmans, A. M. Martin, and D. H. J. O'Dell. Collective excitation frequencies and stationary states of trapped dipolar Bose-Einstein condensates in the Thomas-Fermi regime. *Phys. Rev. A*, 82:033612, Sep 2010. (cited on page 8).

[103] L. Santos, G. V. Shlyapnikov, P. Zoller, and M. Lewenstein. Bose-Einstein Condensation in Trapped Dipolar Gases. *Phys. Rev. Lett.*, 85:1791–1794, Aug 2000. (cited on page 9).

[104] L. Chomaz, R. M. W. van Bijnen, D. Petter, G. Faraoni, S. Baier, J. H. Becher, M. J. Mark, F. Wächtler, L. Santos, and F. Ferlaino. Observation of roton mode population in a dipolar quantum gas. *Nature Physics*, 14(5):442–446, 2018. (cited on pages 9, 10).

[105] L Santos, GV Shlyapnikov, and M Lewenstein. Roton-maxon spectrum and stability of trapped dipolar Bose-Einstein condensates. *Physical Review Letters*, 90(25):250403, Jun 2003. (cited on page 9).

[106] L. Landau. Theory of the superfluidity of Helium II. *Phys. Rev.*, 60:356–358, Aug 1941. (cited on pages 9, 33).

[107] R. N. Bisset and P. B. Blakie. Crystallization of a dilute atomic dipolar condensate. *Phys. Rev. A*, 92:061603, Dec 2015. (cited on page 10).

[108] Holger Kadau, Matthias Schmitt, Matthias Wenzel, Clarissa Wink, Thomas Maier, Igor Ferrier-Barbut, and Tilman Pfau. Observing the Rosensweig instability of a quantum ferrofluid. *Nature*, 530(7589):194–197, 02 2016. (cited on pages 10, 27).

[109] L. Chomaz, S. Baier, D. Petter, M. J. Mark, F. Wächtler, L. Santos, and F. Ferlaino. Quantum-Fluctuation-Driven Crossover from a Dilute Bose-Einstein Condensate to a Macrodroplet in a Dipolar Quantum Fluid. *Phys. Rev. X*, 6(4):041039, Nov 2016. (cited on pages 10, 11, 158).

[110] Tsin D Lee, Kerson Huang, and Chen N Yang. Eigenvalues and eigenfunctions of a Bose system of hard spheres and its low-temperature properties. *Physical Review*, 106(6):1135, Jun 1957. (cited on page 10).

[111] T. D. Lee, Kerson Huang, and C. N. Yang. Eigenvalues and Eigenfunctions of a Bose System of Hard Spheres and Its Low-Temperature Properties. *Phys. Rev.*, 106:1135–1145, Jun 1957. (cited on page 10).

[112] Ralf Schützhold, Michael Uhlmann, Yan Xu, and Uwe Fischer. Mean-field expansion in Bose-Einstein condensates with finite-range interactions. *Int. J. Mod. Phys. B*, 20(24):3555–3565, 2006. (cited on page 10).

[113] Aristeu R. P. Lima and Axel Pelster. Quantum fluctuations in dipolar Bose gases. *Phys. Rev. A*, 84(4):041604, Oct 2011. (cited on page 10).

[114] A. R. P. Lima and A. Pelster. Beyond mean-field low-lying excitations of dipolar Bose gases. *Phys. Rev. A*, 86(6):063609, Dec 2012. (cited on page 10).

[115] Axel Griesmaier, Jürgen Stuhler, Tobias Koch, Marco Fattori, Tilman Pfau, and Stefano Giovanazzi. Comparing Contact and Dipolar Interactions in a Bose-Einstein Condensate. *Phys. Rev. Lett.*, 97(25):25040, dec 2006. (cited on page 10).

[116] D. Baillie and P. B. Blakie. Droplet Crystal Ground States of a Dipolar Bose Gas. *Phys. Rev. Lett.*, 121:195301, Nov 2018. (cited on page 11).

[117] Matthias Schmitt, Matthias Wenzel, Fabian Böttcher, Igor Ferrier-Barbut, and Tilman Pfau. Self-bound droplets of a dilute magnetic quantum liquid. *Nature*, 539(7628):259–262, 11 2016. (cited on page 11).

[118] J. Hertkorn, J.-N. Schmidt, M. Guo, F. Böttcher, K. S. H. Ng, S. D. Graham, P. Uerlings, T. Langen, M. Zwierlein, and T. Pfau. Pattern formation in quantum ferrofluids: From supersolids to superglasses. *Phys. Rev. Research*, 3:033125, Aug 2021. (cited on pages 11, 64).

[119] R. N. Bisset, R. M. Wilson, D. Baillie, and P. B. Blakie. Ground-state phase diagram of a dipolar condensate with quantum fluctuations. *Phys. Rev. A*, 94(3):033619, Sep 2016. (cited on page 11).

[120] Fabian Böttcher, Jan-Niklas Schmidt, Matthias Wenzel, Jens Hertkorn, Mingyang Guo, Tim Langen, and Tilman Pfau. Transient Supersolid Properties in an Array of Dipolar Quantum Droplets. *Phys. Rev. X*, 9:011051, Mar 2019. (cited on pages 11, 62, 63, 125).

[121] L. Tanzi, E. Lucioni, F. Famà, J. Catani, A. Fioretti, C. Gabbanini, R. N. Bisset, L. Santos, and G. Modugno. Observation of a Dipolar Quantum Gas with Metastable Supersolid Properties. *Phys. Rev. Lett.*, 122:130405, Apr 2019. (cited on pages 11, 62, 63, 125).

[122] L. Chomaz, D. Petter, P. Ilzhöfer, G. Natale, A. Trautmann, C. Politi, G. Durastante, R. M. W. van Bijnen, A. Patscheider, M. Sohmen, M. J. Mark, and F. Ferlaino. Long-Lived and Transient Supersolid Behaviors in Dipolar Quantum Gases. *Phys. Rev. X*, 9:021012, Apr 2019. (cited on pages 11, 62, 63, 125, 158).

[123] Maximilian Sohmen, Claudia Politi, Lauritz Klaus, Lauriane Chomaz, Manfred J. Mark, Matthew A. Norcia, and Francesca Ferlaino. Birth, Life, and Death of a Dipolar Supersolid. *Phys. Rev. Lett.*, 126:233401, Jun 2021. (cited on pages 11, 64, 65, 94).

[124] P. Ilzhöfer, M. Sohmen, G. Durastante, C. Politi, A. Trautmann, G. Natale, G. Morpurgo, T. Giamarchi, L. Chomaz, M. J. Mark, and F. Ferlaino. Phase coherence in out-of-equilibrium supersolid states of ultracold dipolar atoms. *Nature Physics*, 17(3):356–361, 2021. (cited on pages 12, 113).

[125] G Natale, RMW van Bijnen, A Patscheider, D Petter, MJ Mark, L Chomaz, and F Ferlaino. Excitation spectrum of a trapped dipolar supersolid and its experimental evidence. *Physical review letters*, 123(5):050402, Aug 2019. (cited on pages 11, 13).

[126] E. Poli, D. Baillie, F. Ferlaino, and P. B. Blakie. Excitations of a two-dimensional supersolid. *Physical Review A*, 110:053301, 11 2024. (cited on pages 12, 64, 94, 113, 114, 126).

[127] Pramodh Senarath Yapa and Thomas Bland. Supersonic shear waves in dipolar supersolids. 10 2024. (cited on pages 12, 113, 126).

[128] E. M. Lifshitz and L. P. Pitaevskii. *Statistical Physics, Part 2, vol. 9 (Course of theoretical physics)*. Pergamon Press, Oxford, 1980. (cited on page 12).

[129] Mingyang Guo, Fabian Böttcher, Jens Hertkorn, Jan-Niklas Schmidt, Matthias Wenzel, Hans Peter Büchler, Tim Langen, and Tilman Pfau. The low-energy Goldstone mode in a trapped dipolar supersolid. *Nature*, 564:386, 2019. (cited on pages 13, 62, 64, 96, 113).

[130] L Tanzi, SM Roccuzzo, E Lucioni, F Famà, A Fioretti, C Gabbanini, G Modugno, A Recati, and S Stringari. Supersolid symmetry breaking from compressional oscillations in a dipolar quantum gas. *Nature*, 574(7778):382–385, October 2019. (cited on pages 13, 96).

[131] L Tanzi, JG Maloberti, G Biagioni, A Fioretti, C Gabbanini, and G Modugno. Evidence of superfluidity in a dipolar supersolid from nonclassical rotational inertia. *Science*, 371(6534):1162–1165, 2021. (cited on pages 13, 62, 76, 76, 78, 78, 78, 80, 126).

[132] G. Biagioni, N. Antolini, B. Donelli, L. Pezzè, A. Smerzi, M. Fattori, A. Fioretti, C. Gabbanini, M. Inguscio, L. Tanzi, and G. Modugno. Measurement of the superfluid fraction of a supersolid by Josephson effect. *Nature*, 629:773–777, 5 2024. (cited on pages 13, 81, 113).

[133] A. Trautmann, P. Ilzhöfer, G. Durastante, C. Politi, M. Sohmen, M. J. Mark, and F. Ferlaino. Dipolar Quantum Mixtures of Erbium and Dysprosium Atoms. *Phys. Rev. Lett.*, 121:213601, Nov 2018. (cited on pages 14, 127).

[134] Albert Frisch. *Dipolar quantum gases of Erbium*. PhD thesis, Ph. D. thesis, University of Inssbruck, 2014. (cited on pages 15, 158).

[135] W. M. Haynes, D. R. Lide, and T. J. Bruno. Abundance of elements in the earth's crust and in the sea. In *CRC Handbook of Chemistry and Physics*, pages 14–17. CRC Press, 97th edition, 2016-2017. (cited on page 15).

[136] S. Sugimoto. Current status and recent topics of rare-earth permanent magnets. *Journal of Physics D: Applied Physics*, 44(6):064001, feb 2011. (cited on page 15).

[137] Philipp Ilzhöfer. *Creation of Dipolar Quantum Mixtures of Erbium and Dysprosium*. PhD thesis, Universität Innsbruck, 2020. (cited on pages 15, 18, 18, 19, 19, 19, 20, 28, 31, 32).

[138] Seo Ho Youn, Mingwu Lu, Ushnish Ray, and Benjamin L. Lev. Dysprosium magneto-optical traps. *Phys. Rev. A*, 82:043425, Oct 2010. (cited on pages 15, 17).

[139] Nathaniel Q Burdick, Yijun Tang, and Benjamin L Lev. Long-Lived Spin-Orbit-Coupled Degenerate Dipolar Fermi Gas. *Phys. Rev. X*, 6(3):031022, aug 2016. (cited on page 15).

[140] Thomas Chalopin, Tanish Satoor, Alexandre Evrard, Vasiliy Makhalov, Jean Dalibard, Raphael Lopes, and Sylvain Nascimbene. Probing chiral edge dynamics and bulk topology of a synthetic Hall system. *Nature Physics*, 16(10):1017–1021, 2020. (cited on page 15).

[141] Christopher J. Foot, editor. *Atomic Physics*. Oxford University Press Inc., New York, 2005. (cited on pages 15, 25, 26).

[142] J. G. Conway and B. G. Wybourne. Low-Lying Energy Levels of Lanthanide Atoms and Intermediate Coupling. *Phys. Rev.*, 130:2325–2332, Jun 1963. (cited on page 16).

[143] W. C. Martin, R. Zalubas, and L. Hagan. Atomic energy levels - the rare earth elements (the spectra of lanthanum, cerium, praseodymium, neodymium, promethium, samarium, europium, gadolinium, terbium, dysprosium, holmium, erbium, thulium, ytterbium, and lutetium). Technical report, NATIONAL STANDARD REFERENCE DATA SYSTEM, United States, 1978. PB–282067. (cited on page 16).

[144] Mingwu Lu, Seo Ho Youn, and Benjamin L. Lev. Spectroscopy of a narrow-line laser-cooling transition in atomic dysprosium. *Phys. Rev. A*, 83:012510, 2011. (cited on page 17).

[145] Mingwu Lu, Seo Ho Youn, and Benjamin L Lev. Trapping Ultracold Dysprosium: A Highly Magnetic Gas for Dipolar Physics. *Phys. Rev. Lett.*, 104(6):063001–4, feb 2010. (cited on page 17).

[146] P. Ilzhöfer, G. Durastante, A. Patscheider, A. Trautmann, M. J. Mark, and F. Ferlaino. Two-species five-beam magneto-optical trap for erbium and dysprosium. *Phys. Rev. A*, 97:023633, Feb 2018. (cited on pages 17, 20).

[147] Alexander Kramida, Yuri Ralchenko, Joseph Reader, and NIST ASD Team. NIST Atomic Spectra Database, 2023. (cited on page 17).

[148] Yann Allain. Build you own Quantum Computer @ Home - 99% of discount - Hacker Style !, 2019. (cited on page 18).

[149] Gianmaria Durastante. *Creation of Erbium-Dysprosium Dipolar Quantum Mixtures and Their Interspecies Feshbach Resonances*. PhD thesis, Univeristät Innsbruck, 2020. (cited on page 18).

[150] Maximilian Sohmen. *Supersolidity in Dipolar Quantum Gases in and out of Equilibrium*. PhD thesis, Universität Innsbruck, 2021. (cited on pages 18, 27, 27, 27, 28, 28, 117, 118).

[151] Claudia Politi. *Many-body quantum phases of dipolar gases*. PhD thesis, Universität Innsbruck, 2022. (cited on pages 18, 22, 22).

[152] Johannes Schindler. *Characterization of an Erbium Atomic Beam*. Master thesis, Universität Innsbruck, 2011. (cited on page 19).

[153] Benedict Franz Hochreiter. *Optimisation of a spin-flip Zeeman slower and laser locking to a broad spectral line*. Master thesis, Universität Innsbruck, 2020. (cited on page 19).

[154] H. J. Metcalf and P. van der Straten. Laser cooling and trapping of atoms. *Journal of the Optical Society of America B*, 20(5):887, 2003. (cited on pages 19, 19, 20).

[155] R. Maruyama, R. H. Wynar, M. V. Romalis, A. Andalkar, M. D. Swallows, C. E. Pearson, and E. N. Fortson. Investigation of sub-Doppler cooling in an ytterbium magneto-optical trap. *Physical Review A*, 68(1):011403, jul 2003. (cited on page 20).

[156] Akio Kawasaki, Boris Braverman, Qinqin Yu, and Vladan Vuletic. Two-color magneto-optical trap with small magnetic field for ytterbium. *Journal of Physics B: Atomic, Molecular and Optical Physics*, 48(15):155302, aug 2015. (cited on page 20).

[157] Hidetoshi Katori, Tetsuya Ido, Yoshitomo Isoya, and Makoto Kuwata-Gonokami. Magneto-optical trapping and cooling of strontium atoms down to the photon recoil temperature. *Phys. Rev. Lett.*, 82:1116–1119, 1999. (cited on page 20).

[158] S. Snigirev, A. J. Park, A. Heinz, I. Bloch, and S. Blatt. Fast and dense magneto-optical traps for strontium. *Physical Review A*, 99(6):063421, jun 2019. (cited on page 20).

[159] W. Winkler, K. Danzmann, A. Rüdiger, and R. Schilling. Heating by optical absorption and the performance of interferometric gravitational-wave detectors. *Phys. Rev. A*, 44:7022–7036, Dec 1991. (cited on page 22).

[160] K B Davis, M O. Mewes, and W Ketterle. An analytical model for evaporative cooling of atoms. *Applied Physics B Laser and Optics*, 60(2-3):155–159, jul 1995. (cited on pages 23, 24).

[161] A. Patscheider, L. Chomaz, G. Natale, D. Petter, M. J. Mark, S. Baier, B. Yang, R. R. W. Wang, J. L. Bohn, and F. Ferlaino. Determination of the scattering length of erbium atoms. *Phys. Rev. A*, 105:063307, Jun 2022. (cited on pages 24, 30, 158, 158).

[162] Rudolf Grimm, Matthias Weidemüller, and Yurii B. Ovchinnikov. Optical Dipole Traps for Neutral Atoms. *Adv. At. Mol. Opt. Phys.*, 42:95–170, 2000. (cited on page 24).

[163] D. E. Pritchard. Trapping and Cooling Neutral Atoms. In D. C. Lorents, W. E. Meyerhof, and J. R. Peterson, editors, *Electronic and atomic collisions : invited papers of the XIV International Conference on the Physics of Electronic and Atomic Collisions*. Elsevier, Palo Alto, 1985. (cited on page 25).

[164] V. B. Makhalov, K. A. Martiyanov, and A. V. Turlapov. Primary vacuometer based on an ultracold gas in a shallow optical dipole trap. *Metrologia*, 53(6):1287–1294, dec 2016. (cited on page 25).

[165] F. Claude, L. Lafforgue, J. J. A. Houwman, M. J. Mark, and F. Ferlaino. Optical manipulation of spin states in ultracold magnetic atoms via an inner-shell Hz transition. *Physical Review Research*, 6:L042016, 10 2024. (cited on page 25).

[166] F. Ferlaino, S. Knoop, M. Mark, M. Berninger, H. Schöbel, H.-C. Nägerl, and R. Grimm. Collisions between tunable halo dimers: Exploring an elementary four-body process with identical bosons. *Phys. Rev. Lett.*, 101(2):023201, 2008. (cited on page 25).

[167] C. Cohen-Tannoudji, J. Dupont-Roc, and G. Grynberg. *Atom-Photon Interactions, Basic Processes and Applications*. WILEY-VCH Verlag GmbH & Co. KGaA, Weinheim, 2004. (cited on page 26).

[168] Klaus Hueck, Niclas Luick, Lennart Sobirey, Jonas Siegl, Thomas Lompe, Henning Moritz, Logan W. Clark, and Cheng Chin. Calibrating high intensity absorption imaging of ultracold atoms. *Optics Express*, 25(8):8670, apr 2017. (cited on page 26).

[169] C. C. Bradley, C. A. Sackett, and R. G. Hulet. Bose-Einstein condensation of lithium: Observation of limited condensate number. *Phys. Rev. Lett.*, 78:985–989, Feb 1997. (cited on page 27, 27).

[170] Steven Chu. Cold atoms and quantum control. *Nature*, 416(6877):206–210, mar 2002. (cited on page 29).

[171] Eddy Timmermans, Paolo Tommasini, Mahir Hussein, and Arthur Kerman. Feshbach resonances in atomic Bose–Einstein condensates. *Physics Reports*, 315(1):199–230, 1999. (cited on page 30).

[172] C. J. Pethick and H. Smith. *Bose-Einstein condensation in dilute gases*. Cambridge University Press, 2002. (cited on pages 30, 37, 37).

[173] Gianmaria Durastante, Claudia Politi, Maximilian Sohmen, Philipp Ilzhöfer, Manfred J. Mark, Matthew A. Norcia, and Francesca Ferlaino. Feshbach resonances in an erbium-dysprosium dipolar mixture. *Phys. Rev. A*, 102:033330, Sep 2020. (cited on pages 30, 158).

[174] C. Chin, V. Vuletić, A. J. Kerman, and S. Chu. High resolution Feshbach spectroscopy of cesium. *Phys. Rev. Lett.*, 85:271, 2000. (cited on page 30).

[175] P. J. Leo, C. J. Williams, and P. S. Julienne. Collision properties of ultracold ^{133}Cs atoms. *Phys. Rev. Lett.*, 85:2721–2724, 2000. (cited on page 30).

[176] Yijun Tang, Andrew Sykes, Nathaniel Q. Burdick, John L. Bohn, and Benjamin L. Lev. s-wave scattering lengths of the strongly dipolar bosons ^{162}Dy and ^{164}Dy. *Phys. Rev. A*, 92:022703, Aug 2015. (cited on pages 30, 158).

[177] S. Baier, M. J. Mark, D. Petter, K. Aikawa, L. Chomaz, Z. Cai, M. Baranov, P. Zoller, and F. Ferlaino. Extended Bose-Hubbard models with ultracold magnetic atoms. *Science*, 352(6282):201–205, 2016. (cited on pages 30, 117).

[178] A De Troyer, A Van Itterbeek, and G.J Van Den Berg. Measurements on the viscosity of liquid helium by means of the oscillating disc method. *Physica*, 17(1):50–62, 1951. (cited on page 33).

[179] A. C. Hollis-Hallett. Experiments with oscillating disk systems in liquid helium II. *Proceedings of the Royal Society of London. Series A. Mathematical and Physical Sciences*, 210(1102):404–426, jan 1952. (cited on page 33).

[180] R.P. Feynman. Chapter II Application of Quantum Mechanics to Liquid Helium. volume 1 of *Progress in Low Temperature Physics*, pages 17–53. Elsevier, 1955. (cited on pages 33, 35).

[181] L. Onsager. Statistical hydrodynamics. *Il Nuovo Cimento*, 6(S2):279–287, mar 1949. (cited on pages 33, 34, 35).

[182] Edgar Hall and William Frank Vinen. The rotation of liquid helium II I. Experiments on the propagation of second sound in uniformly rotating helium II. *Proceedings of the Royal Society of London. Series A. Mathematical and Physical Sciences*, 238(1213):204–214, dec 1956. (cited on page 33).

[183] W.F. Vinen. Vortex lines in liquid helium II. *Physica*, 24:S13–S17, sep 1958. (cited on pages 33, 60).

[184] William Frank Vinen and David Shoenberg. The detection of single quanta of circulation in liquid helium II. *Proceedings of the Royal Society of London. Series A. Mathematical and Physical Sciences*, 260(1301):218–236, 1961. (cited on page 33).

[185] G. W. Rayfield and F. Reif. Quantized Vortex Rings in Superfluid Helium. *Phys. Rev.*, 136:A1194–A1208, Nov 1964. (cited on page 33).

[186] R. Doll and M. Näbauer. Experimental Proof of Magnetic Flux Quantization in a Superconducting Ring. *Physical Review Letters*, 7(2):51–52, jul 1961. (cited on page 33).

[187] Bascom S. Deaver and William M. Fairbank. Experimental evidence for quantized flux in superconducting cyclinders. *Physical Review Letters*, 7(2):43–46, 1961. (cited on page 33).

[188] W. A. Little and R. D. Parks. Observation of Quantum Periodicity in the Transition Temperature of a Superconducting Cylinder. *Physical Review Letters*, 9(1):9–12, jul 1962. (cited on page 33).

[189] B. P. Anderson, P. C. Haljan, C. E. Wieman, and E. A. Cornell. Vortex Precession in Bose-Einstein Condensates: Observations with Filled and Empty Cores. *Physical Review Letters*, 85:2857–2860, 10 2000. (cited on page 33, 33).

[190] K. W. Madison, F. Chevy, W. Wohlleben, and J. Dalibard. Vortex formation in a stirred Bose-Einstein condensate. *Phys. Rev. Lett.*, 84:806–809, Jan 2000. (cited on pages 33, 38, 38, 40).

[191] Subhasis Sinha and Yvan Castin. Dynamic Instability of a Rotating Bose-Einstein Condensate. *Physical Review Letters*, 87(19):190402, oct 2001. (cited on pages 33, 38).

[192] A. Recati, F. Zambelli, and S. Stringari. Overcritical Rotation of a Trapped Bose-Einstein Condensate. *Physical Review Letters*, 86(3):377–380, jan 2001. (cited on pages 33, 38).

[193] K. W. Madison, F. Chevy, V. Bretin, and J. Dalibard. Stationary states of a rotating Bose-Einstein condensate: Routes to vortex nucleation. *Phys. Rev. Lett.*, 86:4443–4446, May 2001. (cited on pages 33, 38, 38, 96).

[194] C. Raman, J. R. Abo-Shaeer, J. M. Vogels, K. Xu, and W. Ketterle. Vortex Nucleation in a Stirred Bose-Einstein Condensate. *Physical Review Letters*, 87(21):210402, nov 2001. (cited on pages 33, 40, 42).

[195] P. Rosenbusch, V. Bretin, and J. Dalibard. Dynamics of a Single Vortex Line in a Bose-Einstein Condensate. *Physical Review Letters*, 89, 2002. (cited on page 33).

[196] P. Engels, I. Coddington, P. C. Haljan, and E. A. Cornell. Nonequilibrium Effects of Anisotropic Compression Applied to Vortex Lattices in Bose-Einstein Condensates. *Physical Review Letters*, 89:1–4, 2002. (cited on pages 33, 38).

[197] V. Schweikhard, I. Coddington, P. Engels, V. P. Mogendorff, and E. A. Cornell. Rapidly Rotating Bose-Einstein Condensates in and near the Lowest Landau Level. *Phys. Rev. Lett.*, 92:040404, Jan 2004. (cited on pages 33, 42).

[198] Vincent Bretin, Sabine Stock, Yannick Seurin, and Jean Dalibard. Fast Rotation of a Bose-Einstein Condensate. *Physical Review Letters*, 92:050403, 2 2004. (cited on pages 33, 42).

[199] V. Bretin, P. Rosenbusch, F. Chevy, G. V. Shlyapnikov, and J. Dalibard. Quadrupole Oscillation of a Single-Vortex Bose-Einstein Condensate: Evidence for Kelvin Modes. *Phys. Rev. Lett.*, 90:100403, 2003. (cited on pages 33, 44, 60).

[200] Richard J Fletcher, Airlia Shaffer, Cedric C Wilson, Parth B Patel, Zhenjie Yan, Valentin Crépel, Biswaroop Mukherjee, and Martin W Zwierlein. Geometric squeezing into the lowest Landau level. *Science*, 372(6548):1318–1322, 2021. (cited on page 33).

[201] Biswaroop Mukherjee, Airlia Shaffer, Parth B Patel, Zhenjie Yan, Cedric C Wilson, Valentin Crépel, Richard J Fletcher, and Martin Zwierlein. Crystallization of bosonic quantum Hall states in a rotating quantum gas. *Nature*, 601(7891):58–62, 2022. (cited on page 33).

[202] Nir Navon, Alexander L. Gaunt, Robert P. Smith, and Zoran Hadzibabic. Emergence of a turbulent cascade in a quantum gas. *Nature*, 539(7627):72–75, nov 2016. (cited on pages 33, 61).

[203] G. Del Pace, K. Xhani, A. Muzi Falconi, M. Fedrizzi, N. Grani, D. Hernandez Rajkov, M. Inguscio, F. Scazza, W. J. Kwon, and G. Roati. Imprinting Persistent Currents in Tunable Fermionic Rings. *Physical Review X*, 12:041037, 10 2022. (cited on pages 33, 38, 38).

[204] Guillaume Gauthier, Matthew T Reeves, Xiaoquan Yu, Ashton S Bradley, Mark A Baker, Thomas A Bell, Halina Rubinsztein-Dunlop, Matthew J Davis, and Tyler W Neely. Giant vortex clusters in a two-dimensional quantum fluid. *Science*, 364:1264–1267, 2019. (cited on pages 34, 38).

[205] Shaun P Johnstone, Andrew J Groszek, Philip T Starkey, Christopher J Billington, Tapio P Simula, and Kristian Helmerson. Evolution of large-scale flow from turbulence in a two-dimensional superfluid. *Science*, 364:1267–1271, 2019. (cited on page 34).

[206] M. W. Zwierlein, J. R. Abo-Shaeer, A. Schirotzek, C. H. Schunck, and W. Ketterle. Vortices and superfluidity in a strongly interacting Fermi gas. *Nature (London)*, 435(7045):1047–1051, 2005. (cited on pages 34, 35, 96).

[207] Lauritz Klaus, Thomas Bland, Elena Poli, Claudia Politi, Giacomo Lamporesi, Eva Casotti, Russell N. Bisset, Manfred J. Mark, and Francesca Ferlaino. Observation of vortices and vortex stripes in a dipolar condensate. *Nature Physics*, 18(12):1453–1458, 2022. (cited on pages 34, 37).

[208] Scott Beattie, Stuart Moulder, Richard J. Fletcher, and Zoran Hadzibabic. Persistent Currents in Spinor Condensates. *Physical Review Letters*, 110(2):025301, jan 2013. (cited on pages 35, 38, 38).

[209] B. C. Mulkerin, D H J O'Dell, A. M. Martin, and N. G. Parker. Vortices in the two-dimensional dipolar Bose gas. *Journal of Physics: Conference Series*, 497(1):012025, apr 2014. (cited on pages 36, 43, 60).

[210] D. H. J. O'Dell and C. Eberlein. Vortex in a trapped Bose-Einstein condensate with dipole-dipole interactions. *Phys. Rev. A*, 75:013604, Jan 2007. (cited on page 37).

[211] Angela C. White, Brian P. Anderson, and Vanderlei S. Bagnato. Vortices and turbulence in trapped atomic condensates. *Proceedings of the National Academy of Sciences*, 111:4719–4726, 3 2014. (cited on page 37).

[212] Anatoly A. Svidzinsky and Alexander L. Fetter. Stability of a Vortex in a Trapped Bose-Einstein Condensate. *Physical Review Letters*, 84:5919–5923, 6 2000. (cited on page 37).

[213] Lord Kelvin. On vortex atoms. *Proceedings of the Royal Society of Edinburgh*, 4:94–105, 1867. (cited on page 37).

[214] F. Dalfovo and S. Stringari. Shape deformations and angular-momentum transfer in trapped Bose-Einstein condensates. *Phys. Rev. A*, 63:011601, Dec 2000. (cited on page 38).

[215] P. C. Haljan, I. Coddington, P. Engels, and E. A. Cornell. Driving Bose-Einstein-Condensate Vorticity with a Rotating Normal Cloud. *Phys. Rev. Lett.*, 87:210403, Nov 2001. (cited on pages 38, 113).

[216] T. W. Neely, E. C. Samson, A. S. Bradley, M. J. Davis, and B. P. Anderson. Observation of Vortex Dipoles in an Oblate Bose-Einstein Condensate. *Physical Review Letters*, 104:160401, 4 2010. (cited on page 38).

[217] T. W. Neely, A. S. Bradley, E. C. Samson, S. J. Rooney, E. M. Wright, K. J. H. Law, R. Carretero-González, P. G. Kevrekidis, M. J. Davis, and B. P. Anderson. Characteristics of Two-Dimensional Quantum Turbulence in a Compressible Superfluid. *Physical Review Letters*, 111:235301, 12 2013. (cited on page 38).

[218] Woo Jin Kwon, Geol Moon, Jae yoon Choi, Sang Won Seo, and Yong il Shin. Relaxation of superfluid turbulence in highly oblate Bose-Einstein condensates. *Physical Review A*, 90:063627, 12 2014. (cited on page 38).

[219] E. C. Samson, K. E. Wilson, Z. L. Newman, and B. P. Anderson. Deterministic creation, pinning, and manipulation of quantized vortices in a Bose-Einstein condensate. *Physical Review A*, 93:023603, 2 2016. (cited on page 38, 38).

[220] W. J. Kwon, G. Del Pace, K. Xhani, L. Galantucci, A. Muzi Falconi, M. Inguscio, F. Scazza, and G. Roati. Sound emission and annihilations in a programmable quantum vortex collider. *Nature*, 600:64–69, 12 2021. (cited on page 38).

[221] Avinash Kumar, Romain Dubessy, Thomas Badr, Camilla De Rossi, Mathieu de Goër de Herve, Laurent Longchambon, and Hélène Perrin. Producing superfluid circulation states using phase imprinting. *Physical Review A*, 97:043615, 4 2018. (cited on page 38).

[222] J. Denschlag, J.E. Simsarian, D. L. Feder, C. W. Clark, L. A. Collins, J. Cubizolles, L. Deng, E. W. Hagley, W. P. Helmerson, K. Reinhardt, S. L. Rolston, B. I. Schneider, and W. D. Phillips. Generating solitons by phase engineering of a Bose-Einstein condensate. *Science*, 287:97–101, 2000. (cited on page 38).

[223] Chad N. Weiler, Tyler W. Neely, David R. Scherer, Ashton S. Bradley, Matthew J. Davis, and Brian P. Anderson. Spontaneous vortices in the formation of Bose-Einstein condensates. *Nature*, 455:948–951, 10 2008. (cited on page 38).

[224] Giacomo Lamporesi, Simone Donadello, Simone Serafini, Franco Dalfovo, and Gabriele Ferrari. Spontaneous creation of Kibble-Zurek solitons in a Bose-Einstein condensate. *Nature Physics*, 9:656–660, 2013. (cited on page 38).

[225] L. Corman, L. Chomaz, T. Bienaimé, R. Desbuquois, C. Weitenberg, S. Nascimbène, J. Dalibard, and J. Beugnon. Quench-induced supercurrents in an annular bose gas. *Physical Review Letters*, 113, 9 2014. (cited on page 38).

[226] L. Chomaz, L. Corman, T. Bienaimé, R. Desbuquois, C. Weitenberg, S. Nascimbène, J. Beugnon, and J. Dalibard. Emergence of coherence via transverse condensation in a uniform quasi-two-dimensional Bose gas. *Nat. Commun.*, 6:6162, 2015. (cited on page 38).

[227] S. Donadello, S. Serafini, T. Bienaimé, F. Dalfovo, G. Lamporesi, and G. Ferrari. Creation and counting of defects in a temperature-quenched Bose-Einstein condensate. *Physical Review A*, 94, 8 2016. (cited on page 38).

[228] Junhong Goo, Younghoon Lim, and Y. Shin. Defect Saturation in a Rapidly Quenched Bose Gas. *Physical Review Letters*, 127, 9 2021. (cited on page 38).

[229] J. P. Joule. On the effects of magnetism upon the dimensions of iron and steel bars. *The London, Edinburgh and Dublin philosophical magazine and journal of science*, 30:22, 1847. (cited on page 39).

[230] NB Ekreem, AG Olabi, T Prescott, A Rafferty, and MSJ Hashmi. An overview of magnetostriction, its use and methods to measure these properties. *Journal of Materials Processing Technology*, 191(1-3):96–101, 2007. (cited on page 39).

[231] Wolfgang Petrich, Michael H. Anderson, Jason R. Ensher, and Eric A. Cornell. Stable, Tightly Confining Magnetic Trap for Evaporative Cooling of Neutral Atoms. *Physical Review Letters*, 74:3352–3355, 4 1995. (cited on page 39).

[232] Thomas Bland, Giacomo Lamporesi, Manfred J Mark, and Francesca Ferlaino. Vortices in dipolar Bose-Einstein condensates. *arXiv preprint arXiv:2303.13263*, 2023. (cited on pages 39, 39, 40, 61, 95, 125).

[233] J. R. Abo-Shaeer, C. Raman, and W. Ketterle. Formation and Decay of Vortex Lattices in Bose-Einstein Condensates at Finite Temperatures. *Physical Review Letters*, 88(7):070409, feb 2002. (cited on pages 41, 43, 44, 60).

[234] Alexei A. Abrikosov. On the Magnetic Properties of Superconductors of the Second Group. *J. Exptl. Theoret. Phys.*, (32):1442–1452, jun 1957. (cited on page 42).

[235] Daniel Cribier, B Jacrot, L Madhav Rao, and B Farnoux. Mise en evidence par diffraction de neutrons d'une structure periodique du champ magnetique dans le niobium supraconducteur. *Physics letters*, 9(2):106–107, 1964. (cited on page 42).

[236] U. Essmann and H. Träuble. The direct observation of individual flux lines in type II superconductors. *Physics Letters A*, 24(10):526–527, 1967. (cited on page 42).

[237] V. K. Tkachenko. On vortex lattices. *Soviet Physics JETP*, 22:1282–1286, 1966. (cited on pages 42, 60).

[238] NR Cooper, EH Rezayi, and SH Simon. Vortex lattices in rotating atomic Bose gases with dipolar interactions. *Phys. Rev. Lett.*, 95(20):200402, 2005. (cited on pages 43, 60).

[239] Jian Zhang and Hui Zhai. Vortex Lattices in Planar Bose-Einstein Condensates with Dipolar Interactions. *Phys. Rev. Lett.*, 95:200403, Nov 2005. (cited on pages 43, 60, 125).

[240] Yongyong Cai, Yongjun Yuan, Matthias Rosenkranz, Han Pu, and Weizhu Bao. Vortex patterns and the critical rotational frequency in rotating dipolar Bose-Einstein condensates. *Physical Review A*, 98(2):023610, aug 2018. (cited on page 43).

[241] N. G. Parker and D. H. J. O'Dell. Thomas-Fermi versus one- and two-dimensional regimes of a trapped dipolar Bose-Einstein condensate. *Physical Review A*, 78:041601, 10 2008. (cited on page 43).

[242] Yongyong Cai, Matthias Rosenkranz, Zhen Lei, and Weizhu Bao. Mean-field regime of trapped dipolar Bose-Einstein condensates in one and two dimensions. *Physical Review A*, 82:043623, 10 2010. (cited on page 43).

[243] Emil Lundh, J.-P. Martikainen, and Kalle-Antti Suominen. Vortex nucleation in Bose-Einstein condensates in time-dependent traps. *Physical Review A*, 67:063604, 6 2003. (cited on page 43).

[244] L.D. Landau and E.M. Lifshitz. *Fluid Mechanics: Volume 6*. Number Bd. 6. Butterworth-Heinemann, 2 edition, jan 1987. (cited on page 43).

[245] Sydney Goldstein. Fluid Mechanics in the First Half of this Century. *Annual Review of Fluid Mechanics*, 1(1):1–29, jan 1969. (cited on page 60).

[246] S. Yi and H. Pu. Vortex structures in dipolar condensates. *Phys. Rev. A*, 73:061602, Jun 2006. (cited on page 60).

[247] Christopher Ticknor, Ryan M. Wilson, and John L. Bohn. Anisotropic Superfluidity in a Dipolar Bose Gas. *Phys. Rev. Lett.*, 106:065301, Feb 2011. (cited on page 60).

[248] B. C. Mulkerin, R. M. W. van Bijnen, D. H. J. O'Dell, A. M. Martin, and N. G. Parker. Anisotropic and Long-Range Vortex Interactions in Two-Dimensional Dipolar Bose Gases. *Phys. Rev. Lett.*, 111:170402, Oct 2013. (cited on page 60).

[249] I. Coddington, P. Engels, V. Schweikhard, and E. A. Cornell. Observation of Tkachenko Oscillations in Rapidly Rotating Bose-Einstein Condensates. *Physical Review Letters*, 91:100402, 9 2003. (cited on page 60).

[250] M. Cozzini, L. P. Pitaevskii, and S. Stringari. Tkachenko Oscillations and the Compressibility of a Rotating Bose-Einstein Condensate. *Physical Review Letters*, 92:220401, 6 2004. (cited on page 60).

[251] C. F. Barenghi, R. J. Donnelly, and W. F. Vinen. Friction on quantized vortices in helium II. A review. *Journal of Low Temperature Physics*, 52:189–247, 8 1983. (cited on page 60).

[252] Yuan Tang, Wei Guo, Hiromichi Kobayashi, Satoshi Yui, Makoto Tsubota, and Toshiaki Kanai. Imaging quantized vortex rings in superfluid helium to evaluate quantum dissipation. *Nature Communications*, 14(1):2941, may 2023. (cited on page 60).

[253] T. Bland, G. W. Stagg, L. Galantucci, A. W. Baggaley, and N. G. Parker. Quantum Ferrofluid Turbulence. *Physical Review Letters*, 121(17):174501, oct 2018. (cited on page 61).

[254] Alexander L. Fetter. Rotating trapped Bose-Einstein condensates. *Rev. Mod. Phys.*, 81:647–691, May 2009. (cited on pages 61, 94).

[255] Yifei He, Ziting Chen, Haoting Zhen, Mingchen Huang, Mithilesh K Parit, and Gyu-Boong Jo. Exploring the Berezinskii-Kosterlitz-Thouless Transition in a Two-dimensional Dipolar Bose Gas. 2:1–14, mar 2024. (cited on page 61).

[256] P. W. Anderson. More Is Different. *Science*, 177(4047):393–396, 1972. (cited on page 62).

[257] Eugene P. Gross. Classical theory of boson wave fields. *Annals of Physics*, 4(1):57–74, may 1958. (cited on pages 62, 113).

[258] Bertram M. Schwarzschild. The original evidence of supersolidity in helium-4 is explained away. *Physics Today*, 65:19–21, 12 2012. (cited on page 62).

[259] Matthew A Norcia, Elena Poli, Claudia Politi, Lauritz Klaus, Thomas Bland, Manfred J Mark, Luis Santos, Russell N Bisset, and Francesca Ferlaino. Can angular oscillations probe superfluidity in dipolar supersolids? *arXiv:2111.07768*, 2021. (cited on page 62).

[260] Eva Casotti, Elena Poli, Lauritz Klaus, Andrea Litvinov, Clemens Ulm, Claudia Politi, Manfred J. Mark, Thomas Bland, and Francesca Ferlaino. Observation of vortices in a dipolar supersolid. *Nature*, 635:327–331, 11 2024. (cited on page 62).

[261] Matthew A. Norcia, Claudia Politi, Lauritz Klaus, Elena Poli, Maximilian Sohmen, Manfred J. Mark, Russell N. Bisset, Luis Santos, and Francesca Ferlaino. Two-dimensional supersolidity in a dipolar quantum gas. *Nature*, 596(7872):357–361, Aug 2021. (cited on page 62).

[262] G. Birkl, S. Kassner, and H. Walther. Multiple-shell structures of laser-cooled 24Mg+ ions in a quadrupole storage ring. *Nature*, 357:310–313, 5 1992. (cited on page 64).

[263] M. G. Raizen, J. M. Gilligan, J. C. Bergquist, W. M. Itano, and D. J. Wineland. Ionic crystals in a linear Paul trap. *Physical Review A*, 45:6493–6501, 5 1992. (cited on page 64).

[264] Shmuel Fishman, Gabriele De Chiara, Tommaso Calarco, and Giovanna Morigi. Structural phase transitions in low-dimensional ion crystals. *Phys. Rev. B*, 77:064111, Feb 2008. (cited on page 64).

[265] Efrat Shimshoni, Giovanna Morigi, and Shmuel Fishman. Quantum Zigzag Transition in Ion Chains. *Phys. Rev. Lett.*, 106:010401, Jan 2011. (cited on page 64).

[266] E. Poli, T. Bland, C. Politi, L. Klaus, M. A. Norcia, F. Ferlaino, R. N. Bisset, and L. Santos. Maintaining supersolidity in one and two dimensions. *Phys. Rev. A*, 104:063307, Dec 2021. (cited on page 64, 64).

[267] T. Bland, E. Poli, L. A. Peña Ardila, L. Santos, F. Ferlaino, and R. N. Bisset. Alternating-domain supersolids in binary dipolar condensates. *Phys. Rev. A*, 106:053322, Nov 2022. (cited on pages 64, 127).

[268] J-N Schmidt, Jens Hertkorn, Mingyang Guo, Fabian Böttcher, Matthias Schmidt, Kevin SH Ng, Sean D Graham, Tim Langen, Martin Zwierlein, and Tilman Pfau. Roton Excitations in an Oblate Dipolar Quantum Gas. *Physical Review Letters*, 126(19):193002, May 2021. (cited on page 64).

[269] T. Bland, E. Poli, C. Politi, L. Klaus, M. A. Norcia, F. Ferlaino, L. Santos, and R. N. Bisset. Two-Dimensional Supersolid Formation in Dipolar Condensates. *Phys. Rev. Lett.*, 128:195302, May 2022. (cited on pages 64, 64, 65).

[270] PB Blakie, D Baillie, L Chomaz, and F Ferlaino. Supersolidity in an elongated dipolar condensate. *Physical Review Research*, 2(4):043318, Dec 2020. (cited on page 64).

[271] Giulio Biagioni, Nicolò Antolini, Aitor Alaña, Michele Modugno, Andrea Fioretti, Carlo Gabbanini, Luca Tanzi, and Giovanni Modugno. Dimensional Crossover in the Superfluid-Supersolid Quantum Phase Transition. *Physical Review X*, 12:021019, 4 2022. (cited on page 64).

[272] Alexander D. Cronin, Jörg Schmiedmayer, and David E. Pritchard. Optics and interferometry with atoms and molecules. *Reviews of Modern Physics*, 81:1051–1129, 7 2009. (cited on page 65).

[273] A.J Leggett. On the Superfluid Fraction of an Arbitrary Many-Body System at T=0. *J. Stat. Phys.*, 93:927, 1998. (cited on page 76).

[274] S. M. Roccuzzo, A. Recati, and S. Stringari. Moment of inertia and dynamical rotational response of a supersolid dipolar gas. *Physical Review A*, 105:023316, 2 2022. (cited on pages 76, 76, 81, 126).

[275] SM Roccuzzo, A Gallemí, A Recati, and S Stringari. Rotating a supersolid dipolar gas. *Physical review letters*, 124(4):045702, Jan 2020. (cited on pages 77, 77, 78, 95).

[276] D. Guéry-Odelin and S. Stringari. Scissors Mode and Superfluidity of a Trapped Bose-Einstein Condensed Gas. *Phys. Rev. Lett.*, 83:4452–4455, 1999. (cited on page 78).

[277] P. B. Wigley, P. J. Everitt, K. S. Hardman, M. R. Hush, C. H. Wei, M. A. Sooriyabandara, P. Manju, J. D. Close, N. P. Robins, and C. C. N. Kuhn. Non-destructive shadowgraph imaging of ultra-cold atoms. *Optics Letters*, 41(20):4795, oct 2016. (cited on pages 81, 114).

[278] Graham D Bruce, James Mayoh, Giuseppe Smirne, Lara Torralbo-Campo, and Donatella Cassettari. A smooth, holographically generated ring trap for the investigation of superfluidity in ultracold atoms. *Physica Scripta*, T143:014008, 2 2011. (cited on page 81).

[279] V. Boyer, R. M. Godun, G. Smirne, D. Cassettari, C. M. Chandrashekar, A. B. Deb, Z. J. Laczik, and C. J. Foot. Dynamic manipulation of Bose-Einstein condensates with a spatial light modulator. *Physical Review A*, 73:031402, 3 2006. (cited on page 81).

[280] Marija Šindik, Tomasz Zawiślak, Alessio Recati, and Sandro Stringari. Sound, Superfluidity, and Layer Compressibility in a Ring Dipolar Supersolid. *Physical Review Letters*, 132:146001, 4 2024. (cited on page 81).

[281] Francesco Ancilotto, Manuel Barranco, Martí Pi, and Luciano Reatto. Vortex properties in the extended supersolid phase of dipolar Bose-Einstein condensates. *Physical Review A*, 103(3):033314, Mar 2021. (cited on pages 94, 94, 95).

[282] Shigeyuki Ishida, Akira Iyo, Hiraku Ogino, Hiroshi Eisaki, Nao Takeshita, Kenji Kawashima, Keiichi Yanagisawa, Yuuga Kobayashi, Koji Kimoto, Hideki Abe, Motoharu Imai, Jun ichi Shimoyama, and

Michael Eisterer. Unique defect structure and advantageous vortex pinning properties in superconducting $CaKFe_4As_4$. *npj Quantum Materials*, 4:27, 6 2019. (cited on page 94).

[283] Elena Poli, Thomas Bland, Samuel J. M. White, Manfred J. Mark, Francesca Ferlaino, Silvia Trabucco, and Massimo Mannarelli. Glitches in Rotating Supersolids. *Physical Review Letters*, 131:223401, 11 2023. (cited on pages 94, 114).

[284] Marija Šindik, Alessio Recati, Santo Maria Roccuzzo, Luis Santos, and Sandro Stringari. Creation and robustness of quantized vortices in a dipolar supersolid when crossing the superfluid-to-supersolid transition. *Physical Review A*, 106:L061303, 12 2022. (cited on page 96, 96).

[285] A Gallemí, SM Roccuzzo, S Stringari, and A Recati. Quantized vortices in dipolar supersolid Bose-Einstein-condensed gases. *Physical Review A*, 102(2):023322, Aug 2020. (cited on page 96).

[286] T. Macrì, F. Maucher, F. Cinti, and T. Pohl. Elementary excitations of ultracold soft-core bosons across the superfluid-supersolid phase transition. *Phys. Rev. A*, 87:061602(R), Jun 2013. (cited on page 96).

[287] F. Wächtler and L. Santos. Ground-state properties and elementary excitations of quantum droplets in dipolar Bose-Einstein condensates. *Phys. Rev. A*, 94(4):043618, Oct 2016. (cited on page 113).

[288] Teruo Matsushita. *Flux Pinning in Superconductors*, volume 198. Springer International Publishing, 3 edition, 2022. (cited on page 113).

[289] D. Dew-Hughes. Flux pinning mechanisms in type II superconductors. *The Philosophical Magazine: A Journal of Theoretical Experimental and Applied Physics*, 30(2):293–305, 1974. (cited on page 113).

[290] Leticia Tarruell and Laurent Sanchez-Palencia. Quantum simulation of the Hubbard model with ultracold fermions in optical lattices. *Comptes Rendus. Physique*, 19:365–393, 9 2018. (cited on page 113).

[291] Julian Léonard, Sooshin Kim, Joyce Kwan, Perrin Segura, Fabian Grusdt, Cécile Repellin, Nathan Goldman, and Markus Greiner. Realization of a fractional quantum Hall state with ultracold atoms. *Nature*, 619:495–499, 7 2023. (cited on page 113).

[292] J. M. Lattimer and M. Prakash. The Physics of Neutron Stars. *Science*, 304:536–542, 4 2004. (cited on page 113).

[293] J. M. Lattimer and M. Prakash. Neutron Star Structure and the Equation of State. *The Astrophysical Journal*, 550:426–442, 3 2001. (cited on page 113).

[294] Malvin Ruderman, Tianhua Zhu, and Kaiyou Chen. Neutron Star Magnetic Field Evolution, Crust Movement, and Glitches. *The Astrophysical Journal*, 492:267–280, 1 1998. (cited on page 113).

[295] J. R. Fuentes, C. M. Espinoza, A. Reisenegger, B. Shaw, B. W. Stappers, and A. G. Lyne. The glitch activity of neutron stars. *Astronomy & Astrophysics*, 608:A131, 12 2017. (cited on pages 113, 126).

[296] Rainer Blatt and Christian F Roos. Quantum simulations with trapped ions. *Nature Physics*, 8(4):27, 2012. (cited on page 115).

[297] I. Pogorelov, T. Feldker, Ch. D. Marciniak, L. Postler, G. Jacob, O. Krieglsteiner, V. Podlesnic, M. Meth, V. Negnevitsky, M. Stadler, B. Höfer, C. Wächter, K. Lakhmanskiy, R. Blatt, P. Schindler, and T. Monz. Compact Ion-Trap Quantum Computing Demonstrator. *PRX Quantum*, 2:020343, 6 2021. (cited on page 115).

[298] Jwo-Sy Chen, Erik Nielsen, Matthew Ebert, Volkan Inlek, Kenneth Wright, Vandiver Chaplin, Andrii Maksymov, Eduardo Páez, Amrit Poudel, Peter Maunz, and John Gamble. Benchmarking a trapped-ion quantum computer with 30 qubits. *Quantum*, 8:1516, 11 2024. (cited on page 115).

[299] H.C. Nägerl, Ch. Roos, H. Rohde, D. Leibfried, J. Eschner, F. Schmidt-Kaler, and R. Blatt. Addressing and Cooling of Single Ions in Paul Traps. *Fortschritte der Physik*, 48:623–636, 5 2000. (cited on page 115).

[300] N. M. Linke, D. T. C. Allcock, D. J. Szwer, C. J. Ballance, T. P. Harty, H. A. Janacek, D. N. Stacey, A. M. Steane, and D. M. Lucas. Background-free detection of trapped ions. *Applied Physics B*, 107:1175–1180, 6 2012. (cited on page 115).

[301] Christian Gross and Waseem S. Bakr. Quantum gas microscopy for single atom and spin detection. *Nature Physics*, 17:1316–1323, 12 2021. (cited on pages 115, 127).

[302] Richard P. Feynman. Quantum mechanical computers. *Foundations of Physics*, 16:507–531, 6 1986. (cited on page 115).

[303] W. S. Bakr, A. Peng, M. E. Tai, R. Ma, J. Simon, J. I. Gillen, S. Folling, L. Pollet, and M. Greiner. Probing the Superfluid-to-Mott Insulator Transition at the Single-Atom Level. *Science*, 329(5991):547–550, 2010. (cited on page 116).

[304] J. F. Sherson, C. Weitenberg, M. Endres, M. Cheneau, I. Bloch, and Kuhr S. Single-atom-resolved fluorescence imaging of an atomic Mott insulator. *Nature*, 467:68, 2010. (cited on page 116).

[305] Philipp M. Preiss, Ruichao Ma, M. Eric Tai, Alexander Lukin, Matthew Rispoli, Philip Zupancic, Yoav Lahini, Rajibul Islam, and Markus Greiner. Strongly correlated quantum walks in optical lattices. *Science*, 347:1229–1233, 3 2015. (cited on page 116).

[306] Rajibul Islam, Ruichao Ma, Philipp M. Preiss, M. Eric Tai, Alexander Lukin, Matthew Rispoli, and Markus Greiner. Measuring entanglement entropy in a quantum many-body system. *Nature*, 528:77–83, 12 2015. (cited on page 116).

[307] Adam M. Kaufman, M. Eric Tai, Alexander Lukin, Matthew Rispoli, Robert Schittko, Philipp M. Preiss, and Markus Greiner. Quantum thermalization through entanglement in an isolated many-body system. *Science*, 353(6301):794–800, 2016. (cited on page 116).

[308] Alexander Lukin, Matthew Rispoli, Robert Schittko, M. Eric Tai, Adam M. Kaufman, Soonwon Choi, Vedika Khemani, Julian Léonard, and Markus Greiner. Probing entanglement in a many-body–localized system. *Science*, 364:256–260, 4 2019. (cited on page 116).

[309] Matthew Rispoli, Alexander Lukin, Robert Schittko, Sooshin Kim, M. Eric Tai, Julian Léonard, and Markus Greiner. Quantum critical behaviour at the many-body localization transition. *Nature*, 573:385–389, 9 2019. (cited on page 116).

[310] Julian F. Wienand, Simon Karch, Alexander Impertro, Christian Schweizer, Ewan McCulloch, Romain Vasseur, Sarang Gopalakrishnan, Monika Aidelsburger, and Immanuel Bloch. Emergence of fluctuating hydrodynamics in chaotic quantum systems. *Nature Physics*, 20:1732–1737, 11 2024. (cited on page 116).

[311] Takeshi Fukuhara, Adrian Kantian, Manuel Endres, Marc Cheneau, Peter Schauß, Sebastian Hild, David Bellem, Ulrich Schollwöck, Thierry Giamarchi, Christian Gross, Immanuel Bloch, and Stefan Kuhr. Quantum dynamics of a mobile spin impurity. *Nature Physics*, 9:235–241, 4 2013. (cited on page 116).

[312] An Luo, Yong-Guang Zheng, Wei-Yong Zhang, Ming-Gen He, Ying-Chao Shen, Zi-Hang Zhu, Zhen-Sheng Yuan, and Jian-Wei Pan. Microscopic Study on Superexchange Dynamics of Composite Spin-1 Bosons. *Physical Review Letters*, 133:043401, 7 2024. (cited on page 116).

[313] Daniel Greif, Maxwell F. Parsons, Anton Mazurenko, Christie S. Chiu, Sebastian Blatt, Florian Huber, Geoffrey Ji, and Markus Greiner. Site-resolved imaging of a fermionic Mott insulator. *Science*, 351:953–957, 2 2016. (cited on page 116).

[314] Lawrence W. Cheuk, Matthew A. Nichols, Katherine R. Lawrence, Melih Okan, Hao Zhang, and Martin W. Zwierlein. Observation of 2D Fermionic Mott Insulators of K40 with Single-Site Resolution. *Physical Review Letters*, 116:235301, 6 2016. (cited on page 116).

[315] Takeshi Fukuhara, Peter Schauß, Manuel Endres, Sebastian Hild, Marc Cheneau, Immanuel Bloch, and Christian Gross. Microscopic observation of magnon bound states and their dynamics. *Nature*, 502(7469):7, 2013. (cited on page 116).

[316] Joannis Koepsell, Jayadev Vijayan, Pimonpan Sompet, Fabian Grusdt, Timon A. Hilker, Eugene Demler, Guillaume Salomon, Immanuel Bloch, and Christian Gross. Imaging magnetic polarons in the doped Fermi–Hubbard model. *Nature*, 572:358–362, 8 2019. (cited on page 116).

[317] Lawrence W. Cheuk, Matthew A. Nichols, Katherine R. Lawrence, Melih Okan, Hao Zhang, Ehsan Khatami, Nandini Trivedi, Thereza Paiva, Marcos Rigol, and Martin W. Zwierlein. Observation of spatial charge and spin correlations in the 2D Fermi-Hubbard model. *Science*, 353(6305):1260–1264, 2016. (cited on page 116).

[318] Maxwell F. Parsons, Anton Mazurenko, Christie S. Chiu, Geoffrey Ji, Daniel Greif, and Markus Greiner. Site-resolved measurement of the spin-correlation function in the Fermi-Hubbard model. *Science*, 353(6305):1253–1256, 2016. (cited on page 116).

[319] Martin Boll, Timon A. Hilker, Guillaume Salomon, Ahmed Omran, Jacopo Nespolo, Lode Pollet, Immanuel Bloch, and Christian Gross. Spin- and density-resolved microscopy of antiferromagnetic correlations in Fermi-Hubbard chains. *Science*, 353(6305):1257–1260, 2016. (cited on page 116).

[320] Peter T. Brown, Debayan Mitra, Elmer Guardado-Sanchez, Peter Schauß, Stanimir S. Kondov, Ehsan Khatami, Thereza Paiva, Nandini Trivedi, David A. Huse, and Waseem S. Bakr. Spin-imbalance in a 2D Fermi-Hubbard system. *Science*, 357:1385–1388, 9 2017. (cited on page 116).

[321] C Trefzger, C Menotti, B Capogrosso-Sansone, and M Lewenstein. Ultracold dipolar gases in optical lattices. *Journal of Physics B: Atomic, Molecular and Optical Physics*, 44(19):193001, 2011. (cited on pages 116, 127).

[322] Jason S. Rosenberg, Lysander Christakis, Elmer Guardado-Sanchez, Zoe Z. Yan, and Waseem S. Bakr. Observation of the Hanbury Brown–Twiss effect with ultracold molecules. *Nature Physics*, 18:1062–1066, 9 2022. (cited on pages 116, 116, 117).

[323] Lysander Christakis, Jason S. Rosenberg, Ravin Raj, Sungjae Chi, Alan Morningstar, David A. Huse, Zoe Z. Yan, and Waseem S. Bakr. Probing site-resolved correlations in a spin system of ultracold molecules. *Nature*, 614:64–69, 2 2023. (cited on page 116).

[324] Lin Su, Alexander Douglas, Michal Szurek, Robin Groth, S. Furkan Ozturk, Aaron Krahn, Anne H. Hébert, Gregory A. Phelps, Sepehr Ebadi, Susannah Dickerson, Francesca Ferlaino, Ognjen Marković, and Markus Greiner. Dipolar quantum solids emerging in a Hubbard quantum simulator. *Nature*, 622:724–729, 10 2023. (cited on pages 116, 117, 127).

[325] J. G. Danzl, M. J. Mark, E. Haller, M. Gustavsson, R. Hart, J. Aldegunde, J. M. Hutson, and H.-C. Nägerl. An ultracold high-density sample of rovibronic ground-state molecules in an optical lattice. *Nat. Phys.*, 6:26, 2010. (cited on page 116).

[326] M. A. Baranov, M. Dalmonte, G. Pupillo, and P. Zoller. Condensed Matter Theory of Dipolar Quantum Gases. *Chemical Reviews*, 112(9):5012–5061, Sep 2012. PMID: 22877362. (cited on page 117).

[327] Omjyoti Dutta, Mariusz Gajda, Philipp Hauke, Maciej Lewenstein, Dirk-Sören Lühmann, Boris A Malomed, Tomasz Sowiński, and Jakub Zakrzewski. Non-standard Hubbard models in optical lattices: a review. *Reports on Progress in Physics*, 78(6):066001, 2015. (cited on page 117).

[328] B. Capogrosso-Sansone, C. Trefzger, M. Lewenstein, P. Zoller, and G. Pupillo. Quantum phases of cold polar molecules in 2D optical lattices. *Phys. Rev. Lett.*, 104(12):125301, Mar 2010. (cited on page 117).

[329] G. G. Batrouni, R. T. Scalettar, V. G. Rousseau, and B. Grémaud. Competing Supersolid and Haldane Insulator Phases in the Extended One-Dimensional Bosonic Hubbard Model. *Physical Review Letters*, 110:265303, 6 2013. (cited on page 117).

[330] Luca Barbiero, Arianna Montorsi, and Marco Roncaglia. How hidden orders generate gaps in one-dimensional fermionic systems. *Physical Review B*, 88:035109, 7 2013. (cited on page 117).

[331] Bo Yan, Steven A. Moses, Bryce Gadway, Jacob P. Covey, Kaden R. A. Hazzard, Ana Maria Rey, Deborah S. Jin, and Jun Ye. Observation of dipolar spin-exchange interactions with lattice-confined polar molecules. *Nature*, 501:521–525, 2013. (cited on page 117).

[332] Chen Cheng, Bin-Bin Mao, Fu-Zhou Chen, and Hong-Gang Luo. Phase diagram of the one-dimensional t-J model with long-range dipolar interactions. *EPL (Europhysics Letters)*, 110:37002, 5 2015. (cited on page 117).

[333] Masao Ogata and Hidetoshi Fukuyama. The t–J model for the oxide high-Tc superconductors. *Reports on Progress in Physics*, 71:036501, 3 2008. (cited on page 117).

[334] Sarang Gopalakrishnan, Benjamin L. Lev, and Paul M. Goldbart. Frustration and Glassiness in Spin Models with Cavity-Mediated Interactions. *Physical Review Letters*, 107:277201, 12 2011. (cited on page 117).

[335] Alexey V. Gorshkov, Salvatore R. Manmana, Gang Chen, Eugene Demler, Mikhail D. Lukin, and Ana Maria Rey. Quantum magnetism with polar alkali-metal dimers. *Phys. Rev. A*, 84:033619, Sep 2011. (cited on page 117).

[336] Jonathan Simon, Waseem S. Bakr, Ruichao Ma, M. Eric Tai, Philipp M. Preiss, and Markus Greiner. Quantum simulation of antiferromagnetic spin chains in an optical lattice. *Nature*, 472:307–312, 4 2011. (cited on page 117).

[337] R. Islam, C. Senko, W. C. Campbell, S. Korenblit, J. Smith, A. Lee, E. E. Edwards, C.-C. J. Wang, J. K. Freericks, and C. Monroe. Emergence and Frustration of Magnetism with Variable-Range Interactions in a Quantum Simulator. *Science*, 340:583–587, 5 2013. (cited on page 117).

[338] N. Y. Yao, M. P. Zaletel, D. M. Stamper-Kurn, and A. Vishwanath. A quantum dipolar spin liquid. *Nature Physics*, 14:405–410, 4 2018. (cited on page 117).

[339] Ahmet Keleş, Erhai Zhao, and W. Vincent Liu. Scrambling dynamics and many-body chaos in a random dipolar spin model. *Physical Review A*, 99:053620, 5 2019. (cited on page 117).

[340] Steven A Moses, Jacob P Covey, Matthew T Miecnikowski, Bo Yan, Bryce Gadway, Jun Ye, and Deborah S Jin. Creation of a low-entropy quantum gas of polar molecules in an optical lattice. *Science*, 350(6261):659–662, nov 2015. (cited on page 117).

[341] Andrzej Syrwid, Emil Blomquist, and Egor Babaev. Dissipationless Vector Drag—Superfluid Spin Hall Effect. *Physical Review Letters*, 127:100403, 8 2021. (cited on page 117).

[342] Pochung Chen and Min-Fong Yang. Quantum phase transitions in a two-species hard-core boson Hubbard model in two dimensions. *Physical Review B*, 82:180510, 11 2010. (cited on page 117).

[343] Yongqiang Li, Liang He, and Walter Hofstetter. Anisotropic pair superfluidity of trapped two-component Bose gases in an optical lattice. *New Journal of Physics*, 15:093028, 9 2013. (cited on page 117).

[344] Rukmani Bai, Deepak Gaur, Hrushikesh Sable, Soumik Bandyopadhyay, K. Suthar, and D. Angom. Segregated quantum phases of dipolar bosonic mixtures in two-dimensional optical lattices. *Physical Review A*, 102:043309, 10 2020. (cited on page 117).

[345] Thomas Bilitewski, G. A. Domínguez-Castro, David Wellnitz, Ana Maria Rey, and Luis Santos. Tunable momentum pair creation of spin excitations in dipolar bilayers. *Physical Review A*, 108:013313, 7 2023. (cited on page 117).

[346] Shraddha Anand, Conor E. Bradley, Ryan White, Vikram Ramesh, Kevin Singh, and Hannes Bernien. A dual-species Rydberg array. *Nature Physics*, 20:1744–1750, 11 2024. (cited on page 117).

[347] Maximilian Sohmen, Manfred J. Mark, Markus Greiner, and Francesca Ferlaino. A ship-in-a-bottle quantum gas microscope setup for magnetic mixtures. *SciPost Physics*, 15:182, 11 2023. (cited on page 117).

[348] W. Hänsel, P. Hommelhoff, T. W. Hänsch, and J. Reichel. Bose–Einstein condensation on a microelectronic chip. *Nature*, 413:498–501, 10 2001. (cited on page 118).

[349] W. Hänsel, J. Reichel, P. Hommelhoff, and T. W. Hänsch. Magnetic Conveyor Belt for Transporting and Merging Trapped Atom Clouds. *Physical Review Letters*, 86:608–611, 1 2001. (cited on page 118).

[350] Markus Greiner, Immanuel Bloch, Theodor W. Hänsch, and Tilman Esslinger. Magnetic transport of trapped cold atoms over a large distance. *Physical Review A*, 63:031401, 2 2001. (cited on page 118).

[351] Stefan Minniberger, Fritz Diorico, Stefan Haslinger, Christoph Hufnagel, Christian Novotny, Nils Lippok, Johannes Majer, Christian Koller, Stephan Schneider, and Jörg Schmiedmayer. Magnetic conveyor belt transport of ultracold atoms to a superconducting atomchip. *Applied Physics B*, 116:1017–1021, 9 2014. (cited on page 118).

[352] H J Lewandowski, D M Harber, D L Whitaker, and E A Cornell. Simplified System for Creating a Bose-Einstein Condensate. *Journal of Low Temperature Physics*, 132, 2003. (cited on page 118).

[353] S. Händel, A. L. Marchant, T. P. Wiles, S. A. Hopkins, and S. L. Cornish. Magnetic transport apparatus for the production of ultracold atomic gases in the vicinity of a dielectric surface. *Review of Scientific Instruments*, 83, 1 2012. (cited on page 118).

[354] M. Miranda, A. Nakamoto, Y. Okuyama, A. Noguchi, M. Ueda, and M. Kozuma. All-optical transport and compression of ytterbium atoms into the surface of a solid immersion lens. *Physical Review A*, 86:063615, 12 2012. (cited on pages 118, 118, 123).

[355] Matthias Wenzel. *A dysprosium quantum gas in highly controllable optical traps*. PhD thesis, 3 2015. (cited on pages 118, 118, 123).

[356] Till Klostermann, Cesar R. Cabrera, Hendrik von Raven, Julian F. Wienand, Christian Schweizer, Immanuel Bloch, and Monika Aidelsburger. Fast long-distance transport of cold cesium atoms. *Physical Review A*, 105:043319, 4 2022. (cited on page 118).

[357] Alex J. Matthies, Jonathan M. Mortlock, Lewis A. McArd, Adarsh P. Raghuram, Andrew D. Innes, Philip D. Gregory, Sarah L. Bromley, and Simon L. Cornish. Long-distance optical-conveyor-belt transport of ultracold Cs133 and Rb87 atoms. *Physical Review A*, 109:023321, 2 2024. (cited on page 118).

[358] Julian Léonard, Moonjoo Lee, Andrea Morales, Thomas M Karg, Tilman Esslinger, and Tobias Donner. Optical transport and manipulation of an ultracold atomic cloud using focus-tunable lenses. *New Journal of Physics*, 16:093028, 9 2014. (cited on page 118).

[359] G. Unnikrishnan, C. Beulenkamp, D. Zhang, K. P. Zamarski, M. Landini, and H.-C. Nägerl. Long distance optical transport of ultracold atoms: A compact setup using a Moiré lens. *Review of Scientific Instruments*, 92, 6 2021. (cited on page 118).

[360] Yicheng Bao, Scarlett S Yu, Loïc Anderegg, Sean Burchesky, Derick Gonzalez-Acevedo, Eunmi Chae, Wolfgang Ketterle, Kang-Kuen Ni, and John M Doyle. Fast optical transport of ultracold molecules over long distances. *New Journal of Physics*, 24:093028, 9 2022. (cited on page 118).

[361] Damien Bloch, Britton Hofer, Sam R. Cohen, Maxence Lepers, Antoine Browaeys, and Igor Ferrier-Barbut. Anisotropic polarizability of Dy at 532 nm on the intercombination transition. *Physical Review A*, 110:033103, 9 2024. (cited on pages 119, 121).

[362] Claudia Politi. Optical dipole trap for an erbium and dysprosium mixture. Master's thesis, 2017. (cited on page 119).

[363] M. Abad, M. Guilleumas, R. Mayol, M. Pi, and D. M. Jezek. Vortices in Bose-Einstein condensates with dominant dipolar interactions. *Physical Review A - Atomic, Molecular, and Optical Physics*, 79, 6 2009. (cited on page 125).

[364] Alessio Recati and Sandro Stringari. Supersolidity in ultracold dipolar gases. *Nature Reviews Physics*, 5:735–743, 10 2023. (cited on page 126).

[365] Thomas Bland, Francesca Ferlaino, Massimo Mannarelli, Elena Poli, and Silvia Trabucco. Exploring Pulsar Glitches with Dipolar Supersolids. *Few-Body Systems*, 65:81, 8 2024. (cited on page 126).

[366] Annette N. Carroll, Henrik Hirzler, Calder Miller, David Wellnitz, Sean R. Muleady, Junyu Lin, Krzysztof P. Zamarski, Reuben R. W. Wang, John L. Bohn, Ana Maria Rey, and Jun Ye. Observation of Generalized t-J Spin Dynamics with Tunable Dipolar Interactions. 4 2024. (cited on page 127).

[367] Ben Kain and Hong Y. Ling. Polarons in a dipolar condensate. *Phys. Rev. A*, 89:023612, Feb 2014. (cited on page 127).

[368] P. O. Fedichev, M. W. Reynolds, and G. V. Shlyapnikov. Three-Body recombination of ultracold atoms to a weakly bound s level. *Phys. Rev. Lett.*, 77:2921–2924, 1996. (cited on page 158).

[369] Tino Weber, Jens Herbig, Michael Mark, Hanns-Christoph Nägerl, and Rudolf Grimm. Three-body recombination at large scattering lengths in an ultracold atomic gas. *Phys. Rev. Lett.*, 91, 2003. (cited on page 158).

[370] E. Braaten and H.-W. Hammer. Universality in few-body systems with large scattering length. *Phys. Rep.*, 428:259–390, 2006. (cited on page 158).

[371] Milan Krstajić, Péter Juhász, Jiří Kučera, Lucas R. Hofer, Gavin Lamb, Anna L. Marchant, and Robert P. Smith. Characterization of three-body loss in $^{\{}166\}Er$ and optimized production of large Bose-Einstein condensates. *Physical Review A*, 108:063301, 12 2023. (cited on page 158).

[372] T. Maier, H. Kadau, M. Schmitt, M. Wenzel, I. Ferrier-Barbut, T. Pfau, A. Frisch, S. Baier, K. Aikawa, L. Chomaz, M. J. Mark, F. Ferlaino, C. Makrides, E. Tiesinga, A. Petrov, and S. Kotochigova. Emergence of Chaotic Scattering in Ultracold Er and Dy. *Phys. Rev. X*, 5:041029, Nov 2015. (cited on page 158).

[373] Y. Tang, A. G. Sykes, N. Q. Burdick, J. M. DiSciacca, D. S. Petrov, and B. L. Lev. Anisotropic Expansion of a Thermal Dipolar Bose Gas. *Phys. Rev. Lett.*, 117:155301, Oct 2016. (cited on page 158).

[374] E. Lucioni, L. Tanzi, A. Fregosi, J. Catani, S. Gozzini, M. Inguscio, A. Fioretti, C. Gabbanini, and G. Modugno. Dysprosium dipolar Bose-Einstein condensate with broad Feshbach resonances. *Phys. Rev. A*, 97:060701, Jun 2018. (cited on page 158).

[375] Fabian Böttcher, Matthias Wenzel, Jan-Niklas Schmidt, Mingyang Guo, Tim Langen, Igor Ferrier-Barbut, Tilman Pfau, Raúl Bombín, Joan Sánchez-Baena, Jordi Boronat, and Ferran Mazzanti. Dilute dipolar quantum droplets beyond the extended Gross-Pitaevskii equation. *Phys. Rev. Research*, 1:033088, Nov 2019. (cited on page 158).

[376] S. Baier, D. Petter, J. H. Becher, A. Patscheider, G. Natale, L. Chomaz, M. J. Mark, and F. Ferlaino. Realization of a Strongly Interacting Fermi Gas of Dipolar Atoms. *Phys. Rev. Lett.*, 121:093602, Aug 2018. (cited on page 158).

[377] C. Politi, A. Trautmann, P. Ilzhöfer, G. Durastante, M. J. Mark, M. Modugno, and F. Ferlaino. Interspecies interactions in an ultracold dipolar mixture. *Phys. Rev. A*, 105:023304, Feb 2022. (cited on page 158).

Appendix

A

Feshbach resonances for ^{164}Dy and ^{162}Dy

As discussed in Sec. 2.2.5 the exact value of the magnetic field is important to know the interaction length between the atoms a_{s}. In addition to a constant background a_{bg}, a_{s} varies in the vicinity of Feshbach resonances (FBR)[88] where it actually goes through a pole. FBRs are typically detected as loss resonances in the atom number as three-body recombination scales with $\propto a_{\mathrm{s}}^4$ [368, 369, 370].
In this process, two atoms form a bound state and collide with a third particle, inducing a relaxation into a more deeply bound molecule. The binding energy gets released as kinetic energy large enough so that all three atoms are ejected from the trap. The corresponding loss rate can be written as [88]

$$\dot{N}_{3B}(t) = -\int_V L_3 n^3(\mathbf{r}, t) d^3 r \tag{A.1}$$

where L_3 is the three-body loss coefficient, which has to be measured and depends on the temperature of the sample [371] and on the few-body details of the collision [88]. This loss is seen in spectroscopy as shown in Fig. 2.9 and A.1-A.4. Here we evaporate the atoms to a temperature of T $\approx$ 400 nK (Fig. A.1-A.3) or T $\approx 2\mu$K (Fig. A.4) before ramping/quenching[1] the magnetic field to the final value B and holding the cloud at this field for $t_{\mathrm{hold}} = 300$ ms.
By fitting a Gaussian to the peaks, the central position and the width of the loss feature can be defined. Combining this data with coupled channel calculations, this can give a very accurate determination of the scattering length for a given magnetic field [88], but in our case, the complex scattering properties of lanthanides do not allow an accurate coupled-channel modelling to calculate a_{s} [134, 372, 173]. For example, the scattering length of dysprosium around 5 G has been experimentally studied by different groups with significant differences of $a_{\mathrm{s}}(B)$ [176, 373, 374, 375]. Other techniques to determine the scattering length are cross thermalisation measurements [161], lattice modulation spectroscopy [109, 376, 161] or the study of interactions between mixtures [377]. In the context of this thesis we approximate the scattering length at the magnetic fields used in the included papers by experimentally measuring the in-situ ground state of the degenerate gas and compare it to eGPE simulations with the same parameters as trap frequencies and atom number and the only free parameter being the scattering length, which allows precisions of $\Delta a_0 < \pm 2\, a_0$ since the supersolid phase is usually very narrow as can be seen, for example, in [122].

---

[1] The quenching time of the magnetic field is limited by the inductance of the coils and is on the order of $\approx 10\,\mu$s for the coils used in the experiment.

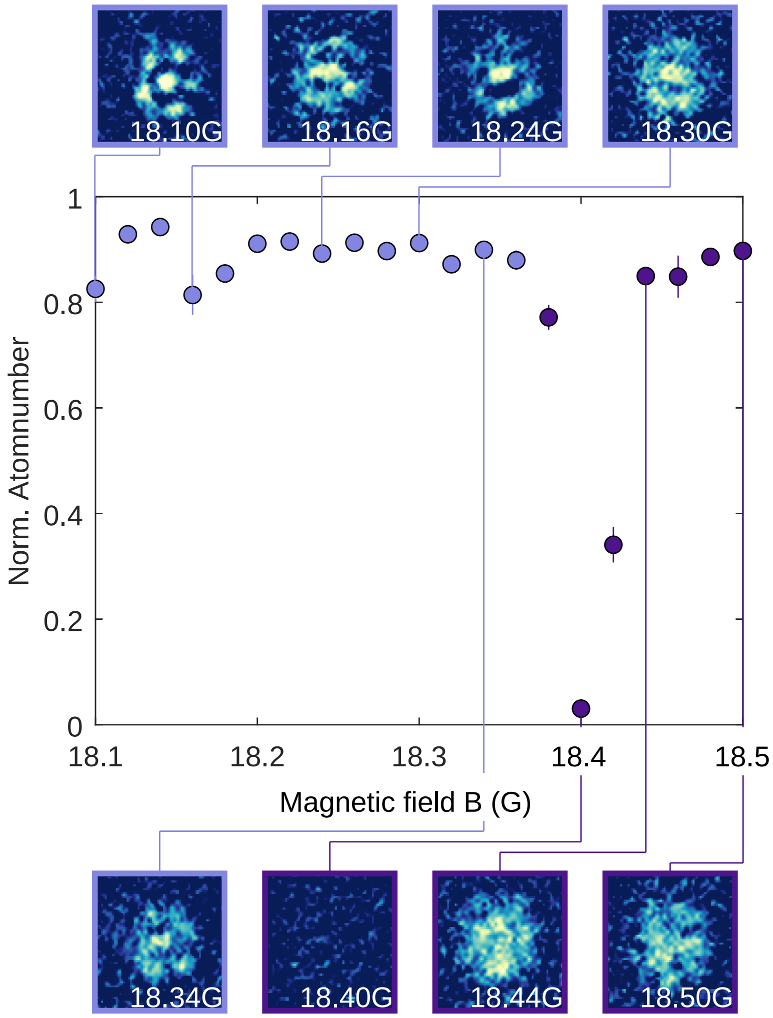

Figure A.1: Atom-loss spectroscopy of ^{164}Dy between $B = 18.1 - 18.5\,\mathrm{G}$. For the spectroscopy the atoms are evaporated at $B_{\mathrm{evap}} = 19.5\,\mathrm{G}$ down to $T \approx 400\,\mathrm{nK}$ before the magnetic field is quenched to the final value B and held for $t_{\mathrm{hold}} = 300\,\mathrm{ms}$. The different colours indicate if the corresponding ground state after condensation is modulated (●) or not condensed/assigned (●). The atom number is averaged over 3-4 repetitions and normalised to the maximum average atom number measured in the range $B = 16.5 - 23.5\,\mathrm{G}$. The error bars show the standard error. (Top/Bottom) Single shot images showing the corresponding ground state at this field. Here, the atoms are evaporated to condensation at the final magnetic field B and held for $t_{\mathrm{hold}} = 100\,\mathrm{ms}$ to ensure, that the quantum gas is in its ground state. Images are shown for $B = [18.10, 18.16, 18.24, 18.30, 18.34, 18.40, 18.44, 18.50]\,\mathrm{G}$.

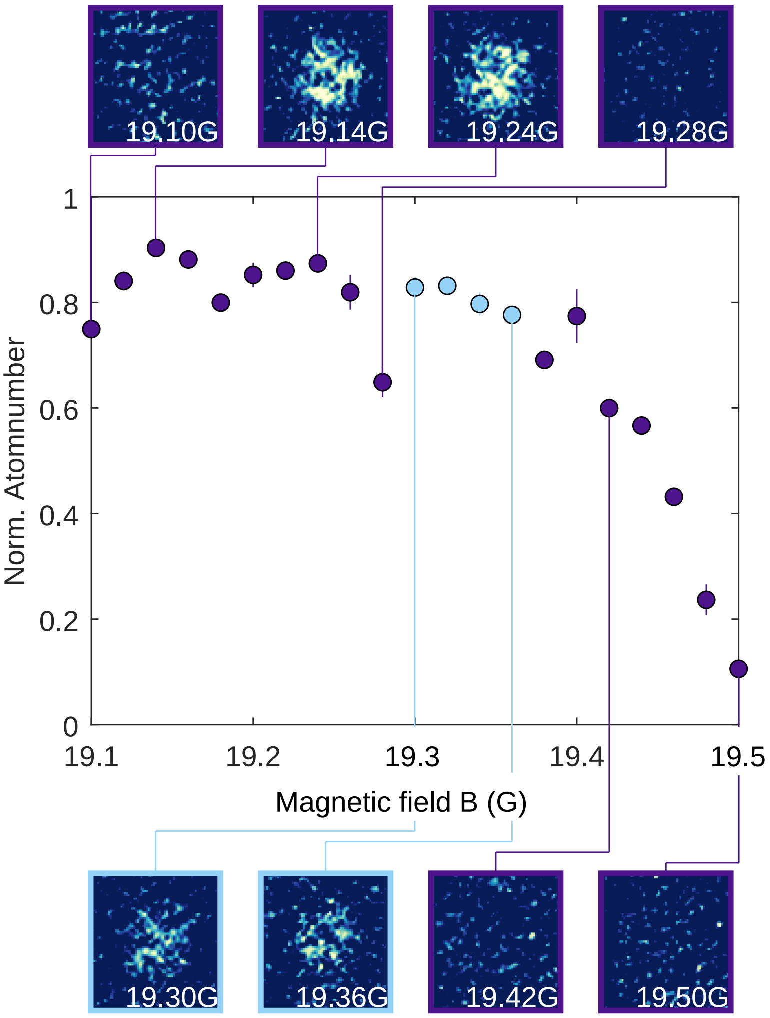

Figure A.2: Atom-loss spectroscopy of ^{164}Dy **between** $B = 19.1 - 19.5\,\mathrm{G}$**.** For the spectroscopy the atoms are evaporated at $B_{\mathrm{evap}} = 19.5\mathrm{G}$ down to $T \approx 400\,\mathrm{nK}$ before the magnetic field is quenched to the final value B and held for $t_{\mathrm{hold}} = 300\,\mathrm{ms}$. The different colours indicate if the corresponding ground state after condensation is modulated (○) or not condensed/assigned (●). The atom number is averaged over 3-4 repetitions and normalised to the maximum average atom number measured in the range $B = 16.5 - 23.5\,\mathrm{G}$. The error bars show the standard error. (Top/Bottom) Single shot images showing the corresponding ground state at this field. Here, the atoms are evaporated to condensation at the final magnetic field B and held for $t_{\mathrm{hold}} = 100\,\mathrm{ms}$ to ensure, that the quantum gas is in its ground state. Images are shown for $B = [19.10, 19.14, 19.24, 19.28, 19.30, 19.36, 19.42, 19.50]\,\mathrm{G}$.

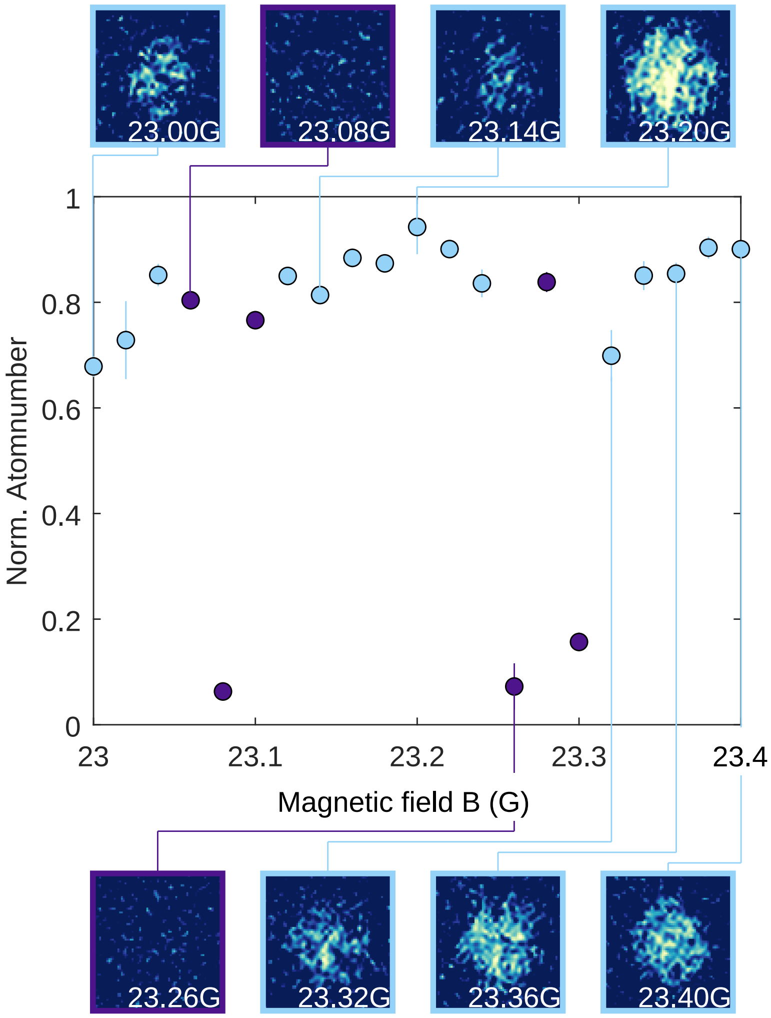

Figure A.3: Atom-loss spectroscopy of ^{164}Dy between $B = 23.0 - 23.4$ G. For the spectroscopy the atoms are evaporated at $B_{\text{evap}} = 19.5$ G down to $T \approx 400$ nK before the magnetic field is quenched to the final value B and held for $t_{\text{hold}} = 300$ ms. The different colours indicate if the corresponding ground state after condensation is modulated (○) or not condensed/assigned (●). The atom number is averaged over 3-4 repetitions and normalised to the maximum average atom number measured in the range $B = 16.5 - 23.5$ G. The error bars show the standard error. (Top/Bottom) Single shot images showing the corresponding ground state at this field. Here, the atoms are evaporated to condensation at the final magnetic field B and held for $t_{\text{hold}} = 100$ ms to ensure, that the quantum gas is in its ground state. Images are shown for $B = [23.00, 23.08, 23.14, 23.20, 23.26, 23.32, 23.36, 23.40]$ G.

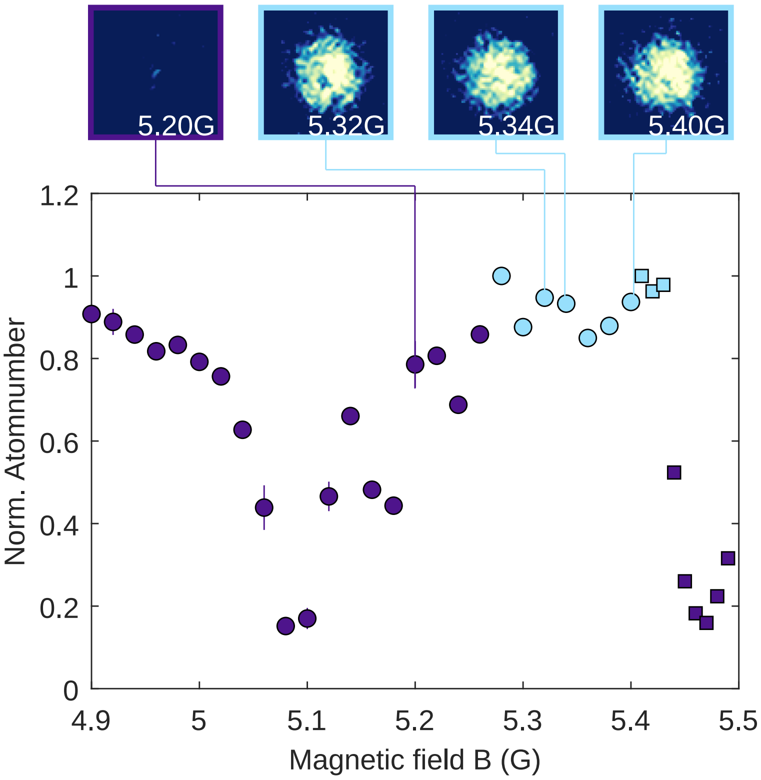

Figure A.4: Atom-loss spectroscopy of ^{162}Dy between $B = 4.9 - 5.5\,\mathrm{G}$**.** For the spectroscopy the atoms are evaporated at $B_{\mathrm{evap}} = 2.48\,\mathrm{G}$ down to $T \approx 2\,\mu\mathrm{K}$ before the magnetic field is ramped to the final value B over a ramptime $t_{\mathrm{ramp}} = 10\,\mathrm{ms}$ and held for $t_{\mathrm{hold}} = 300\,\mathrm{ms}$. The different colours indicate if the corresponding ground state after condensation is modulated (○) or not condensed/assigned (●). The atom number is averaged over 3-4 repetitions and normalised to the maximum average atom number. The error bars show the standard error. (Top) Single shot images showing the corresponding ground state at this field. Here, the atoms are evaporated to condensation at $B = 5\,\mathrm{G}$ and ramped to the final magnetic field B for $t_{\mathrm{ramp}} = 1\,\mathrm{ms}$ and held for $t_{\mathrm{hold}} = 100\,\mathrm{ms}$ to ensure, that the quantum gas is in its ground state. Images are shown for $B = [5.20, 5.32, 5.34, 5.40]\,\mathrm{G}$.

B

Magnetic Field calibration

As discussed in Sec. 2.2.5, our experiments depend heavily on accurate knowledge of our magnetic fields. The most precise probe we have for calibrating the magnetic field are our atoms. We use two different methods to calibrate the coils: Radio-frequency (RF) spectroscopy and Atom-loss spectroscopy around Feshbach resonances.

Atom-Loss spectroscopy has already been described in Sec. A. We can take advantage of the fact that we have a large spectrum of many very narrow resonances of $\Delta B < 100\,\mathrm{mG}$, and by knowing the exact positions of these Feshbach resonances we can calibrate our magnetic field coils.

The RF spectroscopy method does not require prior knowledge of the Feshbach resonance spectrum, but instead exploits the fact that due to the Zeeman effect an external magnetic field shifts the different spin states m_J of the atoms. The energy shift of the different states is linear for typical magnetic fields of the experiment. For the energy difference of successive spin states $\Delta m_\mathrm{J} = 1$ the energy can be calculated as $\Delta E = g_\mathrm{J} \Delta m_\mathrm{J} \mu_\mathrm{B} B$ with $g_\mathrm{J} = 1.24166(7)$ as discussed in Ch. 2.1. We can drive the transition between these states using frequencies in the RF regime and by measuring the resonance frequencies $f_\mathrm{RF} = 1.738\,\mathrm{MHzG^{-1}}|B|$ we can determine the magnetic field.

In detail, we trap our atoms in the ODT and apply a short RF pulse via an RF ring antenna placed under the vertical magnetic field coils, which is a coil with a single winding, and drive transitions between the different Zeeman states. We can scan the RF frequency sent to the antenna, and once we are on resonance, the driving brings atoms into the excited spin state, resulting in the loss of atoms due to spin-relaxation processes.

An example of such a measurement to calibrate the compensation cage in the y-direction is shown in Fig. B.1. The signals are shown in Fig. B.1 a for different powers of the RF signal. It can be seen that at high power, the signal is power broadened, which makes it easier to find the initial signal. By reducing the power, we get a much narrower signal, and for 30 dB the signal has a width of $\Delta f \approx 20\,\mathrm{kHz}$. This allows us to measure the magnetic field with a precision of $\Delta B < 20\,\mathrm{mG}$. To calibrate the coil, we measure the resonance frequencies for different currents applied to the coils and fit them with a linear function $|B| = a \times I + |B_0|$ as shown in Fig. B.1.

For the vortex measurements we want to make sure that the magnetic field strength $|B|$ does not vary for different angles ϕ, since the final magnetic field is a superposition of each field created by three different pairs of coils as described in Sec. 2.2.5. Therefore we measure the magnetic field for different angles ϕ, check that the magnetic field does not change, and recalibrate the magnetic field coils if necessary. Since

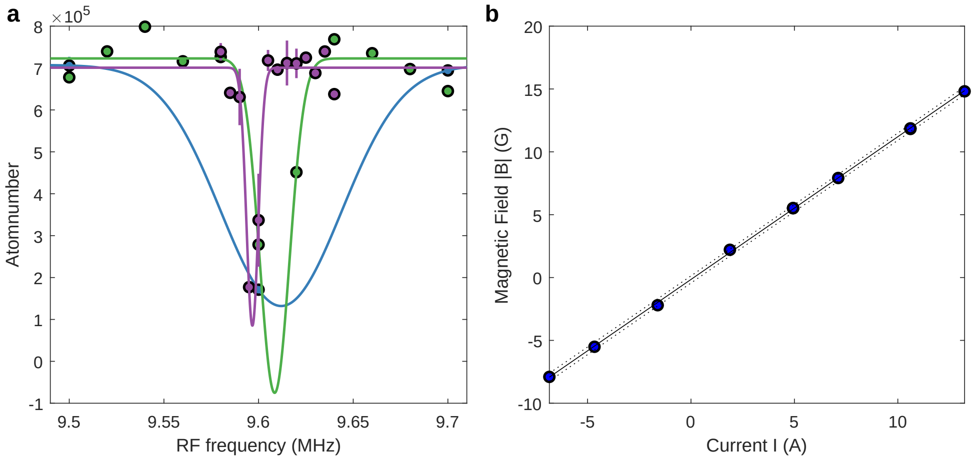

Figure B.1: Radio-Frequency spectroscopy to calibrate the magnetic field of the compensation cage in y-direction. a) The atomnumber for different RF frequencies is measured for the RF amplifier attenuated by 10 dB (●), 20 dB (●) and 30 dB (●) and the corresponding Gaussian fits. The signal from the 30 dB measurement is used to determine the resonance. b) The resonant frequencies for different voltages applied to the coils are plotted. The resonance frequencies are translated to magnetic fields via $B = f_{\mathrm{RF}}/1.738\,\mathrm{MHz\,G^{-1}}$. A linear fit is applied giving $|B| = 1.146\,\mathrm{G/A} \times I - 0.15\,\mathrm{G}$

some magnetic field values cannot be measured by RF spectroscopy in our experiment, due to crosstalk between the RF amplifier for the RF signal and the measured coils, we perform atom-loss spectroscopy around known Feshbach resonances as described in Sec. A. An example is shown in Fig. B.2, where we have checked the rotation at a magnetic field $|B| = 17\mathrm{G} - 17.3\,\mathrm{G}$ with ^{164}Dy . The white lines show the narrow resonances, which we are using as references. We can see that the magnetic field $|B|$ remains constant over the whole rotation in an error region of $\Delta B < 20\,\mathrm{mG}$.

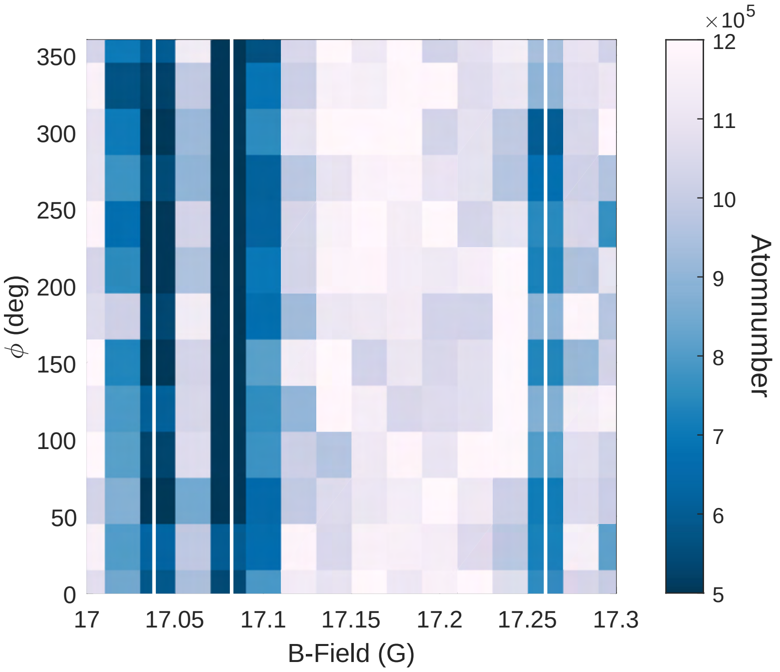

Figure B.2: Feshbach resonance spectrum between $B = 17 - 17.3$ G for $\theta = 30^\circ$ and $\phi = 0^\circ - 360^\circ$ Feshbach loss spectroscopy is performed for different magnetic fields B and angles ϕ. The cloud is evaporated at 17 G at $\theta = 30^\circ$ and at the angle ϕ. The magnetic field strength is then quenched to the final value B and held for $t_{\mathrm{hold}} = 500$ ms. The cloud is imaged horizontally after $t_{\mathrm{TOF}} = 26$ ms. The position of the loss features, indicated by the white lines, do not change for the different ϕ within the measurement accuracy $\Delta B = 20$ mG.